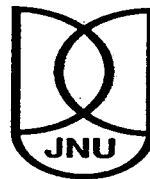# Characterization of entanglement and dynamics of quantum correlations in nonclassical systems

A Thesis

Submitted for the Degree of

DOCTOR OF PHILOSOPHY

HIMADRI SHEKHAR DHAR

School of Physical Sciences
Jawaharlal Nehru University
New Delhi - 110 067, INDIA
June 2014

Dedication

To Amma,
my first friend,
teacher and guide
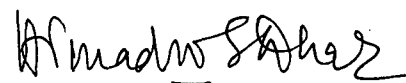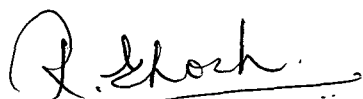
and

Baba and Ma,
for their love, care
and unconditional support

I hereby declare that the work reported in this thesis is entirely original and has been carried out by me independently in the School of Physical Sciences, Jawaharlal Nehru University, New Delhi under the supervision of Prof. Rupamanjari Ghosh, and partly in Harish-Chandra Research Institute, Allahabad under the co-supervision of Dr. Aditi Sen(De). I also declare that this work has not formed the basis of award of any Degree, Diploma, Fellowship, Associateship or similar title of any University or Institution.
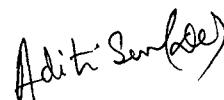
June 2014

Himadri Shekhar Dhar

Prof. Rupamanjari Ghosh

Thesis Supervisor

Dr. Aditi Sen(De)

Thesis Co-Supervisor

Prof. Subhasis Ghosh

Dean

School of Physical Sciences

Jawaharlal Nehru University

New Delhi - 110 067

India

Acknowledgment

The last five years have been an exciting journey filled with wonderful experiences and memories. As it nears its end, this important milestone is a testament to the efforts of many who have supported me along the way. Beyond the few words in this acknowledgment, I shall forever be indebted to them for their various contributions.

I am extremely fortunate to have worked under the tutelage of Prof. Rupamanjari Ghosh at Jawaharlal Nehru University (JNU), New Delhi. Under her guidance, my formative years in research have been an enriching experience, and I shall always be grateful. Prof. Ghosh has always provided direction and critical insight to my research, all the while providing me the independence to explore new and interesting ideas and set up successful collaborations. Her efforts to ensure I inculcate meticulous presentation and writing skills, as part of my research training, is noteworthy. She has ably guided me through all aspects of my scholarly life and has been an inspiration and I would like to thank her for being a gracious and kind supervisor.

I shall always be grateful to Dr. Aditi Sen(De), my co-supervisor at Harish-Chandra Research Institute (HRI), Allahabad, for introducing me to the beautiful world of quantum information and encouraging me to pursue a career in research. She has been my teacher and research advisor since my Masters and is largely responsible for shaping my research interests. I would like to thank her for her guidance at every step of my research and her selfless attention and encouragement to perform better. My gratitude for Aditi di is not just limited to research. I am grateful for her care and hospitality, especially during my various trips to Allahabad. Working with her has been an experience beyond words and I am grateful to have known her and been her student.

I would also like to take the opportunity to express my gratitude to Dr. Ujjwal Sen at HRI, who along with Aditi di, has been instrumental in giving direction to my research work. Ujjwal da has collaborated with me on most of my projects and significantly contributed to the development of my doctoral thesis. He has been a wonderful teacher and a mentor. I

Contents

List of Publications

Journal Articles:

1. **Himadri Shekhar Dhar**, Arpita Chatterjee, and Rupamanjari Ghosh, *Mapping generalized Jaynes-Cummings interaction into correlated finite-sized systems*, Journal of Physics B: At. Mol. Opt. Phys. **47**, 135501 (2014).

2. **Himadri Shekhar Dhar**, Rupamanjari Ghosh, Aditi Sen(De), and Ujjwal Sen, *Cumulative quantum work-deficit versus entanglement in the dynamics of an infinite spin chain*, Physics Letters A **378**, 1258 (2014).[†]

3. Lavisha Jindal, Ameya Deepak Rane, **Himadri Shekhar Dhar**, Aditi Sen(De), and Ujjwal Sen, *Patterns of Genuine Multipartite Entanglement in Frustrated Quantum Spin Systems*, Physical Review A **89**, 012316 (2014).

4. **Himadri Shekhar Dhar**, Aditi Sen(De), and Ujjwal Sen, *Characterizing Genuine Multisite Entanglement in Isotropic Spin Lattices*, Physical Review Letters **111**, 070501 (2013).[†]

5. **Himadri Shekhar Dhar**, Subhashish Banerjee, Arpita Chatterjee, and Rupamanjari Ghosh, *Controllable quantum correlations of two-photon states generated using classically driven three-level atoms*, Annals of Physics **331**, 97 (2013).[†]

6. **Himadri Shekhar Dhar**, Aditi Sen(De), and Ujjwal Sen, *Density Matrix Recursion Method: Genuine Multisite Entanglement Distinguishes Odd from Even Quantum Heisenberg Ladders*, New Journal of Physics **15**, 013043 (2013).[†]

[†]The results in this article are a part of the thesis.

7. Arpita Chatterjee, **Himadri Shekhar Dhar**, and Rupamanjari Ghosh, *Nonclassical properties of states engineered by superpositions of quantum operations on classical states*, Journal of Physics B: At. Mol. Opt. Phys. **45**, 205501 (2012).

8. **Himadri Shekhar Dhar**, Rupamanjari Ghosh, Aditi Sen(De), and Ujjwal Sen, *Quantum discord surge heralds entanglement revival in an infinite spin chain*, EPL (formerly Europhysics Letters) **98**, 30013 (2012).[†]

9. **Himadri Shekhar Dhar** and Aditi Sen(De), *Entanglement in resonating valence bond states: ladder versus isotropic lattices*, Journal of Physics A: Math. Theor. **44**, 465302 (2011).[†]

Conference Proceedings:

1. **Himadri Shekhar Dhar**, Rupamanjari Ghosh, Aditi Sen(De), and Ujjwal Sen, *Role of an information-theoretic measure of quantum correlation in a dynamical phase transition of entanglement*, Proc. SPIE **8173**, 81731P (2011).[†]

2. **Himadri Shekhar Dhar**, Aditi Sen(De), and Ujjwal Sen, *Scaling of Genuine Multisite Entanglement in 2D Heisenberg Spin Systems*. (To appear in Physics Teacher, India).[†]

Preprints:

1. **Himadri Shekhar Dhar**, Arpita Chatterjee, and Rupamanjari Ghosh, *Generating continuous variable entangled states for quantum teleportation using a superposition of number-conserving operations*, arXiv:1312.6226. (Under review).[‡]

2. Uttam Singh, Utkarsh Mishra, and **Himadri Shekhar Dhar**, *Decoherence-protected Multipartite Quantum Correlations Using Weak Measurement Reversal*, arXiv:1403.2939. (Under review).

[†]The results in this article are a part of the thesis.
[‡]The results in this article are a part of Appendix A.

Selected conference presentations:

1. *Generating continuous variable nonclassical states using superposition of number conserving quantum operations*, conference talk at the International Program on Quantum Information: IPQI-2014, Institute of Physics, Bhubaneshwar, India, 17–28 February 2014.

2. *Characterizing genuine multipartite entanglement in 2D quantum spin lattices*, selected talk at the 13th Asian Quantum Information Science Conference: AQIS-2013, The Institute of Mathematical Sciences, Chennai, India, 25–30 August 2013.

3. *Scaling genuine multisite entanglement in 2D Heisenberg spin systems*, talk selected for the "Best physicist" award at the 31st Young Physicist's Colloquium: YPC-2013, organized by the Indian Physical Society at Saha Institute of Nuclear Physics, Kolkata, India, 22–23 August 2013.

4. *Quantum discord surge heralds entanglement revival in an infinite spin chain*, poster presented at the Quantum Discord Workshop, Center for Quantum Technologies, National University of Singapore, Singapore, 9–13 January 2012.

5. *Bipartite and multipartite entanglement in resonating valence bond ladders*, conference talk at the International School and Conference on Quantum Information: ISCQI-2011, Institute of Physics, Bhubaneshwar, India, 13–22 December 2011.

6. *Role of an information-theoretic measure of quantum correlation in a dynamical phase transition of entanglement*, poster presented at the International Conference on Fiber Optics and Photonics: PHOTONICS-2010, Indian Institute of Technology, Guwahati, India, 11–15 December 2010.

Abstract

In recent years, quantum information theory (QIT) has been on the foreground of contemporary research in quantum physics and has heralded a new era in information science and computation. At the quantum scale, the intrinsic nonclassicality of nature is the fundamental resource that enables us to design futuristic protocols for quantum computation and communication. Importantly, this allows QIT to proliferate in broader physical regimes and permits descriptions of quantum protocols in different physical systems, in condensed matter, quantum optics, nanoscience, and biochemistry. Experimental advances in ion-traps, photonic systems and optical lattices have ensured simulation of quantum many-body systems that may serve as substrates for application of QIT protocols and other quantum tasks.

The characterization and classification of quantum correlations in physical systems is a fundamental aspect of understanding the nonclassical world. The first major development in the characterization of quantum correlation in composite physical systems is the measure of entanglement, which is an important resource for performing various quantum information and computation tasks, such as quantum dense coding, quantum teleportation, quantum key distribution, and one-way quantum computation. Though the operationality of entanglement is well developed for low-dimensional quantum systems, its characterization in multipartite systems, which are important for developing scalable quantum devices, is a formidable task. Further, the broad concept of quantum correlations is not completely captured by entanglement. Information-theoretic quantum correlations such as quantum discord and quantum work-deficit, described independently of the entanglement-separability criteria, are important indicators of nonclassicality. The primary motivation of the research in my thesis is borne from these two interesting aspects of quantum correlations, viz., the characterization of entanglement in large multipartite quantum states (**Part I**) and the study of the dynamics of information-theoretic quantum correlations in relation to entanglement in quantum systems (**Part II**). The principal research work in the thesis utilizes the theoretical concepts and tools of QIT and its interface with quantum many-body physics and quantum optics.

Chapter 1 is an introduction to the thesis and focuses on the development of nonclassicality in different quantum systems. From a purely physical perspective, the concept of nonclassicality is dependent on the quantum system under study and a clear understanding of what is classical. In quantum optics, this can arise from the nature of the statistics of the optical field or the correlations shared by the quadrature components. In QIT, the nonclassicality is measured by the correlations shared by two or many parts of a quantum system. We begin the introduction with a brief background on the origin of nonclassicality, followed by a short review on nonclassicality and quantum correlations in different physical systems. We then discuss the entanglement-separability criteria for characterizing quantum correlations in composite quantum states. We introduce the basic concepts and theoretical formulations that lead to detection and analytical quantification of bipartite entanglement using measures such as entanglement distillation, entanglement of formation, concurrence and logarithmic negativity. We then extend the formulation of entanglement for multiparty quantum systems and discuss the characterization and quantification of multipartite entanglement. Next, we introduce the information-theoretic measures of quantum correlations such as quantum discord, quantum work-deficit and measurement-induced disturbance. We end with a brief discussion on nonclassicality in continuous variable systems arising from quasiprobability distribution, photon statistics and quadrature correlations, with an extension of entanglement and information-theoretic quantum correlations in the continuous variable regime.

In **Part I** of the thesis, we study the characterization of entanglement in a class of large superposed states, obtained from nearest-neighbor dimer coverings on spin-1/2 lattices, also called resonating valence bond (RVB) states, which are possible ground states of the Heisenberg spin-1/2 lattices. RVB systems are of interest to the condensed matter physics community, for their possible connection to high-T_c superconductivity and exotic topological phases. RVB states have been experimentally simulated using ultracold atoms in optical lattices and are of interest in QIT for its possible role in fault-tolerant quantum computation.

In **Chapter 2**, we investigate the behavior of bipartite and multipartite entanglement in a quantum spin-1/2 ladder, with RVB ground states, and contrast it with the results for isotropic quantum lattices. Using quantum information theory concepts such as monogamy of entanglement and quantum telecloning, we obtain analytical bounds for the behavior of entanglement in quantum spin-1/2 ladders. Further, using QIT properties such as strong sub-additivity of von Neumann entropy, we show that infinite or periodic isotropic quantum spin-1/2 lattices are always genuinely multipartite entangled. We then perform a numerical analysis of the amount of bipartite and multipartite entanglement in the two-leg RVB ladder. We observe that the amount of nearest-neighbor bipartite entanglement in the rails of the ladder decreases with increasing size in contrast to the behavior of bipartite entanglement

along the rungs of the ladder. Further, the multipartite entanglement decreases with increasing size. The obtained numerical values strictly follow the analytical bounds obtained from QIT. The behavior of bipartite and multipartite entanglement in the RVB ladder is in stark contrast with their behavior for isotropic RVB systems, which tends to have negligible bipartite entanglement with finite multipartite entanglement. We observe that a change in geometry of RVB systems can radically alter the qualitative behavior of both bipartite and multipartite entanglement. We conclude with a discussion on possible application of such systems in QIT protocols.

In **Chapter 3**, we extend our study on RVB systems to characterize genuine multipartite entanglement in multi-legged quantum spin-1/2 ladders and isotropic lattices with a large number of spin sites. Calculation of relevant physical quantities, such as entanglement, for large sized lattices, is limited by computational difficulty. In this chapter, we introduce a new iterative analytical technique, the density matrix recursion method, to efficiently calculate reduced density matrices of large RVB states. This allows us to characterize the behavior of genuine multipartite entanglement, in large RVB systems, using a computable measure called the generalized geometric measure. We apply this technique to distinguish between even and odd multi-legged ladders. Specifically, we show that while genuine multipartite entanglement decreases with increasing system size for the even-legged ladder, it does the opposite for odd-legged ones. For the isotropic lattice, the iterative analytical method is used to calculate the entanglement of finite-size 2D lattices, which through finite-size scaling, enables us to obtain an estimate of the genuine multipartite entanglement in an infinite square lattice. We conclude with a discussion on extrapolating the method for investigating other single- and multiparty properties of such states.

In **Part II** of the thesis, we study the dynamics of information-theoretic quantum correlation measures and entanglement in two archetypal quantum systems from many-body physics and quantum optics. The first is the infinite anisotropic XY-spin chain in a transverse magnetic field while the second is a three-level atom interacting with classical optical fields. Since no unique analytical results exist that operationally relate the two paradigms of quantum correlations, viz. entanglement-separability and information-theoretic, finding quantitative relations between them in many-body systems or in quantum optical models may provide interesting insights.

In **Chapter 4**, we investigate the dynamics of information-theoretic measures of quantum correlation and entanglement, in a time-evolved nonequilibrium state of the infinite anisotropic quantum XY spin chain in a transverse time-dependent field. It is observed that nearest-neighbor entanglement undergoes a dynamical phase transition with respect to the field parameter leading to entanglement death and occasional revival. We show that

the dynamical phase transition of entanglement is qualitatively related to the dynamics of information-theoretic measures of quantum correlation such as quantum discord and quantum work-deficit. We derive quantitative relations showing that the entanglement death and subsequent revival are heralded by the rate of increase of quantum discord in the vicinity of the critical value of entanglement death. Further, the revival of entanglement is also directly related to the cumulative quantum work-deficit during the dynamical evolution of the system. The behavior of quantum correlation also provides useful leads on other important aspects of the dynamics such as quantum quenching.

In **Chapter 5**, we analytically derive and characterize the dynamics of two-photon quantum correlations generated by the interaction of a three-level atom in the Ξ, Λ, or V configuration, with two classical external driving fields. Using the example of a rubidium atom in each configuration, in the presence of level decays, under the rotating-wave approximation and using the single-photon approximation, one can compute information-theoretic correlations, such as measurement induced disturbance, quantum discord, and quantum work-deficit, and compare the results with that of entanglement, for the generated two-photon state. It is observed that the qualitative hierarchy, monotonicity and steady-state behavior of the quantum correlations can be controlled through the choice of parameters such as atomic decay constants and external driving field strengths.

In **Chapter 6**, we summarize the basic results of the thesis and briefly discuss future directions that emanate from the results obtained in the research work.

In **Appendix A**, we provide an example for the generation of entanglement in continuous variable (CV) optical states, using a superposition of number-conserving non-Gaussian operations. The bimode entangled states are observed to be efficient quantum channels in CV quantum teleportation protocols. The study demonstrates the ready applicability of CV states in quantum information protocols.

The thesis is an attempt to contribute to the rapidly developing field of quantum information and its contemporary applications in many-body systems and quantum optics. The characterization of entanglement and the dynamics of quantum correlations in relevant quantum systems are important steps in identifying useful resources for designing futuristic quantum technologies. The characterization of multisite entanglement in spin lattices are crucial for understanding of the distribution of quantum correlation in large quantum systems that can be harnessed in developing scalable quantum computers. With the advent of quantum devices that require the transfer of quantum information between discrete spin systems and optical cavities and storage of information, the study of the dynamics of quantum correlations in both many-body and optical quantum systems is of great relevance.

CHAPTER 1

Introduction

What we observe is not Nature itself, but Nature exposed to our method of questioning. – Werner Heisenberg

Nonclassicality is a fundamental feature of modern physics and the existence of quantum correlation is one of its prominent signatures. Present day science predominantly ascribes quantum physics as the theory to describe Nature and often relies on inherent quantum correlation in physical systems to explain various exotic phenomena that are beyond the realm of classical physics. In the Introduction, we take a look at a slightly specialized description of quantum correlation, primarily those that are relevant to the field of quantum information theory and its interface with quantum many-body physics and quantum optics.

1.1 Background

The advent of quantum theory in the early 20th Century introduced concepts that radically challenged the classical elements of contemporary physics and its description of Nature. An important example is the presence of nonclassical correlation in a quantum mechanical description of composite physical systems. Nonclassical correlations allow a complete description of a composite system without providing all the information about its subsystems, and was mentioned by Schrödinger as the "characteristic trait of quantum mechanics" [1] and originally referred as "Verschränkung" or entanglement. The first instance of confrontation with the classical viewpoint of physics, when quantum correlations are considered, was raised by Einstein, Podolsky and Rosen (EPR), who were troubled by the violation of the conjunction of "objective reality" and "locality" in the quantum description of a physical system with spatially separated subsystems, as mentioned in their seminal paper of 1935 [2]. Over the years, important theoretical and experimental results have supported and enriched the quantum viewpoint of the physical world and established quantum theory as one of the foundational cornerstones of modern physics [3]. Significantly, the enigmatic trait of the quantum world arising due to quantum correlations is at the heart of major developments in the 21st Century quantum physics and is the fundamental resource for quantum information processing [4–6].

The signature of nonlocal quantum correlations was first quantified through the seminal derivation of Bell inequalities in 1964 [7]. Bell showed that for any local variable based theoretical description of quantum mechanics, the bipartite correlation, in any experimental setup, was statistically constrained by the Bell inequalities. In the following years, the experimental demonstration [8] of the violation of the Bell inequalities in certain entangled states[1] confirmed the impossibility of any local variable description of quantum phenomena. The violation of Bell inequalities led to a critical interest in quantum correlations for future development of concepts such as quantum communication and the possibility of developing computational devices with no classical analogue [10, 11]. However, it was not until the late 20th Century, that the quantum correlation, in its quintessential form of entanglement, was established in terms of local quantum operations and classical operations [12]. In subsequent years, various detection and quantification procedures for bipartite entanglement, such as inequalities derived from the von Neumann entropy [13, 14], majorization conditions [15], and positive partial transpose criteria [16, 17], were studied (for a review, see [6]). In the early 21st Century, the idea of quantum correlation was extended beyond the

---

[1]Most Bell inequality experiments suffer from certain loopholes in the experimental design or the measurement. For a review of the various loopholes and their eradication in contemporary Bell experiments, see [9].

entanglement-separability paradigm by the introduction of information-theoretic character-
izations of quantum correlation [18–20]. These measures sought to broaden the scope of
quantum correlation in composite systems and demonstrated that residual correlation of
nonclassical nature could be obtained in unentangled or separable quantum systems (for a
review, see [21]). Over the last decade or so, quantum correlation was established as a re-
source that enables performance of certain quantum tasks beyond the measures of classical
resources. It has been the cornerstone of the relatively new interdisciplinary field of quantum
information theory (QIT) and quantum computation [4, 5].

The impact of quantum correlation in modern day research can hardly be overstated.
Besides playing a predominant role in the development of quantum information theory, the
extensive work on entanglement theory [6] and information-theoretic quantum correlations
[21] have generated an enormous interest in inter-disciplinary research. Important results
from quantum information are routinely applied to study interesting quantum phenomena in
a host of different disciplines, such as many-body physics [22], quantum optics [23, 24], quan-
tum gravity and black holes [25], and quantum biology [26]. Apart from inter-disciplinary
research, a significant development has also been made in our fundamental understanding of
the foundations of quantum mechanics [27]. Interesting features such as quantum contextu-
ality [28], quantum measurements [29] and quantum nonlocality [9] have received substantial
attention from the perspective of quantum information theory.

This introductory chapter is arranged as follows. We begin with a brief review of nonclas-
sicality and quantum correlation in composite systems in Section 1.2. We quantify quantum
correlation measures from two different perspectives, namely the entanglement-separability
paradigm and the information-theoretic perspective. In Section 1.3, we introduce and discuss
the entanglement-separability paradigm. We discuss the different monotones of entanglement
and their detection schemes. The section also contains a brief discussion on the quantifica-
tion of multipartite entanglement measures. In Section 1.4, we present the formalism and
quantification of information-theoretic quantum correlations. We then present a brief discus-
sion on nonclassicality in continuous variable systems in Section 1.5, ending with an outline
of the thesis in Section 1.6.

1.2 Nonclassicality and quantum correlation: A short review

The fundamental basis of what constitutes nonclassicality or how quantum correlations are
conceptually formulated is not limited to a single theoretical framework. In a broad sense,
nonclassicality arises when composite physical systems or degrees of freedom are correlated
in ways that are inaccessible to classical objects [21]. The earliest forms of quantifiable
nonclassicality in two-party quantum states (bipartite quantum states) arose from the Bell

inequality violation of such states. The conceptualization of quantum correlation has evolved over the years. The fundamental idea that violation of Bell inequality was the key principle of defining quantum correlation suffered a setback when it was shown that there exist certain entangled states that do not violate the Bell inequalities and hence, violation of Bell inequality is a sufficient but not necessary condition for entanglement [12]. This led to the realization that states without entanglement are those which can be prepared using local quantum operations and classical communication (LOCC) [6]. The set of states that cannot be prepared using LOCC are then called entangled. Consequently the set of separable states is smaller than the set of states that do not violate Bell inequalities. Incidentally, LOCC may introduce other features such as local indistinguishability of orthogonal quantum states that may not be possible in the classical realm [30] (also see [21]). There may exist states that are separable yet nonclassical, as revealed by the conceptualization of information-theoretic measures of quantum correlation. The set of states that are truly free from all forms of quantum correlation is significantly smaller than the set of separable states emerging from the entanglement-separability criteria, leading to a widely acknowledged fact that the states in the quantum domain are always quantum correlated.

Entanglement has been a key ingredient in numerous QIT applications such as quantum teleportation [31], quantum dense coding [32], and quantum key distribution [33]. It is also known to play an important role in the development of quantum computing, such as measurement-based (one-way) quantum computing [34] and linear optics quantum computing [35] (cf. [36]) (for a detailed discussion, see Reference [6]). Entanglement measures, such as entanglement of formation [37, 38] and logarithmic negativity [39] have been used in the analysis of quantum critical phenomena [40, 41], quantum phase transitions [22, 42], tensor-network simulations [43, 44], and quantum spin channels [45] (for a review, see Reference [22]). In particular, entanglement is proposed to be an universal indicator of quantum critical phenomena. This has allowed the development of novel interdisciplinary interfaces of quantum information theory with quantum many-body physics [22] and quantum optics [23, 24]. However, the formal structure of entanglement, despite great strides in recent decades, is still incomplete. The detection and quantitative characterization of entanglement in higher dimensional mixed bipartite systems and in complex multipartite states is still not tractable nor well-defined [6].

In recent years, it has been established that the essence of nonclassical correlation and resources can be taken beyond the typical domain of entanglement [21]. With the introduction of information-theoretic concepts, the definition of quantum correlation and what constitutes truly separable or non-quantum correlated physical states has undergone drastic changes. The first protocol that considered shared quantum resources beyond entanglement

was the protocol for deterministic quantum computation with one qubit (DQC1), which achieved exponential speed up using a resource qubit very weakly entangled to a group of maximally mixed qubits [46]. Within a few years, a quantum correlation measure beyond the entanglement-separability criteria, and from an information-theoretic perspective, was done with the introduction of the measure of quantum discord [18, 19]. The possibility of connecting quantum discord to the performance of certain computation tasks [47] heralded a new discourse in the perception of quantum correlation. It was later shown that quantum discord has a finite scaling with the efficiency of the DQC1 protocol, even though entanglement is negligible [48][2]. Another information-theoretic quantum correlation measure based on *negentropy* and local and global *work extraction* was introduced, called quantum work-deficit [20]. Subsequently, other measures of quantum correlation, all harnessing certain information-theoretic properties were introduced, such as measurement induced disturbance [50, 51], quantum dissonance [52], relative entropy of discord [53] and others (for an extensive review, see [21]). These information-theoretic quantum correlation measures have significant role in important quantum tasks such as local broadcasting [54], state discrimination [55], state merging [56] and quantum metrology [57]. Quantum correlation measures such as quantum discord and quantum work-deficit have also been extensively applied to study many-body phenomena such as quantum phase transitions [58], dynamics in many-body systems [59] and in open quantum systems [60]. However in contrast to entanglement, the operational significance and interpretation of information-theoretic quantum correlation are still debatable. As mentioned earlier, the set of all information-theoretic quantum correlated states is much larger than the set of all entangled states, leading to almost all dynamical maps retaining residual quantities of quantum correlation. This makes the study of identifying quantum processes that contain truly useful quantum correlation, a difficult task.

In a slightly different direction, the ideas of nonclassicality were formalized in a different manner for multi-photon electromagnetic fields in quantum optics, partly through the seminal results on quantum theory of optical coherence [61, 62] and atom-photon interaction [63] (also see [64]). The description of normal or symmetric ordered correlation functions using suitable quasiprobability distribution allows the classification of nonclassicality in quantum optical fields, with a sufficient criteria set by the negativity of such quasiprobability functions [61, 64]. Important milestones in quantum correlation of optical states were also achieved in experimental demonstration of two-photon interferometry [65] and generation of entangled states [8, 66]. Further, experimental observations of nonclassical phenomena such as sub-Poissonian statistics, quadrature squeezing and photon antibunching (see [64]) provided sig-

---

[2]In Reference [49], the authors have claimed that their results to the model of DQC1, shows that quantum discord is possibly not the reason behind its speedup.

nificant indicators of nonclassicality. In recent years, the notion of entanglement-separability and other information-theoretic measures of quantum correlation have been extended to continuous variable optical multi-photon states, that have been extensively applied in numerous quantum information protocols [21, 24].

A more detailed discussion on the different aspects of nonclassicality and the development of the various characterizations of quantum correlation is beyond the scope of this thesis. We limit our brief discussion to only those measures of quantum correlation that have, in recent years, been extensively applied to study various quantum information protocols and are important tools in studying quantum many-body and quantum optical systems. Further, we only consider the detailed analysis of quantum correlation measures that are directly relevant to the thesis. In the next section (Section 1.3), we start by describing the entanglement-separability paradigm that include subsections on entanglement detection (Section 1.3.1), monotones (Section 1.3.2), bipartite entanglement measures (Section 1.3.3) and multipartite entanglement (Section 1.3.4). We discuss information-theoretic quantum correlation in Section 1.4. and some interesting facets of characterizing continuous variable nonclassicality in Section 1.5.

1.3 Entanglement-separability paradigm

The entanglement-separability paradigm is borne out of Schrödinger's initial assessment of the characteristic feature of composite quantum systems [1]. For an entangled state, the total information of the subsystems does not yield the complete information of the whole system. In this section, we will define entangled states and present a basic picture of the operational tools involved in detecting and quantifying entanglement and its characterization in various physical systems.

Let us now consider a formal mathematical description of the idea of entanglement. For a bipartite quantum state, the associated Hilbert space $\mathcal{H}$ is a tensor product of the space of its subsystems, $\mathcal{H}_\mu \otimes \mathcal{H}_\nu$. We call a bipartite pure quantum state, $|\psi\rangle$, in the Hilbert space $\mathcal{H}_\mu \otimes \mathcal{H}_\nu$, entangled, if it cannot be represented in the product form $|\psi_\mu\rangle \otimes |\psi_\nu\rangle$, where $|\psi_\mu\rangle \in \mathcal{H}_\mu$ and $|\psi_\nu\rangle \in \mathcal{H}_\nu$. States of the form $|\psi_\mu\rangle \otimes |\psi_\nu\rangle$ are called product or separable pure states. The concept of entanglement can be given a clear information-theoretic basis in this case. A product or separable state allows the total information of the composite system $|\psi\rangle$ to be obtained from its reduced subsystems $|\psi_\mu\rangle$ and $|\psi_\nu\rangle$. For entangled states, such decompositions are not allowed and the most general form is given by the relation,

$$|\psi\rangle = \sum_i^{d_\mu} \sum_j^{d_\nu} a_{ij} |\mu_i\rangle \otimes |\nu_j\rangle \tag{1.1}$$

where, d_μ and d_ν are the dimensions of the two subsystems. $\{|\mu_i\rangle\}$ and $\{|\nu_i\rangle\}$ are orthonormal bases in the subsystem Hilbert spaces, $\mathcal{H}_\mu$ and $\mathcal{H}_\nu$, respectively. A maximally entangled state has the form $|\psi\rangle = \frac{1}{\sqrt{d}} \sum_i^d |\mu_i\rangle \otimes |\nu_i\rangle$, where $d = \min(d_\mu, d_\nu)$.

The extension of the entanglement-separability paradigm to mixed bipartite states is not straightforward. For mixed states, the idea of separability extends beyond that of simple product states, as a convex decomposition over a set of product states, is also a separable state. An efficient method to formalize the separability condition in bipartite mixed states is using local operation and classical communication between the subsystems [12]. Let ρ be the density matrix of a mixed bipartite quantum state in the Hilbert space $\mathcal{H}_\mu \otimes \mathcal{H}_\nu$. For ρ to be separable, it must be of the general form

$$\rho = \sum_i p_i \, |\alpha_\mu^i\rangle\langle\alpha_\mu^i| \otimes |\beta_\nu^i\rangle\langle\beta_\nu^i|, \qquad (1.2)$$

where p_i are the classical probabilities, with $\sum_i p_i = 1$. $|\alpha_\mu^i\rangle(\in \mathcal{H}_\mu)$ and $|\beta_\nu^i\rangle(\in \mathcal{H}_\nu)$ are the locally prepared subsystems using an LOCC protocol. The mixed bipartite state is entangled if it can not be prepared in the form of Equation (1.2).

The idea of entanglement-separability in terms of representation as a product of subsystems (for pure states) or convex decomposition of products (for mixed states) can also be generalized to multiparty quantum systems. However, the extension is challenging due to different possible partitions available in a multiparty state. The simplest extension for pure states is that of k-separability. An N–party pure state, $|\psi\rangle_N$ is said to be k-separable if it can be written as a product of k pure subsystems, $|\mu_1\rangle \otimes |\mu_2\rangle ... \otimes |\mu_k\rangle$. For $k < N$, some of the N particles are entangled. If $k = N$, then the state is fully multipartite separable. A detailed discussion on multipartite entanglement is done in Section 1.3.4.

From the above discussion it is clear that entangled states cannot be prepared using local operations on each particle in a bipartite or an N-party state, followed by classical communication. For entanglement, there must exist prior interaction directly between the subsystems or via ancilla states leading to entanglement swapping [67]. This implies that for an initial separable state, the physical system is operated with a global unitary operator in the joint Hilbert space, $\mathcal{H}_\mu \otimes \mathcal{H}_\nu$ [68] to generate entanglement.

1.3.1 Detection of entanglement

The detection of entanglement and its quantification is a non-trivial problem. Even for bipartite systems, finding the convex decomposition, in the form of Equation (1.2), to establish the mixed state separability is a complicated procedure. There does not exist any general, operationally necessary and sufficient criteria to detect entanglement for arbitrary dimensions. However, over the years, several criteria have been developed to detect and quantify

entanglement, under specific constraints, using various numerical and operational aspects [69]. For arbitrarily large dimensions, the detection of entanglement is a NP-hard complexity problem [70]. In the following segment, we discuss some well-known entanglement detection protocols. For a broader review, see Reference [6] and [69].

1.3.1.1 Schmidt rank

For pure bipartite states in arbitrary finite dimensions, the Schmidt decomposition of the state and its rank is a necessary and sufficient indicator of entanglement. A bipartite pure state, $|\psi\rangle$, can be written in a general form given by Equation (1.1) and represented in terms of its Schmidt decomposition as

$$|\psi\rangle = \sum_i^s \lambda_i |\tilde{\mu}_i\rangle \otimes |\tilde{\nu}_i\rangle, \tag{1.3}$$

where $\{|\tilde{\mu}_i\rangle\}$ and $\{|\tilde{\nu}_i\rangle\}$ are orthonormal bases in the subsystem Hilbert spaces, $\mathcal{H}_\mu$ and $\mathcal{H}_\nu$, respectively. $s(\leq d = \min(d_\mu, d_\nu))$ and λ_i's are real numbers known as the Schmidt rank and the Schmidt coefficients, respectively. The derivation of Equation (1.3) from the general form [Equation (1.1)] is not very difficult. From Equation (1.1), we know that the coefficients a_{ij} form a $d_\mu \times d_\nu$ matrix, satisfying the condition $\sum_{ij} a_{ij}^* a_{ij} = 1$. a_{ij} can be written using a diagonal matrix, in its singular value decomposition of the form, $a_{ij} = \sum_{i'} v_{ii'} \lambda_{i'} w_{i'j}^*$, where v_{ij} and w_{ij} are unitary matrices and $\lambda_{i'}$ are the eigenvalues of the modulus of the a_{ij} matrix. Equation (1.1), using the decomposition can be written as, $|\psi\rangle = \sum_i^{d_\mu} \sum_j^{d_\nu} \sum_{i'} v_{ii'} \lambda_{i'} w_{i'j}^* |\mu_i\rangle \otimes |\nu_j\rangle$. Replacing, $|\tilde{\mu}_{i'}\rangle = \sum_i^{d_\mu} v_{ii'} |\mu_i\rangle$ and $|\tilde{\nu}_{i'}\rangle = \sum_i^{d_\nu} w_{i'j}^* |\nu_j\rangle$, we obtain the Schmidt decomposition in Equation (1.3).

The Schmidt rank s, is the rank of the matrix a_{ij}, and also the rank of both the subsystems. Drawing comparison with earlier discussion on separable pure states, we can conclude that they have Schmidt rank, $s = 1$. For rank, $s > 1$, the bipartite pure system is entangled. For maximally entangled states, the Schmidt rank, $s = d$, with Schmidt coefficients $\lambda_i = 1/\sqrt{d}$ (for all i). The Schmidt rank s can be easily obtained as the maximum rank of the reduced density matrices of the state, say $\mathrm{tr}_B(|\psi\rangle\langle\psi|)$.

1.3.1.2 Positive maps

The detection of bipartite pure entangled state using Schmidt decomposition is relatively simple as compared to mixed entangled states. The difficulty arises in establishing the separability criteria in terms of states that can be prepared using LOCC and can be written in the form given by Equation (1.2). Interestingly, a novel way of detecting separability in mixed bipartite systems is by analyzing the effect of positive maps on separable states of the form given by Equation (1.2) [17].

If $\mathcal{B}(\mathcal{H})$ is the set of all bounded operators in the Hilbert space $\mathcal{H}$, a linear positive map $\Lambda: \mathcal{B}(\mathcal{H}) \to \mathcal{B}(\mathcal{H})$, maps positive operators $\rho \in \mathcal{B}(\mathcal{H})$ onto positive operators $\Lambda(\rho) \in \mathcal{B}(\mathcal{H})$,

for all positive operators ρ. Positive or positive semi-definite operators have non-negative eigenvalues. Positive maps are hermiticity preserving but not always trace preserving. As most quantum systems under consideration can, in principle, be entangled to a much larger quantum system, any quantum operation on the space of density matrices must additionally be positive for the joint operation: a positive map (Λ) on the system of interest and the identity operation on the rest of the larger system. Hence, the extended map $\mathbb{I}_d \otimes \Lambda$: $\mathcal{B}(\mathcal{H}_d \otimes \mathcal{H}) \rightarrow \mathcal{B}(\mathcal{H}_d \otimes \mathcal{H})$, where $\mathbb{I}_d$ is the identity operator on the d-dimensional Hilbert space, must be positive for all quantum operation. Positive maps (Λ) are called completely positive maps when they are positive for all such extensions.

However all positive maps are not completely positive, an example being the transposition map ($\mathbb{T}$). Such positive maps are extremely useful in obtaining a separability criteria for the LOCC generated states in Equation (1.2). Let us apply the map ($\mathbb{I}_\mu \otimes \Lambda_\nu$), where Λ_ν is a positive but not completely positive map, on the state ρ from Equation (1.2). This gives us the relation,

$$
\begin{aligned}
(\mathbb{I}_\mu \otimes \Lambda_\nu)(\rho) &= \sum_i p_i \, \mathbb{I}_\mu(|\alpha_\mu^i\rangle\langle\alpha_\mu^i|) \otimes \Lambda_\nu(|\beta_\nu^i\rangle\langle\beta_\nu^i|), \\
&= \sum_i p_i \, |\alpha_\mu^i\rangle\langle\alpha_\mu^i| \otimes \tilde{\rho}_i^\nu,
\end{aligned}
\tag{1.4}
$$

since Λ_ν is a positive map, $\tilde{\rho}_i^\nu$ is a density matrix in $\mathcal{H}_\nu$. Hence, for separable states, $(\mathbb{I}_\mu \otimes \Lambda_\nu)(\rho)$ is always a valid description of a density matrix. In particular, it is positive. Therefore, the condition $(\mathbb{I}_\mu \otimes \Lambda_\nu)(\rho) \ngeq 0$, implies that the state ρ is entangled. For the state to be separable, it must satisfy the condition $(\mathbb{I}_\mu \otimes \Lambda_\nu)(\rho) \geq 0$, for all Λ_ν. However, the general classification of positive maps in higher dimension is not a completely understood problem.

A well-known detection for entanglement using positive maps, is that of partial transposition. The non-positive partial transpose (NPT), for the state ρ^{PT} ($= (\mathbb{I} \otimes \mathbb{T})\rho$) is an important entanglement detection criteria – the Peres-Horodecki or the partial transposition criteria [16]. Due to global properties of the transposition operation, the map can be applied on any one of the subsystems. $\rho^{PT} \ngeq 0$, i.e., ρ^{PT} has atleast one negative eigenvalue, implies that ρ is entangled. For smaller dimensions, viz. 2×2 and 2×3, the NPT criteria is a necessary and sufficient criteria for entanglement [17]. In higher dimensions, the NPT criteria is a sufficient condition for entanglement but not necessary. This is due to the fact that there exist positive partial transpose (PPT) states that are known to be entangled. Such states are examples of *bound entangled* states, that are defined as entangled states from which entanglement distillation is not possible [71]. Numerical evidence suggests that there may also exist NPT bound entangled states. However, a definite answer has not been obtained [72].

1.3.1.3 Entanglement witness

A special form of the Hahn-Banach theorem can be stated in the following way. For a point ρ outside a compact convex set $\mathcal{F}$, in a Banach space of finite dimensions, there will always exist a hyperplane that separates the point ρ from the set $\mathcal{F}$. If we consider, $\mathcal{F}$ to be the subset of all separable states[3] in space of all linear operators $\mathcal{B}(\mathcal{H})$, then there will always exist a hyperplane separating the set from an entangled state ρ. Let us define the hyperplane by a perpendicular vector $\mathcal{W}$ on the hyperplane, directed towards the space $\mathcal{F}$. The "projection", $\text{tr}(\mathcal{W}\rho_{sep})$, of any separable state (ρ_{sep}) on the hyperplane $\mathcal{W}$ is positive. Further, entangled states on the other side of the hyperplane have a negative projection on $\mathcal{W}$. In the language of linear operators, for an entangled state ρ, we can always obtain an operator $\mathcal{W} \in \mathcal{B}(\mathcal{H})$, such that the innerproduct for all separable states, $\text{tr}(\mathcal{W}\rho_{sep}) \geq 0$, while $\text{tr}(\mathcal{W}\rho) < 0$. We call the Hermitian operator $\mathcal{W}$ an entanglement witness [73].

The PPT criteria can be used to form an entanglement witness. Let ρ^{PT} be the partial transpose of an NPT state ρ. Let the state $|\xi\rangle$ be one of the eigenvectors of ρ^{PT}, corresponding to a negative eigenvalue. Set $\mathcal{W} = |\xi\rangle\langle\xi|$. It is straightforward to note that $\text{tr}(\mathcal{W}\rho) < 0$ for the entangled state ρ (not PPT bound entangled) and $\text{tr}(\mathcal{W}\rho_{sep}) \geq 0$ for all separable states.[4] $\mathcal{W}$ is therefore an entanglement witness for ρ.

The importance of entanglement witnesses is that it can be conveniently implemented in physical systems as the witnesses are Hermitian. It is currently one of the useful tools to detect entangled states in an experimental setting [74]. However, it is not possible to characterize all entangled states using a single entanglement witness and furthermore, given an entangled state, finding an optimal entanglement witness operator is a challenging task.

1.3.1.4 Entropic inequalities and majorization

The initial conceptualization of entanglement from the perspective of information, was only achieved after the formalization of the idea of what constituted *information* in a composite quantum system. This consisted in using the using concept of von Neumann entropy, $S(\rho) = -\text{tr}(\rho\log\rho)$ [75], to quantify the information content of a quantum state ρ, in analogy with the classical Shannon entropy, $H(X) = -\sum_i p_i \log p_i$ (where $p_i > 0$ and $\sum_i p_i = 1$), of a classical random variable X.

In terms of the von Neumann entropy $S(\rho)$, Schrödinger's idea of an entangled system containing more information than the sum of its subsystems could be quantified. It was shown that the subsystems of an entangled state could be more disordered than the composite system, which is not possible for classical random varaibles and their marginals [13]. In terms of general α-entropies the following scalar separability criteria is obtained [14]. For a

---

[3]One can show that the set of separable states is convex and compact.

[4]The above example has been taken from Reference [68].

separable state,

$$S_\alpha(\rho) \geq S_\alpha(\rho_\mu), \ \ S_\alpha(\rho) \geq S_\alpha(\rho_\nu), \tag{1.5}$$

where $S_\alpha(\rho) = \frac{1}{1-\alpha} \log \mathrm{tr} \rho^\alpha$, and $\rho_{\mu(\nu)} = \mathrm{tr}_{\nu(\mu)}(|\psi\rangle\langle\psi|)$ is the reduced density matrix of the subsystem of the state $|\psi\rangle$ in the $\mathcal{H}_\mu \otimes \mathcal{H}_\nu$ Hilbert space. $S_\alpha(\rho)$ reduces to the von Neumann entropy for $\alpha = 1$. However, this property could be violated by certain entangled states [6].

A stricter version of the entropic inequality can be obtained using majorization [15]. The concept of majorization [76] can be introduced as follows: For two vectors $x = (x_1, x_2, x_3, ..., x_n)$ and $y = (y_1, y_2, y_3, ..., y_n)$, we say x is majorized by y, or $x \prec y$, if

$$\sum_{i=1}^{k} x_i^\downarrow \leq \sum_{i=1}^{k} y_i^\downarrow, \text{ for } 0 < k \leq n - 1, \text{with equality at } k = n, \tag{1.6}$$

where, $x^\downarrow(y^\downarrow)$ is $x(y)$ with coefficients in descending order, i.e., $x_1^\downarrow \geq x_2^\downarrow \geq ... \geq x_n^\downarrow$ ($y_1^\downarrow \geq y_2^\downarrow \geq ... \geq y_n^\downarrow$). For probability distributions, $x \prec y$ implies that $H(x) \geq H(y)$.

The majorization concept leads to a separability criteria, as obtained in Reference [15]. For separable states,

$$\varepsilon(\rho) \prec \varepsilon(\rho_\mu), \ \ \varepsilon(\rho) \prec \varepsilon(\rho_\nu), \tag{1.7}$$

where, $\varepsilon(\rho)$, $\varepsilon(\rho_\nu)$, and $\varepsilon(\rho_\mu)$ are the vectors of the eigenvalues of ρ, ρ_ν, and ρ_μ, respectively. To correct the dimensions of the reduced density matrices ρ_ν and ρ_μ, with respect to ρ, additional zeroes are appended to the eigenvalue set. The entropic inequality in Equation (1.5), is a less stringent condition compared to the majorization condition, given by Equation (1.6).

The majorization condition and the entropic inequalities establishes a crucial link between thermodynamics and entanglement. For any two vectors x and y, the condition $x \prec y$, implies that x is more disordered than y as x can be obtained by mixing the vectors from permutationally ordered elements of y [76, 77]. Interestingly, from the separability criteria [Equation (1.7)], for a quantum state to be entangled, the global state can be less disordered than its subsystems, which is not possible in classical disordered systems. The majorization condition also plays an important role in defining the criteria required for transformation of a quantum state into another, using local operations and classical communication and is useful in defining entanglement monotones, as discussed in Section 1.3.2.

1.3.2 Entanglement monotones

From the last section, we learn that the detection of generic entangled or separable states is in general a difficult problem even in low dimensions. However, for purposes of application in useful theoretical models, it is essential to obtain suitable measures and quantifiers of

entanglement. The lack of an universal detector of mixed state separability makes the task of quantifying entanglement a complicated process.

In general, the fundamental concept, central to the definition of entanglement measures is that, there exist quantum operations that do not generate or increase quantum correlation when applied to physical systems, though they may generate, increase, decrease or not affect the classical correlation in the system. Any physical parameter or quantity that does not increase under such operations is a valid measure of quantum correlation or entanglement [78]. The most notable example of such a set of quantum operations is the set of local operations with classical communication. LOCC are known to generate classical correlation without generating entanglement.[5] This leads us to the definition of *entanglement monotones* [78], which are functions that do not increase under LOCC, and are suitable candidates for quantifying entanglement. Entanglement measures are usually required to be entanglement monotones.

For pure states, entanglement monotones can be characterized using the concept of majorization [77]. Any quantum pure state $|\psi\rangle$ can be transformed to another quantum state $|\phi\rangle$ using LOCC operations, provided the Schmidt coefficients, in descending order $(\lambda_i^\downarrow)$, of the two states follow the majorization criteria ,

$$\sum_{i=1}^{k} \lambda_i^\downarrow(|\psi\rangle) \leq \sum_{i=1}^{k} \lambda_i^\downarrow(|\phi\rangle), \text{ for } 0 < k \leq s - 1, \text{with equality at } k = s, \qquad (1.8)$$

where s is the Schmidt rank. If the above criteria are satisfied, then $\lambda^{|\psi\rangle} \prec \lambda^{|\phi\rangle}$. As discussed in Section 1.3.1.4, we again find the majorization condition establishes a crucial link between disorder and entanglement. For allowable transformations using LOCC, $\lambda^{|\psi\rangle}$ is required to be more disordered than $\lambda^{|\phi\rangle}$. For a pure quantum state, the Schmidt coefficients are eigenvalues of its reduced density matrices of the subsystem. The majorization condition therefore implies, that pure quantum states can only be transformed from states with higher disordered subsystems than that of the target state, by using LOCC.

Using the majorization condition, one can formulate a simple criterion to be satisfied by all entanglement monotones. Since, entanglement cannot be increased under LOCC, an entanglement monotone $\mathcal{E}$ has to satisfy the condition,

$$\mathcal{E}(|\psi\rangle) \geq \mathcal{E}(|\phi\rangle), \text{ for } \lambda^{|\psi\rangle} \prec \lambda^{|\phi\rangle}. \qquad (1.9)$$

Hence, an entanglement monotone is a Schur concave function. A straightforward monotone that can be obtained using the concept of majorization, Schur concavity, and unitary invariance is the von Neumann entropy of the reduced density matrix of a quantum pure state,

---

[5]It will be discussed later that LOCC operations can generate other forms of (information-theoretic) quantum correlation, independent of the entanglement-separability criteria.

given by

$$S(\rho_{\mu(\nu)}) = -\text{tr}(\rho_{\mu(\nu)} \log \rho_{\mu(\nu)}), \tag{1.10}$$

where $\rho_{\mu(\nu)} = \text{tr}_{\nu(\mu)}(|\psi\rangle\langle\psi|)$ is the reduced density matrix of the subsystem of the state $|\psi\rangle$ in the $\mathcal{H}_\mu \otimes \mathcal{H}_\nu$ Hilbert space. $S(\rho_{\mu(\nu)})$ is actually one of the simplest measures of bipartite pure state entanglement, and in the asymptotic limit can be argued to be the only one. It is called the entropy of entanglement [79]. However, for a complete classification of entanglement in terms of monotones based on majorization a single value is insufficient, in the non-asymptotic limit. For a pure state, a minimum of $d - 1$ monotones are required, where $d = \min(d_\mu, d_\nu)$ is the number of Schmidt coefficients [78].

For mixed states the definition of an entanglement monotone is more involved as compared to that for pure quantum states. This is due to the fact that mixed quantum states contain classical correlation and any suitable entanglement monotone has to identify and retain correlation that are purely of quantum origin. The essential features of a mixed state entanglement monotone are generalized from pure state definitions. A mixed state monotone $\mathcal{E}_{mix}(\rho)$ must be a valid monotone for pure ρ and, more generally, non-increasing under LOCC for all states.

A general way to define a mixed state entanglement monotone is to consider a convex-roof construction [80]. A mixed state can always be presented as a convex combination of a set of pure states, $\rho = \sum_i p_i |\psi_i\rangle\langle\psi_i|$. A mixed state monotone $\mathcal{E}_{mix}(\rho)$, is then defined in terms of the pure state monotone, $\mathcal{E}(|\psi_i\rangle)$, with classical probabilities p_i, as $\mathcal{E}_{mix}(\rho) = \sum_i p_i \, \mathcal{E}(|\psi_i\rangle)$. However, there are numerous possible decompositions of the state ρ in terms of pure states, with none more unique than the other, and each decomposition casting a different numerical value. The convex-roof construction allows such decompositions using the pure state monotone, provided an infimum over all possible decompositions is performed. The construction can be written as,

$$\mathcal{E}_{mix}(\rho) = \min_{\{p_i, |\psi\rangle\}} \sum_i p_i \, \mathcal{E}(|\psi_i\rangle), \tag{1.11}$$

where $\rho = \sum_i p_i |\psi_i\rangle\langle\psi_i|$ is a possible decomposition, with classical probabilities p_i, such that, $\sum_i p_i = 1$ and $p_i \geq 0$. However, the computational intractability of such an optimization problem often renders the generation of meaningful monotones in mixed states, very difficult to perform in any dimension.

1.3.3 Measures of entanglement

The criteria for detection and characterization of entanglement in terms of monotones have been discussed in Sections 1.3.1 and 1.3.2. In the following segment, we discuss some state functions, that are suitable as measures of entanglement and that can be numerically or

algebraically evaluated. To begin, we list some important criteria to define what constitutes an entanglement measure. Firstly, all entanglement measures should decrease on average under LOCC, i.e., all entanglement measures (E) satisfy $\sum_i p_i E(\rho_i) \leq E(\rho)$, where ρ_i are the states obtained from LOCC on ρ with classical probabilities p_i. Additional sets of criteria, such as $E(\rho) = 0$, for ρ separable is also required. Additivity, $E(\rho^{\otimes n}) = nE(\rho)$, and subadditivity, $E(\rho_1 \otimes \rho_2) \leq E(\rho_1) + E(\rho_2)$ are often imposed. However, not all measures satisfy the above criteria and often additional constraints or relaxations have been introduced to cater to different physical or numerical conditions.

1.3.3.1 Distillable entanglement and entanglement cost

An important string of research attempts to quantify entanglement in terms of its efficiency in quantum communication protocols such as quantum teleportation [31]. It is known that a maximally entangled state (say, a Bell singlet state: $|\psi^-\rangle = \frac{1}{\sqrt{2}}(|10\rangle - |01\rangle)$), allows faithful teleportation of a single qubit. This is not true for a general entangled state. The original question that arose was: how many copies (n) of an entangled state (ρ) were required to obtain m $(m \leq n)$ copies of a maximally entangled state $(|\psi^-\rangle\langle\psi^-|)$? In other words, given n copies of an arbitrary state ρ, how many copies of $|\psi^-\rangle\langle\psi^-|$ can be "distilled" in the asymptotic limit $(n \to \infty)$? The rate, $r = \lim_{n\to\infty} m/n$, would give us the number of qubits per copy that can be teleported using the entangled state ρ, thus providing an operational measure of entanglement [81].

The protocol can be concisely presented in the following steps. The two parties apply LOCC (Λ) on n copies of the state, $\rho^{\otimes n}$, to obtain the desired state, $|\psi^-\rangle\langle\psi^-|^{\otimes m}$. The distillable entanglement (E_D) is then the supremum rate over all such LOCC protocols, and can be written as [6]

$$E_D = \sup\left\{r : \lim_{n\to\infty}[\inf_\Lambda ||\Lambda(\rho^{\otimes n}) - |\psi^-\rangle\langle\psi^-|^{\otimes m}|| = 0]\right\}. \tag{1.12}$$

The reverse protocol can also be used to define an entanglement measure, called the entanglement cost (E_C) [6, 81]. It measures the number of copies (m) of $|\psi^-\rangle$ required to generate n copies of the desired entangled state ρ. Though these measures have well understood operational significance, their evaluation for arbitrary quantum states is not tractable. For pure quantum states, both E_D and E_C are equal to the von Neumann entropy of local subsytems. A measure closely related to E_C is the entanglement of formation, which can be algebraically calculated in lower dimensions.

1.3.3.2 Entanglement of formation

For a bipartite system, $|\psi\rangle$, it can be shown that given $nE_f(|\psi\rangle)$ copies of a maximally entangled state, n copies of the state $|\psi\rangle$ can be obtained in the asymptotic limit, using LOCC [79], where, $E_f(|\psi\rangle) = S(\rho_\mu) = S(\rho_\nu)$. where, $S(\rho)$ is the von Neumann entropy. For

two-qubit states, $E_f(|\psi\rangle)$ is the number of singlets required to obtain $|\psi\rangle$. This measure is called the entanglement of formation (EOF). We note that for pure states EOF is equal to the entropy of entanglement and consequently, to E_D and E_C.

The entanglement of formation for a mixed bipartite quantum state [37] is defined using the convex-roof construction [80] or the average entropy of entanglement of its pure state decomposition, optimized over all such possible decompositions. For a bipartite quantum state, $\rho = \sum_i p_i |\psi_i\rangle\langle\psi_i|$, the entanglement of formation is defined as

$$E_f(\rho) = \min_{\{p_i, |\psi_i\rangle\}} \sum_i p_i E_f(|\psi_i\rangle), \tag{1.13}$$

where $E_f(|\psi\rangle)$ is the EOF of the pure state $|\psi\rangle$. The minimization is over all possible pure state decompositions $(p_i, |\psi_i\rangle)$ of the bipartite state, ρ. For two-qubit systems, the EOF has a closed analytical form defined in terms of a quantity called concurrence [38]. For arbitrary dimensions, the convex-roof construction for mixed state EOF is not tractable, though generalizations and bounds of EOF using concurrence have been explored [82].

1.3.3.3 Concurrence

Concurrence is an important entanglement monotone [38], initially derived as a parameter in the calculation of the entanglement of formation. Incidentally, concurrence is an independent measure of entanglement [38], that is not resource-based such as EOF. For a bipartite pure state, the concurrence in defined as $C(|\psi\rangle) = \sqrt{2(1 - \mathrm{tr}(\rho_\mu^2))}$, where $\rho_\mu = \mathrm{tr}_\nu(|\psi\rangle\langle\psi|)$. For a bipartite two-qubit pure state, $C(|\psi\rangle)$ can be obtained in terms of the Schmidt coefficients (λ_1, λ_2) of $|\psi\rangle$ as $2\lambda_1\lambda_2$.

The mixed state concurrence can again be derived using convex-roof construction. However, for a two-qubit density matrix, ρ, concurrence can be alternatively be defined as $C(\rho) = \max[0, \lambda_1 - \lambda_2 - \lambda_3 - \lambda_4]$, where λ_i $(i = 1, 2, 3, 4)$ are the square roots of the eigenvalues of the *spin-flip* operator, $R = \rho\tilde{\rho}$, with $\tilde{\rho} = (\sigma_y \otimes \sigma_y)\rho(\sigma_y \otimes \sigma_y)$, and σ_y is the Pauli spin matrix,

$$\sigma_y = \begin{pmatrix} 0 & -i \\ i & 0 \end{pmatrix}. \tag{1.14}$$

For two-qubit states, the EOF is a monotonically increasing function of concurrence[6] and can be expressed in a closed algebraic form, given by

$$E_f(\rho) = H\left(\frac{1 + \sqrt{1 - C^2(\rho)}}{2}\right), \tag{1.15}$$

where, $H(x) = -x \log_2 x - (1 - x) \log_2(1 - x)$, is the binary entropy.

Concurrence in pure entangled states has been experimentally observed [83] using a pair of photons in a linear optical setup, and a single, local measurement.

---

[6]Concurrence is also a monotonically increasing function of entanglement of formation.

1.3.3.4 Logarithmic negativity

The convex-roof construction for general mixed state entanglement is intractable and difficult to compute in most cases. Measures such as the EOF and concurrence have a closed algebraic form only for two-qubit systems [38] and some isotropic states [84]. Logarithmic negativity (LN) [39] is an entanglement measure that can be algebraically computed for arbitrary dimensional quantum states. The definition of LN is based on the fact that the negativity of the partial transpose of a bipartite quantum state is a sufficient condition for entanglement – the Peres-Horodecki separability criterion [16]. Moreover, for two-qubit systems, the condition is necessary and sufficient [17]. For a detailed discussion, see Section 1.3.1.2.

LN is evaluated by using a quantity called *negativity*, defined for the state ρ as

$$\mathcal{N}(\rho) = \frac{\left\| \rho^{T_\mu} \right\|_1 - 1}{2}, \tag{1.16}$$

where $\left\| \rho^{T_\mu} \right\|_1$ is the trace norm of the partial transpose ρ^{T_μ} of ρ, in the Hilbert space $\mathcal{H}_\mu \otimes \mathcal{H}_\nu$. From the Peres-Horodecki separability criterion, the partial transpose ρ^{T_μ} should be positive for all separable states. Hence $\mathcal{N}(\rho)$ is zero for separable states and can be computed as the sum of the absolute values of the negative eigenvalues of ρ^{T_μ}. LN of ρ is defined as

$$\begin{aligned} E_{\mathcal{N}}(\rho) &= \log_2 \left\| \rho^{T_\mu} \right\|_1 \\ &\equiv \log_2[2\mathcal{N}(\rho) + 1]. \end{aligned} \tag{1.17}$$

LN can be computed for arbitrary dimensional bipartite systems, however, unlike EOF, does not reduce to the entropy of entanglement for pure states, and is zero for PPT bound entangled states. However, non-zero values of LN is a useful upper bound on distillable entanglement [39]. Due to its computational simplicity, LN is often used to calculate entanglement in higher dimensions. Interestingly, LN satisfies the monotonicity condition, $E(\Lambda(\rho)) \leq E(\rho)$, for all LOCC, even though it is not convex [85] and further, is also additive.

Another important measure of entanglement is the relative entropy of entanglement [86], based on the minimal relative entropy distance between an entangled state and the set of all separable states. Interestingly, as we shall see in Section 1.4.4, entanglement measures based on geometric metrics offer a possibility to treat both entanglement and information-theoretic quantum correlation measures within an unified picture [87].

1.3.4 Multipartite entanglement

The presence of entanglement among multiple parties in an N–party quantum system is an extremely important resource for designing scalable quantum devices that can be applied in large-scale quantum computation and multiparty quantum communication [6]. In principle,

the fundamental ideas and criteria for separability in bipartite states can be extended to multipartite states. However, these states are often characterized by varying entanglement along different bipartitions, that make the development of entanglement measures more involved and complicated. Moreover, for mixed multiparty states, there may appear the possibility of multiparty entanglement that cannot be understood by looking at bipartitions. In this segment, we briefly look at the standard extension of the entanglement-separability criteria in multipartite quantum states.

k–separability: Let $|\Psi\rangle$ be a multipartite pure quantum state of N–parties, in the joint Hilbert space, $\mathcal{H}_1 \otimes \mathcal{H}_2 \otimes ... \otimes \mathcal{H}_N$. The multiparty state, $|\Psi\rangle$ is called k–separable if it can be written as a product of k $(1 < k \leq N)$ states $|\psi_i\rangle$, each containing one or many parties, as given by [6, 88]

$$|\Psi\rangle = |\psi_1\rangle \otimes |\psi_2\rangle \otimes ... \otimes |\psi_k\rangle. \tag{1.18}$$

A multipartite state that is separable across all N subsystems is called N–separable or fully multipartite separable. We note that a state that is k–separable is by defintion also p–separable, where $2 \leq p < k$. A pure state that is not separable across any bipartition is called a *genuinely multipartite entangled* pure state. The Greenberger-Horne-Zeilinger [89] and the W [90] states are the common examples of genuine multipartite entangled states. Genuine multipartite entanglement is an important resource from the perspective of many-party quantum communication [91] and is a potential resource for scalable quantum computation [92]. Cluster states are genuine multipartite entangled states that form a promising candidate in building a one-way quantum computer [93]. Multipartite entanglement also has fundamental applications in understanding the role of entanglement to indicate cooperative phenomena in many-body physics [22].

For mixed multiparty states, the k–separable state ϱ, can be obtained by the convex decomposition of k–separable multiparty pure states, given as [6, 88]

$$\varrho = \sum_i p_i \; |\psi_i\rangle\langle\psi_i|, \tag{1.19}$$

where $|\psi_i\rangle$ are k–separable and $\sum_i p_i = 1$. However, the definition of k–separable state ϱ, is not unique as there exist many possible convex decompositions. Further, the separability of k–separable $|\psi_i\rangle$ may occur across different partitions.

A more stringent definition of k–separability for mixed states is in terms of the γ_k–separability, which is defined as [6, 88]

$$\varrho = \sum_i p_i \; \rho_1^i \otimes \rho_2^i \otimes ... \otimes \rho_k^i, \tag{1.20}$$

where each ρ_i contains one or many parties. We observe that the partitions in such separable states are fixed. γ_k–separability coincides with k–separability for pure states.

The quantification of multipartite entanglement is more involved and complicated than bipartite entanglement, primarily due to the fact that each type of entanglement (based on k-separability) demands a different measure, with an unique characterization, to clearly identify the potential of each type of entanglement. General measures of multipartite entanglement may be insensitive to specific types of entanglement and in contrast, detection of a specific type, such as genuine multiparty entanglement, may completely ignore other useful regional entanglements, that can be resourceful in specific quantum tasks [6].

1.3.5 Measures of multipartite entanglement

In this segment, we discuss some of the more important attempts to quantify entanglement beyond the bipartite case.

1.3.5.1 Tangle and global entanglement

A seminal measure of multipartite entanglement in pure 3-party state, $\rho_{\mu\nu\epsilon}$ is the *tangle* [94]. It is defined as $\tau(\rho_{\mu\nu\epsilon}) = \tau(\rho_{\mu:\nu\epsilon}) - \tau(\rho_{\mu:\nu}) - \tau(\rho_{\mu:\epsilon})$. Here, $\tau(\rho_{\mu:\nu\epsilon})$, $\tau(\rho_{\mu:\nu})$ and $\tau(\rho_{\mu:\epsilon})$ refer to the concurrence square along the partitions, $\mu : \nu\epsilon$, $\mu : \nu$ and $\mu : \epsilon$, respectively. The 3-tangle is permutationally invariant and zero for some genuine 3-party entangled states, such as the W state. It is also zero for all states that are product across some partition. On extension to multiparty states with even n, the n-tangle can be defined in terms of the square of a quantity called the n-concurrence [95],[7], which is a suitable generalization of two-qubit concurrence, discussed in Section 1.3.3.3.

A multipartite entanglement monotone for pure states, based on the sum of functions of bipartite entanglement is the global entanglement [96]. The global entanglement, for an n-qubit state in terms of tangles, can be written as [97]

$$E_{gl}^{MW} = \frac{1}{n}\Big[2\sum_{i_1<i_2}\tau_{i_1i_2} + 3\sum_{i_1<i_2<i_3}\tau_{i_1i_2i_3} + ... + n\sum_{i_1<...<i_n}\tau_{i_1...i_n}\Big], \quad (1.21)$$

where $\tau_{i_1i_2}$ is the 2-tangle, $\tau_{i_1i_2i_3}$ is the 3-tangle and $\tau_{i_1...i_n}$ is the n-tangle.

1.3.5.2 Geometric measure of entanglement

An important measure of multipartite entanglement is the geometric measure [98] (also see [88]). A natural geometric definition of the amount of multipartite entanglement of a pure multiparty quantum state is therefore the minimum distance of that state from the set of all states that are multiparty k-separable. A widely used measure of distance is the fidelity subtracted from unity, giving the geometric measure as $\mathcal{G} = 1 - \Lambda^k(|\Psi\rangle)$, where $\Lambda^k(|\Psi\rangle) = \sup_{\{|\eta\rangle\in\mathcal{S}_k\}}|\langle\Psi|\eta\rangle|^2$. The set $\mathcal{S}_k$, is the set of all k-separable states. Replacing the set, $\mathcal{S}_k$, with $\mathcal{S}_N$, we obtain a measure of finite multipartite entanglement, that is not N-separable.

---

[7]As shown in Reference [95] the relations obtained for the n-tangle is not invariant under permutation of qubits for odd n greater than 3.

1.3.5.3 Generalized geometric measure

An efficient and computable geometric measure of genuine multipartite entanglement in pure quantum states is the generalized geometric measure (GGM) [99], that for an N-party pure quantum state $|\Phi\rangle$ is defined as the minimum of this *fidelity-based distance* of the state from the set of all states that are not genuinely multiparty entangled [99]. In other words, the GGM of $|\phi_N\rangle$, denoted by $\mathcal{E}(|\phi_N\rangle)$, is given by

$$\mathcal{E}(|\phi\rangle) = 1 - \Lambda_{\max}^2(|\Phi\rangle), \tag{1.22}$$

where $\Lambda_{\max}(|\Phi\rangle) = \max|\langle\chi|\phi_N\rangle|$, with the maximization being over all N-party quantum states $|\chi\rangle$ that are not genuinely multipartite entangled.

It was shown in Reference [99] that the GGM of a multiparty pure state can be effectively calculated by using

$$\mathcal{E}(|\phi_N\rangle) = 1 - \max\{\lambda_{A:B}^2|A \cup B = \{1, 2, \ldots, N\}, A \cap B = \emptyset\}, \tag{1.23}$$

where $\lambda_{A:B}$ is the maximal Schmidt coefficients in all possible bipartite splits $A : B$ of $|\phi_N\rangle$. The high utility of this measure lies in the fact that it is a measure of genuine multipartite entanglement that can be efficiently computed for any pure state of an arbitrary number of parties in any dimensions.

1.4 Information-theoretic quantum correlation measures

In the previous section, we identified quantum correlation within the entanglement-separability paradigm and attempted to discuss the theoretical framework around which the basic measures of entanglement were characterized. However, as discussed earlier in Section 1.2, the definition of quantum correlation is not exhausted by entanglement and the intuitive idea of nonclassical correlations can be stretched beyond the set of LOCC prepared separable states by using novel information-theoretic concepts.

In this section, we discuss a few measures of information-theoretic quantum correlation. For a complete review of the origin and subsequent theoretical development of information-theoretic quantum correlation measures, please see [21].

1.4.1 Quantum discord

One of the first works that sought to relate the notion of quantum correlation beyond the entanglement-separability criterion, harnessing quantum information-theoretic concepts, was the characterization of a measure called quantum discord (QD) [18, 19].

In classical information theory, the correlation between two random variables is contained in the mutual information between these variables. The mutual information can be arrived

at using the classical Shannon entropy via two distinct methods: first, using the idea of joint probability distribution, and secondly, using the concept of conditional entropy. Extending the definition to the quantum regime and replacing Shannon entropy with the von Neumann entropy, we obtain two distinct, inequivalent but classically equal expressions for mutual information. QD is defined as the difference between the two expressions for mutual information when extended to the quantum regime.

Classical mutual information can be defined for a joint probability distribution $\{p_{ij}\}$ as

$$I(\{p_{ij}\}) = H(\{p_{i.}\}) + H(\{p_{.j}\}) - H(\{p_{ij}\}), \tag{1.24}$$

where $H(\{q_j\}) = -\sum_j q_j \log_2 q_j$ is the Shannon entropy of the probability distribution $\{q_j\}$, and $\{p_{i.}\}$, $\{p_{.j}\}$ are the marginals of $\{p_{ij}\}$. Using the concept of conditional entropy, we obtain the entropy of the joint probability distribution $\{p_{ij}\}$ as

$$H(\{p_{ij}\}) = H(\{p_{.j}\}) + H(\{p_{i|j}\}) = H(\{p_{i.}\}) + H(\{p_{j|i}\}), \tag{1.25}$$

where $\{p_{i|j}\}$ and $\{p_{j|i}\}$ are the conditional probability distributions. Plugging Equation (1.25) in the expression for $H(\{p_{ij}\})$ in Equation (1.24), gives us an alternate but equivalent classical expression for mutual information,

$$I(\{p_{ij}\}) = H(\{p_{i.}\}) - H(\{p_{i|j}\}) = H(\{p_{.j}\}) - H(\{p_{j|i}\}). \tag{1.26}$$

In the quantum regime, the total correlation in any bipartite quantum system, ρ, in the joint Hilbert space $\mathcal{H}_\mu \otimes \mathcal{H}_\nu$, can be measured by using quantum mutual information [100] (see also [101]):

$$I(\rho) = S(\rho_\mu) + S(\rho_\nu) - S(\rho), \tag{1.27}$$

where $S(\rho')$ is the von Neumann entropy of the quantum state ρ', and ρ_μ and ρ_ν are the reduced density matrices of ρ. This quantifies the classical expression in Equation (1.24). To obtain the quantum equivalent of the classical mutual information in Equation (1.26), we need the quantum conditional entropy, $S(\rho_{\mu|\nu})$, which is defined as the lack of information about one subsystem (say, ρ_μ) when that of the other subsystem (ρ_ν) is known. The complete knowledge of a subsystem invokes a partial measurement on the composite system ρ, as described below.

For a bipartite quantum system ρ, measuring on the subsystem ν using the set of projectors $\{\Pi_i^\nu\}$[8] (where $\Pi_i^\nu \Pi_j^\nu = \delta_{ij}\Pi_i^\nu$, $\sum_i \Pi_i^\nu = \mathbb{I}_\nu$, with $\mathbb{I}_\nu$ being the identity operator on the Hilbert space on which ρ_ν is defined), produces the post-measurement states

---

[8]In general, rank-1 positive operator valued measurements (POVM) are needed to optimize the quantum discord. However, projective measurements give a very tight upper bound on discord and there exists only a small set of discordant states for which an insignificant numerical difference is observed, as mentioned in Reference [21].

$\rho^i = \frac{1}{p_i}(\mathbb{I}_\mu \otimes \Pi_i^\nu \rho \mathbb{I}_\mu \otimes \Pi_i^\nu)$, where $\mathbb{I}_\mu$ is the identity operator on subsystem μ, and $p_i = \mathrm{tr}_{\mu\nu}(\mathbb{I}_\mu \otimes \Pi_i^\nu \rho \mathbb{I}_\mu \otimes \Pi_i^\nu)$. The conditional quantum states that are produced at μ, due to the measurement at ν, are $\rho_{\mu|i} = \frac{1}{p_i}\mathrm{tr}_\nu(\mathbb{I}_\mu \otimes \Pi_i^\nu \rho \mathbb{I}_\mu \otimes \Pi_i^\nu)$, with probability p_i. The quantum conditional entropy [4] is then defined as $S(\rho_{\mu|\nu}) = \min_{\{\Pi_i^\nu\}} \sum_i p_i S(\rho_{\mu|i})$, and similarly, $S(\rho_{\nu|\mu})$. By using this definition, the classical expression in Equation (1.26) can be quantized as

$$J(\rho) = S(\rho_\mu) - S(\rho_{\mu|\nu}). \tag{1.28}$$

It has been argued that $J(\rho)$ can be used to quantify classical correlation in ρ [18].

Quantum discord $(Q(\rho))$ is then defined as the difference between the total mutual information $I(\rho)$ and the classical correlation $J(\rho)$, given by

$$Q(\rho) = I(\rho) - J(\rho). \tag{1.29}$$

Since, $I(\rho) \geq J(\rho)$, $Q(\rho)$ is always non-negative. For nonsymmetric ρ, QD is in general not symmetric to measurements on the μ and ν subsystem, since $J(\rho)$ is dependent on the measured subsystem. QD is positive for all quantum states, due to the concavity of conditional entropy [102] and is invariant under local unitary transformations, however, it is not contractive under general local transformations [21].

1.4.2 Quantum work-deficit

Another information-theoretic measure of quantum correlation, based on the thermodynamic properties of information, is the quantum work-deficit (QWD) [20]. The concept of QWD is based on the fact that information can be treated as a thermodynamic resource [103]. Given a quantum state ρ, one defines the allowed class of global quantum operations, called *closed operations* (CO), as arbitrary sequences of the following operations: (G1) unitary operations and (G2) dephasing ρ by using a set of projectors $\{\Pi_i\}$, i.e., $\rho \rightarrow \sum_i \Pi_i \rho \Pi_i$, where $\Pi_i \Pi_j = \delta_{ij}\Pi_i$, $\sum_i \Pi_i = \mathbb{I}$, with $\mathbb{I}$ being the identity operator on the Hilbert space $\mathcal{H}$ on which ρ is defined. Under this class of operations, it can be shown (see [20, 104]) that the number of pure qubits that can be extracted from ρ is $I_G(\rho) = N - S(\rho)$, where $N = \log_2 \dim \mathcal{H}$.

Correspondingly, the allowed class of local operations is called *closed local operations and classical communication* (CLOCC), and is defined as arbitrary compositions of the following operations: (L1) local unitary operations, (L2a) local dephasing and (L2b) sending a completely dephased subsystem from one party to another over a noiseless quantum channel. Let us consider a bipartite quantum state ρ. The number of qubits that can be extracted from a bipartite quantum state ρ under CLOCC is

$$I_L(\rho_{AB}) = N - \inf_{\Lambda \in CLOCC}[S(\rho'_\mu) + S(\rho'_\nu)], \tag{1.30}$$

TH-23842

where $\rho'_\mu = \text{tr}_\nu(\Lambda(\rho))$, $\rho'_\nu = \text{tr}_\mu(\Lambda(\rho))$. QWD is then defined as

$$\Delta(\rho_{AB}) = I_G(\rho_{AB}) - I_L(\rho_{AB}). \tag{1.31}$$

Interestingly, the characterization of quantum work-deficit uses a lot of the thermodynamic tools used in entanglement theory, such as pure state distillation and stringent forms of LOCC. Both quantum work-deficit and quantum discord reduce to the von Neumann entropy of local subsystems for pure bipartite quantum states. QWD can be classified as i-way QWD ($i = 0, 1, 2$), depending on the way the classical communication is performed in the CLOCC protocol [21, 104]. The 1-way QWD is equivalent to quantum discord [21] for states with maximally mixed marginals.

1.4.3 Measurement induced disturbance

Measurement induced disturbance (MID) is derived from the understanding that a truly classical state, with respect to some measurement, will remain unchanged after the measurement [50]. Let us consider a bipartite density matrix ρ. If Π_i^μ and Π_j^ν are complete von Neumann measurements (one dimensional projections) for subsystems μ and ν, respectively, for a classical state,

$$\rho = \sum_{ij} \Pi_i^\mu \otimes \Pi_j^\nu \rho \Pi_i^\mu \otimes \Pi_j^\nu. \tag{1.32}$$

The states ρ that do not satisfy Equation (1.32) are essentially quantum in nature. MID measures the quantumness in a bipartite state ρ by measuring the difference in the quantum mutual information between the state ρ and its least disturbed classical state obtained by the measurement, $\rho_{cl} = \sum_i \mathcal{P}_i \rho \mathcal{P}_i$, where $\mathcal{P}_i$ are the spectral projections of the state ρ. Thus, MID can be defined as

$$\mathcal{M}(\rho) = \mathcal{I}(\rho) - \mathcal{I}(\rho_{cl}), \tag{1.33}$$

where $\mathcal{I}(\rho) \equiv S(\rho_\mu) + S(\rho_\nu) - S(\rho)$ is the quantum mutual information [100]. $S(\rho) = -\text{tr}(\rho \log_2 \rho)$ is the von Neumann entropy of a quantum state ρ. ρ_μ and ρ_ν are the reduced density matrices of the subsystem μ and ν, respectively. $\mathcal{M}(\rho)$ is the nonclassical measure of measurement induced disturbance [50] and unlike other information-theoretic measure of quantum correlation, based on projective measurements, does not introduce any optimization on the measured states. Hence, MID serves as an upper bound on other information-theoretic quantum correlation [21].

1.4.4 Geometric measures of quantum discord

An independent information-theoretic measure of quantum correlation can be defined as a geometric distance from the set of zero-discord states. This is similar to the relative entropy

of entanglement [86], which is the minimum relative entropy distance of a state from the set of separable states. Relative entropy, defined as $S(\rho||\sigma) = -\mathrm{tr}(\rho\log\sigma) - S(\rho)$, where $S(\rho)$ is the von Neumann entropy, is not a true distance metric, as it is not symmetric, $S(\rho||\sigma) \neq S(\sigma||\rho)$ [86]. The first instance of defining both entanglement measures and information-theoretic quantum correlation within an unified framework, was done by using the relative entropy [87]. The relative entropy of quantum discord (Q_R) is defined as the distance of a state ρ from the set $\mathcal{S}_c$, of zero-discord states. Mathematically, Q_R can be written as

$$Q_R(\rho) = \min_{\{\xi \in \mathcal{S}_c\}} S(\rho||\xi), \tag{1.34}$$

where ρ and ξ are density operators in the relevant Hilbert space.

The geometric discord, based on a true distance metric, was done by using the Hilbert-Schmidt distance [49]. The definition can be written as

$$Q_G(\rho) = \min_{\{\xi \in \mathcal{S}_c\}} ||\rho - \xi||^2 = \min_{\{\xi \in \mathcal{S}_c\}} \mathrm{tr}\left[(\rho - \xi)^2\right]. \tag{1.35}$$

The measure is called the geometric quantum discord (GQD). The nearest classically correlated state ξ can be obtained following an optimal projective measurement in one of the subsytems, $\xi = \sum_i \Pi_i^\mu \otimes \mathbb{I}_\nu \, \rho \, \Pi_i^\mu \otimes \mathbb{I}_\nu$. The GQD can then be set as an optimization over all measurements, similar to the general QD, and can be written as, $Q_G(\rho) = \min_{\{\Pi_i^\mu\}} \mathrm{tr}\left[(\rho - \xi)^2\right]$. The most remarkable advantage of GQD is that the optimization involved in the definition of discord is suitably replaced by exact analytical expressions [49] (also see, [21]), for certain bipartite systems. However, the GQD suffers from certain inconsistencies. The significant drawback is that the measure at times gives unphysical results, such as it can increase even under trivial local reversible operations on the unmeasured party, such as a reversible addition of an ancilla state to the unmeasured subsystem, as shown in Reference [105], which is undesirable in any indicator of quantum correlation.

The geometric quantum discord can also be quantified using a distance metric other than the Hilbert-Schmidt distance. One notable definition uses the Bures metric [106], to define the geometric discord. The Bures distance is monotonous and Riemannian and satisfies some of the more important conditions required of a quantum correlation measure [106].

1.5 Nonclassicality in continuous variable quantum systems

In this section, we discuss a few well-known indicators of nonclassicality in multi-photon optical fields, which are the most widely investigated prototype of continuous variable (CV) quantum systems. The primary motivation for using CV systems in QIT is the relative ease with which the system can be controlled and manipulated to generate quantum correlation

in quadrature variables such as momentum and position or alternatively, in the discrete, infinite dimensional energy eigenstates of electromagnetic fields, using established quantum optical methods [23, 24]. Most well-known QIT protocols can be suitably reformulated in the CV picture, allowing a better platform for experimental realization using linear quantum optics and advanced photonics [24, 107]. Other notable examples of CV systems include vibrational modes of solids, bosonic atomic ensembles, Bose-Einstein condensates, nuclear spins in a quantum dot, and Josephson junctions [107].

As discussed in Section 1.2, the concept of nonclassicality in quantum optics was initially developed independently of the characterization of entanglement and information-theoretic quantum correlation in discrete systems and were based primarily on the nonclassical aspects of the quantized field in terms of its statistical behavior and various experimental phenomena. We start the section with a short description of CV nonclassicality in terms of the Wigner quasiprobability function and briefly discuss the nonclassical indicators associated with sub-Poissonian statistics and quadrature squeezing. The last segment contains a brief discussion on entanglement and information-theoretic quantum correlation from the CV perspective. For a more detailed reading on nonclassicality of the electromagnetic field, including quasiprobabilies in phase-space representation, photon statistics, optical squeezing, and other interesting phenomena such as quantum interferometry, please see [64].

Wigner function: The nonclassicality of a quantum state can be studied in terms of its phase-space distribution characterized by the Wigner distribution. For a quantum state $\hat{\rho}$, the Wigner function of the system is defined in terms of the coherent state basis [64] as

$$W(\beta, \beta^*) = \frac{2}{\pi^2} e^{2|\beta|^2} \int d^2\gamma \langle -\gamma | \hat{\rho} | \gamma \rangle e^{-2(\beta^*\gamma - \beta\gamma^*)}, \tag{1.36}$$

where $|\gamma\rangle = \exp(-|\gamma|^2/2 + \gamma\hat{a}^\dagger)|0\rangle$ is a coherent state. By using the relation [108]

$$\sum_{n=k}^{\infty} {}_nC_k \, y^{n-k} = (1-y)^{-k-1}, \tag{1.37}$$

the Wigner function can be expressed in series form as

$$W(\beta, \beta^*) = \frac{2}{\pi} \sum_{k=0}^{\infty} (-1)^k \langle \beta, k | \hat{\rho} | \beta, k \rangle, \tag{1.38}$$

where $|\beta, k\rangle$ is the displaced number state [64].

A state with a non-positive Wigner function is essentially nonclassical, as it cannot be described in terms of a positive quasiclassical probability distribution in the coherent state representation. However, for a classical state, the positivity of the Wigner function is a necessary condition but not sufficient. For example, the Wigner function of the squeezed

state is Gaussian and positive everywhere but the state is a well-known nonclassical state [64].

We may consider a more generalized distribution function, viz. a parametrized quasiprobability function $\mho^{(F)}(\beta)$ describing a field state $\hat{\rho}$, defined as [109]

$$\mho^{(F)}(\beta) \equiv \frac{1}{\pi}\mathrm{Tr}\{\hat{\rho}\hat{T}^{(F)}(\beta)\}, \tag{1.39}$$

where the operator $\hat{T}^{(F)}(\beta)$ is given by $\hat{T}^{(F)}(\beta) = \frac{1}{\pi}\int\exp(\beta\xi^* - \beta^*\xi)\hat{D}^{(F)}(\xi)d^2\xi$, with $\hat{D}^{(F)}(\xi) = e^{F|\xi|^2/2}\hat{D}(\xi)$ and $\hat{D}(\xi) = e^{\xi\hat{a}^\dagger - \xi^*\hat{a}}$. The function $\mho^{(F)}(\beta)$ can be rewritten in the number-state basis as $\mho^{(F)}(\beta) = \frac{1}{\pi}\sum_{n,m}\rho(n,m)\langle n|\hat{T}^{(F)}(\beta)|m\rangle$, where the matrix elements of the operator $\hat{T}^{(F)}(\beta)$ are given by

$$\langle n|\hat{T}^{(F)}(\beta)|m\rangle = \left(\frac{n!}{m!}\right)^{1/2}\left(\frac{2}{1-F}\right)^{m-n+1}\left(\frac{F+1}{F-1}\right)^n \beta^{*m-n}$$
$$\times \exp\left(-\frac{2|\beta|^2}{1-F}\right)L_n^{m-n}\left(\frac{4|\beta|^2}{1-F^2}\right), \tag{1.40}$$

in terms of the associated Laguerre polynomials $L_n^{m-n}(x)$. The above equation gives explicitly the F-dependence of $\mho^{(F)}(\beta)$. For the special values of $F = 1, 0$ and -1, $\mho^{(F)}(\beta)$ becomes the Glauber-Sudarshan P, the Wigner W, and the Husimi Q functions, respectively (for a description, see [64]). The negativity of $\mho^{(F)}(\beta)$ for any value of the parameter F indicates nonclassical nature of the state.

The nonclassical nature of a positive Wigner function can be determined using other nonclassical features of the state, such as sub-Poissonian statistics and quadrature squeezing. These features, discussed later, can be attributed to the negative values which arise due to the dispersion of normally-ordered observables that are not captured by the Wigner function [110]. In such cases, the nonclassicality is often manifested by the negativity of the F-parametrized distribution. The Wigner function can be mathematically extended to encompass multimode CV systems.

Sub-Poissonian statistics: Mandel's Q parameter: The quantum character of a field can be demonstrated either in measurements of time intervals τ between detected photons demonstrating antibunching, or in photon counting measurements yielding sub-Poissonian statistics. The condition for sub-Poissonian photon statistics is given by $\langle(\Delta\hat{n})^2\rangle - \langle\hat{n}\rangle < 0$, where $\hat{n}$ is the number operator, which makes the normalized second-order intensity correlation function, $\gamma(0) < 1$. The states with sub-Poissonian statistics have no classical description.

To determine the photon statistics of a single-mode radiation field, we consider Mandel's Q parameter defined as [111]

$$Q \equiv \frac{\langle\hat{a}^{\dagger 2}\hat{a}^2\rangle - \langle\hat{a}^\dagger\hat{a}\rangle^2}{\langle\hat{a}^\dagger\hat{a}\rangle}. \tag{1.41}$$

$Q = 0$ stands for Poissonian photon statistics. $Q < 0$ corresponds to the case of sub-Poissonian distribution. This means that a nonclassical state often shows negative Q values. *Squeezing*: The quadrature squeezing of a field can be used to study its nonclassical properties. To analyze the squeezing properties of the radiation field, we introduce two hermitian quadrature operators

$$\hat{X} = \hat{a} + \hat{a}^\dagger, \ \hat{Y} = -i(\hat{a} - \hat{a}^\dagger).$$
(1.42)

These two quadrature operators satisfy the commutation relation $[\hat{X}, \hat{Y}] = 2i$, and, as a result, the uncertainty relation $(\Delta\hat{X})^2(\Delta\hat{Y})^2 \geq 1$. A state is said to be squeezed if either $(\Delta\hat{X})^2$ or $(\Delta\hat{Y})^2$ is less than its coherent state value. To review the principle of quadrature squeezing [112], we define an appropriate quadrature operator

$$\hat{X}_\theta = \hat{X}\cos\theta + \hat{Y}\sin\theta = \hat{a}e^{-i\theta} + \hat{a}^\dagger e^{i\theta}.$$
(1.43)

The squeezing of $\hat{X}_\theta$ is characterized by the condition $\langle : (\Delta\hat{X}_\theta)^2 : \rangle < 0$, where the double dots denote the normal ordering of operators. After expanding the terms in $\langle : (\Delta\hat{X}_\theta)^2 : \rangle$ and minimizing its value over the whole angle θ, one gets

$$
\begin{aligned}
S_{\text{opt}} &= \langle : (\Delta\hat{X}_\theta)^2 : \rangle_{\text{min}} \\
&= -2|\langle \hat{a}^{\dagger 2}\rangle - \langle \hat{a}^\dagger\rangle^2| + 2\langle \hat{a}^\dagger\hat{a}\rangle - 2|\langle \hat{a}^\dagger\rangle|^2.
\end{aligned}
$$
(1.44)

The nonclassical states correspond to the negative values of S_{opt}, $-1 \leq S_{\text{opt}} < 0$.

The negativity of the Q function and squeezing are not necessary conditions for identifying nonclassical regimes of quantum states but are sufficient ones. As mentioned earlier, the Q function and the squeezing parameter S can be negative and hence nonclassical for states that have a positive Wigner function, as shown in [110]. Conversely, there are also instances where states with partial negative Wigner functions have positive Q functions [113].

Quantum correlation in continuous variable systems: A typical CV state can have two types of representations, both in the infinite-dimensional Hilbert space. A bipartite CV state can be represented in terms of two-mode continuous variable momentum and position basis or in the discrete, but infinite-dimensional two-mode number state basis. The archetypal bipartite entangled CV state is the two-mode squeezed vacuum state (TSVS). In the phase-space representation, the Wigner function of the TSVS is given by [114]

$$W(x_1, x_2, p_1, p_2) = \frac{4}{\pi^2} \exp\left\{e^{-2r}\left[(x_1 + x_2)^2 + (p_1 - p_2)^2\right] - e^{2r}\left[(x_1 - x_2)^2 + (p_1 + p_2)^2\right]\right\},$$
(1.45)

where r is the squeezing parameter. For $r \to \infty$, the state reduces to the form $\delta(x_1 - x_2)\delta(p_1 + p_2)$, which is a maximally entangled state [23], as envisioned by the EPR argument

[2]. In the number state basis, the TSVS is given by

$$|\psi\rangle_{TSVS} = S(r)|0\rangle_1|0\rangle_2 = \exp\left[\hat{a}_1^\dagger \hat{a}_2^\dagger - \hat{a}_1\hat{a}_2\right]|0\rangle_1|0\rangle_2 = \sqrt{1-\lambda^2}\sum_n \lambda^n |n\rangle_1|n\rangle_2, \quad (1.46)$$

where $\lambda = \tanh^2 r$. The number-state basis for the TSVS state above, is also the Schmidt basis and the bipartite entanglement can be quantified by the von Neumann entropy or entanglement entropy. The analytical form is given by [115]

$$E_{TSVS} = -\log_2(1-\lambda) - \lambda\log_2\lambda/(1-\lambda) = \cosh^2 r\log_2\cosh^2 r - \sinh^2 r\log_2\sinh^2 r. \quad (1.47)$$

Importantly, pure Gaussian states, which are the most resourceful CV states with respect to quantum information theory protocols [107], can all be transformed using local transformations to two-mode squeezed vacuum states, enabling easy quantification. The principal criteria for a two-mode pure state to be entangled are the following i) Schmidt rank greater than 1, ii) von Neumann entropy of reduced state is finite, and iii) it violates nonlocality [24].

The mixed state entanglement of a CV state can be defined in terms of the positive partial transpose (PPT) criteria. For example, it is known that a N-mode Gaussian state with a non-positive PPT is entangled. To completely understand the problem, one needs to characterize the PPT criterion for CV states [116]. The transposition operation in the CV regime, is given by the following operation, $\xi^T = \Gamma\xi^T = (x_1, -p_1, x_2, -p_2, ..., x_N, -p_N)^T$, where $\xi = (x_1, p_1, x_2, p_2, ..., x_N, p_N)$ is the set of the position and momentum variables of the N-mode CV state. Similarly, in vector notation, $\hat{\xi} = (\hat{x}_1, \hat{p}_1, ..., \hat{x}_N, \hat{p}_N)$. For, Gaussian states, the transposition can be represented as a transformation in the covariance matrix (V^N), such that $V^N \to \Gamma V^N \Gamma$. The covariance matrix V^N has the second moments of $\hat{\xi}$ as it elements, $V_{ij}^N = \frac{1}{2}\langle\{\Delta\hat{\xi}_i, \Delta\hat{\xi}_j\}\rangle$, where $\Delta\hat{\xi}_i = \hat{\xi}_i - \langle\hat{\xi}_i\rangle$ and $\{,\}$ is the anti-commutator. The $2N \times 2N$ real, symmetric covariance matrix must satisfy the uncertainty relation, $V^N + i\Omega \geq 0$ [117], where for annihilation (creation) operators $\hat{a}$ ($\hat{a}^\dagger$), we define $\hat{b} = (\hat{a}_1, \hat{a}_1^\dagger, \hat{a}_2, \hat{a}_2^\dagger, ..., \hat{a}_N, \hat{a}_N^\dagger)$, and $\Omega_{ij} = [\hat{b}_i, \hat{b}_j]$, is a $2N \times 2N$ matrix whose elements are the bosonic commutations.

The partial transposition can be applied using the matrix $\Gamma_\mu \oplus \mathbb{I}_\nu$ on a bipartite Gaussian system μ and ν, with N_μ and N_μ modes, respectively. The criterion that the following transformation of the covariance matrix,

$$(\Gamma_\mu \oplus \mathbb{I}_\nu)\, V^{\{N_\mu+N_\nu\}}\, (\Gamma_\mu \oplus \mathbb{I}_\nu) + i\Omega \ngeq 0, \quad (1.48)$$

violates the uncertainty relation, is a sufficient criterion for inseparability [116, 118]. For Gaussian states with $N_\mu = N_\nu = 1$ [116] and $N_\mu = 1$, and $N_\mu = N$ [118], the condition is also necessary. It also holds for general $N_\mu \times N_\nu$ Gaussian states that are bisymmetric [119].

For an arbitrary bipartite two-mode CV state ρ, the inseparabilty criteria can be formulated independent of the partial transposition, using the position and momentum uncertainty and the Cauchy-Schwarz inequality [120], given as

$$\langle(\Delta\hat{u})^2\rangle_\rho + \langle(\Delta\hat{v})^2\rangle_\rho \geq \bar{a}^2|\langle[\Delta\hat{x}_1,\Delta\hat{p}_1]\rangle_\rho|^2 + |\langle[\Delta\hat{x}_2,\Delta\hat{p}_2]\rangle_\rho|^2/\bar{a}^2, \tag{1.49}$$

where, $\hat{u} = |\bar{a}|\hat{x}_1 - \hat{x}_2/\bar{a}$, $\hat{v} = |\bar{a}|\hat{p}_1 - \hat{p}_2/\bar{a}$, and $\bar{a}$ is an arbitrary non-zero parameter[9].

The information-theoretic measure of quantum discord can be extended to two-mode Gaussian states, with the subsystem measurement being a single-mode POVM [121] performed using homodyne measurements [122]. Any two-mode Gaussian state has a covariance matrix, V^2, such that,

$$V^2 = \begin{pmatrix} A & C \\ C^T & B \end{pmatrix}, \tag{1.50}$$

where, $A = a\mathbb{I}$, $B = b\mathbb{I}$ and $C = \mathrm{diag}\{c, c'\}$. The quantum discord can then be written as,

$$Q_{cv}(\rho) = h(\sqrt{\det A}) - h(p_+) - h(p_-) - \min_{\{V_0^1\}} h(\sqrt{\det\beta}), \tag{1.51}$$

where, the function $h(x)$ is defined as,

$$h(x) = \frac{1+x}{2}\log\left(\frac{1+x}{2}\right) - \frac{x-1}{2}\log\left(\frac{x-1}{2}\right), \tag{1.52}$$

and $p_\pm$ are the eigenvalues given by $2p_\pm^2 = Z \pm \sqrt{Z^2 - 4\det V^2}$, where $Z = A + B + 2C$. $\beta = B - C(A - V_0^1)^{-1}C^T$. V_0^1 refers to all pure single-mode Gaussian state covariance matrix [21, 121].

1.6 Outline of thesis

In this section, we present a short outline of the division of the chapters in the thesis and the central problem being addressed. The thesis is divided into two parts (**I** and **II**), with two chapters in each part. The primary results presented in the thesis are adapted from References [123–128].

In **Part I** of the thesis, we study the characterization of entanglement in a class of large superposed states, obtained from nearest-neighbor dimer coverings on spin-1/2 lattices, also called resonating valence bond (RVB) states [129], which are possible ground states of the Heisenberg spin-1/2 lattices. RVB systems have generated a lot of interest for possible connection to high-T_c superconductivity and exotic topological phases [129]. RVB states have been experimentally simulated using ultracold atoms in optical lattices and are of interest in QIT for its possible role in fault-tolerant quantum computation.

---

[9]The Equation (1.49) has been taken from Reference [24].

In **Chapter 2**, we investigate the behavior of bipartite and multipartite entanglement properties of a quantum spin-1/2 ladder, with RVB ground states, and contrast it with the results for isotropic quantum lattices [123]. Using quantum information theory concepts such as monogamy of entanglement and quantum telecloning, we obtain analytical bounds for the behavior of entanglement in quantum spin-1/2 ladders. Further, using QIT properties such as strong sub-additivity of von Neumann entropy, we show that infinite or periodic isotropic quantum spin-1/2 lattices, are always genuinely multipartite entangled. We follow this with a numerical estimation of the amount of bipartite and multipartite entanglement in the two-leg RVB ladder. We observe that the amount of nearest-neighbor bipartite entanglement in the rails of the ladder decreases with increasing size in contrast to the behavior of bipartite entanglement along the rungs of the ladder. Further, the multipartite entanglement decreases with increasing size. The obtained numerical values strictly follow the analytical bounds obtained from QIT. The behavior of bipartite and multipartite entanglement in the RVB ladder is in stark contrast with their behavior for isotropic RVB systems, which tends to have negligible bipartite entanglement with finite multipartite entanglement. We observe that a change in geometry of RVB systems can radically alter the qualitative behavior of both bipartite and multipartite entanglement.

In **Chapter 3**, we extend our study of RVB systems to characterize genuine multipartite entanglement in multi-legged quantum spin-1/2 ladder and isotropic lattices with a large number of spin sites [124, 125]. Calculating relevant physical quantities, such as entanglement, for large sized lattices, is limited by computational difficulty. However, we introduce a new iterative analytical technique, the density matrix recursion method, to efficiently calculate reduced density matrices of large RVB states. This allows us to characterize the behavior of genuine multipartite entanglement in large RVB systems using a computable measure called generalized geometric measure. We apply this technique to distinguish between even and odd multi-legged ladders. Specifically, we show that while genuine multipartite entanglement decreases with increasing system size for the even-legged ladder, it does the opposite for odd-legged ones [124]. For the isotropic lattice, the iterative analytical method is used to calculate the entanglement of finite-size 2D lattices, which through finite-size scaling, enables us to obtain an estimate of the genuine multipartite entanglement in an infinite square lattice [125].

In **Part II** of the thesis, we study and compare the dynamics of information-theoretic quantum correlation measures and entanglement in two archetypal quantum systems from many-body physics and quantum optics. The first is the infinite anisotropic XY-spin chain in a transverse magnetic field while the second is a three-level atom interacting with classical optical fields. Since no unique analytical results exist relating that operationally relate

the two paradigms of quantum correlation, viz. entanglement-separability and information-theoretic, finding quantitative relations between them in many-body systems or in quantum optical models may provide interesting insights.

In **Chapter 4**, we investigate the dynamics of information-theoretic measures of quantum correlation and entanglement, in a time-evolved nonequilibrium state of the infinite anisotropic quantum XY spin chain in a transverse time-dependent field [126, 127]. It is observed that nearest-neighbor entanglement undergoes a dynamical phase transition with respect to the field parameter leading to entanglement death and occasional revival. We show that the dynamical phase transition of entanglement is qualitatively related to the dynamics of information-theoretic quantum correlation measures such as quantum discord and quantum work-deficit. We derive quantitative relations showing that the entanglement death and subsequent revival are heralded by the rate of increase of quantum discord [126] in the vicinity of the critical value of entanglement death. Further, the revival of entanglement is also directly related to the cumulative quantum work-deficit during the dynamical evolution of the system [127]. The behavior of quantum correlation also provides useful insights on other important aspects of the dynamics such as quantum quenching.

In **Chapter 5**, we analytically derive and characterize the dynamics of two-photon quantum correlation generated by the interaction of a three-level atom in the Ξ, Λ, or V configuration, with two classical external driving fields [128]. Using the example of a rubidium atom in each configuration, in the presence of level decays, under the rotating-wave approximation and using the single-photon approximation, one can compute information-theoretic correlation, such as measurement induced disturbance, quantum discord, and quantum work-deficit, and compare the results with that of entanglement, for the generated two-photon state. It is observed that the qualitative hierarchy, monotonicity and steady-state behavior of the quantum correlation can be controlled through the choice of parameters such as atomic decay constants and external driving field strengths.

In **Chapter 6**, we summarize the basic results of the thesis and briefly discuss future directions that emanate from the results obtained in the research work.

In **Appendix A**, we provide an example for the generation of entanglement in CV optical states, using a superposition of number-conserving non-Gaussian operations. The bimode entangled states are observed to be efficient quantum channels in CV quantum teleportation protocols. The study demonstrates the ready applicability of CV states in quantum information protocols.

[1] E. Schrödinger, Proc. Cambridge Phil. Soc. **31**, 555 (1935).

[2] A. Einstein, B. Podolsky, and N. Rosen, Phys. Rev. **47**, 777 (1935).

[3] C. Cohen-Tannoudji, B. Diu, and F. Laloe, *Quantum Mechanics, Vol. 1 and 2*, Wiley, New York (1977).

[4] M.A. Nielsen and I.L. Chuang, *Quantum Computation and Quantum Information*, Cambridge Univ. Press, Cambridge (2000).

[5] D. Bouwmeester, A. Ekert, and A. Zeilinger, *The Physics of Quantum Information: Quantum Cryptography, Quantum Teleportation, Quantum Computation*, Springer, New York (2000).

[6] R. Horodecki, P. Horodecki, M. Horordecki and K. Horodecki, Rev. Mod. Phys. **81**, 865 (2009).

[7] J.S. Bell, Physics (Long Island City, N.Y.) **1**, 195 (1965).

[8] A. Aspect, P. Grangier and G. Roger, Phys. Rev. Lett. **47**, 460 (1981); A. Aspect, J. Dalibard and G. Roger, Phys. Rev. Lett. **49**, 1804 (1982).

[9] N. Brunner, D. Cavalcanti, S. Pironio, V. Scarani, and S. Wehner, Rev. Mod. Phys. **86**, 419 (2014).

[10] R. P. Feynman, Int. J. Theor. Phys. **21**, 467 (1982).

[11] C.H. Bennett and G. Brassard, *Proceedings of the IEEE International Conference on Computers, Systems and Signal Processing*, IEEE Computer Society, New York, (1984). pp. 175179; D. Deutsch, Proc. R. Soc. London, Ser. A **400**, 97 (1985).

[12] R.F. Werner, Phys. Rev. A **40**, 4277 (1989).

[13] P. Horodecki, and R. Horodecki, Phys. Lett. A **194**, 147 (1994).

[14] R. Horodecki, P. Horodecki, and M. Horodecki, Phys. Lett. A **210**, 377 (1996).

[15] M.A. Nielsen and J. Kempe, Phys. Rev. Lett. **86**, 5184 (2001).

[16] A. Peres, Phys. Rev. Lett **77**, 1413 (1996).

[17] M. Horodecki, P. Horodecki, and R. Horodecki, Phys. Lett. A **223**, 1 (1996).

[18] L. Henderson and V. Vedral, J. Phys. A **34**, 6899 (2001).

[19] H. Ollivier and W.H. Zurek, Phys. Rev. Lett. **88**, 017901 (2001).

[20] J. Oppenheim, M. Horodecki, P. Horodecki, and R. Horodecki, Phys. Rev. Lett. **89**, 180402 (2002); M. Horodecki, K. Horodecki, P. Horodecki, R. Horodecki, J. Oppenheim, A. Sen(De), and U. Sen, Phys. Rev. Lett. **90**, 100402 (2003).

[21] K. Modi, A. Brodutch, H. Cable, T. Paterek, and V. Vedral, Rev. Mod. Phys. **84**, 1655 (2012).

[22] M. Lewenstein, A. Sanpera, V. Ahufinger, B. Damski, A. Sen(De), and U. Sen, Adv. Phys. **56**, 243 (2007); L. Amico, R. Fazio, A. Osterloh, and V. Vedral, Rev. Mod. Phys. **80**, 517 (2008).

[23] S.L. Braunstein and A.K. Pati, *Quantum Information with Continuous Variables*, Kluwer Academic, Dordrecht (2003).

[24] S.L. Braunstein and P. van Loock, Rev. Mod. Phys. **77**, 513 (2005).

[25] L. Susskind and J. Lindesay, *An introduction to black holes, information and the string theory revolution: The holographic universe*, World Scientific, Hackensack, NJ (2005).

[26] P. Ball, Nature (London) **474**, 272 (2011), and references therein.

[27] A. Zeilinger, Rev. Mod. Phys. **71**, S288 (1999); G. Greenstein and A. Zajonc, *The Quantum Challenge: Modern Research on the Foundations of Quantum Mechanics*, Jones and Bartlett Publishers, Sudbury, MA (2006).

[28] S. Kochen and E.P. Specker, J. Math. Mech. **17**, 59 (1967); A.A. Klyachko, M.A. Can, S. Binicioğlu, and A.S. Shumovsky, Phys. Rev. Lett. **101**, 020403 (2008), and references therein.

[29] V.B. Braginsky and F.Y. Khalili, *Quantum Measurement*, Cambridge Univ. Press, Cambridge (1992).

[30] C.H. Bennett, D.P. DiVincenzo, C.A. Fuchs, T. Mor, E. Rains, P.W. Shor, J.A. Smolin, and W.K. Wootters, Phys. Rev. A **59**, 1070 (1999); C.H. Bennett, D.P. DiVincenzo, T. Mor, P.W. Shor, J.A. Smolin, and B.M. Terhal, Phys. Rev. Lett. **82**, 5385 (1999); J. Walgate, A.J. Short, L. Hardy, and V. Vedral, Phys. Rev. Lett. **85**, 4972 (2000); S. Virmani, M.F. Sacchi, M.B. Plenio, and D. Markham, Phys. Lett. A. **288**, 62 (2001); Y.-X. Chen and D. Yang, Phys. Rev. A **64**, 064303 (2001); D.P. DiVincenzo, T. Mor, P.W. Shor, J.A. Smolin, and B.M. Terhal, Comm. Math. Phys. **238**, 379 (2003); M. Horodecki, A. Sen(De), U. Sen, K. Horodecki, Phys. Rev. Lett. **90**, 047902 (2003).

[31] C.H. Bennett, G. Brassard, C. Crépeau, R. Jozsa, A. Peres and W.K. Wootters, Phys. Rev. Lett. **70**, 1895 (1993).

[32] C.H. Bennett and S.J. Wiesner, Phys. Rev. Lett. **69**, 2881 (1992).

[33] A. Ekert, Phys. Rev. Lett. **67**, 661 (1991).

[34] R. Raussendorf and H.J. Briegel, Phys. Rev. Lett. **86**, 5188 (2001).

[35] E. Knill, R. Laflamme and G. J. Milburn, Nature (London) **409**, 46 (2001).

[36] S. Popescu, Phys. Rev. Lett. **99**, 250501 (2007).

[37] C.H. Bennett, D.P. DiVincenzo, J.A. Smolin, and W.K. Wootters, Phys. Rev. A **54**, 3824 (1996).

[38] S. Hill and W.K. Wootters, Phys. Rev. Lett. **78**, 5022 (1997); W.K. Wootters, Phys. Rev. Lett. **80**, 2245 (1998).

[39] G. Vidal and R. F. Werner, Phys. Rev. A **65**, 032314 (2002).

[40] T. Osborne and M. Nielsen, Phys. Rev. A **66**, 032110 (2002).

[41] A. Osterloh, L. Amico, G. Falci, and R. Fazio, Nature (London) **416**, 608 (2002).

[42] S. Sachdev, *Quantum Phase Transition*, Cambridge Univ. Press, Cambridge (1999).

[43] F. Verstraete, D. Porras, and J.I. Cirac, Phys. Rev. Lett. **93**, 227205 (2004).

[44] G. Vidal, Phys. Rev. Lett. **93**, 040502 (2004).

[45] S. Bose, Phys. Rev. Lett. **91**, 207901 (2003).

[46] E. Knill and R. Laflamme, Phys. Rev. Lett. **81**, 5672 (1998).

[47] R. Laflamme, D. G. Cory, C. Negrevergne, and L. Viola, Quantum Inf. Comput. **2**, 166 (2002).

[48] A. Datta, A. Shaji and C. M. Caves, Phys. Rev. Lett. **100**, 050502 (2008).

[49] B. Dakic, V. Vedral, and C. Brukner, Phys. Rev. Lett. **105**, 190502 (2010).

[50] S. Luo, Phys. Rev. A **77**, 022301 (2008).

[51] A.K. Rajagopal and R.W. Rendell, Phys. Rev. A **66**, 022104 (2002).

[52] I. Chakrabarty, P. Agrawal, and A.K. Pati, Eur. Phys. J. D **65**, 605 (2011).

[53] K. Modi, T. Paterek, W. Son, V. Vedral, and M. Williamson, Phys. Rev. Lett. **104**, 080501 (2010).

[54] M. Piani, P. Horodecki, and R. Horodecki, Phys. Rev. Lett. **100**, 090502 (2008).

[55] C. Invernizzi, M.G.A. Paris, and S. Pirandola, Phys. Rev. A **84**, 022334 (2011).

[56] D. Cavalcanti, L. Aolita, S. Boixo, K. Modi, M. Piani, and A. Winter, Phys. Rev. A **83**, 032324 (2011); V. Madhok and A. Datta, Phys. Rev. A **83**, 032323 (2011).

[57] K. Modi, H. Cable, M. Williamson, and V. Vedral, Phys. Rev. X **1**, 021022 (2011).

[58] R. Dillenschneider, Phys. Rev. B **78**, 224413 (2008); T. Werlang, G.A.P. Ribeiro, G. Rigolin, Phys. Rev. Lett. **83**, 062334 (2011).

[59] T. Werlang, G. Rigolin, Phys. Rev. A **81**, 044101 (2011); J. Maziero, L.C. Cleri, R.M. Serra, M.S. Sarandy, Phys. Lett. A **376**, 1540 (2012).

[60] B. Bellomo, R. Lo Franco, G. Compagno, Phys. Rev. A **86**, 012312 (2012), and references therein.

[61] R.J. Glauber, Phys. Rev. **131** 2766 (1963); E.C.G. Sudarshan, Phys. Rev. Lett. **10** 277 (1963);

[62] L. Mandel and E. Wolf, Rev. Mod. Phys. **37**, 231 (1965).

[63] C. Cohen-Tannoudji, J. Dupont-Roc, and G. Grynberg, *AtomPhoton Interactions: Basic Processes and Applications*, John Wiley and Sons, New York (1992).

[64] M.O. Scully and M.S. Zubairy, *Quantum Optics*, Cambridge Univ. Press, Cambridge (1997).

[65] R.Ghosh and L. Mandel, Phys. Rev. Lett. **59**, 1903 (1987).

[66] J F Clauser and A Shimony, Rep. Prog. Phys. **41**, 1881 (1978).

[67] M. Żukowski, A. Zeilinger, M.A. Horne, and A.K. Ekert, Phys. Rev. Lett. **71**, 4287 (1993).

[68] R. Augusiak, F.M. Cucchietti, and M. Lewenstein, Lecture Notes in Physics **843**, 245 (2012).

[69] O. Gühne and G. Tóth, Phys. Rep. **474**, 1 (2009).

[70] L. Gurvits, STOC **69**, 448 (2003).

[71] M. Horodecki, P. Horodecki, and R. Horodecki, Phys. Rev. Lett. **80**, 5239 (1998).

[72] D.P. DiVincenzo, P.W. Shor, J.A. Smolin, B.M. Terhal, and A.V. Thapliyal, Phys. Rev. A **61**, 062312 (2000); W. Dür, J.I. Cirac, M. Lewenstein, and D. Bruß, Phys. Rev. A **61**, 062313 (2000).

[73] B.M. Terhal, Phys. Lett. A **271**, 319 (2000).

[74] O. Gühne, P. Hyllus, D. Bruß, A. Ekert, M. Lewenstein, C. Macchiavello, and A. Sanpera, J. Mod. Opt. **50**, 1079 (2003).

[75] B. Schumacher, Phys. Rev. A **51**, 2738 (1995).

[76] R. Bhatia, *Matrix Analysis*, Springer, New York, (1997).

[77] M.A. Nielsen, Phys. Rev. Lett. **83**, 436 (1999).

[78] G. Vidal, J. Mod. Opt. **47**, 355 (2000).

[79] C.H. Bennett, H. Bernstein, S. Popescu and B. Schumacher, Phys. Rev. A **53**, 2046 (1996).

[80] A. Uhlmann, Phys. Rev. A **62**, 032307 (2000).

[81] C.H. Bennett, G. Brassard, S. Popescu, B. Schumacher, J.A. Smolin, and W.K. Wootters, Phys. Rev. Lett. **76**, 722 (1996).

[82] F. Mintert, A.R.R. Carvalho, M. Kús, and A. Buchleitner, Phys. Rep. **415**, 207 (2005).

[83] S.P. Walborn, P.H.S. Ribero, L. Davidovich, F. Mintert, and A. Buchleitner, Nature **440**, 1022 (2006).

[84] P. Rungta and C.M. Caves, Phys. Rev. A **67**, 012307 (2003).

[85] M.B. Plenio, Phys. Rev. Lett. **95**, 090503 (2005).

[86] V.Vedral, M.B. Plenio, M.A. Rippin, and P.L. Knight, Phys. Rev. Lett. **78**, 2275 (1997); V. Vedral, Rev. Mod. Phys. **74**, 197 (2002).

[87] K. Modi, T. Paterek, W. Son, V. Vedral, and M. Williamson, Phys. Rev. Lett. **104**, 080501 (2010).

[88] M. Blasone, F. DellAnno, S. De Siena, and F. Illuminati, Phys. Rev. A **77**, 062304 (2008).

[89] D.M. Greenberger, M. A. Horne and A. Zeilinger, *Going Beyond Bells Theorem in Bells Theorem, Quantum Theory, and Conceptions of the Universe*, Kluwer Academic, Dordrecht (1989).

[90] A. Zeilinger, M. A. Horne, and D. M. Greenberger, in *Squeezed States and Quantum Uncertainty*, eds. D. Han, Y. S. Kim, and W. W. Zachary (NASA Conference Publication 3135, NASA, College Park, 1992); W. Dür, G. Vidal, and J. I. Cirac, Phys. Rev. A **62**, 062314 (2000).

[91] A. Sen(De) and U. Sen, Phys. News, **40** 17 (2010).

[92] A. Ekert and R. Jozsa, Rev. Mod. Phys. **68**, 733 (1996); A. Steane, Rep. Prog. Phys. **61**, 117 (1998).

[93] H.J. Briegel, D.E. Browne, W. Dür, R. Raussendorf, and M. Van den Nest, Nature Phys. **5**, 19 (2009).

[94] V. Coffman, J. Kundu, and W.K. Wootters, 2000, Phys. Rev. A 61, 052306.

[95] A. Wong and N. Christensen, Phys. Rev. A **63**, 044301 (2001).

[96] D. A. Meyer and N. R. Wallach, J. Math. Phys. **43**, 4273 (2002).

[97] A. Montakhab and A. Asadian, Phys. Rev. A **77**, 062322 (2008).

[98] H. Barnum and N. Linden, J. Phys. A **34**, 6787 (2001); T.-C. Wei and P.M. Goldbart, Phys. Rev. A **68**, 042307 (2003).

[99] A. Sen(De) and U. Sen, Phys. Rev. A **81**, 012308 (2010); A. Sen(De) and U. Sen, *Bound Genuine Multisite Entanglement: Detector of Gapless-Gapped Quantum Transitions in Frustrated Systems* , arXiv:1002.1253 (2010).

[100] W.H. Zurek, *Quantum Optics, Experimental Gravitation and Measurement Theory*, Plenum, New York (1983).

[101] B. Schumacher and M.A. Nielsen, Phys. Rev. A, **54**, 2629 (1996).

[102] A. Wehrl, Rev. Mod. Phys. **50**, 221 (1978).

[103] R. Landauer, IBM J. Res. Dev., **5** 183 (1961).

[104] M. Horodecki, P. Horodecki, R. Horodecki, J. Oppenheim, A. Sen(De), U. Sen and B. Synak-Radtke, Phys. Rev. A, **71** 062307 (2005).

[105] M. Piani, Phys. Rev. A **86**, 034101 (2012).

[106] D. Spehner and M. Orszag, New J. Phys. **15**, 103001 (2013).

[107] C. Weedbrook, S. Pirandola, R. García-Patrón, N.J. Cerf, T.C. Ralph, J.H. Shapiro, and S. Lloyd, Rev. Mod. Phys. **84**, 621 (2012).

[108] M. Abramowitz and I.A. Stegun, *Handbook of Mathematical Functions*, Dover, New York (1972).

[109] K.E. Cahill and R.J. Glauber, Phys. Rev. **177**, 1882 (1969).

[110] J. Janszky, M.G. Kim, and M.S. Kim, Phys. Rev. A **53**, 502 (1996).

[111] L. Mandel, Opt. Lett. **4**, 205 (1979).

[112] A. Lukš, V. Peřinová, and J. Peřina, Opt. Commun. **67**, 149 (1988).

[113] X. Xu, L. Hu, and H. Fan, Opt. Commun. **283**, 1801 (2010).

[114] S.L. Braunstein and H.J. Kimble, Phys. Rev. Lett. **80**, 869 (1998).

[115] S.M. Barnett and S.J. Phoenix, Phys. Rev. A **40**, 2404 (1989); S.J. van Enk, Phys. Rev. A **60**, 5095 (1999).

[116] R. Simon, Phys. Rev. Lett. **84**, 2726 (2000).

[117] R. Simon, N. Mukunda, and B. Dutta, Phys. Rev. A **49**, 1567 (1994).

[118] R.F. Werner and M.M. Wolf, Phys. Rev. Lett. **86**, 3658 (2001).

[119] A. Serafini, G. Adesso, and F. Illuminati, Phys. Rev. A **71**, 032349 (2005).

[120] L.-M. Duan, G. Giedke, J. I. Cirac, and P. Zoller, Phys. Rev. Lett. **84**, 2722 (2000).

[121] G. Adesso and A. Datta, Phys. Rev. Lett. **105**, 030501 (2010).

[122] G. Giedke and J.I. Cirac, Phys. Rev. A **66**, 032316 (2002).

[123] H. S. Dhar and A. Sen (De), J. Phys. A: Math. Theor. **44**, 465302 (2011).

[124] H. S. Dhar, A. Sen (De) and U. Sen, New J. Phys. **15**, 013043 (2013).

[125] H. S. Dhar, A. Sen (De) and U. Sen, Phys. Rev. Lett. **111**, 070501 (2013).

[126] H. S. Dhar , R. Ghosh, A. Sen (De) and U. Sen, EPL **98**, 30013 (2012).

[127] H. S. Dhar, R. Ghosh, A. Sen (De) and U. Sen, Phys. Lett. A **378**, 1258 (2014).

[128] H. S. Dhar, S. Banerjee, A. Chatterjee and R. Ghosh, Ann. Phys. **331**, 97 (2013).

[129] P. W. Anderson, Science **235**, 1196 (1987).

Characterization of entanglement in quantum spin-1/2 lattices

In this part of the thesis, we investigate the characterization of both bipartite and multipartite entanglement in quantum spin-1/2 lattices, with short-range dimer covered ground states, the so called resonating valence bond states. We first use quantum information theory concepts to study the behavior of entanglement in ladder and isotropic quantum spin-1/2 lattices. We then devise a recursion technique to obtain the behavior of entanglement in large quantum spin-1/2 systems. The results obtained provide us with valuable information regarding the distribution and scaling of entanglement in quantum spin systems and its strong dependence on geometry.

CHAPTER 2

Entanglement in quantum spin-1/2 lattices:
ladder versus isotropic resonating valence bond liquids

*If people did not sometimes do silly things, nothing intelligent would ever get
done.* – Ludwig Wittgenstein

In this chapter, we study the behavior of bipartite as well as multipartite entanglement
in quantum spin-1/2 lattices, with possible resonating valence bond (RVB) liquid
ground states. We compare the behavior of entanglement of RVB liquids on a two-
legged pseudo-2D ladder with isotropic 2D or 3D lattices. Although there is negligible
bipartite entanglement present in the rails of the RVB ladder, as is the case for
isotropic RVB lattices, we show that the system possesses significant amounts of
bipartite entanglement in the steps of the RVB ladder. Further, we also establish
that the genuine multipartite entanglement in the RVB ladder system is substantially
low in contrast to isotropic RVB lattices. Therefore, both the properties of bipartite
as well as multipartite entanglement in the RVB ladder are contrary to the behavior
of entanglement in isotropic RVB lattices, indicating that the geometry of the lattice
can play a significant role in quantum information processing tasks. Our results also
indicate that numerical and analytical investigations obtained on two-legged ladders
cannot infer the quantum correlation content in two-dimensional isotropic lattices.[1]

2.1 Introduction

In quantum many-body physics, quantum spin-1/2 lattices have received a lot of attention due to its importance in the description of different important nonclassical phenomena. Quantum spin-1/2 states, that we consider, are formed by the superposition of short-range dimer coverings, also known as short-range resonating valence bond (RVB) states [1-4], and have potential use ranging from the description of covalent bond structure in organic molecules [1, 2] to fault-tolerant quantum computation [5]. Such quantum spin-1/2 states, under the RVB ansatz, have been used to study many fundamental aspects of quantum many-body physics, such as Mott insulators [4], high-temperature superconductivity [6, 7], insulator-superconductor transitions in doped diamonds [8] and topological quantum computers [5]. Further, such RVB states have interesting short-range and multipartite entanglement [9] properties that can be exploited for applications in quantum information theory (QIT) [10-16].

The quantum spin-1/2 ladder in the intermediate regime between the one- and two-dimensional lattice structures [17] is an interesting platform to investigate quantum many-body phenomena. The characteristic pseudo 2-D structure of ladder states (obtained by assembling spin chains one next to the other to form *ladders* of increasing width) have recently generated a lot of interest in theoretical condensed matter physics. It has been found that ground states of antiferromagnetic Heisenberg models (with suitable couplings) on *even ladders* (consisting of two or more even number of chains) can be RVB states [18-20]. RVB ladder states have been proposed in the study of superconductivity in systems, such as doped $(VO)_2P_2O_7$ [18] and the study of transitions from 1-D RVB chains to 2-D RVB spin systems [19]. Quantum information concepts, such as entanglement and fidelity, have been studied on different spin ladder systems [21], and protocols for transmission of quantum states through such systems have also been presented [22] (cf. [23]). Quantum properties of such systems have also been tested experimentally in several systems or proposals thereof have been presented, including in compounds and cold gas [24-27].

In this chapter, we study the behavior of entanglement in quantum spin-1/2 ladders, with possible RVB liquid ground states, and contrast the results with that of an isotropic lattice in two or higher dimensions. To elaborate, we consider ladders consisting of two chains ($2 \times M$ ladders, N = 2M spins), of different lengths and show that the bipartite as well as multipartite entanglement characteristics of an RVB ladder state are significantly different from that of an isotropic RVB lattice. Bipartite entanglement between neighboring sites are of two different types for the case of a RVB ladder due to the asymmetry of the ladder lattice. We show that while the bipartite entanglement of the neighboring sites on

the rails of the RVB ladder is insignificant, that of the steps (or rungs) is substantial. This intuitively suggests that multipartite entanglement of the RVB ladder is negligible which is confirmed by considering measures of multipartite entanglement. This observation is in sharp contrast with that of an isotropic 2D or 3D RVB lattice, where the single type of nearest-neighbor (NN) bipartite entanglement is negligible, while the state is genuinely multiparty entangled [11]. We reach our conclusions via analytical bounds on entanglement measures using QIT concepts and also by exact numerical calculations. The asymmetry inherent in the ladder makes the analytical study of bipartite entanglement interesting and far from straightforward. The change in the entanglement properties can be attributed to the change in the geometry of the RVB system: a ladder is not isotropic. Our results show that this change in geometry has a marked effect on the entanglement properties of the system, and hence, on quantum information tasks possible therein. While it is expected that the value of entanglement should be different for a change in geometry, we find that such a change can effectively change the qualitative behavior of entanglement in the system.

The chapter is arranged in the following way. We start with a brief introduction and mathematical formulation of the RVB liquid state in Section 2.2. We then discuss the characterization of bipartite and multipartite entanglement for the considered RVB lattice in Section 2.3. In Section 2.5, we analytically study the properties and bounds on entanglement in RVB systems, using quantum information concepts. We obtain numerical results for the bipartite and multipartite entanglement in finite-sized, two-legged RVB ladders in Section 2.4. We end with a short concluding statement in Section 2.6.

2.2 Resonating valence bond liquids

Resonating valence bond states were introduced in 1938 by Pauling in organic, and later in metals and intermetallic, compounds [1, 2]. It was extensively studied in many-body physics ever since Anderson, in 1973, who presented the idea of using such states to explain the behavior of Mott insulators [3, 4]. The importance of RVB states grew immensely after the proposition of relating such states with high-temperature superconductivity [6, 7]. The possibility of topological quantum computation using RVB states have been proposed [5], and the entanglement properties of such states in isotropic two- and three-dimensional lattices have also been explored [10–16]. Quantum spin-1/2 lattices with RVB substrates, have been successfully simulated by using atoms in optical lattices [28, 29], and, also by using interacting photons [30]. As mentioned earlier, the short-range RVB ladders are believed to be possible ground states of certain undoped Heisenberg spin ladders, that is supported by various numerical methods which include mean field theory [31], quantum Monte Carlo [32, 33], and Lanczos [18, 34]. In isotropic 2D systems, RVB–like dimer states are found

to be ground states of a frustrated antiferromagnet on the 1/5-depleted square lattice [35, 37], the J_1-J_2-J_3 antiferromagnetic Heisenberg model [38, 39], and certain textured spin gases in general. The RVB ground state can be expressed in terms of cluster Hamiltonians [40]. In general, the RVB ground state can be expressed in terms of the Rokhsar-Kivelson Hamiltonian [41, 42].

The study of entanglement characteristics were done for the RVB liquid state, which we now define in this segment. The periodic two-dimensional RVB ladder, or the isotropic RVB lattice under consideration can be divided into two sub-lattices (see Figure 2.1), A and B, in such a way that all the nearest-neighbour sites of any site on sub-lattice A belong to sub-lattice B, and vice-versa. Such a lattice is called a bipartite lattice. Each lattice site on such a bipartite system is occupied by a qubit, which can, for example, be a two-level atom or the spin degree of freedom of an electron. For the quantum spin-1/2 lattice under consideration, the qubit is the spin of an electron. For such a system the RVB state is defined as the equal superposition of all the possible dimer (singlet) coverings that can be formed by nearest-neighbour directed dimers. Between site i in sublattice A and site j in sublattice B, a directed dimer is defined as $|(i,j)\rangle = \frac{1}{\sqrt{2}}(|\downarrow\uparrow\rangle - |\uparrow\downarrow\rangle)$, where $|\uparrow\rangle$ and $|\downarrow\rangle$ are respectively the spin-up and spin-down states in the z-direction, at the corresponding lattice site. The (unnormalised) RVB state can then be written as [43]

$$|\psi\rangle = \sum |(a_1, b_1)(a_2, b_2)\cdots(a_N, b_N)\rangle , \qquad (2.1)$$

where a_i and b_j are site positions and the summation is over all dimer coverings such that the dimers in every covering satisfy $a_i \in A$ and $b_j \in B$ (see Figure 2.2 for all possible coverings on a 5 × 3 RVB ladder with open boundary conditions). Since the dimer coverings

Figure 2.1: RVB liquid on a ladder. Blue and black balls belong to two different sublattices, A and B, respectively. Singlets are shown in bold arrows and the figure demonstrates one particular dimer covering. Singlets are always from sublattice A to sublattice B. Rungs/steps are shown in green elliptical boundary and rails are shown in red boxes.

²Also see Figure 3.1 in Section 3.2.
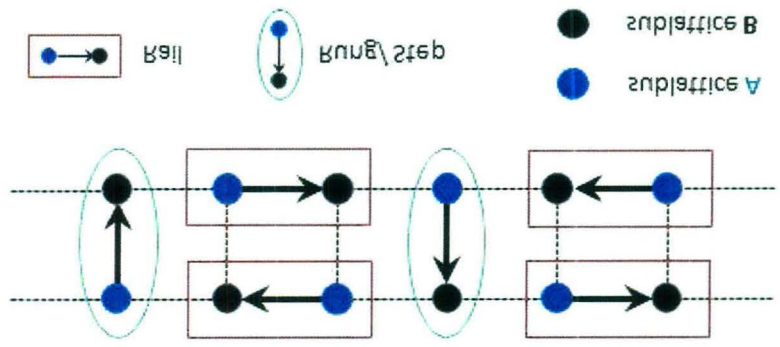
that constitute the RVB state are formed by using only NN dimers, the state $|\psi\rangle$ is generally referred to as an *RVB liquid*. In the remainder of the text, the term RVB state will refer to an RVB liquid state, unless otherwise stated.

The dimer coverings are formed by nearest-neighbor dimers, with each dimer being from a site in sublattice A to a nearest-neighbor site in sublattice B. Moreover, we consider the periodic boundary condition i.e., the corresponding strips (rails) are joined at the ends. The condition is slightly different for ladders with an odd number of steps, as compared to the ones with an even number of them. For ladders with an even number of steps, the ends of the ladder are such that any leg of the ladder has sites of different sublattices at the two ends, so that the ends of the ladder can be joined by dimers in a *normal way* for attaining periodic boundary condition, in the sense that there are two faces of the ribbon formed and painting the ribbon with a brush only paints one face of the ribbon, if the brush is not lifted. The situation is different for ladders with an odd number of steps, where to connect the ends of the ladder with dimers beginning in one sublattice and ending in another, one has to *twist* the ribbon, so that after joining, the ribbon forms a Möbius strip. In the latter case, the same mode of painting as in the even-steps case, will paint the whole ribbon (without lifting the brush).

2.3 Characterization of entanglement in RVB liquid

From the perspective of QIT, concepts such as entanglement [9] and other information-theoretic quantum correlation [44] have been applied to understand quantum critical phenomena in spin systems [45, 46]. Incidentally, large dimerized spin systems with exotic topological phases [3, 47], such as an RVB liquid, are a crucial many-body substrate that can be a useful resource in QIT applications, such as fault-tolerant computation [5]. In this section, we characterize the NN bipartite entanglement and the genuine multisite entanglement in quantum spin-1/2 RVB systems.

We begin by deriving the nearest-neighbor bipartite states of an RVB liquid. To obtain the bipartite density matrix, ρ_{12}, between any site (say, 1) in A and one of its nearest neighbors (say, 2) in B, we take the partial trace of the whole RVB liquid over all sites except 1 and 2: $\rho_{12} = \mathrm{Tr}_{\overline{12}} |\psi\rangle \langle\psi|$, where $\mathrm{Tr}_{\overline{12}}$ represents the partial trace over all sites other than 1 and 2. Rotational invariance of $|\psi\rangle$ implies that ρ_{12} (and all other reduced density matrices of $|\psi\rangle$) is also rotationally invariant. The only rotationally invariant two-qubit states are the singlet and the maximally mixed state. Therefore, ρ_{12} is the Werner state [48], given by

$$\rho_{12}(p) = p\,|(i,j)\rangle\,\langle(i,j)| + \frac{1-p}{4}I_4, \tag{2.2}$$
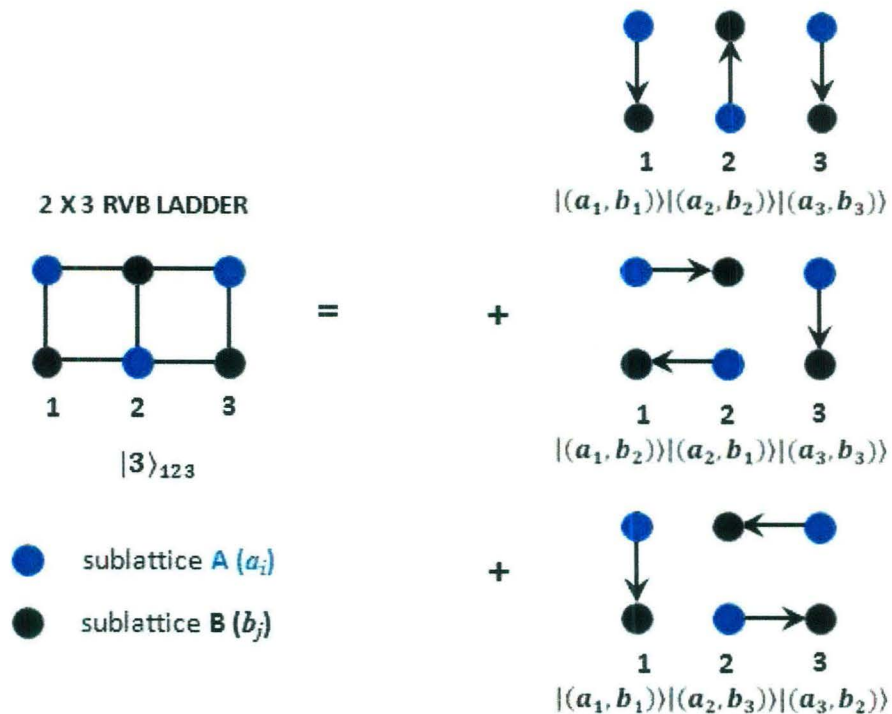
Figure 2.2: There are 3 possible dimer coverings on a 2×3 RVB ladder with open boundary conditions, contributing to the summation of the RVB state $|\psi\rangle = |3\rangle_{123}$, given by Equation (2.1). The sublattices are the same as defined in Figure 2.1. The dimers in every covering satisfy $a_i \in A$ and $b_j \in B$. The singlets are shown by arrows.

where the *mixing* or *Werner parameter*, p satisfies $-1/3 \leq p \leq 1$, and I_4 is the identity operator of the four-dimensional complex Hilbert space. Bipartite entanglement (BE) measures, such as entanglement of formation [49] and concurrence [50, 51], are monotonic functions of p. Hence, instead of calculating entanglement measures explicitly, we will investigate the behavior of p with respect to increase of system size. Note here that the Werner state is entangled for $p > 1/3$ [48].

From the geometry of the RVB ladder, it intuitively seems that the Werner parameter p will be different for the steps and the rails and there are two types of nearest-neighbor bipartite states: along any one of the rails, and on a step (see Figure 2.1). We denote the Werner parameter p of a Werner state along a rail as p_r, while that on a step as p_s. Under the considered periodic boundary conditions, all the bipartite states along the rails are equivalent to one another, and so are the states on the steps. The two-qubit states on the rails and steps, however, may be inequivalent. A ladder has the property that every site on it is on the boundary. However, the boundary for a rail-state is different from that of a step-state: the former touches only one edge of the boundary, while the latter touches both.

Intuitively, this difference in the relative placing of the rail- and step-states in the general structure of the ladder, will lead to different Werner parameters.

The genuine multipartite entanglement in the RVB liquid state can be calculated using the generalized geometric measure (GGM) [52, 53], defined in Section 1.3.4. To calculate the GGM one needs to obtain the maximal Schmidt coefficient square in all possible bipartite splits $A : B$ of $|\psi\rangle$, which can be obtained from the square root of the eigenvalues of the reduced density matrix, $\rho_A = \text{tr}_B |\psi\rangle\langle\psi|$, as shown in Equation (1.23). Hence, the GGM can be calculated by obtaining the n-site reduced density matrices of the pure RVB liquid state, $|\psi\rangle$ corresponding to different bipartition splits. The bipartite state (ρ_{12}) in Equation (2.2) is a possible two-site reduced density matrix. Similarly, an n-site reduced density matrix is obtained using, $\rho_{12...n} = \text{tr}_{\overline{12...n}} |\psi\rangle\langle\psi|$.[3]

2.4 Numerical evaluation of entanglement in RVB ladders using periodic boundary conditions

In this section, we obtain numerical values using exact diagonalization, to obtain the bipartite and multipartite entanglement in finite-size, two-legged RVB ladders. The bipartite entanglement is quantified using the Werner parameter p, and the genuine multipartite entanglement is quantified using the generalized geometric measure.

2.4.1 Bipartite Entanglement: Steps versus Rails

We know, by symmetry, there are only two types of nearest-neighbor bipartite states in the RVB liquid on a ladder: along any one of the rails, and on a step, with Werner parameter p_r and p_s, respectively.

As shown in Figure 2.3, the values of p_r consistently decrease with the increasing system size N, and hence bipartite entanglement on the rails decreases with the increasing N, similar to the case of an isotropic lattice. Interestingly, the bipartite entanglement (BE) of the steps *increases* with respect to N (see Figure 2.4).[4] This complementary behavior of the NN bipartite entanglement between the rails and the steps is further supported by the analytical results obtained from quantum information tools such as monogamy of entanglement and

---

[3]The derivation of reduced density matrices in arbitrary sized RVB lattices is numerically constrained by the sheer size of Hilbert space. As shown in the next chapter (Section 3.3), this can be overcome using innovative analytical techniques based on recursion of the density matrix [15, 16].

[4]There is a slight decrease in BE before the increase occurs. This effect is due to the periodic nature of the RVB liquid. There is a slight difference in the periodic boundary conditions between ladders made of an even number of steps and those with an odd number of steps, as mentioned earlier. The BE values for the odd and even cases are separately monotonically increasing, while finite-size effects have led to small oscillations between neighboring even and odd step system-sizes, for very small system sizes. This is observed at lower values of N, but blurs out at higher values. It does not affect the predictions qualitatively.

asymmetric quantum telecloning in Section 2.5.
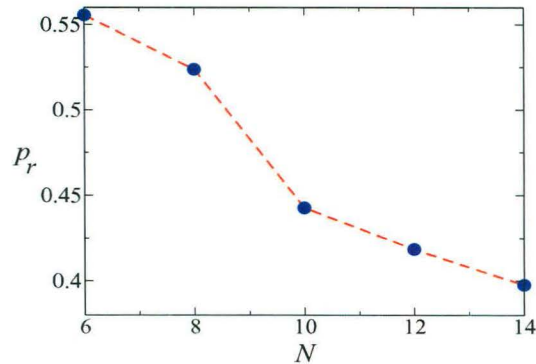
Figure 2.3: Bipartite entanglement on the rails. The decrease of the entanglement parameter p_r with increasing N is clearly seen. Here, $N = 2M$ is even.
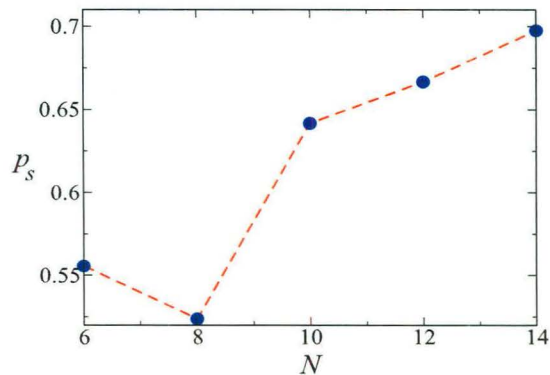
Figure 2.4: Bipartite entanglement on the steps. In sharp contrast to the isotropic case, bipartite entanglement on the steps, as parametrized by p_s, *increases* with increasing system size N. Here, $N = 2M$ is even.

Therefore, already at the level of bipartite entanglement, one obtains a trade-off between the two different forms of nearest-neighbor entanglement, in the case of an RVB liquid on a ladder. Contrast this with the case of a square lattice or any other isotropic lattice, where the corresponding RVB states have only a single type of nearest-neighbor entanglement due to its symmetry and its value decreases with increasing system size [11].

2.4.2   Negligible genuine multipartite entanglement

The numerical results in Section 2.4.1 on the values of NN bipartite entanglement already suggest that the RVB liquid on a ladder has negligible or no genuine multiparty entanglement. This is due to the fact that for a multipartite state, maximal bipartite entanglement in any of its two-party reduced density matrices leads to no genuine multipartite entanglement, which

is evident from the results presented, that the bipartite entanglement of the states on the steps are near-maximal or maximal. A maximally entangled state in $d \otimes d$ must be pure[5] (cf. [54]), and hence cannot have any correlation, classical or quantum, with the other part of the quantum system (cf. [55]).[6]

In this segment, we concretize these evidences by direct computation of a measure of genuine multiparty entanglement for the systems under study.

To quantify the amount of genuine multiparty entanglement present in the RVB liquid on ladders of different sizes, we consider a genuine multipartite entanglement measure called generalized geometric measure (GGM) [52, 53] (see Section 2.3).
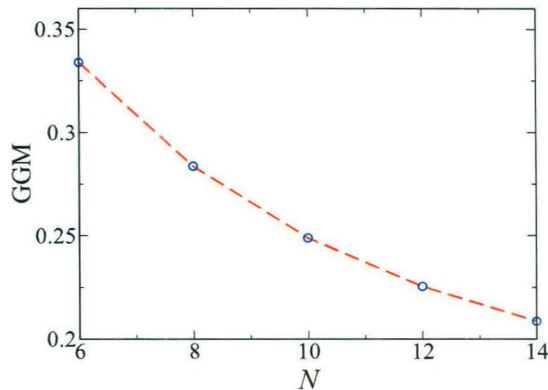
Figure 2.5: Genuine multipartite entanglement measure of RVB liquid on ladders. The figure clearly shows that the genuine multipartite entanglement decreases with the increase of system size N. Here, $N = 2M$ is even.

In Figure 2.5, we find that indeed the GGM for the RVB liquid on a ladder, decreases with increasing N. We also notice that when performing the maximization for obtaining the GGM, the maximum Schmidt coefficient is obtained when the maximum number of steps are included on one side of the bipartition. This can be explained by the complementary behavior of bipartite entanglement in steps and rails as discussed earlier. Therefore, the trend of multipartite as well as bipartite entanglements indicate that for large N, only bipartite entanglement in the steps will remain, while bipartite entanglement of the rails as well as multipartite entanglement of the whole RVB liquid will disappear.

---

[5]M. Horodecki, U. Sen, W.K. Wootters, and A. Sen(De), private communication (2002).

[6]For a clearer explanation, check the theorem on Section 2.5.3 or consult the section on mutipartite entanglement in Section 1.3.4.

2.5 Analytical estimate of entanglement from quantum information tasks

The behavior of bipartite and multipartite entanglement in short-range RVB lattices can be characterized using concepts of quantum information theory such as monogamy of entanglement [56, 57], asymmetric quantum cloning [58] and strong sub-additivity of von Neumann entropy [59]. In Reference [11], it was shown using the monogamy of entanglement and quantum telecloning properties, that while large isotropic, 2D or higher dimensional RVB lattices have finite multisite entanglement, they possess negligible bipartite entanglement. Using a variation of these quantum information-theoretic tools, we derive upper bounds on entanglement for the pseudo-2D RVB liquid ladders and demonstrate that the results cannot be extrapolated to isotropic 2D lattices [13]. We also present an exhaustive proof to show that isotropic RVB lattices, with necessary boundary conditions, are always genuinely multisite entangled [16], which from numerical results in Section 2.4.2, is known to be untrue for RVB ladders. A qualitative analysis using QIT properties shows that the change in geometry affects the behavior of both bipartite and multipartite entanglement [13].

2.5.1 Upper bound on bipartite entanglement from monogamy of entanglement

A first estimate on the bipartite entanglement can be obtained by using the quantum information-theoretic property of *monogamy of entanglement* [56, 57]. Let us consider an arbitrary site i_A, say on sublattice A of the bipartite lattice. Each site is surrounded by three NN sites, belonging to the sublattice B. Rotational invariance of the state $|\psi\rangle$ ensures that all the three NN bipartite states are in Werner states, of which two have Werner parameter p_r (along the rail), and one has p_s (along the step). The monogamy of entanglement [56, 57] demands that

$$2\tau(\rho_r) + \tau(\rho_s) \leq \tau_{1:\text{rest}}(|\psi\rangle).$$ (2.3)

$\tau(\rho)$ is the concurrence [50, 51] of the bipartite state ρ, as defined in Section 1.3.3.3. For a Werner state, $\rho(p)$, $\tau(\rho) = (3p - 1)^2/4$. Further, $\tau_{1:\text{rest}}(|\psi\rangle)$ is the tangle of the state $|\psi\rangle$ in any bipartition of one site to rest of the sites, and is bounded by 1, i.e., $\tau_{1:\text{rest}}(|\psi\rangle) \leq 1$. Hence, the tangle for the NN rail/step state is $\tau(\rho(p_{r/s})) = (3p_{r/s} - 1)^2/4$, so that the monogamy inequality reads [13]

$$\frac{(3p_r - 1)^2}{2} + \frac{(3p_s - 1)^2}{4} \leq 1.$$ (2.4)

The bound on p_r and p_s obtained in the form of the above inequality is depicted in Figure 2.6. The 2D projection of the surface in Figure 2.6 clearly shows that the allowed value for p_s can go up to 1 while the same for p_r is ≤ 0.8. The complementary behavior between the
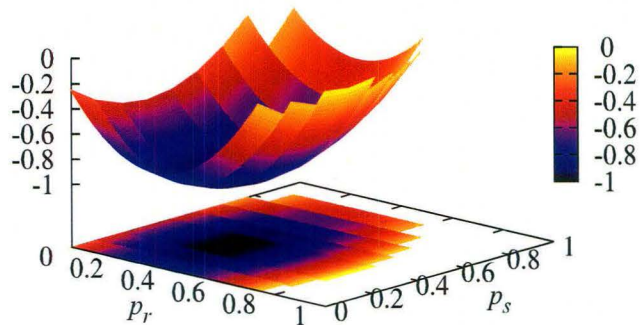
Figure 2.6: Estimate of Werner parameters from the monogamy of entanglement. The allowed combinations of p_r and p_s are those for which the surface $(3p_r-1)^2/2+(3p_s-1)^2/4-1$ is negative, and can be read off from the projection of the surface.

entanglement in the rails and steps can be anticipated from the monogamy inequality and Figure 2.6. A numerical increase in p_s with increasing ladder size will imply a decrease in p_r. The monogamy relation here is enunciated by using the three NN sites of any given lattice. In principle, it is not necessary to restrict oneself to only the NN sites, and a monogamy relation using all sites of the lattice can also be considered. Such a non-NN site monogamy relation is relatively simple to handle in isotropic states due to symmetry but is complicated for the case of an RVB ladder. Since the RVB liquid involves only nearest-neighbor dimer coverings, it is plausible that a monogamy relation involving only nearest-neighbor sites will be sufficiently strong to obtain the information required from it.

For isotropic 2D RVB lattice $p_r = p_s = p$, the monogamy bound on p, for four NN sites is given by $p \leq 2/3$. For R non-NN bipartite states, the monogamy relation for isotropic RVB states can be written as, $R \times (3p - 1)^2/4 \leq 1$, and the bound on p reduces to [11],

$$p \leq \frac{2}{3\sqrt{R}} + \frac{1}{3}. \tag{2.5}$$

2.5.2 Bounds on bipartite entanglement from asymmetric telecloning

More stringent estimates on bipartite entanglement can be obtained by using information-theoretic properties of a general quantum teleportation channel [60, 61] and the distribution of information in asymmetric quantum cloning [58].

Asymmetric quantum telecloning: The optimal fidelity of quantum teleportation using a $d \times d$ bipartite system is directly related to its maximal singlet fraction $\mathcal{F}$, by the relation

$$f = \frac{\mathcal{F}d + 1}{d + 1}, \tag{2.6}$$

where f is the fidelity of teleportation [61]. For a generalized $d \times d$ Werner state, the singlet

fraction is related to the Werner parameter p, by the relation,

$$\mathcal{F} = p + \frac{1-p}{d^2}. \tag{2.7}$$

Hence, the optimal fidelity of quantum teleportation in terms of the Werner parameter, using Equations (2.6) and (2.7), is given by the relation (Equation (14) in Reference [61]),

$$f = p + \frac{1-p}{d}. \tag{2.8}$$

If the NN bipartite states in an RVB ladder ($d = 2$) are used as quantum teleportation channels, the fidelity of teleporting an arbitrary auxiliary qubit from any site i_A, in sublattice A, to its three neighboring sites, in sublattice B, will depend on the Werner parameter p_r (along the rails) and p_s (along the steps). From Equation (2.10), the teleportation fidelity of the output state using NN sites on the same rail (as i_A) and the NN site along the step is given by,

$$f_r = (p_r + 1)/2, \qquad f_s = (p_s + 1)/2. \tag{2.9}$$

However, quantum mechanics implies that the fidelities of the output states in any teleportation protocol along $1 + n$ bipartite quantum channels cannot exceed the fidelities of $1 + n$ approximate clones of the initial state in the optimal $1 \rightarrow (1+n)$ asymmetric quantum cloning machine [58] (also see [62]). For $n > 1$, the corresponding fidelities in the optimal $1 \rightarrow (1 + n)$ asymmetric cloning, can be written as (Equation (1) in Reference [58]),

$$f_1^{cl} = 1 - \frac{2}{3}y^2, \qquad f_n^{cl} = \frac{1}{2} + \frac{1}{3n}[y^2 + \sqrt{n(n+2)}xy], \tag{2.10}$$

where, $x^2 + y^2 = 1$. For quantum teleportation along the three NN bipartite sites in an RVB ladder, the fidelity is constrained by the optimal $1 \rightarrow (1 + 2)$ asymmetric quantum cloning, corresponding to one NN along the step and two along the rails ($n = 2$) of the site i_A. Hence, the expression for asymmetric cloning in Equation (2.10) can be rewritten as,

$$f_s^{cl} = 1 - \frac{2}{3}y^2, \qquad f_r^{cl} = \frac{1}{2} + \frac{1}{6}[y^2 + 2\sqrt{2}xy]. \tag{2.11}$$

The fidelity constraint implies that, $f_r \leq f_r^{cl}$ and $f_s \leq f_s^{cl}$. Taking, $x = \cos\theta$ and $y = \sin\theta$, and using Equations (2.9) and (2.11) for the expression of teleportation and cloning fidelities, we obtain the following bound on the Werner parameters p_r and p_s,

$$p_r \leq \frac{1}{3}(\sin^2\theta + \sqrt{2}\sin 2\theta), \qquad p_s \leq 1 - \frac{4}{3}\sin^2\theta, \tag{2.12}$$

for all possible θ. This gives us the bound from asymmetric telecloning [13].

From the asymmetric telecloning bound obtained in Equation (2.12), we note here that if $\theta \rightarrow 0$, it would imply $p_r \leq 0$ and $p_s \leq 1$. Moreover, $p_r \leq 0$ will imply no bipartite
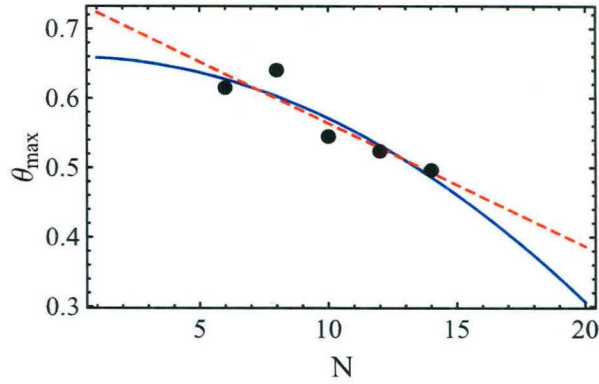
Figure 2.7: Decrease of θ_{max} for increasing N. The dots represent θ_{max} obtained from Equation (2.12) corresponding to $N = 6, 8, 10, 12, 14$. Red (dashed) and blue lines are respectively linear $(0.741298 - 0.0177198x)$ and quadratic $(0.659286 - 0.00088135x^2)$ fits of the points. The corresponding mean square errors are 1.22×10^{-3} for the linear fit and 1.06×10^{-3} for the quadratic.

entanglement in the rails while there can be some — in principle, maximal — entanglement in the steps. The question remains whether θ will converge to zero for large RVB ladders.

To obtain estimates of θ, we insert the values of p_r and p_s, that have been obtained from the numerical simulations (for different N), in the inequalities in Equation (2.12) [13]. We then solve the above inequalities to obtain $\theta \in S_1^N$ for the first inequality for a fixed N, and similarly $\theta \in S_2^N$. We now consider the allowed θ lying in the intersection $S_1^N \cap S_2^N$, and plot $\theta_{max} = \max\{\theta : \theta \in S_1^N \cap S_2^N\}$ with respect to N. We find that θ_{max} is decreasing with the increase of the size of the lattice, as shown in Figure 2.7. The dots in Figure 2.7 represent θ_{max} obtained numerically from Equation (2.12) corresponding to system-sizes $N = 6, 8, 10, 12, 14$. We then fit this data with linear as well as quadratic equations. The respective mean square errors are 1.22×10^{-3} and 1.06×10^{-3}. Both fits predict a vanishing θ_{max} for larger N [13]. Therefore, the inequalities in Equation (2.12) also show the complementary behavior between the bipartite entanglement in two NN sites along the rails and steps. We observe that the entanglement in the steps is near-maximal or maximal, while along the rails it vanishes. Hence, one can infer that as the system approaches the thermodynamic limit ($N \to \infty$), the system reduces to a series of near-maximally entangled steps with minimal entanglement along the rails. Another perspective of the same facts, as obtainable regarding bipartite entanglement from Equation (2.12), is given in Figure 2.8.

For isotropic 2D RVB lattice, $p_r = p_s = p$, the fidelity of the output states in the teleportation protocol cannot exceed the fidelity of n approximate clones of the initial state in the optimal $1 \to n$ symmetric cloning, which is equal to $\frac{2n+1}{3n}$ [63]. For $n = 4$ NN in the 2D RVB lattice the optimal cloning is equal to $3/4$. Hence, the bound from telecloning is
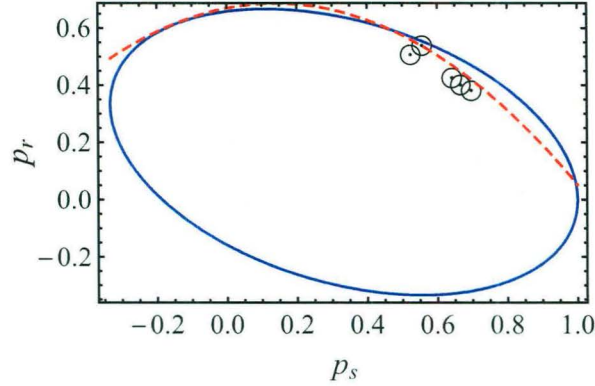
Figure 2.8: Complementary behavior of the entanglement on the rail with that on the step. The bound on p_r and p_s, as obtained from the Equation (2.12), for all possible values of θ, is depicted by the ellipse in the figure. The allowed combinations of p_r and p_s fall inside the ellipse. The (red) open curve is the quadratic fit $(-0.858x^2 + 0.241x + 0.67)$ of the (black) circles, which are in turn the values found by exact calculations for $N = 6, 8, 10, 12, 14$. All calculated points are within the bounding ellipse. It is evident that as p_s attains the maximum value 1, the value of p_r goes to 0.

given by $\frac{p+1}{2} \leq \frac{3}{4}$, which implies $p \leq \frac{1}{2}$. Using $n = R$ non-NN bipartite states the bound on entanglement can be further lowered [11]. The fidelity inequality for non-NN bipartite states is given by,

$$\frac{p+1}{2} \leq \frac{2R+1}{3R} = \frac{1}{3} + \frac{2}{3R} \tag{2.13}$$

For high values of R, the bound on p is given by, $p \leq \frac{1}{3}$, which is the separability limit [11]. The telecloning bound for p in isotropic RVB states is tighter that the bound obtained from monogamy of entanglement.

The analytical bounds on the two types of NN bipartite entanglement present in the RVB liquid on ladders give us evidence that there is negligible or no multipartite entanglement for large RVB ladders, in contrast to the case of isotropic lattices [11], as maximal entanglement in any two-party reduced state implies that the parent multiparty state is not genuinely multiparty entangled. In the next segment, we observe that isotropic RVB lattices are always genuinely multisite entangled, in contrast to two-legged RVB ladders.

2.5.3 Genuine multisite entanglement of isotropic RVB lattices using strong subadditivity

As mentioned earlier, a multiparty pure state is said to be genuinely multisite entangled if it is entangled across every possible bipartition of the system. In this section, we show that all isotropic RVB state with infinite number of spins or with suitable boundary conditions are always genuinely multisite entangled. We exploit the rotational invariance of RVB liquids

and the strong subadditivity of von Neumann entropy [59] to prove the following theorem.

Theorem: *The pure state formed by superpositions of dimer coverings is genuinely multisite entangled for all isotropic quantum spin-1/2 lattices of arbitrary dimensions that are periodic or infinite in all directions and all covering functions that are isotropic over the lattice [16].*
Proof. The superposition state of the quantum spin-1/2 lattice consisting of, say $2N$ particles, such as the RVB liquid state in Equation (2.1), is a pure quantum state. To prove that this superposed state is genuinely multisite entangled, we are required to prove that the partial density matrix of the state across any bipartition cannot be pure. In other words, the density matrix of any p spins, formed by tracing the remaining $2N - p$ spins, is always mixed and, hence entangled to the rest. We conveniently divide the proof into the two cases where the number of spins (a) is finite in at least one part of the bipartition and (b) is infinite in both the parts.

a) Finite case: For a rotationally invariant state, such as the dimer covered spin-1/2 state under consideration, it is known that the partial density matrix of an arbitrary number of spins is also rotationally invariant. Moreover, for an odd number of spin-1/2 particles, there is no pure quantum state that is rotationally invariant. Hence, any odd bipartition of the system is always entangled to the rest of the system (see Figure 2.9(a)). For example, any single-site density matrix is $\frac{1}{2}\mathcal{I}$, where $\mathcal{I}$ is the 2×2 identity matrix, and therefore is maximally entangled to the rest of the lattice.

Let us now consider the case of a bipartition with an even (finite) number of spins in one part. Consider any set X of an even number of sites. Let the partial density matrix of these sites in X, corresponding to the state $|\psi\rangle$, be $\rho^{(X)}$. Let us assume that $\rho^{(X)}$ is pure, which would imply that $|\psi\rangle$ is separable, contrary to the statement of the theorem. Let $X = X' \cup c$, where c contains an arbitrary but fixed odd number of sites $< |X|$. ($|S|$ denotes the cardinality of the set S.) In particular, $|c|$ can be unity. For an isotropic lattice, we can always find another equivalent set of spins, $Y' \cup c$, such that $|Y'| = |X'|$, which is again pure (by the assumption) (see Figure 2.9(b)). The strong subadditivity of von Neumann entropy [59] implies

$$S(\rho^{(X')}) + S(\rho^{(Y')}) \leq S(\rho^{(X' \cup c)}) + S(\rho^{(Y' \cup c)}), \qquad (2.14)$$

where $S(\cdot)$ denotes the von Neumann entropy. Since $\rho^{(X)}$ and $\rho^{(Y)}$ are pure, and since von Neumann entropy is non-negative, we have $S(\rho^{(X')}) + S(\rho^{(Y')}) = 0$, which in turn implies that $\rho^{(X')}$ and $\rho^{(Y')}$ are pure. This immediately implies that $\rho^{(c)}$ is pure. This is a contradiction as $|c|$ is odd. This part of the proof was partially presented in Reference [11].

b) Infinite case: Let us begin with the case of an infinite 2D square, dimer covered lattice partitioned into two half-planes by an infinite horizontal line. Let us assume that the
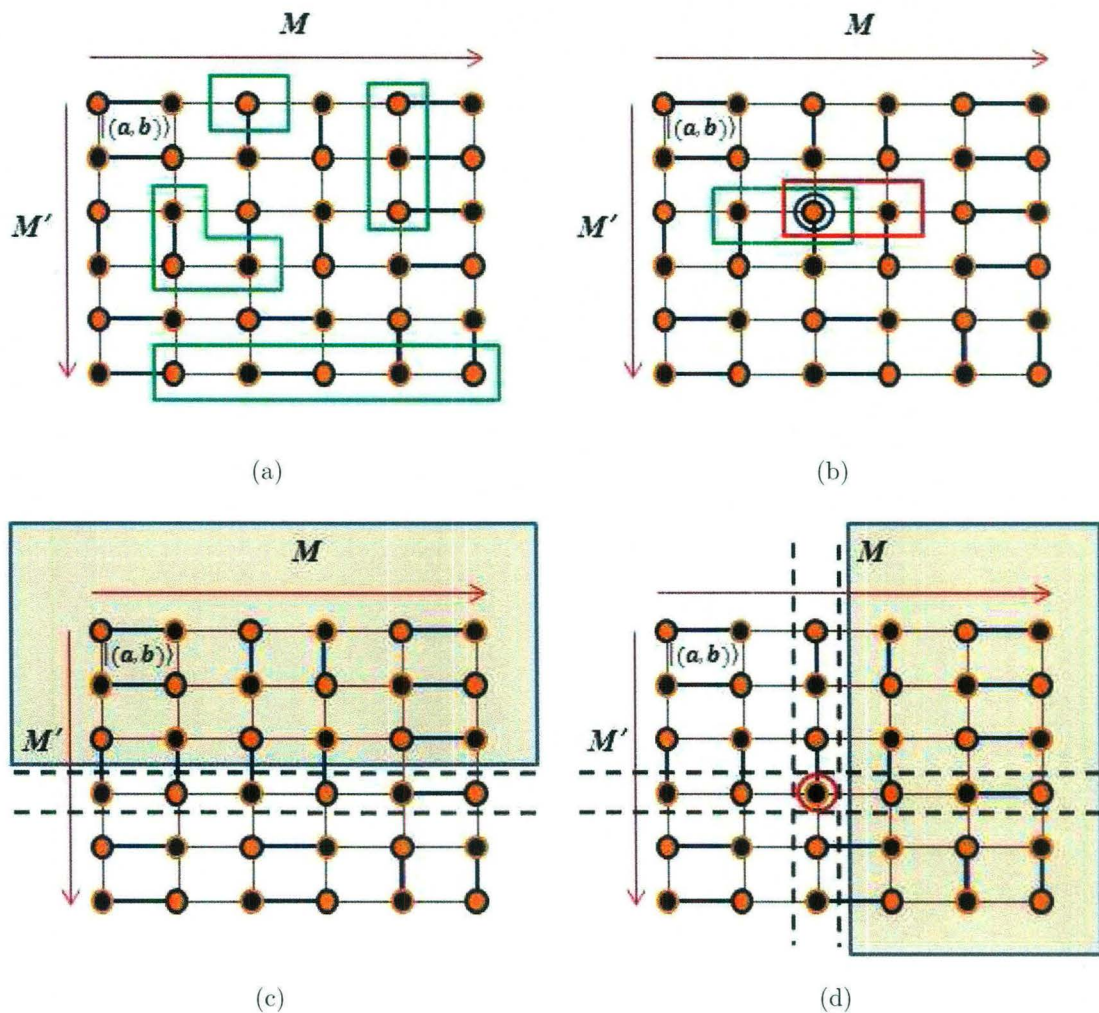
Figure 2.9: The entanglement of different finite and infinite bipartitions in an isotropic RVB lattice. (a) The *odd:rest* bipartition of the RVB lattice is always entangled as any odd rotationally invariant subsystem is always mixed. The odd partitions are shown in green boxes. (b) The *even:rest* bipartition. It can be proved that, by using strong subadditivity of von Neumann entropy, the existence of separable pure even partitions will imply the existence of smaller odd subsystems that are pure, which is not possible. In the figure the two even bipartitions (red and green boxes) have a common, odd single-site subsystem (shown by a blue circle). Assuming the even squares to be pure, will imply by strong subadditivity, that the odd circle is pure, which is not possible. (c) The proof can be extended to *infinite half-plane* bipartitions (shown by the shaded blue box). Assuming such bipartitions to be separable, one can isolate strips (shown between horizontal dotted lines) of pure subsystems along the horizontal, using the isotropy of the system. (d) Similarly, $\pi/2$ *radians rotated, infinite half-plane* bipartitions (shown by the rotated shaded blue box) give us vertical strips of pure subsystems (shown between vertical dotted lines). We observe that the strips of horizontal and vertical pure subsystems, can be aligned to contain a common odd, single-site subsystem (shown in (d) by a red circle), that by strong subadditivity should also be pure, which again is impossible.

reduced states are pure, contrary to the statement of the theorem. Let H_P denote the sites in one such half-plane. Consider now the set $H_P \cup L_H$, where L_H is the infinite horizontal strip of sites with single-site width and that is directly adjacent to H_P (see Figure 2.9(c)). By isotropy, if $\rho^{(H_P)}$ is pure, $\rho^{(H_P \cup L_H)}$ is also pure. Consequently, we can again use strong subadditivity to show that $\rho^{(L_H)}$ is pure. Now if $\rho^{(L_H)}$ is pure, by isotropy, $\rho^{(L_V^{(p_1,p_2)})}$ is also pure, where $L_V^{(p_1,p_2)}$ is the infinite vertical strip of sites with single-site width and that is obtained from L_H by rotating it by $\pi/2$ radians around the site with Cartesian coordinates (p_1, p_2) (see Figure 2.9(d)). Again using strong subadditivity, we find that $\rho^{(p_1,p_2)}$ is pure, which is a contradiction. A similar proof works for boundaries that are not straight lines.

One needs a separate proof for the case when we want to prove that the infinite horizontal strip L_{H^r} having a width of r sites is not a product with the remaining portion of the lattice. Assume, if possible, that $\rho^{(L_{H^r})}$ is pure. Then, by isotropy, $\rho^{(L_{V^r}^{(p_1,p_2)})}$ is also pure, where $L_{V^r}^{(p_1,p_2)}$ is obtained from L_{H^r} by a $\pi/2$ rotation around (p_1, p_2). Again applying strong subadditivity, we have that the reduced state of the $2r$ spins in $L_{H^r} \cap L_{V^r}^{(p_1,p_2)}$ is pure, which is a contradiction (by the (a) part of the proof). The proof can be extended to other infinite strips. The proof of the (a) and (b) part also works, with suitable modifications, for isotropic RVB lattices of arbitrary geometry and dimensions, e.g. the triangular and hexagonal lattices in 2D and the cubic lattice. ∎

The theorem analytically proves that all isotropic RVB states, with periodic boundaries, are genuinely multisite entangled. However, analytical results from monogamy of entanglement and asymmetric cloning show that this is not true for RVB ladders. In the next section, we use numerical simulation to exactly evaluate the bipartite and multipartite entanglement properties in finite-size RVB ladders. We observe that the numerical estimates are in agreement with the analytical results obtained. Figure 2.9 is an illustration of the different finite and infinite bipartitions considered in the proof.

2.6 Conclusion

In conclusion, we have considered the resonating valence bond liquid state on a ladder and isotopic lattice, with periodic boundary conditions. For the RVB ladder state, we have presented two qualitatively different behavior of nearest-neighbor bipartite entanglement: While the bipartite entanglement on the steps is increasing, that on the rails is decreasing, with the increase in the size of the lattice. Both analytical and numerical results support the argument. Moreover, genuine multipartite entanglement of the ladder decreases with increasing system size. This is in sharp contrast with the situation in isotropic lattices, where RVB liquid state has negligible bipartite entanglement, but substantial multipartite entanglement. The observation is supported by analytical study of entanglement in isotropic

RVB lattices.

Intuitively, the change in geometry is expected to change the quantitative entanglement properties of the system. However, what makes the findings interesting is that there is a drastic qualitative difference in bipartite and multipartite entanglement properties due to this change. The complementary behavior of bipartite entanglement in the steps and rails of the RVB ladder is an important feature that has been observed for a change in the geometry and cannot be a priori predicted by using our knowledge about isotropic systems, regardless of how the geometry is manipulated. Furthermore, a decrease in multipartite entanglement with increase in system size is highly unexpected and is a deviation from the observed results in isotropic RVB states. The asymptotic nature of multipartite entanglement has been reversed with an introduction of asymmetry along a dimension in an isotropic 2D square lattice, to obtain a ladder. This can potentially be exploited in the future for developing quantum information networks.

The results show that geometry can play an important role in determining the entanglement properties of multiparty quantum states. Moreover, these results reveal that studies in many-body physics, at least for tasks related to quantum computation, on ladders cannot be extrapolated to two-dimensional lattices.

[1] L. Pauling, Proc. R. Soc. London, Ser. A **196**, 343 (1949).

[2] L. Pauling, *The Nature of Chemical Bonds*, Cornell Univ. Press, Ithaca, NY (1960).

[3] P.W. Anderson, Mater. Res. Bull. **8**, 153 (1973).

[4] P. Fazekas and P.W. Anderson, Philos. Mag. **30**, 423 (1974).

[5] A.Y. Kitaev, Ann. Phys. (Leipzig) **303**, 2 (2003).

[6] P.W. Anderson, Science **235**, 1196 (1987).

[7] G. Baskaran, Indian J. Phys. **89**, 583 (2006).

[8] E.A. Ekimov, V.A. Sidorov, E.D. Bauer, N.N. Mel'nik, N.J. Curro, J.D. Thompson and S.M. Stishov, Nature (London) **428**, 542 (2004).

[9] R. Horodecki, P. Horodecki, M. Horodecki, and K. Horodecki, Rev. Mod. Phys. **81**, 865 (2009).

[10] S. Furukawa and G. Misguich, Phys. Rev. B **75**, 214407 (2007).

[11] A. Chandran, D. Kaszlikowski, A. Sen(De), U. Sen, and V. Vedral, Phys. Rev. Lett. **99**, 170502 (2007).

[12] R. Ramanathan, D. Kaszlikowski, M. Wiesniak, and V. Vedral, Phys. Rev. B **78**, 224513 (2008).

[13] H.S. Dhar and A. Sen(De), J. Phys. A: Math. Theor. **44**, 465302 (2011).

[14] H. Ju, A.B. Kallin, P. Fendley, M.B. Hastings, and R.G. Melko, Phys. Rev. B **85**, 165121 (2012). D. Poilblanc, N. Schuch, D. Pérez-García, and J.I. Cirac, Phys. Rev. B **86**, 014404 (2012). J.-M. Stéphan, H. Ju, P. Fendley, and R.G. Melko, New. J. Phys. **15**, 015004 (2013).

[15] H.S. Dhar, A. Sen(De) and U. Sen, New J. Phys. **15**, 013043 (2013).

[16] H.S. Dhar, A. Sen(De) and U. Sen, Phys. Rev. Lett. **111**, 070501 (2013).

[17] E. Dagatto and T.M. Rice, Science **271**, 618 (1996).

[18] E. Dagatto, J. Riera, and D. Scalapino, Phys. Rev. B **45**, 5744 (1992)

[19] S.R. White, R.M. Noack, and D.J. Scalapino, Phys. Rev. Lett. **73**, 886 (1994).

[20] G. Sierra and M.A. Martin-Delgado, Phys. Rev. B **56**, 8774 (1997).

[21] J.-L. Song, S.-J. Gu, and H.-Q. Lin, Phys. Rev. B **74**, 155119 (2006). A.B. Kallin, I. Gonzalez, M.B. Hastings, and R.G. Melko, Phys. Rev. Lett. **103**, 117203 (2009). A. Tribedi and I. Bose, Phys. Rev. A **79**, 012331 (2009). I.A. Kovàcs and F. Iglòi, Phys. Rev. B **80**, 214416 (2009). D. Poilblanc, Phys. Rev. Lett. **105**, 077202 (2010). A.M. Läuchli and J. Schliemann, Phys. Rev. B **85**, 054403 (2012).

[22] Y. Li, T. Shi, B. Chen, Z. Song, and C.-P. Sun, Phys. Rev. A **71**, 022301 (2005).

[23] H. Katsura, N. Kawashima, A.N. Kirillov, V.E. Korepin, S. Tanaka, J. Phys. A: Math. Theor. **43**, 255303 (2010).

[24] S. Ohsugi, K. Magishi, S. Matsumoto, Y. Kitaoka, T. Nagata, and J. Akimitsu Phys. Rev. Lett. **82**, 4715 (1999).

[25] J.E. Lorenzo, L.P. Regnault, C. Boullier, N. Martin, S. Vanishri, and C. Marin, Phys. Rev. B **83**, 140413 (2011).

[26] A.E. Feiguin and M.P.A. Fisher, Phys. Rev. B **83**, 115104 (2011).

[27] M. Dalmonte, P. Zoller, and G. Pupillo, Phys. Rev. Lett. **107**, 163202 (2011), and references therein.

[28] M. Greiner, O. Mandel, T. Esslinger, T.W. Hansch and I. Bloch, Nature **415**, 39 (2002).

[29] F. Verstraete, J.I. Cirac and J.I. Latorre, Phys. Rev. A **79**, 032316 (2009).

[30] X.-S. Ma, B. Dakic, W. Naylor, A. Zeilinger and P. Walther, Nature Phys. **7**, 399 (2011).

[31] S. Gopalan, T.M. Rice, and M. Sigrist, Phys. Rev. B **49**, 8901 (1994).

[32] M. Greven, R.J. Birgeneau, and U.-J. Wiese, Phys. Rev. Lett. **77**, 1865 (1996).

[33] B. Frischmuth, B. Ammon, and M. Troyer, Phys. Rev. B **54**, R3714(R) (1996).

[34] Y. Nishiyama, N. Hatano, and M. Suzuki, J. Phys. Soc. Jpn. **65**, 560 (1996).

[35] I. Bose and P. Mitra, Phys. Rev. B **44**, 443 (1991).

[36] I. Bose, Phys. Rev. B **45**, 13072 (1992).

[37] I. Bose and A. Ghosh, Phys. Rev. B **56**, 3149 (1997).

[38] B. Kumar, Phys. Rev. B **66**, 024406 (2002).

[39] M. Mambrini, A. Läuchli, D. Poilblanc, and F. Mila, Phys. Rev. B **74**, 144422 (2006).

[40] A.K. Pal and I. Bose, J. Phys. B: At. Mol. Opt. Phys. **44**, 045101 (2011).

[41] D. Rokhsar and S.A. Kivelson, Phys. Rev. Lett. **61**, 2376 (1988).

[42] J. Cano and P. Fendley, Phys. Rev. Lett. **105**, 067205 (2010).

[43] S. Liang, B. Doucot, and P.W. Anderson, Phys. Rev. Lett. **61**, 365 (1988).

[44] K. Modi, A. Brodutch, H. Cable, T. Paterek, and V. Vedral, Rev. Mod. Phys. **84**, 1655 (2012).

[45] M. Lewenstein, A. Sanpera, V. Ahufinger, B. Damski, A. Sen(De), and U. Sen, Adv. Phys. **56**, 243 (2007).

[46] L. Amico, R. Fazio, A. Osterloh, and V. Vedral, Rev. Mod. Phys. **80**, 517 (2008).

[47] X.G. Wen, F. Wilczek, and A. Zee, Phys. Rev. B **39**, 11413 (1989).

[48] R.F. Werner, Phys. Rev. A **40**, 4277 (1989).

[49] C.H. Bennett, D.P. DiVincenzo, J.A. Smolin, and W.K. Wootters, Phys. Rev. A **54**, 3824 (1996).

[50] S. Hill and W.K. Wootters, Phys. Rev. Lett. **78**, 5022 (1997).

[51] W.K. Wootters, Phys. Rev. Lett. **80**, 2245 (1998).

[52] A. Sen(De) and U. Sen, Phys. Rev. A **81**, 012308 (2010).

[53] A. Sen(De) and U. Sen, *Bound Genuine Multisite Entanglement: Detector of Gapless-Gapped Quantum Transitions in Frustrated Systems*, arXiv:1002.1253 (2010).

[54] R. Garisto and L. Hardy, Phys. Rev. A **60**, 827 (1999).

[55] A. Ekert, Phys. Rev. Lett. **67**, 661 (1991).

[56] V. Coffman, J. Kundu, and W.K. Wootters, Phys. Rev. A **61**, 052306 (2000).

[57] T.J. Osborne and F. Verstraete, Phys. Rev. Lett. **96**, 220503 (2006).

[58] S. Iblisdir, A. Acín, N.J. Cerf, R. Filip, J. Fiurasek, and N. Gisin, Phys. Rev. A **72**, 042328 (2005).

[59] E.H. Lieb and M.B. Ruskai, J. Math. Phys. (N.Y.) **14**, 1938 (1973).

[60] C.H. Bennett, G. Brassard, C. Crépeau, R. Jozsa, A. Peres, and W.K. Wootters Phys. Rev. Lett. **70**, 1895 (1993).

[61] P. Horodecki, M. Horodecki, and R. Horodecki, Phys. Rev. A **60**, 1888 (1999).

[62] M. Murao, D. Jonathan, M.B. Plenio, and V. Vedral, Phys. Rev. A **59**, 156 (1999).

[63] V. Scarani, S. Iblisdir, N. Gisin, and Antonio Acín , Rev. Mod. Phys. **77**, 1225 (2005).

CHAPTER 3

Characterization of genuine multisite entanglement in quantum spin-1/2 lattices: density matrix recursion method

---

The most exciting phrase to hear in science, the one that heralds new discovery, is not 'Eureka!' but 'that's funny'. – Isaac Asimov

We introduce an analytical iterative method, the density matrix recursion method (DMRM), to generate arbitrary reduced density matrices of superpositions of short-range dimer coverings in quantum spin-1/2 ladders and isotropic square lattices, with or without periodic boundary condition, for an arbitrary number of spins. The method can be used to efficiently calculate bipartite as well as multipartite physical properties, including entanglement. We apply this technique to characterize the genuine multisite entanglement in multi-legged resonating valence bond (RVB) ladders and isotropic 2D RVB lattices. We distinguish between even- and odd-legged RVB ladders, and specifically show that while genuine multisite entanglement decreases with increasing system size for the even-legged ladders, it does the opposite for odd-legged ones. For the case of finite-sized isotropic RVB lattices, we calculate the genuine multisite entanglement, which through finite-size scaling, enables us to obtain an estimate of the multisite entanglement of the infinite square RVB lattice. The method can be a useful tool to investigate other single- and multisite properties of such quantum spin-1/2 states.[1]

3.1   Introduction

As discussed in the previous chapters, genuine multisite entanglement is an important re-
source in quantum information protocols and is known to offer significant advantage in quan-
tum tasks in comparison to bipartite entanglement [1]. In particular, it is the basic ingredient
in measurement-based quantum computation [2], and is beneficial in various quantum com-
munication protocols [3], including secret sharing [4–7] (cf. [8, 9]). An understanding of the
multipartite entanglement content is potentially advantageous, in assessing the importance
of a quantum state state for future applications, over that of bipartite measures. This is
due to the fact that the former takes into account the distribution of information between
the multisite sub-regions of the entire system and the hidden correlation are not ignored
due to tracing out [10–15]. Apart from the conventional information tasks, the study of
multisite entanglement turns out to be important in understanding many-body phenomena,
such as quantum phase transitions [16–22] and to understand transport properties in the
evolution of photosynthetic complexes [23, 24]. Although bipartite entanglement in the case
of two spin-1/2 particles is rather well-understood, the situation is quite different in the
case of classification and quantification of entanglement in higher dimensions as well as in
multiparty systems. The fact that many-particle systems can have different types of useful
entanglement, depending on the particular information processing protocols under study,
makes the quantification a formidable task (see Section 1.3). While there are several char-
acterizations of multiparty entanglement measures known in the literature [1, 25–44], it is
in general difficult to compute them for large systems. As shown in Section 2.3, for pure
multisite states, it is possible to use the *generalized geometric measure* [45, 46], which is a
computable geometric measure of genuine multisite entanglement.

As discussed in Section 2.1, the quantum spin-1/2 lattice states, with short-range dimer
coverings, known as resonating valence bond (RVB) states [47], are of considerable interest in
high-temperature superconductivity [48, 49], cooperative phenomena in many-body systems
[50–53], and quantum computation [54]. These short-range dimer states can be efficiently
simulated in laboratories using atoms in optical lattices [55–57] or in cavities using interacting
photons [58]. We also observed that such systems have entanglement properties that are
dependent on the geometry of the system [59]. As such, quantum spin ladders and isotropic
states have uniquely different quantum characteristics (see Chapter 2). A striking feature of
the quantum RVB ladder is that the extrapolation from the 1D spin chain to the 2D square
lattice by gradually increasing the number of legs is not straightforward. For example, the
quantum characteristics of the Heisenberg ladder ensures that the odd- and the even-legged
ladder ground states have different correlation properties. *Even ladders* have a finite-gapped

ground state excitation and have exponential decay of two-site correlation, while *odd ladders* are gapless and have power-law decay [53, 60–62]. Such effects also occur in quantum spin liquids, as observed in References [63, 64]. Although the odd- and even-legged Heisenberg ladders belong to different universality class, in the infinite limit it must converge to the same class for 2D systems [62]. Similarly, the characteristic difference in odd- and even-legged ladders may lead to interesting entanglement properties of the system, which for infinite legs must converge to the entanglement properties of the 2D lattice.

In Section 2.2, we have considered a class of large superposed states, the resonating valence bond (RVB) liquid states on ladders and isotropic lattices. We have observed using quantum information theory (QIT) concepts that bipartite and multipartite entanglement properties qualitatively differ for RVB ladder states and isotropic lattices [59]. Further, we have observed that exact numerical calculation of such entanglement properties is limited to small spin systems $(2N = 14)$.[2] This is due to the fact that calculating the bipartite or multipartite entanglement in large-sized quantum spin-1/2 lattices, formed by the superposition of short-range dimer coverings (RVB states), is numerically challenging.[3] Within a dimer-covering approach [53], it is possible to derive energy density and spin-correlation functions for two-legged ladders by using generating functions [65] or state iterations [62]. Approximate solutions may also be obtained for the four-legged ladder [66]. For further work in this direction, including density matrix renormalization group and quantum Monte Carlo calculations in 2D Heisenberg ladders, see Reference [67].

In this chapter, we introduce an analytical iterative technique, the *density matrix recursion method* (DMRM), to obtain the reduced density matrix of arbitrary number of sites of a state on a quantum spin-1/2 RVB ladder (with multiple number of legs) or the 2D square RVB lattice, with both open and periodic boundary conditions. We start with the DMRM formalism for the multi-legged quantum spin-1/2 ladder, with nearest-neighbor (NN) dimer coverings. We find separate iterative methods for even and odd ladders. These partial density matrices obtained using DMRM can be used to calculate and study single-, two-, and multi-site physical properties of the many-body quantum spin-1/2 system, including two-site correlation and bipartite as well as multipartite entanglement. We then apply the DMRM method to facilitate the calculation of the genuine multipartite entanglement, using the *generalized geometric measure* (GGM) [45, 46]. The results allow us to distinguish between even- and odd-legged RVB ladders and, specifically, show that while genuine multisite entanglement decreases with increasing system size for the even-legged ladders, it increases with size

---

[2] Let's say that the RVB lattice has even $2N$ number of spins.

[3] This is due to the exponential increase in the number of the terms in the superposition, in the computational basis, with increase in system size. Hence calculation of multisite physical properties in multi-legged ladder or isotropic states becomes difficult.

for odd-legged ones. Incidentally, we also find that the convergence of the GGM, for a given odd- or even-legged ladder, occurs for relatively small ladder lengths of the corresponding ladder. The DMRM formalism for odd- and even- legged ladders is then extended to study the genuine multisite entanglement properties of finite-sized isotropic 2D quantum spin-1/2 lattices. The method enables us to calculate the GGM for moderately large lattices and perform finite-size scaling [68] to predict the genuine multisite entanglement for the infinite two-dimensional square lattice. We observe that the distinctly different behavior of multisite entanglement in odd- and even-legged ladders, converge as the number of legs of the ladders are increased. This implies that in the infinite limit, the scaling of entanglement in odd- and even-legged ladders must be similar to that of the isotropic 2D quantum RVB system.

The paper is organized as follows. We introduce the model multi-legged and isotropic RVB liquid state in Section 3.2. The density matrix recursion method is introduced and defined in Section 3.3. The multisite entanglement behavior of odd versus even multi-legged ladder is discussed in Section 3.4. The use of DMRM for isotropic square RVB lattice and the finite-size scaling of genuine multisite entanglement is performed in Section 3.5. We present a conclusion in Section 3.6.

3.2 Multi-legged and isotropic RVB liquid

Within a short-range dimer-covering approach, the quantum spin-1/2 state under consideration consists of an equal superposition of nearest-neighbor directed dimer pairs from sublattice A to sublattice B on the bipartite lattice, defined in Section 2.2. The highly superposed state is called the resonating valence bond (RVB) liquid state. The 2D quantum spin-1/2 bipartite lattice consists of coupled parallel, M horizontal spin chains with $\mathcal{N}$ sites on each chain (see Figure 3.1).[4] The chains in the horizontal, also referred as legs of the lattice, are labelled as 1 to M. The total number of spin-1/2 sites in the entire bipartite lattice is $2N$ ($= M \times \mathcal{N}$). Alternately, the $\mathcal{N}$ vertical chains, referred as rungs of the lattice, are labelled from 1 to n, similar to the horizontal sites on the chain, and each rung contains M spins (see Figure 3.1 for a better description). The periodic quantum spin-1/2 state is conditionally defined by allowing dimer states to be formed between rungs 1 and n [65]. Of course as numbers, $n = \mathcal{N}$. The bipartite lattice model can be formalised to study the pseudo-2D multi-legged ladder as well as the isotropic 2D square quantum spin-1/2 lattice, with RVB liquid ground state. The multi-legged ladder states correspond to lattices for which $M \leq \mathcal{N}$. Note that for RVB lattice, the total number of spins ($2N$) is always even, since lattices are formed by superpositions of dimer pairs. We only consider multi-legged ladder with even

---

[4]Also see Figure 2.1 for the illustration of a bipartite RVB lattice on a two-legged ladder.

number of rungs to allow the periodic coupling between rungs 1 and n, to occur between sublattice A and sublattice B (cf. Section 2.2).[5] From Figure 3.1, we observe that by forcing $M = \mathcal{N}$ (for even M), we have an 2D square RVB lattice with total spin $2N = M^2$. We note that a perfect isotropic lattice has equal number of legs and rungs. Hence,⸱there⸱can be no square RVB lattice for odd M, since $2N$ is always even. For odd M, we consider the imperfect lattice with either the leg or rung shorter by a unit, i.e., either $M = \mathcal{N}'(= \mathcal{N} + 1)$ or $M = \mathcal{N}'(= \mathcal{N} - 1)$, such that $M \times \mathcal{N}'$ is always even. Hence, the RVB multi-legged ladder states can also be imposed as finite-size RVB square lattices, albeit, with appropriate boundary conditions.

As defined in Equation (2.1) in Section 2.2, the (unnormalized) quantum spin-1/2 RVB liquid state under study is given by [69]

$$|\mathcal{N}\rangle = \sum_k \left[\prod_{i,j} |(a_i, b_j)\rangle \right]_k , \tag{3.1}$$

where $|(a_i, b_j)\rangle$ refers to a dimer between sites a_i and b_j on the bipartite lattice, where (i, j) are NN sites with $i \neq j$. A product of all such dimers on the spin-1/2 lattice constitutes an RVB *covering*. The summation refers to the superposition of all such dimer product states that give us the superposed short-range dimer covering states. Again, as mentioned in Section 2.2, it is believed that these short-range dimer covered states are possible solutions of the two-dimensional antiferromagnetic Heisenberg systems based on the understanding of the RVB theory and using numerical methods, such as the density matrix renormalization group [62, 70].

3.3 Density matrix recursion method

The genuine multisite entanglement is quantified using a computable measure called the *generalized geometric measure* [45, 46]. The formulation of GGM for RVB spin liquids has been shown in Section 2.3. The computation of the GGM depends on the efficient generation of arbitrary reduced density matrices across all possible bipartitions of the spin system. We now introduce the density matrix recursion method as an analytical iterative technique for efficiently generating arbitrary local density matrices for quantum spin-1/2 lattices with even and odd number of spins on the vertical edge, M. The mathematical description can then be suitably extended to encapsulate the reduced density matrices for multi-legged ladders

---

[5]For even-legged lattices, we only consider even number of rungs and the boundary condition that does not involve the *twist* in the ribbon as considered for the two-leg RVB ladders in Section 2.2. This is done to allow a consistent formulation of the density matrix recursion method for both even- and odd-legged RVB lattices. For odd-legged lattices, the number of rungs is always even as the total number of spins, $2N$, in any dimer-covered lattice is by definition even.
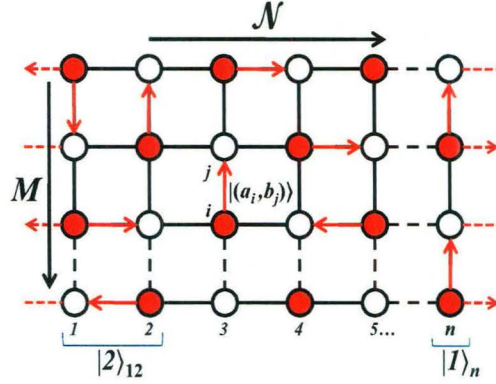
Figure 3.1: The quantum spin-1/2 RVB state in the form of a *bipartite lattice*, with M horizontal and $\mathcal{N}$ vertical chains. The isotropic 2D lattice can be visualized by demanding that $M = \mathcal{N}$. The bipartite lattice is shown by the solid circles of sublattice A with hollow ones for sublattice B. The red arrows (solid) show the nearest-neighbor dimer states $(|(a_i, b_j)\rangle)$ from a site in sublattice A to another in B. The arrows (dashed) at the boundary indicate that the lattice is with periodic boundary condition. The dashed lines indicate that the number of legs and rungs can be extended beyond the illustrated number of sites. The figure also shows the two-rung RVB state, $|2\rangle$, and the single-rung RVB state, $|1\rangle$, which will be profusely used in the analytical iteration method presented.

and isotropic 2D RVB lattices. The DMRM technique allows us to efficiently investigate the scaling of entanglement properties, using numerical simulation, from RVB ladder state to the 2D isotropic RVB state.

3.3.1 Quantum spin-1/2 lattice with even M spins

Let us denote a quantum spin-1/2 lattice as $(M, \mathcal{N})$, when there are M spins along the vertical edge and $\mathcal{N}$ spins in the horizontal edge, such that $M \times \mathcal{N}$ $(=2N)$ is the total number of spins. Alternately, we can say that the lattice has M horizontal and $\mathcal{N}$ vertical chains. For an even spins on the vertical edge, M is even. Let the state of an $(M, \mathcal{N} + 2)$ quantum spin-1/2 lattice be given by $|M, \mathcal{N} + 2\rangle$. The state $|M, \mathcal{N} + 2\rangle$, in this case, can be written using smaller lattice states $|M, \mathcal{N} + 1\rangle$ and $|M, \mathcal{N}\rangle$. We drop the first M from the states, as it remains unchanged.

$$
\begin{aligned}
|\mathcal{N} + 2\rangle &= |\mathcal{N} + 1\rangle|1\rangle_{n+2} + |\mathcal{N}\rangle|\bar{2}\rangle_{n+1,n+2} \\
&= |\mathcal{N}\rangle|2\rangle_{n+1,n+2} + |\mathcal{N} - 1\rangle|\bar{2}\rangle_{n,n+1}|1\rangle_{n+2},
\end{aligned}
\tag{3.2}
$$

where the subscripts correspond to the numbering of the sites on the horizontal side on the lattice. Here, $|1\rangle_i$ refers to the state $|M, 1\rangle$ at the column i, and $|2\rangle_{i,j}$ refers to the state $|M, 2\rangle$ at the columns i and j. The state $|\bar{2}\rangle_{i,j}$ can be written as

$$
|\bar{2}\rangle_{i,j} = |2\rangle_{i,j} - |1\rangle_i|1\rangle_j.
$$

The term $|\bar{2}\rangle_{n+1,n+2}$ contains all the coverings of a two rung lattice denoted by the state $|2\rangle_{n+1,n+2}$, apart from the coverings formed by the product of the two rungs $|1\rangle_{n+1}|1\rangle_{n+2}$. The subtraction removes possible repetition of states between the two terms in the recursion for $|\mathcal{N}+2\rangle$ in relation (3.2).

The density matrix for the state given by Equation (3.2) is given by,

$$\rho^{(\mathcal{N}+2)} = |\mathcal{N}+2\rangle\langle\mathcal{N}+2|. \tag{3.3}$$

If, for example, we trace out all but two rungs (say $n+1$ and $n+2$) from the state, we will obtain a two-rung state (mixed state) containing $2 \times M$ spins, where M is the number of spins on the vertical edge of the lattice. Note that M is even here. These reduced states can then be used to calculate the multisite entanglement properties of the quantum spin-1/2 lattice. In particular,

$$
\begin{aligned}
\rho^{(2)}_{(n+1,n+2)} &= \text{tr}_{1..n}(|\mathcal{N}+2\rangle\langle\mathcal{N}+2|) = \text{tr}_{1..n}[|\mathcal{N}\rangle\langle\mathcal{N}||2\rangle\langle2|_{(n+1,n+2)} \\
&+ |\mathcal{N}-1\rangle\langle\mathcal{N}-1||\bar{2}\rangle\langle\bar{2}|_{(n,n+1)}|1\rangle\langle1|_{(n+2)} \\
&+ |\mathcal{N}\rangle|2\rangle_{n+1,n+2}\langle\mathcal{N}-1|\langle\bar{2}|_{n,n+1}\langle1|_{n+2} \\
&+ |\mathcal{N}-1\rangle|\bar{2}\rangle_{n,n+1}|1\rangle_{n+2}\langle\mathcal{N}|\langle2|_{n+1,n+2}].
\end{aligned}
\tag{3.4}
$$

Tracing over the rungs 1 to n, we get

$$
\begin{aligned}
\rho^{(2)}_{(n+1,n+2)} &= \mathcal{Z}_\mathcal{N}|2\rangle\langle2|_{(n+1,n+2)} + \mathcal{Z}_{\mathcal{N}-1}\bar{\rho}_{n+1} \otimes |1\rangle\langle1|_{(n+2)} \\
&+ (|2\rangle_{n+1,n+2}\langle1|_{n+2}\langle\xi_\mathcal{N}|_{n+1} + h.c.),
\end{aligned}
\tag{3.5}
$$

where $\mathcal{Z}_\mathcal{N} = \langle\mathcal{N}|\mathcal{N}\rangle$, $\bar{\rho}_{n+1} = \text{tr}_n[|\bar{2}\rangle\langle\bar{2}|_{(n,n+1)}]$, and

$$\langle\xi_\mathcal{N}|_{n+1} = \langle\bar{2}|_{n,n+1}\langle\mathcal{N}-1|\mathcal{N}\rangle. \tag{3.6}$$

For our analysis, we consider a spin-1/2 quantum lattice states, with NN dimers, that is periodic along the horizontal axis [65] (cf. Reference [71]). The periodic boundary condition entails that the lattice also form dimer states between the rungs 1 and n. Accounting for the additional states in the spin lattice, due to the periodicity, the recursion relation can be modified into (see Figure 3.2)

$$|\mathcal{N}+2\rangle_P = |\mathcal{N}+2\rangle_{1,n+2} + |\mathcal{N}\rangle_{2,n+1}|\bar{2}\rangle_{n+2,1}, \tag{3.7}$$

where the subscript P stands for a periodic lattice state. Throughout the section, a state without a subscript P will imply a state with open boundary conditions. The density matrix
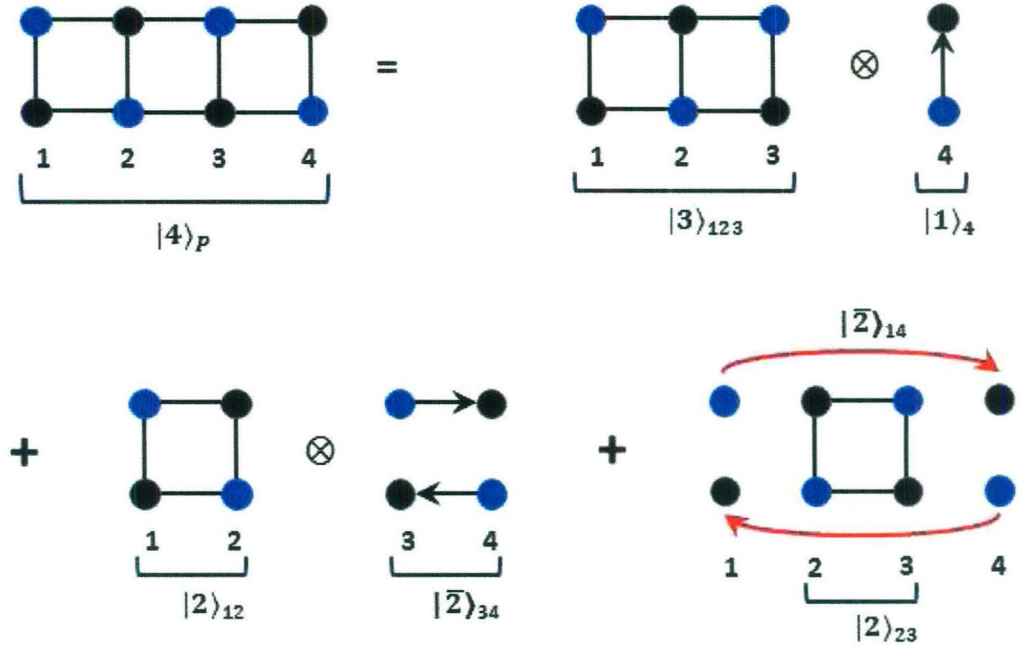
Figure 3.2: An illustration of the recursion relation for an even M lattice, with periodic boundary condition, $|\mathcal{N}+2\rangle_P$, as given by Equation (3.7), for $M=2$ and $\mathcal{N}=2$. Solid lines in a lattice refer to states with all possible dimer coverings, whereas bold arrows refer to specific singlet between the sites. The figure shows that a $|4\rangle_P$ state, with 2 horizontal chains and a periodic boundary condition, can be recursively generated using the open boundary states $|3\rangle$, $|2\rangle$ and $|1\rangle$. The recursion also uses the state, $|\bar{2}\rangle_{i,j} = |2\rangle_{i,j} - |1\rangle_i|1\rangle_j$. The bold red arrows demonstrate the periodic boundary condition. The sublattices are defined in a manner consistent with Figure 2.1.

for the periodic state can be calculated by using the recursion relation in Equation (3.7):

$$
\begin{aligned}
\rho_P^{(\mathcal{N}+2)} &= |\mathcal{N}+2\rangle\langle\mathcal{N}+2|_P \\
&= |\mathcal{N}+2\rangle\langle\mathcal{N}+2| + |\mathcal{N}+2\rangle\langle\mathcal{N}|_{2,n+1}\langle\bar{2}|_{n+2,1} \\
&+ |\mathcal{N}\rangle_{2,n+1}|\bar{2}\rangle_{1,n+2}\langle\mathcal{N}+2| \\
&+ |\mathcal{N}\rangle\langle\mathcal{N}|_{(2,n+1)}|\bar{2}\rangle\langle\bar{2}|_{(1,n+2)}.
\end{aligned}
\tag{3.8}
$$

As done for the lattice with open boundary conditions, we trace out all but two rungs (say $n+1$ and $n+2$) from the periodic state in Equation (3.8), to obtain a two-rung state (mixed state) containing $2 \times M$ spins.

$$
\rho_{P(n+1,n+2)}^{(2)} = \mathrm{tr}_{1..n}(|\mathcal{N}+2\rangle\langle\mathcal{N}+2|_P)
\tag{3.9}
$$

is the reduced two-rung state of the periodic lattice. The reduced state, for periodic boundary

condition, upon tracing out all but two rungs at $(n+1, n+2)$, is given by the relation

$$
\begin{aligned}
\rho_P^{(2)} &= \rho_{n+1,n+2}^{(2)} + \mathrm{tr}_{1..n}[|\mathcal{N}\rangle\langle\mathcal{N}|_{(2,n+1)}|\bar{2}\rangle\langle\bar{2}|_{(1,n+2)} \\
&\quad + (|\mathcal{N}\rangle_{2,n+1}|\bar{2}\rangle_{1,n+2}\langle\mathcal{N}+2| + \mathrm{H.c.})] \\
&= \rho_{n+1,n+2}^{(2)} + \beta_{1(n+1,n+2)}^{(2)} + (\beta_{2(n+1,n+2)}^{(2)} + \mathrm{H.c.}),
\end{aligned}
\tag{3.10}
$$

where $\rho_{n+1,n+2}^{(2)}$ can be obtained from Equation (3.5), and

$$
\begin{aligned}
\beta_1^{(2)} &= \mathcal{Z}_{\mathcal{N}-1}|1\rangle\langle1|_{(n+1)} \otimes \bar{\rho}_{n+2} + \mathcal{Z}_{\mathcal{N}-2}\bar{\rho}_{n+1} \\
&\otimes \bar{\rho}_{n+2} + (|1\rangle\langle\xi_{\mathcal{N}-1}|_{(n+1)} \otimes \bar{\rho}_{n+2} + h.c.), \text{ and}
\end{aligned}
\tag{3.11}
$$

$$
\begin{aligned}
\beta_2^{(2)} &= |2\rangle_{n+1,n+2}\langle1|_{n+1}\langle\xi_{\mathcal{N}}|_{n+2} + |2\rangle_{n+1,n+2} \\
&\times \sum_{i=1}^{\mathcal{N}}\langle\mathcal{F}_i|_{n+2}\langle\xi_{\mathcal{N}-i}|_{n+1} + \bar{\rho}_{n+1} \otimes |1\rangle_{n+2}\langle\xi_{\mathcal{N}}|_{n+2} \\
&+ \tfrac{1}{\mathcal{Z}_1}(|\mathcal{F}_1\rangle_{n+1}|1\rangle_{n+2}\langle1|_{n+1}\sum_{i=1}^{\mathcal{N}}\langle\mathcal{F}_i|_{n+2}\mathcal{Y}_{\mathcal{N}-1}^1),
\end{aligned}
\tag{3.12}
$$

and $\mathcal{Y}_{\mathcal{N}}^1 = \langle\mathcal{N}|\mathcal{N}-1\rangle|1\rangle$.

The different inner products can be calculated as follows: The recursion begins with evaluating $\langle1|\bar{2}\rangle = \sum_{i=1}^{k}\alpha_i^1|\alpha_i\rangle$, where $\{|\alpha_i\rangle\}_i$ forms an independent set of vectors consisting of certain non nearest-neighbor singlet combinations of an $(1, \mathcal{N}+2)$ spin system. Here k is numerically calculated; e.g., $|\alpha_1\rangle=|1\rangle$. In general, we can write

$$
_n\langle\alpha_j|\bar{2}\rangle_{n,n+1} = (-1)^{n-1}\sum_i\alpha_i^j|\alpha_i\rangle_{n+1}.
\tag{3.13}
$$

Using this relation, we generate the inner product recursions:

$$
\begin{aligned}
\mathcal{Z}_{\mathcal{N}} &= \mathcal{Z}_1\mathcal{Z}_{\mathcal{N}-1} + \mathcal{Z}_2'\mathcal{Z}_{\mathcal{N}-2} + 2(-1)^{n-1}\sum_i\alpha_i^1\mathcal{Y}_{\mathcal{N}-1}^i, \\
\mathcal{Y}_{\mathcal{N}}^j &= {}_n\langle\alpha_j|_{(1,n-1}\langle\mathcal{N}-1|\mathcal{N}\rangle_{1,n}) \\
&= \mathcal{A}_{j1}\mathcal{Z}_{\mathcal{N}-1} + (-1)^{n-1}\sum_i\alpha_i^j\mathcal{Y}_{\mathcal{N}-1}^i,
\end{aligned}
\tag{3.14}
$$

and

$$
\langle\xi_{\mathcal{N}}|_{n+1} = \langle\bar{2}|_{n,n+1}\langle\mathcal{N}-1|\mathcal{N}\rangle = \sum_{i=1}^{\mathcal{N}}\mathcal{Z}_{\mathcal{N}-i}\langle\mathcal{F}_i|_{n+1},
\tag{3.15}
$$

where $\mathcal{Z}_2'$ and $\mathcal{A}_{ij}$ are $\langle\bar{2}|\bar{2}\rangle$ and $\langle\alpha_i|\alpha_j\rangle$, respectively. $\langle\mathcal{F}_i|_{n+1} = {}_{n,n+1}\langle\bar{2}|\mathcal{F}_{i-1}\rangle_n$ and $|\mathcal{F}_0\rangle_n = |1\rangle_n$. On expanding, we can write

$$
\langle\mathcal{F}_i|_{n+1} = {}_{n,n+1}\langle\bar{2}|\mathcal{F}_{i-1}\rangle_n = \sum_k g_k^i\langle\alpha_k|_{n+1},
\tag{3.16}
$$

where $g_j^i = \sum_k g_k^{i-1}\alpha_j^k$. Hence all the terms can be recursively calculated provided the parameters for small spin systems can be accurately estimated. The terms $\alpha_i^j(i, j = 1 \text{ to } k)$, of $\mathcal{Z}_1$, $\mathcal{Z}_2'$, and $\mathcal{A}_{ij}$ need to be exactly calculated. The value of k needs to be determined for a small system size by solving the linear equation system in $_n\langle\alpha_j|\bar{2}\rangle_{n,n+1}$.

3.3.2 Quantum spin-1/2 lattice with odd M spins

Let us now consider a quantum spin-1/2 lattice, $|M,\mathcal{N}+2\rangle$, when there are odd M spins along the vertical edge and even $\mathcal{N}+2$ spins in the horizontal edge, such that $M \times (\mathcal{N}+2)$ $(= 2N)$ is the total number of spins. The periodic recursion for the lattice with odd spins on the vertical edge, M, is rather different from that of the even M lattice. This is due to the fact that there exists no analogous state for $|1\rangle$ in the odd M lattice.[6] The state $|\mathcal{N}\rangle$, with open boundary conditions, can be written as a series of $\mathcal{N} = 2$, odd M lattices, given by the state $|2\rangle_{i,j}$, where the M has been dropped (as was done for even M states in Section 3.3.1).

$$
\begin{aligned}
|\mathcal{N}+2\rangle &= |\mathcal{N}\rangle|2\rangle_{n+1,n+2} \\
&= |2\rangle_{1,2}|2\rangle_{3,4}\cdots|2\rangle_{n+1,n+2}
\end{aligned}
\tag{3.17}
$$

The corresponding density matrix, using the above equation, can be written as,

$$
\begin{aligned}
\rho^{(\mathcal{N}+2)} &= |\mathcal{N}+2\rangle\langle\mathcal{N}+2| \\
&= \rho^{(\mathcal{N})}_{1,n} \otimes \rho^{(2)}_{n+1,n+2} \\
&= \rho^{(2)}_{1,2} \otimes \rho^{(2)}_{3,4} \cdots \otimes \rho^{(2)}_{n+1,n+2}.
\end{aligned}
\tag{3.18}
$$

For obtaining the two-rung reduced density matrix, we trace out the rungs ranging from 1 to n, as done for the even M lattice. The reduced state for the odd M lattice, using Equation (3.18), is given by,

$$
\begin{aligned}
\rho^{(2)}_{(n+1,n+2)} &= \mathrm{tr}_{1..n}[|\mathcal{N}+2\rangle\langle\mathcal{N}+2|] \\
&= \mathrm{tr}_{1..n}[\rho^{(2)}_{1,2} \otimes \rho^{(2)}_{3,4} \cdots \otimes \rho^{(2)}_{n+1,n+2}] \\
&= \mathcal{Z}_{\mathcal{N}}|2\rangle\langle2|_{(n+1,n+2)},
\end{aligned}
\tag{3.19}
$$

where $\mathcal{Z}_{\mathcal{N}} = \langle\mathcal{N}|\mathcal{N}\rangle = \mathcal{Z}_2^{N/2}$ and $\mathcal{Z}_2 = \langle2|2\rangle$.

Applying the periodic recursion for the odd $|M,\mathcal{N}+2\rangle$ horizontal spin lattice, using Equation (3.17), we obtain the following recursion relation,

$$
|\mathcal{N}+2\rangle_P = |\mathcal{N}\rangle_{1,n}|2\rangle_{n+1,n+2} + |\mathcal{N}\rangle_{2,n+1}|2\rangle_{n+2,1}
\tag{3.20}
$$

where $|2\rangle_{n+1,1}$ is a periodic two-rung, odd M lattice formed between rungs at sites $n+1$ and 1. We observe that there is no repetition of terms in $|\mathcal{N}+2\rangle$ and $|\mathcal{N}+2\rangle_P$ and hence no subtraction of states is required, as is needed for the even M lattice. This is possible due to the absence of $|1\rangle$ state in the odd-legged state.

---

[6]Since, $|1\rangle$ is a representation of the state $|M,1\rangle$, it will only be a valid dimer-pair superposition state for even M. For odd M, no single vertical column dimer superposed state is possible.
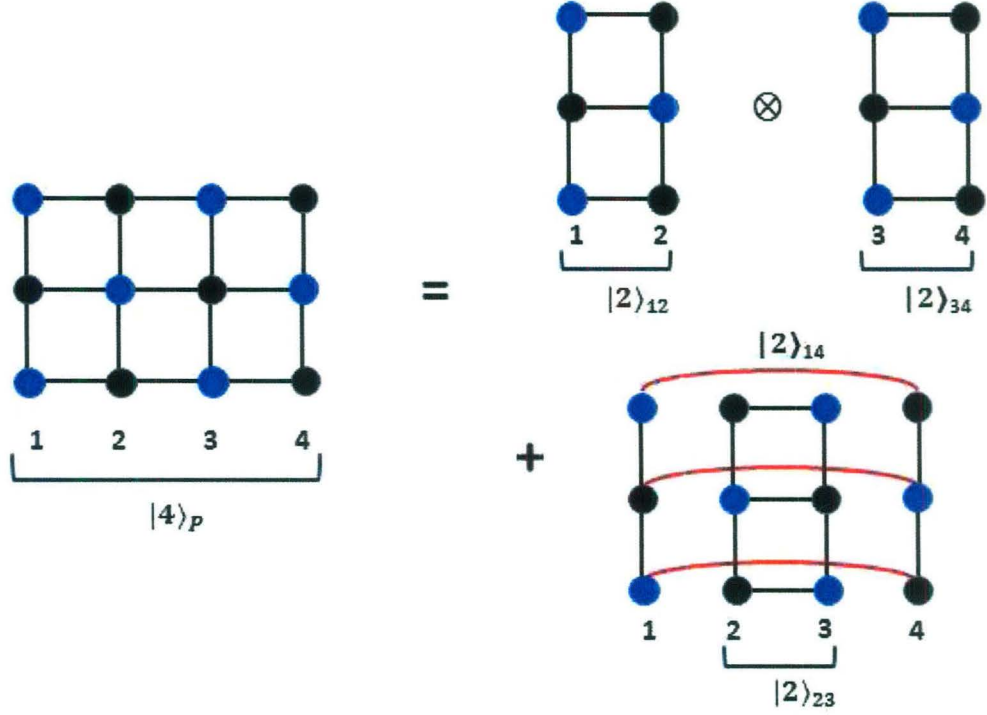
Figure 3.3: An illustration of the recursion relation for an odd M lattice, with periodic boundary condition, $|\mathcal{N}+2\rangle_P$, as given by Equation (3.7), for $M = 3$ and $\mathcal{N} = 2$. Solid lines in a lattice refer to states with all possible dimer coverings. The figure shows that a $|4\rangle_P$ state, with 3 horizontal chains and a periodic boundary condition, can be recursively generated using the open boundary states $|2\rangle$. The bold red lines demonstrate the periodic boundary condition. The sublattices are defined in a manner consistent with Figure 2.1.

The density matrix for the periodic odd lattice, can now be calculated, using (3.20):

$$\rho_P^{\mathcal{N}+2} = |\mathcal{N}+2\rangle\langle\mathcal{N}+2|_P. \tag{3.21}$$

The reduced density matrices can be obtained by tracing out the requisite number of spins. In particular, for obtaining a two-rung reduced density matrix for the periodic odd lattice, we trace out the rungs ranging from 1 to n in the expression given by Equation (3.21):

$$
\begin{aligned}
\rho_{P(n+1,n+2)}^{(2)} &= \mathrm{tr}_{1..n}[|\mathcal{N}+2\rangle\langle\mathcal{N}+2|_P] \\
&= \mathrm{tr}_{1..n}[|\mathcal{N}\rangle\langle\mathcal{N}|_{1,n}|2\rangle\langle2|_{n+1,n+2} + |\mathcal{N}\rangle\langle\mathcal{N}|_{2,n+1}|2\rangle\langle2|_{n+2,1} \\
&\quad + (|\mathcal{N}\rangle_{1,n}|2\rangle_{n+1,n+2}\langle\mathcal{N}|_{2,n+1}\langle2|_{1,n+2} + h.c.)].
\end{aligned} \tag{3.22}
$$

Upon further simplification, using Equation (3.19), the above equation reads

$$
\begin{aligned}
\rho_{P(n+1,n+2)}^{(2)} &= \mathcal{Z}_{\mathcal{N}}|2\rangle\langle2|_{(n+1,n+2)} + \mathcal{Z}_{\mathcal{N}-2}\bar{\rho}_{n+1} \otimes \bar{\rho}_{n+2} \\
&\quad + (|2\rangle_{n+1,n+2}\langle\Omega_{\mathcal{N}}|_{n+1,n+2} + h.c.),
\end{aligned} \tag{3.23}
$$

where the expression for $\langle \Omega_{\mathcal{N}}|$ is given by,

$$\langle \Omega_{\mathcal{N}}|_{n+1,n+2} = \langle 2|_{1,n+2}\langle \mathcal{N}|_{2,n+1}|\mathcal{N}\rangle_{1,n}, \tag{3.24}$$

and $\mathcal{Z}_{\mathcal{N}}$ has been defined earlier. The recursion to obtain $\langle \Omega_{\mathcal{N}}|$ can be written as,

$$\langle \Omega_{\mathcal{N}}|_{n+1,n+2} = \langle 2|_{1,n+2}\langle \mathcal{N}|_{2,n+1}|\mathcal{N}\rangle_{1,n}$$

$$= \langle 2|_{1,n+2}\langle 2|_{2,3}\cdots\langle 2|_{n,n+1}|2\rangle_{1,2}|2\rangle_{3,4}\cdots|2\rangle_{n-1,n}. \tag{3.25}$$

Hence the computation involves writing an algorithm to iterate the step $\langle 2|_{i,i+3}\langle 2|_{i+1,i+2}|2\rangle_{i,i+1}$. Once the reduced density matrices are obtained by the iterative method, we can again use them to obtain the different single- and multi-site physical quantities of the odd M quantum lattice. Together with the characterization of reduced density matrices, in Section 3.3.1, we obtain an analytical method to calculate any properties, including classical and quantum correlation measures, in 2D RVB spin liquids.

3.4 Even-legged vs odd-legged RVB ladders

To illustrate the effectiveness of the DMRM, we apply it to obtain the multisite entanglement of multi-legged ladders with both even and odd number of legs.

In particular, we consider two-, four- and six-legged ladders among even ladders, and three-, five- and seven-legged ladders among odd ones. For even-legged ladders, the formalism developed in Section 3.3.1, for quantum spin-1/2 lattices with even spins along the vertical edge, is applied. The iterative variables for the two-, four- and six-legged ladders can be evaluated by using their explicitly calculated initial set of values. The iterations provide the reduced density matrices of the system, which are thereafter utilized to obtain the GGM.

We use the specific example of the two- and four-legged ladders to demonstrate the numerical calculation of some of the initial parameters to be applied to the recursion. For a two-legged ladder ($M = 2$), the relevant initial parameter is,

$$\mathcal{Z}_0 = 1, \quad \mathcal{Z}_1 = \langle 1|1\rangle = 2,$$

$$\mathcal{Z}_2' = \langle \bar{2}|\bar{2}\rangle = 4. \tag{3.26}$$

The term $_n\langle 1|\bar{2}\rangle_{n,n+1} = \sum_{i=1}^{k} \alpha_i^1|\alpha_i\rangle_{n+1} = |1\rangle_{n+1}$. This implies the parameter $k = 1$. Hence, $\alpha_i^1 = 0, \forall \ i \neq 1$. $\alpha_1^1 = 1$ and $|\alpha_1\rangle = |1\rangle$. Hence, the term $\mathcal{A}_{ij} = \langle \alpha_i|\alpha_j\rangle = 0, \forall \ i \neq 1, j \neq 1$. $\mathcal{A}_{11} = \langle \alpha_1|\alpha_1\rangle = \langle 1|1\rangle = 2$. The recursion relation for $\mathcal{Z}_{\mathcal{N}}$ and $\mathcal{Y}_{\mathcal{N}}^j$ can then be simplified to the following form:

$$\mathcal{Z}_{\mathcal{N}} = 2\mathcal{Z}_{\mathcal{N}-1} + 4\mathcal{Z}_{\mathcal{N}-2} + 2\mathcal{Y}_{\mathcal{N}-1}^1,$$

$$\mathcal{Y}_{\mathcal{N}}^1 = {}_n\langle 1|(_{1,n-1}\langle \mathcal{N} - 1|\mathcal{N}\rangle_{1,n})$$

$$= 2\mathcal{Z}_{\mathcal{N}-1} + \mathcal{Y}_{\mathcal{N}-1}^1. \tag{3.27}$$

The initial term $\mathcal{Y}_1^1 = \langle 1|1 \rangle = 2$. Further, the recursion for the term $\langle \xi |$ can also be simplified, as shown,

$$\langle \xi_\mathcal{N}|_{n+1} = \langle \bar{2}|_{n,n+1} \langle \mathcal{N} - 1|\mathcal{N} \rangle = \sum_{i=1}^{\mathcal{N}} \mathcal{Z}_{\mathcal{N}-i} \langle 1|_{n+1}, \tag{3.28}$$

where $\langle \mathcal{F}_i|_{n+1} = \langle 1|_{n+1}$. The above set of numerical initial parameter and simplified recursions allows us to calculate the reduced density matrix $\rho_P^{(2)}$, using Equation (3.10), for the two-legged ladder.

A similar analysis can also be extended for the four-legged ladder to calculate the relevant initial parameters and recursion relations. For a four-legged ladder ($M = 4$), the relevant initial parameter is,

$$\mathcal{Z}_0 = 1, \quad \mathcal{Z}_1 = \langle 1|1 \rangle = 4,$$
$$\mathcal{Z}_2' = \langle \bar{2}|\bar{2} \rangle = 136. \tag{3.29}$$

Proceeding in a manner similar to that for the two-legged ladder, we obtain the term,

$$\begin{aligned}
{}_n\langle 1|\bar{2} \rangle_{n,n+1} &= \sum_{i=1}^{k} \alpha_i^1 |\alpha_i \rangle_{n+1} \\
&= 5|1 \rangle_{n+1} + 1|\bar{1} \rangle_{n+1}, \tag{3.30}
\end{aligned}$$

where $|\bar{1} \rangle_{n+1}$ is a single-rung state with a periodic dimer covering between the topmost and lowermost spin sites. This implies the parameter $k = 2$. Hence, $\alpha_i^1 = 0, \forall\, i \neq (1,2)$, such that $\alpha_1^1 = 5$ and $\alpha_2^1 = 1$. The states $|\alpha_1 \rangle = |1 \rangle$ and $|\alpha_2 \rangle = |\bar{1} \rangle$. This leads to additional initial parameters for the four-legged ladder, as shown,

$$\begin{aligned}
{}_n\langle \bar{1}|\bar{2} \rangle_{n,n+1} &= \sum_{i=1}^{k} \alpha_2^1 |\alpha_i \rangle_{n+1} \\
&= 2|1 \rangle_{n+1} + 3|\bar{1} \rangle_{n+1}. \tag{3.31}
\end{aligned}$$

Hence, $\alpha_i^2 = 0, \forall\, i \neq (1,2)$, such that $\alpha_1^2 = 2$ and $\alpha_2^2 = 3$. The term $\mathcal{A}_{ij} = \langle \alpha_i|\alpha_j \rangle = 0, \forall\, i \neq (1,2)$, $j \neq (1,2)$, such that

$$\begin{aligned}
\mathcal{A}_{11} &= \langle \alpha_1|\alpha_1 \rangle = \langle 1|1 \rangle = 4 \\
\mathcal{A}_{22} &= \langle \alpha_2|\alpha_2 \rangle = \langle 2|2 \rangle = 4 \\
\mathcal{A}_{12} &= \langle \alpha_1|\alpha_2 \rangle = \langle 1|2 \rangle = 2 \\
\mathcal{A}_{12} &= \mathcal{A}_{21} \tag{3.32}
\end{aligned}$$

The recursion relation for $\mathcal{Z}_{\mathcal{N}}$ and $\mathcal{Y}_{\mathcal{N}}^{j}$ can then be simplified to the following form:

$$
\begin{aligned}
\mathcal{Z}_{\mathcal{N}} &= 4\mathcal{Z}_{\mathcal{N}-1} + 136\mathcal{Z}_{\mathcal{N}-2} + 10\mathcal{Y}_{\mathcal{N}-1}^{1} + 2\mathcal{Y}_{\mathcal{N}-1}^{2}, \\
\mathcal{Y}_{\mathcal{N}}^{1} &= {}_{n}\langle 1|({}_{1,n-1}\langle \mathcal{N} - 1|\mathcal{N}\rangle_{1,n}) \\
&= 4\mathcal{Z}_{\mathcal{N}-1} + 5\mathcal{Y}_{\mathcal{N}-1}^{1} + 1\mathcal{Y}_{\mathcal{N}-1}^{2}. \\
\mathcal{Y}_{\mathcal{N}}^{2} &= {}_{n}\langle \bar{1}|({}_{1,n-1}\langle \mathcal{N} - 1|\mathcal{N}\rangle_{1,n}) \\
&= 2\mathcal{Z}_{\mathcal{N}-1} + 2\mathcal{Y}_{\mathcal{N}-1}^{1} + 3\mathcal{Y}_{\mathcal{N}-1}^{2}.
\end{aligned}
\tag{3.33}
$$

The initial term of the recursion for $\mathcal{Y}_{\mathcal{N}}^{1}$ and $\mathcal{Y}_{\mathcal{N}}^{2}$, is given by

$$
\begin{aligned}
\mathcal{Y}_{1}^{1} &= \langle 1|1\rangle = \mathcal{A}_{11} = 4, \\
\mathcal{Y}_{1}^{2} &= \langle \bar{1}|1\rangle = \mathcal{A}_{12} = 2.
\end{aligned}
\tag{3.34}
$$

The term $\langle \xi_{\mathcal{N}}|_{n+1} = \sum_{i=1}^{\mathcal{N}} \mathcal{Z}_{\mathcal{N}-i}\langle \mathcal{F}_{i}|_{n+1}$ can also be obtained by iterations of the term $\langle \mathcal{F}_{i}|_{n+1} = {}_{n,n+1}\langle \bar{2}|\mathcal{F}_{i-1}\rangle_{n} = \sum_{k} g_{k}^{i}\langle \alpha_{k}|_{n+1}$. The initial parameters for the iteration are given by, $|\mathcal{F}_{0}\rangle_{n} = |1\rangle_{n}$ and $|\mathcal{F}_{1}\rangle_{n} = {}_{n-1}\langle 1|\bar{2}\rangle_{n-1,n} = 5|1\rangle_{n} + 1|\bar{1}\rangle_{n}$, which can be suitable represented to obtain the recursion on the term g_{k}^{i}. Hence, the set of initial parameter and recursions allows us to obtain the reduced density matrix $\rho_{P}^{(2)}$, using Equation (3.10).

Similar calculation for initial parameters and recursion relation can also be obtained for six- and higher-legged ladders, however, the analytical expressions for the recursions become more complicated.[7]

For odd-legged quantum spin ladders, with odd spins along the vertical edge, the DMRM formalism developed in Section 3.3.2 is applied. In the case of odd-legged ladders, the recursion relations have simple analytical expressions but are numerically more challenging. We consider the odd-legged ladder with $M = 3, 5$, and 7 legs. Since, the odd-legged ladder state, $|\mathcal{N}\rangle$, without periodic boundary condition, can be written in terms of a product of two-rung states, $|2\rangle$, as shown in Equation (3.17), the recursion can be solved with relative ease. Let us consider the three-legged ladder. The relevant term required to study the recursion is given by,

$$
\mathcal{Z}_{\mathcal{N}} = \langle \mathcal{N}|\mathcal{N}\rangle = \mathcal{Z}_{2}^{N/2} = 44^{N/2}
\tag{3.35}
$$

where, $\mathcal{Z}_{2} = \langle 2|2\rangle = 44$, for a three-legged ladder. The next recursion term $\langle \Omega_{\mathcal{N}}|$ is obtained by the numerical recursion, given in Equation (3.25). To obtain the reduced density matrix $\rho_{P}^{(2)}$, using Equation (3.25), the iteration of the terms $\mathcal{Z}_{2}$ and $\langle \Omega_{\mathcal{N}}|$ is required, which is analytically simpler than the recursion involved in even-legged ladders. However, the iteration of $\langle \Omega_{\mathcal{N}}|$ for odd-legged ladders can be numerically challenging. Using a similar approach,

---

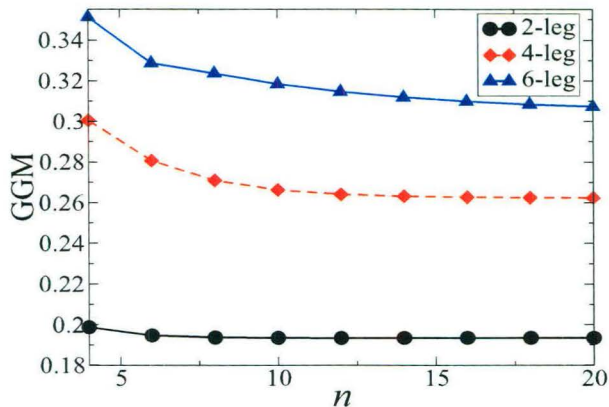[7]The results for $M = 6$, are not included in Reference [71], and have been compiled and presented for the thesis.

Figure 3.4: Genuine multisite entanglement decreases with system-size for even ladders. We perform the iterations for $M = 2$, 4 and 6. The iterations are carried out until 20 rungs, i.e. 40, 80 and 120 sites respectively for $M = 2$, 4 and 6. However in both the cases, the GGM converges much before those sizes. The vertical axis represents the GGM, while the horizontal one represents the number of rungs. Both axes are dimensionless. Though for ladder states, $\mathcal{N} \geq M$, we consider $\mathcal{N} = 4$, as the least number of rungs, for conformity.

the relevant initial parameters for the five-legged ladder is $\mathcal{Z}_2 = 804$, and for seven-legged ladder is $\mathcal{Z}_2 = 14276$.

The evaluation of GGM allows us to compare the multisite entanglements for the even- and odd-legged RVB ladders. The GGMs obtained by the iterative methods clearly capture the characteristic complementary nature of even and odd ladders. We show that the GGM decreases with the increase of system-size in the case of even ladders (Figure 3.4). The opposite is true for odd ladders — the GGM increases with system-size (Figure 3.5).

Although the comparison is made by taking $M = 3$, 5 and 7 among odd ladders, we have actually performed the computations also for $M = 1$, which again shows an increase in GGM with increasing size. In all the cases, the GGM is calculated by considering reduced density matrices upto $2 \times M$ spins: numerical exact diagonalizations corroborate that considering upto 4 spins is already enough. We have performed the iterative algorithms upto 20 rungs in all the cases (which is equivalent to 120 spins for the even six-legged ladder and 140 spins for the odd seven-legged ladder). As seen in the Figures 3.4 and 3.5, the GGM has already converged much before the maximum number of rungs that we have considered.

The recursion relation for reduced density matrices of quantum spin ladder states can be useful in investigating other important aspects of quantum spin systems. The two-site reduced density matrix of superposed dimer-covered state is a Werner state [72] and the bipartite entanglement of the state is a monotone of the Werner parameter. The Werner parameter can also be used to study the ground state energy and spin correlation length (see e.g. [62, 65, 66] and references therein). There is also a correspondence between the entropic
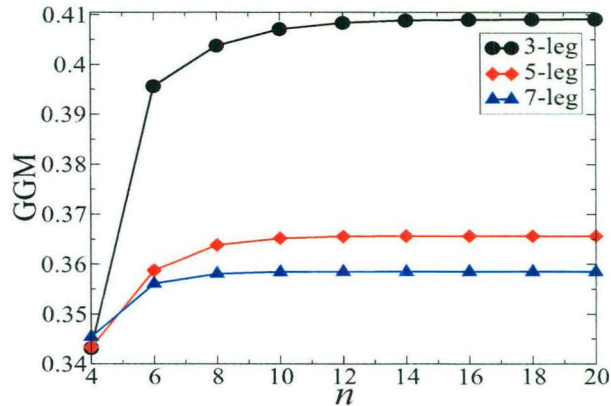
Figure 3.5: Genuine multisite entanglement increases with system-size for odd ladders. We perform the iterations for $M = 3$, 5 and 7. The iterations are until 20 rungs, i.e. 60, 100 and 140 sites respectively for for $M = 3$, 5 and 7. Again in both the cases, the GGM converges much before 20 rungs. The vertical axis represents the GGM, while the horizontal one represents the number of rungs. Both axes are dimensionless. Though for ladder states, $\mathcal{N} \geq M$, we consider $\mathcal{N} = 4$, as the least number of rungs, for conformity.

properties of spin ladder states with entanglement [73].

3.5   Scaling of multisite entanglement in isotropic 2D RVB states

Let us now calculate the genuine multipartite entanglement of quantum spin-1/2 square lattices by using the DMRM technique developed in Section 3.4. The lattice (M, M), for even M, is a 2D square RVB lattice with total spin $2N = M^2$. Hence, for perfect square 2D lattices, the formalism developed in Section 3.3.1, for quantum spin-1/2 lattices with even spins along the vertical edge, is applied with $M = \mathcal{N}$.

We note, that a perfect isotropic lattice has equal even number of spins along the vertical and horizontal edge of the lattice. Hence, there can be no square RVB lattice for odd M, since $2N$ is always even. For odd M, we consider the imperfect lattice with either the leg or rung shorter by a unit, i.e., either $M = \mathcal{N}'(= \mathcal{N} + 1)$ or $M = \mathcal{N}'(= \mathcal{N} - 1)$, such that $2N = M \times \mathcal{N}'$ is always even. Hence, imperfect square 2D lattices, the formalism developed in Section 3.3.2, for quantum spin-1/2 lattices with odd spins along the vertical edge, is applied with $M = \mathcal{N} \pm 1$. Ideally, the appropriate boundary conditions, for the isotropic 2D lattice should also be imposed along the vertical chains. However, in this study, we limit ourselves to horizontal periodic conditions.

We calculate the GGM for perfect as well as imperfect square 2D lattices and observe that for increasing system size, the GGM converges to the value 0.358 (see Figure 3.6). Using finite-size scaling, the behavior of GGM for finite-sized lattices can be used to estimate the
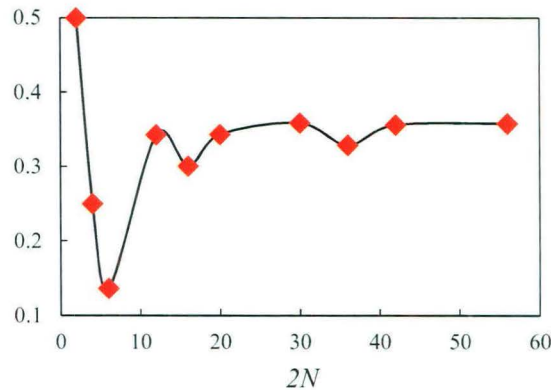
Figure 3.6: The behavior of GGM in the case of a square spin-1/2 lattice, with increasing total number of spins $(2N)$.

GGM for an infinite square lattice. The scaling analysis gives

$$G(|\psi\rangle) \approx G_c(|\psi\rangle) \pm k \; \mathbb{N}^{-x}, \tag{3.36}$$

where $\mathbb{N} = 2N$ and $G_c(|\psi\rangle)$ is an estimated value of GGM for the infinite lattice, based on the average of the last two values of GGM given in Figure 1, with k being a constant. The value of x, as estimated by finite-size scaling, using $G_c(|\phi_N\rangle)=0.358$, is $x = 1.82$, whereas $k=1.77$.

It is shown in Section 2.5.3, that a quantum spin-1/2 lattice with short-range isotropic dimer coverings, with either periodic boundary conditions or is infinite, is always genuinely multipartite entangled, regardless of the geometry and dimension of the isotropic lattice. The DMRM method enables us to estimate the genuine multisite entanglement measure of an infinite square lattice. This gives us a quantitative analysis to the analytical proof obtained in Section 2.5.3. We have checked for small system size, that the square lattice under consideration is long-range entangled, in the sense introduced in Reference [74]. Hence, genuine multisite entanglement can be used as an indicator of topological long-range order, for the RVB liquid states. Moreover, noisy admixtures of these superposed dimer states can be shown to be differential local convertible, implying that such states are deep inside a macroscopic phase of the corresponding quantum many-body system [75, 76].

3.6   Conclusion

In this chapter, we have introduced an analytical iterative technique, the density matrix recursion method, which can be efficiently used to obtain arbitrary reduced density matrices with an arbitrary number of spins, of the states of spin-1/2 quantum spin lattices formed by the superposition of dimer coverings, such as RVB liquids. This technique immediately

allows us to obtain single- and multi-site physical properties of the system. In particular, we use the method to obtain the genuine multisite entanglement in both odd- and even-legged RVB ladder states and find that the genuine multisite entanglement can capture the disparity between the even and odd RVB ladder. The method can also be extended to study finite, isotropic 2D RVB lattices. Finite-size scaling analysis enables us to confirm the existence of high genuine multisite entanglement of an infinite square RVB lattice. The method presented can be a useful tool if such highly superposed systems are considered for performing quantum tasks. Specifically, the iterative method can be employed to derive reduced density matrices that will be fruitful in the calculation of entanglement as well as other important correlation functions.

The behavior of multipartite entanglement of such large superposed quantum spin systems has created a lot of interest due to recent experimental developments. Simulating large qubit systems, using optical superlattices [55–57] and interacting photon states [58], to generate dimer-covered superposed states in the laboratory points to the future applications of such multipartite entangled states, and to potential applications in building cluster states for large scale quantum computation [2] and in quantum metrology [77]. Our analytical method enables the investigation of entanglement properties in these superposed dimer-covered systems with relative control and ease, even for systems containing a considerable number of quantum spins. The results obtained may prove useful in predicting the prospects of the entanglement properties of experimentally generated states for future applications.

[1] R. Horodecki, P. Horodecki, M. Horodecki, and K. Horodecki, Rev. Mod. Phys. **81**, 865 (2009).

[2] H.J. Briegel, D.E. Browne, W. Dür, R. Raussendorf and M. Van den Nest, Nature Phys. **5**, 19 (2009).

[3] A. Sen(De) and U. Sen, Phys. News **40**, 17 (2010), arXiv:1105.2412.

[4] M. Żukowski, M. Horne, and H. Weinfurter, Acta Phys. Pol. **93**, 187 (1998).

[5] M. Hillery, V. Bužek, and A. Berthiaume, Phys. Rev. A **59**, 1829 (1999).

[6] R. Demkowicz-Dobrzanski, A. Sen(De), U. Sen, and M. Lewenstein, Phys. Rev. A **80**, 012311 (2009).

[7] N. Gisin, G. Ribordy, W. Tittel, and H. Zbinden, Rev. Mod. Phy. **74**, 145 (2002).

[8] R. Cleve, D. Gottesman, and H.-K. Lo, Phys. Rev. Lett. **83**, 648 (1999).

[9] A. Karlsson, M. Koashi, and N. Imoto, Phys. Rev. A **59**, 162 (1999).

[10] M.-F. Yang, Phys. Rev. A **71**, 030302 (2005).

[11] X.-F. Qian, T. Shi, Y. Li, Z. Song, and C.-P. Sun, Phys. Rev. A **72**, 012333 (2005).

[12] R. Krischek, C. Schwemmer, W. Wieczorek, H. Weinfurter, P. Hyllus, L. Pezzé, and A. Smerzi, Phys. Rev. Lett. **107**, 080504 (2011).

[13] P. Hyllus, W. Laskowski, R. Krischek, C. Schwemmer, W. Wieczorek, H. Weinfurter, L. Pezzé, and A. Smerzi, Phys. Rev. A **85**, 022321 (2012).

[14] G. Tóth, Phys. Rev. A **85**, 022322 (2012).

[15] M.N. Bera, R. Prabhu, A. Sen(De), and U. Sen, *Multisite Entanglement acts as a Better Indicator of Quantum Phase Transitions in Spin Models with Three-spin Interactions*, arXiv:1209.1523 (2012) and references therein.

[16] T.-C. Wei, D. Das, S. Mukhopadyay, S. Vishveshwara, and P. M. Goldbart, Phys. Rev. A **71**, 060305(R) (2005).

[17] T.R. de Oliveira, G. Rigolin, and M. C. de Oliveira, Phys. Rev. A **73**, 010305(R) (2006).

[18] T.R. de Oliveira, G. Rigolin, M. C. de Oliveira, and E. Miranda, Phys. Rev. Lett. **97**, 170401 (2006).

[19] G. Costantini, P. Facchi, G. Florio, and S. Pascazio, J. Phys. A: Math. Theor. **40**, 8009 (2007).

[20] R. Orús, Phys. Rev. Lett. **100**, 130502 (2008).

[21] R. Orús and T.-C. Wei, Phys. Rev. B **82**, 155120 (2010).

[22] D. Buhr, M.E. Carrington, T. Fugleberg, R. Kobes, G. Kunstatter, D. McGillis, C. Pugh, D. Ryckman, J. Phys. A: Math. Theor. **44**, 365305 (2011).

[23] M. Sarovar, A. Ishizaki, G.R. Fleming, and K.B. Whaley, Nature Phys. **6**, 462 (2010).

[24] J. Zhu, S. Kais, A. Aspuru-Guzik, S. Rodriques, B. Brock, and P. J. Love, J. Chem. Phys. **137**, 074112 (2012).

[25] V. Coffman, J. Kundu, and W. K. Wootters, Phys. Rev. A **61**, 052306 (2000).

[26] G. Vidal, W. Dür, and J.I. Cirac, Phys. Rev. Lett. **85**, 658 (2000).

[27] J. Eisert and H.J. Briegel, Phys. Rev. A **64**, 022306 (2001).

[28] M. Horodecki, P. Horodecki and R. Horodecki, Phys. Lett. A **283**, 1 (2001).

[29] H. Barnum and N. Linden, J. Phys. A: Math. Gen. **34**, 6787 (2001).

[30] D.A. Meyer and N.R. Wallach, J. Math. Phys. **43**, 4273 (2002).

[31] D. Collins, N. Gisin, S. Popescu, D. Roberts and V. Scarani, Phys. Rev. Lett. **88**, 170405 (2002).

[32] T.-C. Wei and P.M. Goldbart, Phys. Rev. A **68**, 042307 (2003).

[33] A. Miyake, Phys. Rev. A **67**, 012108 (2003).

[34] F. Verstraete, J. Dehaene, and B. De Moor, Phys. Rev. A **68**, 012103 (2003).

[35] F. Verstraete, M. Popp, and J. I. Cirac, Phys. Rev. Lett. **92**, 027901 (2004).

[36] C.S. Yu and H.S. Song, Phys. Rev. A **72**, 022333 (2005).

[37] A. Osterloh and J. Siewert, Phys. Rev. A **72**, 012337 (2005).

[38] P. Facchi, G. Florio, and S. Pascazio, Phys. Rev. A **74**, 042331 (2006).

[39] D.L. Deng, Z. S. Zhou, and J. L. Chen, Phys. Rev. A **80**, 022109 (2009).

[40] P. Krammer, H. Kampermann, D. Bruß, R. A. Bertlmann, L. C. Kwek and C. Macchiavello, Phys. Rev. Lett. **103**, 100502 (2009).

[41] M. Huber, F. Mintert, A. Gabriel and B. C. Hiesmayr, Phys. Rev. Lett. **104**, 210501 (2010).

[42] Q.-Q. Shi, R. Orús, J.O. Fjærestad, and H.-Q. Zhou, New J. Phys. **12**, 025008 (2010).

[43] B.-Q. Hu, X.-J. Liu, J.-H. Liu and H.-Q. Zhou, New J. Phys. **13** 093041 (2011).

[44] J.-D. Bancal, N. Brunner, N. Gisin, and Y.-C. Liang, Phys. Rev. Lett. **106**, 020405 (2011).

[45] A. Sen(De) and U. Sen, Phys. Rev. A **81**, 012308 (2010).

[46] A. Sen(De) and U. Sen, *Bound Genuine Multisite Entanglement: Detector of Gapless-Gapped Quantum Transitions in Frustrated Systems*, arXiv:1002.1253 (2010).

[47] P.W. Anderson, Mater. Res. Bull. **8**, 153 (1973).

[48] P.W. Anderson, Science **235**, 1196 (1987).

[49] E. Dagatto and T.M. Rice, Science **271**, 618 (1996).

[50] M. Lewenstein, A. Sanpera, V. Ahufinger, B. Damski, A. Sen(De), and U. Sen, Adv. Phys. **56**, 243 (2007).

[51] L. Amico, R. Fazio, A. Osterloh, and V. Vedral, Rev. Mod. Phys. **80**, 517 (2008).

[52] E. Dagatto J. Riera, and D. Scalapino, Phys. Rev. B **45**, 5744 (1992).

[53] S.R. White, R.M. Noack, and D.J. Scalapino, Phys. Rev. Lett. **73**, 886 (1994).

[54] A.Y. Kitaev, Ann. Phys. (Leipzig) **303**, 2 (2003).

[55] M. Greiner, O. Mandel, T. Esslinger, T.W. Hansch and I. Bloch, Nature **415**, 39 (2002).

[56] F. Verstraete, J.I. Cirac and J.I. Latorre, Phys. Rev. A **79**, 032316 (2009).

[57] S. Nascimbéne, Y.-A. Chen, M. Atala, M. Aidelsburger, S. Trotzky, B. Paredes, and I. Bloch, Phys. Rev. Lett. **108**, 205301 (2012).

[58] X.-S. Ma, B. Dakic, W. Naylor, A. Zeilinger, and P. Walther, Nature Phys. **7**, 399 (2011).

[59] H.S. Dhar and A. Sen(De), J. Phys. A: Math. Theor. **44**, 465302 (2011).

[60] T.M. Rice, S. Gopalan, and M. Sigrist, EPL **23**, 445 (1993).

[61] S. Gopalan, T.M. Rice, and M. Sigrist, Phys. Rev. B **49**, 8901 (1994).

[62] G. Sierra and M.A. Martin-Delgado, Phys. Rev. B **56**, 8774 (1997).

[63] H. Yao and S.A. Kivelson, Phys. Rev. Lett. **108**, 247206 (2012).

[64] H.-C. Jiang, H. Yao and L. Balents, Phys. Rev. B **86**, 024424 (2012) and references therein.

[65] Y. Fan and M. Ma, Phys. Rev B **37**, 1820 (1988).

[66] M. Roncaglia, G. Sierra and M.A. Martin-Delgado, Phys. Rev. B **60**, 12134 (1999).

[67] H.F. Song, N. Laflorencie, S. Rachel, and K. Le Hur, Phys. Rev. B **83**, 224410 (2011).

[68] M.N. Barber, *Finite size scaling, in Phase Transitions and critical phenomena*, Academic Press, London (1983).

[69] S. Liang, B. Doucot, and P.W. Anderson, Phys. Rev. Lett. **61**, 365 (1988).

[70] S.R. White, Phys. Rev. Lett. **69**, 2863 (1992). Phys. Rev. B **48**, 10345 (1993).

[71] H.S. Dhar, A. Sen(De) and U. Sen, New J. Phys. **15**, 013043 (2013).

[72] R.F. Werner, Phys. Rev. A **40**, 4277 (1989).

[73] A.B Kallin, I. Gonzalez, M.B. Hastings, and R.G. Melko, Phys. Rev. Lett. **103**, 117203 (2009).

[74] X. Chen, Z.-C. Gu, and X.-G. Wen, Phys. Rev. B 82, 155138 (2010).

[75] J. Cui, M. Gu, L.C. Kwek, M.F. Santos, H. Fan, and V. Vedral, Nature Comm. **3**, 812 (2012).

[76] A. Hamma, L. Cincio, S. Santra, P. Zanardi, and L. Amico, Phys. Rev. Lett. **110**, 210602 (2013).

[77] V. Giovannetti, S. Lloyd, and L. Maccone, Science **306**, 1330 (2004).

Dynamics of entanglement and information-theoretic quantum correlations

In this part of the thesis, we consider two prototypical models of quantum interaction from many-body physics and quantum optics, namely, an anisotropic XY spin chain, in a transverse magnetic field and a three-level atom interacting with two optical fields. We investigate the behavior of different quantum correlation measures, based on both entanglement-separability and information-theoretic criteria, under different dynamical regimes and conditions, and try to establish some corroborative inter-relation between the measures pertaining to the systems under consideration.

CHAPTER 4

Information-theoretic quantum correlation measures versus entanglement in the dynamics of an infinite spin chain

A theory that explains everything, explains nothing. – Karl Popper

In this chapter, we show that the dynamical phase transition in nearest-neighbor bipartite entanglement of time-evolved states of the infinite, anisotropic quantum XY spin chain, in a transverse time-dependent field, can be quantitatively characterized by the dynamics of information-theoretic quantum correlation measures, such as quantum discord and quantum work-deficit. We show that only those nonequilibrium states exhibit entanglement revival after death, on changing the field parameter during the dynamical phase transition, for which the there is an increase in quantum discord in the vicinity of entanglement collapse or the cumulative quantum work-deficit, during the transition, is above a threshold. The results point to an interesting inter-relation between quantum correlation measures that are conceptualized from different perspectives, viz., the entanglement-separability criteria and information-theoretic concepts.[1]

4.1 Introduction

There have been extensive studies in many-body physics and quantum information theory (QIT), attempting to quantify the key aspects of quantum correlation present between the parts of a system. As introduced in Chapter 1, the foremost among them is the entanglement-separability criteria and its subsequent quantification using measures, such as distillable entanglement, entanglement of formation, and relative entropy of entanglement (see [1] for a review). Entanglement has been extensively used for indicating quantum criticality in phase transitions [2, 3] and in numerous QIT applications, such as quantum teleportation [4], quantum dense coding [5], and quantum key distribution [6]. However, as discussed in Section 1.2, there exist quantum correlation that appear even when entanglement is absent. Several phenomena have been discovered which produce nonclassical results with no shared entanglement identified in the system. These correlations feature in important aspects of QIT, such as quantum *nonlocality without entanglement* [7–9] (cf. [10–13]) and quantum *data hiding in separable states* [14–16]. A natural question then arises: What are the forms of quantum correlation that are responsible for such nonclassical behavior even in the absence of entanglement?

From Section 1.2, we know that early attempts to explore the concept of nonclassicality and correlation, from a perspective that is different from the entanglement-separability paradigm, include those defined in the language of quantum optics [17–20], and the literature on Bell inequalities [21, 22]. Recently, information-theoretic and thermodynamic concepts have been used to define quantum correlation independent of the entanglement-separability paradigm. *Quantum discord* (QD) [23, 24] and *quantum work-deficit* (QWD) [25–27] are quantum correlation measures obtained by quantizing expressions for correlation existing in classical information theory (for a review, see [28]). QD is defined by using the difference in the quantum expressions corresponding to two equivalent definitions of classical mutual information [29]. QWD, on the other hand, is the difference in the amount of negentropy (*work* or *information*) extractable by global and local heat engines [30–32]. A mathematical formulation of QD and QWD is given in Section 1.4.1 and 1.4.2, respectively. These information-theoretic measures have been used to study various aspects of quantum information theory and have been applied to investigate many-body phenomena, such as quantum phase transitions [33–39], correlation dynamics in many-body systems [40–47] and in open quantum systems [48–52] (for a review, see [28]). Further, the application of such measures of quantum correlation in many-body systems may reveal new phenomena which cannot be detected by entanglement. Though there exist nontrivial qualitative relation between information-theoretic and entanglement measures [53–57], for specific quantum

systems, however, in general, there is no operational hierarchy between these measures [58].

In order to probe the interrelation between these measures, we investigate an exactly solvable, prototype model – the infinite anisotropic XY quantum spin chain, in a transverse magnetic field. The nearest-neighbor (NN) entanglement in the time-evolved state of the XY spin chain, at a given fixed time, exhibits critical behavior – a dynamical phase transition (DPT), controlled by the initial value of the transverse field [59]. We study the dynamics of information-theoretic quantum correlation, as quantified by QD and QWD between two neighboring spins, and show that for this particular system, the observed collapse and revival of entanglement (with changing initial value of the transverse field) can be characterized by the behavior of QD and QWD. For instance, entanglement revives after collapse, if QD is an increasing function in the vicinity of the region where entanglement collapse occurs [56].[2] Further, the collapse and revival of entanglement can also be inferred by the *cumulative* QWD in the system during the dynamical evolution. Only those nonequilibrium states exhibit revival after death for which the cumulative QWD is above a threshold value [57]. Both the results are independent of the anisotropy parameter in the quantum XY model. Hence, an increasing QD at the point of entanglement collapse (i.e., at the corresponding time and field strength) or the value of cumulative QWD, above a specific threshold, can be used as an indicator for entanglement revival.

4.2 The quantum XY spin chain

The infinite anisotropic XY spin chain in a transverse field is governed by the Hamiltonian,

$$H = J\sum_i [(1+\gamma)S_i^x S_{i+1}^x + (1-\gamma)S_i^y S_{i+1}^y] - h(t)\sum_i S_i^z, \tag{4.1}$$

where the anisotropy γ is nonzero, and J measures the interaction strength. $S^j = \frac{1}{2}\sigma^j$ $(j = x, y, z)$ are one-half of the Pauli spin matrices at the corresponding site. Note that $\gamma = 0$ corresponds to the XX model while $\gamma = 1$ is the Ising model. Here we consider the models for $\gamma > 0$, so that the interaction and the field parts of the Hamiltonian do not commute, whereby the external field can have nontrivial effects on the evolution. The transverse field is applied in the form of an initial disturbance:

$$h(t) = \begin{cases} a, & t = 0 \\ 0, & t \geq 0, \end{cases} \tag{4.2}$$

where $a \neq 0$.

---

[2]The collapse and revival of entanglement occurs with the changing initial value of the transverse field for a fixed evolution time, and does not, as such imply temporal behavior.

The above Hamiltonian can be realized in a system of cold atoms confined in an optical lattice. The two-component Bose-Bose and Fermi-Fermi mixtures, in the strong coupling limit with suitable tuning of scattering length and additional tunneling in the system can be described by the above Hamiltonian [2, 3] (also see [60]). The dynamics of the system can be simulated by controlling the system parameters and the applied transverse field [61, 62].

4.2.1 Reduced two-qubit density matrix

Let us suppose that the system starts off from the initial state which is a canonical equilibrium state at temperature T. We are interested in the nearest-neighbor (two-site) density matrix of the nonequilibrium evolved state at time t, that started off from the equilibrium state. In general, a two-qubit density matrix is of the form

$$\rho^{12}(t) = \frac{1}{4}\left(I \otimes I + \sum_{j=x,y,z} M^j(t)(\sigma^j \otimes I + I \otimes \sigma^j)\right.$$
$$\left. + \sum_{j,k=x,y,z} T^{jk}(t)\sigma^j \otimes \sigma^k\right),$$

where $T^{jk}(t)$ are the two-site correlation functions, and $M^j(t)$ are the magnetizations. Using properties of the XY Hamiltonian, some simplifications can be made, and the final form of the two-site density matrix of the evolved state is given by [63–66]

$$\rho^{12}_\beta(t) = \frac{1}{4}\left(I \otimes I + M^z(t)(\sigma^z \otimes I + I \otimes \sigma^z)\right.$$
$$+ T^{xy}(t)(\sigma^x \otimes \sigma^y + \sigma^y \otimes \sigma^x)$$
$$\left. + \sum_{j=x,y,z} T^{jj}_\beta(t)\sigma^j \otimes \sigma^j\right). \tag{4.3}$$

Diagonalizing the Hamiltonian via Jordan-Wigner and Fourier transformations, the correlation and the transverse magnetization in Equation (4.3), for an initial temperature T = 0, can be found analytically [63–66]. They are given by,

$$T^{xy}(t) = T^{yx}(t) = S(t), \qquad T^{xx}(t) = G(-1,t), \qquad T^{yy}(t) = G(1,t), \text{and}$$
$$T^{zz}(t) = [M^z(t)]^2 - G(1,t)G(-1,t) + [S(t)]^2 \tag{4.4}$$

where $G(R, t)$ (for $R = \pm 1$)is are given by

$$G(R,t) = \frac{\gamma}{\pi} \int_0^\pi d\phi \, \sin(\phi R) \sin\phi \frac{1}{\Lambda(\tilde{a})\Lambda^2(0)} \times \left\{\gamma^2 \sin^2\phi + (\cos\phi - \tilde{a})\cos\phi\right.$$
$$+ \left. \tilde{a}\cos\phi\cos[2\Lambda(0)\tilde{t}]\right\} - \frac{1}{\pi}\int_0^\pi d\phi \, \cos\phi \frac{1}{\Lambda(\tilde{a})\Lambda^2(0)}$$

$$\times \left(\{\gamma^2 \sin^2\phi + (\cos\phi - \tilde{a})\cos\phi\}\cos\phi - \tilde{a}\gamma^2 \sin^2\phi\cos[2\Lambda(0)\tilde{t}]\right)$$

$S(t)$ and $M^z(t)$ are given respectively by,

$$S(t) = -\frac{\gamma\tilde{a}}{\pi}\int_0^\pi d\phi \sin^2\phi \frac{\sin[2\tilde{t}\Lambda(0)]}{\Lambda(\tilde{a})\Lambda(0)}, \text{ and}$$

$$\begin{aligned}
M^z(t) &= \frac{1}{\pi}\int_0^\pi d\phi \frac{1}{\Lambda(\tilde{a})\Lambda^2(0)} \\
&\times \{\cos[2\Lambda(0)\tilde{t}]\gamma^2\tilde{a}\sin^2\phi] \\
&- \cos\phi[(\cos\phi - \tilde{a})\cos\phi + \gamma^2\sin^2\phi]\}.
\end{aligned}$$

Here $\Lambda(x) = \{\gamma^2\sin^2\phi + [x - \cos\phi]^2\}^{\frac{1}{2}}$, and $\tilde{a} = a/J$, $\tilde{t} = Jt/\hbar$. We will use $\tilde{a}$ and $\tilde{t}$ as the (dimensionless) initial field and time parameters, respectively.

4.2.2 Characterization of the measures

We observe the behavior of the system at a time $\tilde{t}$ after it starts from an initial canonical equilibrium state at zero temperature. The density matrix of the evolved two-qubit state at time $\tilde{t}$ is used to calculate the bipartite entanglement. We use logarithmic negativity (LN) [67], as defined in Section 1.3.3.4, as our measure of entanglement. Other bipartite measures of entanglement, such as entanglement of formation and concurrence [68, 69], defined in Sections 1.3.3.2 and 1.3.3.3, also behave in a similar fashion. For the information theoretic measures of quantum correlation, the characterization is a little nontrivial. In particular, we wish to find the measurement strategy for obtaining the optimal quantum discord and quantum work-deficit, for the nearest-neighbor (two-qubit) density matrix of the evolved state at time $\tilde{t}$. We focus on projection-valued measurements, as discussed in Sections 1.4.1 and 1.4.2. Since the local systems are qubits, the measurement will necessarily involve projecting onto an orthonormal (two-element) basis of a two-dimensional complex Hilbert space. Let that basis be given by

$$\begin{aligned}
|i_1\rangle &= \cos\frac{\theta}{2}|0\rangle + e^{i\phi}\sin\frac{\theta}{2}|1\rangle, \\
|i_2\rangle &= e^{-i\phi}\sin\frac{\theta}{2}|0\rangle + \cos\frac{\theta}{2}|1\rangle,
\end{aligned} \tag{4.5}$$

where $\{|0\rangle, |1\rangle\}$ form the computational qubit basis.

In the case of QWD, the general definition involves two-way communication of dephased states, and is as yet not computable for arbitrary states. We consider the restricted case where only one-way communication is allowed. Again, as the local subsystems are qubits, the most general measurement basis for the dephasing will be of the form in Equation (4.5).

In our analysis, we consider the evolved state after sweeping over the applied initial field strength $\tilde{a}$, at a fixed value of the anisotropy parameter γ for a fixed time of evolution with the

initial state being the equilibrium state of zero temperature. The motivation for considering such a state is the fact that the anisotropic transverse XY model, at zero temperature, undergoes a quantum phase transition (QPT) at $\tilde{a} = 1$, with the change of field at a fixed γ. An initial zero-temperature equilibrium state ensures that thermal fluctuations are absent in the system. This allows us to look for any signature of criticality in the time-evolved nonequilibrium state of the Hamiltonian, with respect to the quantum correlation generated.

4.3 Dynamical behavior of quantum correlation

In the following segments, we look at the dynamical behavior of the NN entanglement and information-theoretic quantum correlation measures in the evolution of the nonequilibrium, time-evolved state of the XY spin chain, as a function of the field paramter $\tilde{a}$ and fixed evolution time $\tilde{t}$.

4.3.1 Dynamical phase transition of bipartite entanglement

We consider the initial states to be equilibruim states at zero temperature. In Figure 4.1, we plot entanglement of the nearest-neighbor evolved state, as a function of time $\tilde{t}$ and the initial field strength $\tilde{a}$, for anisotropy parameter $\gamma = 0.4$ (Figure 4.1(a)) and $\gamma = 0.6$ (Figure 4.1(b)). An important observation from the figures is that for certain fixed evolution times $\tilde{t}$, the entanglement collapses to zero at a certain initial field $\tilde{a}$, but revives to a nonzero value of entanglement at higher initial field, in the dynamic evolution. At other times, the entanglement recedes to zero, and does *not* become nonzero at higher field values. This remarkable behavior of collapse and higher-field revival of bipartite entanglement (as quantified by LN), takes place with respect to the varying initial field ($\tilde{a}$) applied to the system.[3] We call the collapse and revival of entanglement as dynamical phase transition. The results hold irrespective of the value of γ chosen in the range $(0, 1]$.

The DPT of bipartite entanglement is also observed for other computable measures of entanglement, such as concurrence [68, 69]. For two-qubit systems, concurrence and LN vanish if and only if the state is separable [68–72]. Interestingly, we find that there is no DPT when the time-dynamics of the NN quantum discord and quantum work deficit is considered for the same system parameters.

---

[3]A temporal collapse and revival of entanglement can also be observed in Figure 4.1. The entanglement collapses and revives with varying time for certain values of the initial field strength ($\tilde{a} > 1.2$ for Figure 4.1(a)). Our primary interests, however, lie at understanding the correlation that arise close to the zero-temperature QPT at a fixed time of evolution of the quantum state. Note that the QPT at zero temperature also happens at a fixed time. which is $\tilde{t} = 0$. as we sweep over the $\tilde{a}$ axis. The DPT, observed in [59], considers the status of the zero-time transition at nonzero times, if we still sweep over the $\tilde{a}$ axis.
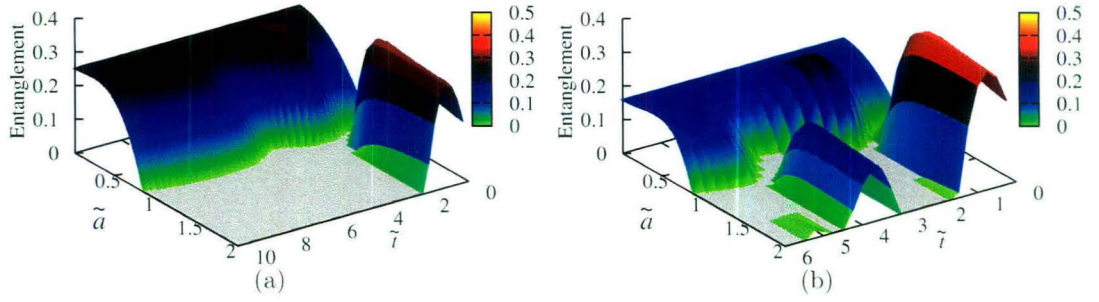
Figure 4.1: Behavior of entanglement, as quantified by logarithmic negativity, is plotted in panels (a) and (b), as functions of the evolution time $\tilde{t}$ and initial field strength $\tilde{a}$, with $\gamma = 0.4$ (a) and $\gamma = 0.6$ (b). Entanglement is measured in ebits. The other axes are dimensionless. The revival of entanglement is distinctly observed at particular times $\tilde{t}$ for a both the fixed values of γ.

Figure 4.2: Behavior of quantum discord with respect to time and transverse field. Quantum discord is plotted in panels (a) and (b), as functions of the evolution time $\tilde{t}$ and initial field strength $\tilde{a}$, with $\gamma = 0.4$ (a) and $\gamma = 0.6$ (b). Quantum discord is is measured in qubits. The other axes are dimensionless. Quantum discord shows different behavior around times $\tilde{t}$, for fixed γ, at which revival of entanglement occurs (See 4.1).

4.3.2 Quantum discord vs entanglement

The dynamics of quantum discord for the nearest-neighbor two-qubit evolved state, as a function of time $\tilde{t}$ and the initial field strength $\tilde{a}$, for anisotropy parameter values $\gamma = 0.4$ and $\gamma = 0.6$ is given in Figure 4.1. The figure shows that QD does not undergo DPT as observed for bipartite entanglement. However, we observe that QD behaves differently at fixed evolution times $\tilde{t}$, for which entanglement revival takes place.

To get a clearer picture of the situation, in Figure 4.3, we plot entanglement, as quantified by logarithmic negativity, and QD for different fixed times $\tilde{t}$, as functions of the initial field strength $\tilde{a}$. We observe that the absolute values of the quantum correlation measures, QD (as measured in qubits) and LN (as measured in ebits) are different. QD is always finite and does not undergo DPT. However, LN is always greater at low values of initial field parameter $\tilde{a}$. The interesting pattern that emerges is that entanglement revival apparently seems to
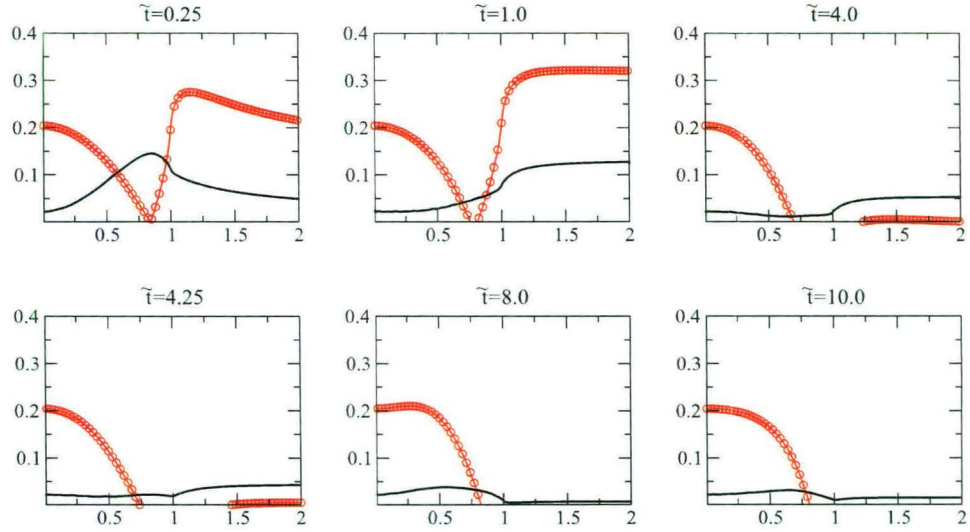
Figure 4.3: Quantum discord (continuous, black) and entanglement (logarithmic negativity) (beaded, red) for fixed times $\tilde{t}$ as functions of the initial field strength $\tilde{a}$. Entanglement collapses to zero and revives at higher-fields for times before $\tilde{t} \approx 2$ and at around $\tilde{t} = 4$. For these and only these times, QD increases around the collapse of LN. LN is measured in ebits, QD in bits, while the horizontal axes denoting the initial field strength $\tilde{a}$ are dimensionless. $\gamma = 0.5$.

occur at instances where QD is increasing in the vicinity of the critical value of $\tilde{a}$, where entanglement collapse occurs. A more quantitative analysis of DPT of entanglement and the behavior of QD is done in Section 4.4.1.

4.3.3 Quantum work-deficit vs entanglement

In Figure 4.4, the dynamics of another information-theoretic measure of quantum correlation, quantum work-deficit, with respect to evolution time $(\tilde{t})$ and the initial field parameter $(\tilde{a})$ is depicted. The figures give us the behavior of QWD, for anisotropy parameters $\gamma=0.4$ (Figure 4.4(a)) and $\gamma=0.6$ (Figure 4.4(b)). The DPT of entanglement, as observed in Figure 4.1, leading to entanglement death and possible revival or its absence, with changing initial field parameter, is closely associated with the dynamics of QWD. Though no DPT is observed for QWD, it is clear from Figure 4.4 that the behavior of QWD is qualitatively different at times when entanglement revival with respect to $\tilde{a}$ is observed, from the times when such revival is absent.

Figure 4.5 shows the behavior of LN and QWD of the time-evolved state, at different fixed times $(\tilde{t})$, as a function of the initial field parameter $\tilde{a}$. The six panels in the figure pertain to different fixed times and each row of the figure corresponds to a particular value of the anisotropy parameter $(\gamma = 0.4, 0.5, 0.6)$. An important observation from the figure is that for certain values of evolution time (Figure 4.5 (a), (c) and (e)), entanglement death
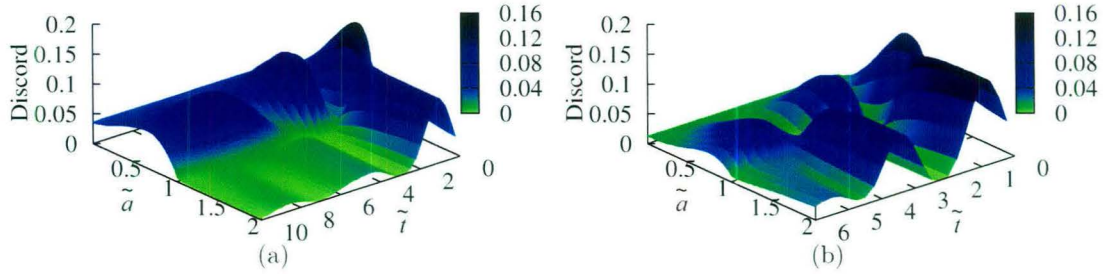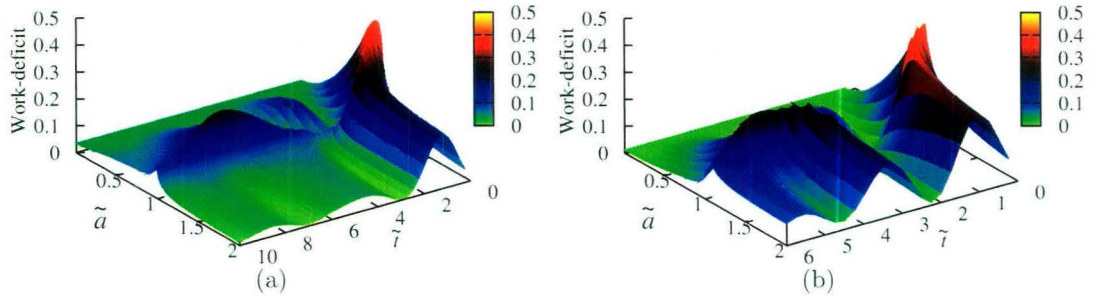
Figure 4.4: Behavior of quantum work-deficit with respect to time and transverse field. Quantum work deficit is plotted in panels (a) and (b), as functions of the evolution time $\tilde{t}$ and initial field strength $\tilde{a}$, with $\gamma = 0.4$ (a) and $\gamma = 0.6$ (b). Quantum work-deficit is measured in qubits. The other axes are dimensionless. The revival of entanglement is seen to be directly related to the amount of work-deficit present at any particular time for a fixed γ, viz. the times for which the quantum work-deficit is significantly high as a function of $\tilde{a}$ correspond to the times at which entanglement revival has taken place (see 4.1).

occurs at a certain initial field value, but entanglement again revives to give nonzero values at some higher initial field. However, for the same anisotropy parameter but different fixed values of evolution time (Figure 4.5 (b), (d) and (f)), entanglement death occurs but does *not* revive with the increase of initial magnetic field. In particular, we observe that at times where revival of entanglement have taken place, the values of QWD are much higher than the times where revival does not occur. Hence, there is an indication that the dynamics of entanglement can be quantified by the behavior of QWD even in the absence of a direct operational relation, which we obtain in Section 4.4.2. In particular, for cases where entanglement revival occurs, the area under the QWD is much larger than for cases where revival is absent. We find that this feature is generic and is observed for the whole range of the anisotropy parameter, $\gamma \neq 0$. Figures 4.4 and 4.5 qualitatively indicate that the behavior of entanglement and QWD is nontrivially related for the model under consideration.

4.3.4 Quenched dynamics

An interesting feature of the dynamics is the sudden quantum quenching of the transverse field, $h(t)$. The initial field, $h(0) = \tilde{a}$, is quantum quenched to $h(t) = 0$ for $t > 0$. For certain values of $\tilde{a}$, the sudden quench could involve a rapid passage of the non-equilibrium system across a quantum critical point [73, 74]. For rapid quenches that cross the critical field $\tilde{a}_c$, the dynamics of quantum correlation are significantly different from those quenches that do not cross any critical point. This can be seen from Figure 4.1 for anisotropy values $\tilde{\gamma} = 0.4$ and $\tilde{\gamma} = 0.6$. For fixed values of $\tilde{a}$, the temporal dynamics of the correlation is different above and below the critical point $\tilde{a}_c$. Such qualitatively different behavior as the
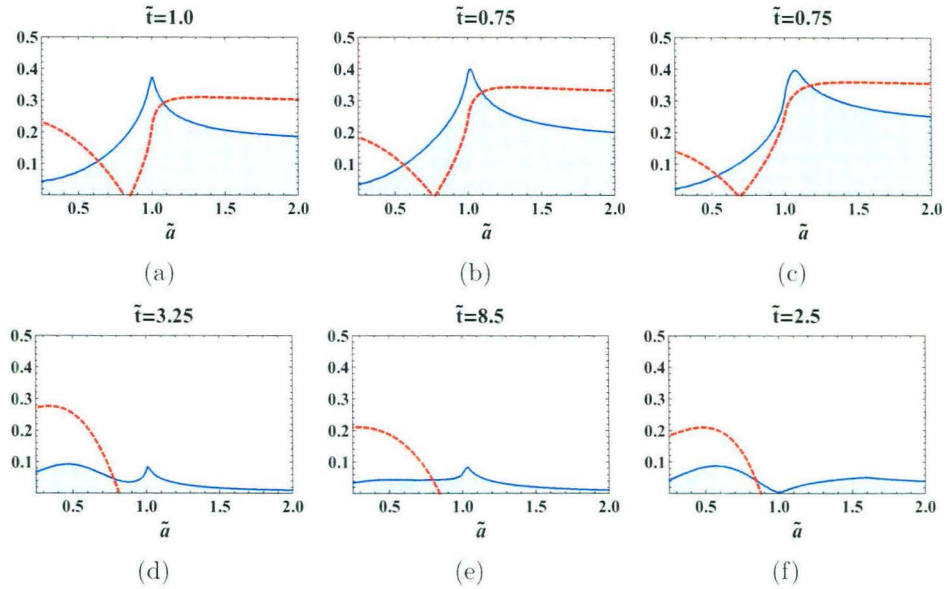
Figure 4.5: Behavior of entanglement (dashed line), measured in ebits, and quantum work-deficit (continuous line), measured in qubits, at fixed times $\tilde{t}$ as functions of the initial field strength $\tilde{a}$, for $\gamma = 0.4$ ((a) and (d)), $\gamma = 0.5$ ((b) and (e)), and $\gamma = 0.6$ ((c) and (f)). $\tilde{a}$ and $\tilde{t}$ are dimensionless parameters. It is seen that entanglement resurrection, after death, takes place only when the area (light blue) under the quantum work-deficit is significantly large. Resurrection takes place in the top panels ((a), (b) and (c)) as opposed to the bottom panels ((d), (e) and (f)) for the same γ in which no revival occurs.

system passes through criticality can be used to study the critical scaling of the quantum correlation under finite quenching and the Kibble-Zurek mechanism [75, 76]. This is also potentially important to results pertaining to quenched quantum dynamical phase transition [77–79] and critical scaling [80–83].

4.4 Quantitative relations: entanglement versus information-theoretic measures

Below, we analyze the quantitative aspect of the inter-relation between information-theoretic measures and entanglement, for the anisotropic, infinite quantum XY spin chain, in a transverse field.

4.4.1 Quantum discord surge heralds entanglement revival

An important question that intuitively arises is: Does there exist any relation between entanglement and QD in the interesting range of initial field strength $\tilde{a}$ and time $\tilde{t}$? The first observation in the numerically simulated dynamical behavior of QD, shown in Figure 3.4, is that QD is nonzero at points where entanglement is zero. We further observe that

the behavior of QD at points where entanglement revival occurs is markedly different (see Figure 4.3).

An exact quantitative response to the question of the role of QD in the collapse and revival of entanglement can be formulated using a relation that ascertains the observed behavior for the considered system. *Consider a time-evolved nonequilibrium bipartite quantum state $\rho_{AB}^a(\tilde{t})$, for an anisotropic XY spin chain in a transverse field, obtained by time-evolution for a duration $\tilde{t}$ and varying with a system parameter $\tilde{a}$. If for a fixed time $\tilde{t}$, the entanglement E vanishes at $\tilde{a} = \tilde{a}_c$, then*

$$\tilde{a}\frac{\partial Q(\rho_{AB})}{\partial \tilde{a}}\bigg|_{\sim \tilde{a}_c} > 0 \implies E(\rho_{AB}) > 0 \text{ for some } |\tilde{a}| > |\tilde{a}_c|. \tag{4.6}$$

Here Q stands for quantum discord[4] and the parameter $\tilde{a}$ is the initial transverse field. From Equation (4.6), it is evident that the QD decreases if one considers DPT along the negative $\tilde{a}$ axis. This is due to the reflection symmetry and surge (dip) in QD is along the positive (negative) direction of the considered physical parameter. Hence we consider just the positive parameter axis and the surge of QD.

Already in Figures 4.2 and 4.3, we see that QD behaves differently at times for which entanglement revival takes place. Only for those times $\tilde{t}$ for which QD is an increasing function of the field strength $\tilde{a}$ at $\tilde{a} = \tilde{a}_c$, $\tilde{a}_c$ being the field strength at which entanglement vanishes for a given $\tilde{t}$, there is a revival of entanglement at a higher value of $\tilde{a}$, as stated in Equation (4.6). In Figure 4.6, we plot the partial derivative of QD with respect to $\tilde{a}$, at $\tilde{a} = \tilde{a}_c$. It is a pictorial representation of the relation given in Equation (4.6). A similar conjecture can also be obtained by studying the correlation dynamics by varying the anisotropy parameter γ even though no consistent DPT is observed for such evolutions.

4.4.2 Cumulative quantum work-deficit vs entanglement

The property of QWD that fosters the dynamical behavior of entanglement can be estimated from Figures 4.1, 4.4 and 4.5. We infer that the revival of entanglement is directly related to the area of the region under QWD as a function of the initial field strength $\tilde{a}$, for a fixed time $\tilde{t}$ and anisotropy γ. To obtain an analytical expression for this relation, we calculate the area under the QWD in the panels of Figure 4.5 under a suitable scaling. By studying the dynamics of QWD and LN for different anisotropy values γ and evolution times $\tilde{t}$, we find that on varying the initial field parameter $\tilde{a}$, the quantum correlation measures, QWD

---

[4]For the specific model, the violation of the inequality in Equation (4.6), usually results in no revival of entanglement. There may, however, exist few intermediary states where entanglement revival occurs in absence of distinct positivity and the collapse-revival behavior of entanglement remains inconclusive. For positive a such resurgence of entanglement without positivity of Equation (4.6) around $a = a_c$, happens in the vicinity of $\tilde{a} = 1$, and so it is plausible that such exceptional cases are related to the zero-temperature QPT in this model [60].
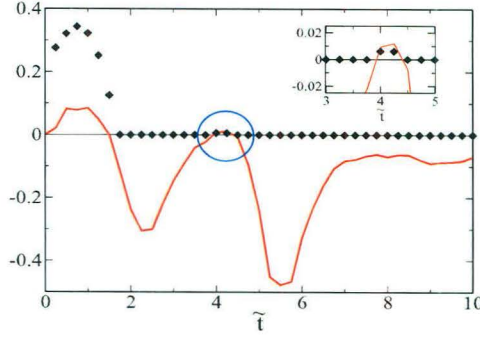
Figure 4.6: Increase of quantum discord at entanglement collapse indicates entanglement revival. The continuous red curve is of the (first) partial derivative of QD (measured in bits) with respect to the initial field strength at $\tilde{a} = \tilde{a}_c$ versus time $\tilde{t}$ (dimensionless). The black diamonds denote the maximum values attained by LN after its collapse (measured in ebits) versus $\tilde{t}$. The continuous curve crosses over zero for $\tilde{t} \lesssim 2$, and again at $\tilde{t} \approx 4$, which are exactly the times for which entanglement revival happens. i.e., where the curve of diamonds is nonzero. The inset magnifies the crossing over zero around $\tilde{t} \approx 4$. Thus the maximum entanglement after collapse is nonzero only at times where the partial derivative curve is positive (since $\tilde{a}$ is positive, the relation in Equation (4.6) holds). $\gamma = 0.5$.

and LN, converge to finite values for $\tilde{a} \geq 2.0$. The DPT is observed in the vicinity of $\tilde{a} \approx 1.0$ and the most interesting dynamics of the quantum correlation occurs around this region. Let $A^\gamma(\tilde{t})$ be the area under the plot of QWD for any particular time $\tilde{t}$ and anisotropy γ, for the initial field parameter ranging from $\tilde{a} = 0.0$ to $\tilde{a} = 2.0$.

We find that *given a known area $A^\gamma(\tilde{t})$ for which a revival of entanglement occurs, any situation with a higher area, $A^\gamma(\tilde{t}')$, will always result in revival of entanglement.* More specifically,

$$A^\gamma(\tilde{t}') \geq A^\gamma(\tilde{t}) \implies \text{Entanglement revival for } \tilde{t}', \tag{4.7}$$

provided $A^\gamma(\tilde{t})$ is known to provide a revival. Hence, one is able to obtain a quantitative expression in terms of QWD that can predict the revival of entanglement in an infinite spin system for a fixed γ, but at different $\tilde{t}$ provided a known case of revival is already obtained for a single set of parameters. Furthermore, we now define a scale factor $S^\gamma(\tilde{t})$ as

$$S^\gamma(\tilde{t}) \equiv \frac{A^\gamma(\tilde{t}) - A^\gamma_{min}}{M}, \tag{4.8}$$

where A^γ_{min} is the lowest value of $A^\gamma(\tilde{t})$ for which a revival is already known. M is an arbitrary scaling parameter, which e.g. can be chosen to be A^γ_{min}. We call $S^\gamma(\tilde{t})$ the cumulative QWD, noting its similarity to cumulative frequency in a probability distribution. The values of $S^\gamma(\tilde{t})$ for different times are plotted in Figure 4.7. It is evident from the panels in Figure 4.7 (for
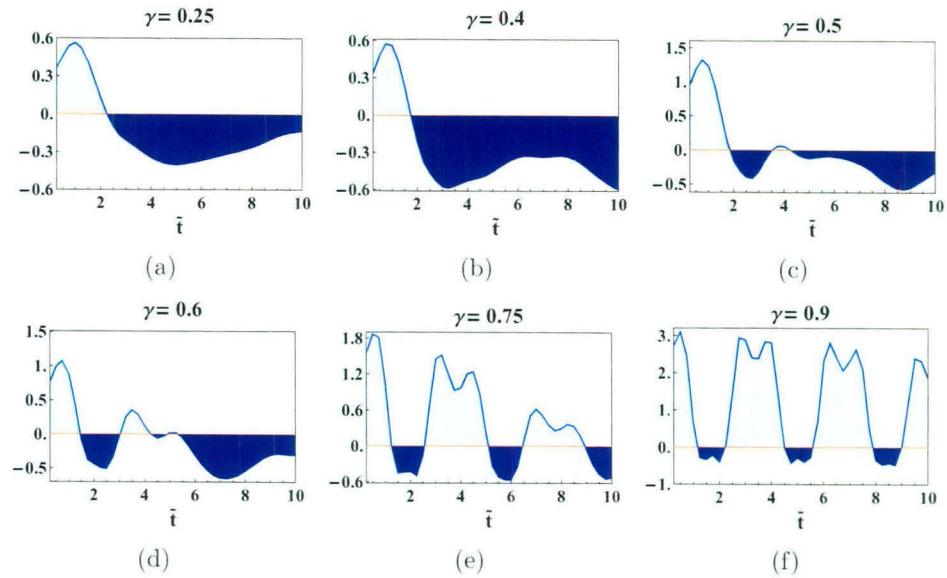
Figure 4.7: Behavior of the scale factor $S^{\gamma}(\tilde{t})$ as a function of time $\tilde{t}$ for different values of the anisotropy parameter γ. For a given γ, the non-negative part (the region of $\tilde{t}$ for which the scale factor is non-negative) corresponds to the region (light blue) where entanglement revival is observed, while the negative region (dark blue) corresponds to no-revival. For the above plots, the scaling parameter M is equal to A^{γ}_{min}. $S^{\gamma}(\tilde{t})$, $\tilde{t}$ and γ are all dimensionless.

different γ) that the following holds:

$$S^{\gamma}(\tilde{t}) \geq 0 \implies \text{revival of entanglement occurs,}$$
$$S^{\gamma}(\tilde{t}) < 0 \implies \text{no revival.} \tag{4.9}$$

The estimation of A^{γ}_{min} requires an optimization. However, Equations (4.8) and (4.9) can be used for a non-optimized A^{γ}_{min}, which in fact leads to Equation (4.7). Comparing Figures 4.4, 4.5 and 4.7, we find that $S^{\gamma}(\tilde{t})$, which is a function of the QWD, correctly signals the times at which entanglement death and revival occurs for different γ. The behavior of $S^{\gamma}(\tilde{t})$ also indicates that with the increase of γ, entanglement revival becomes more and more frequent. In particular, when γ is close to unity and the system is close to the transverse Ising model, the characteristics of $S^{\gamma}(\tilde{t})$ point to an almost periodic entanglement death and revival.

4.5 Conclusion

Quantum correlation of composite quantum systems can broadly be divided into two categories ones that are conceptualized using the entanglement-separability paradigm and those that are defined using information-theoretic concepts. For general mixed states, there exists no

unique operational relation between these two categories of correlation measures. In this work, we have attempted to create a quantitative inter-relation between measures from each of the mentioned categories, namely, the logarithmic negativity, an entanglement measure, and quantum discord and quantum work-deficit, both information-theoretic quantum correlation measures. We have obtained a quantitative relation between these two sets of measures in the time-dynamics of the infinite, anisotropic quantum XY spin-1/2 chain, in an external transverse magnetic field. Entanglement is known to exhibit a dynamical phase transition in the time-evolution of the system: for certain evolution times, the entanglement vanishes at a certain value of the initial magnetic field and revives at higher values, while for other times, the entanglement vanishes and does not show revival. We have observed that the collapse and revival of entanglement, for a given evolution time in its dynamical phase transition, is quantitatively related to the information-theoretic quantum correlation measures, viz. quantum discord and quantum work-deficit. We have shown that an increase of QD in the vicinity of the critical field parameter, where entanglement collapse occurs, indicates a revival of entanglement at higher field parameter values. This behavior can be suitably quantified to an analytical criterion. Further, for the same set of evolution times, we have observed that the revival of entanglement is also related to the area accumulated under the quantum work-deficit curve as a function of the initial magnetic field. An accumulated area under the quantum work-deficit curve that is higher than a certain threshold, *forces* the revival of entanglement to occur.

Studies of information-theoretic measures of quantum correlation, such as QD and QWD, have revealed that such measures give a fine-grained picture of quantum states of distributed systems in comparison to that provided by entanglement. Our study indicates that such a fine-grained picture can show the underlying reason for the dynamics observed for entanglement in quantum many-body systems. The quantitative relation that is obtained between the two categories of quantum correlation measures for the anisotropic quantum XY spin-1/2 models can possibly be extended to other generic quantum many-body systems to obtain a better understanding of nonclassicality in those models. The results may also prove useful in developing a robust operational relation between the two categories of quantum correlation measures.

[1] R. Horodecki, P. Horodecki, M. Horodecki, and K. Horodecki, Rev. Mod. Phys. **81**, 865 (2009).

[2] M. Lewenstein, A. Sanpera, V. Ahufinger, B. Damski, A. Sen(De), and U. Sen, Adv. Phys. **56**, 243 (2007).

[3] L. Amico, R. Fazio, A. Osterloh, and V. Vedral, Rev. Mod. Phys. **80**, 517 (2008).

[4] C.H. Bennett, G. Brassard, C. Crépeau, R. Jozsa, A. Peres, and W.K. Wootters, Phys. Rev. Lett. **70**, 1895 (1993).

[5] C.H. Bennett and S.J. Wiesner, Phys. Rev. Lett. **69**, 2881 (1992).

[6] A.K. Ekert, Phys. Rev. Lett. **67**, 661 (1991).

[7] C.H. Bennett, D.P. DiVincenzo, C.A. Fuchs, T. Mor, E. Rains, P.W. Shor, J.A. Smolin, and W.K. Wootters, Phys. Rev. A **59**, 1070 (1999).

[8] C.H. Bennett, D.P. DiVincenzo, T. Mor, P.W. Shor, J.A. Smolin, and B.M. Terhal, Phys. Rev. Lett. **82**, 5385 (1999).

[9] D.P. DiVincenzo, T. Mor, P.W. Shor, J.A. Smolin, and B.M. Terhal, Comm. Math. Phys. **238**, 379 (2003).

[10] J. Walgate, A.J. Short, L. Hardy, and V. Vedral, Phys. Rev. Lett. **85**, 4972 (2000).

[11] S. Virmani, M.F. Sacchi, M.B. Plenio, and D. Markham, Phys. Lett. A **288**, 62 (2001).

[12] Y.-X. Chen and D. Yang, Phys. Rev. A **64**, 064303 (2001).

[13] Y.-X. Chen and D. Yang, Phys. Rev. A **65**, 022320 (2002).

[14] B.M. Terhal, D.P. DiVincenzo, and D.W. Leung, Phys. Rev. Lett. **86**, 5807 (2001).

[15] D.P. DiVincenzo, D.W. Leung, and B.M. Terhal, IEEE Trans. Inf. Theo. **48**, 580 (2002).

[16] T. Eggeling and R.F. Werner, Phys. Rev. Lett. **89**, 097905 (2002).

[17] L. Mandel and E. Wolf, Rev. Mod. Phys. **37**, 231 (1965).

[18] A. Venugopalan and R. Ghosh, Phys. Rev. A **44**, 6109 (1991).

[19] E. Shchukin and W. Vogel, Phys. Rev. Lett. **96**, 200403 (2006).

[20] A. Chatterjee, H.S. Dhar, and R. Ghosh, J. Phys. B: At. Mol. Opt. Phys. **45**, 205501 (2012), and references therein.

[21] N.D. Mermin, Rev. Mod. Phys. **65**, 803 (1993).

[22] M.D. Reid, P.D. Drummond, W.P. Bowen, E.G. Cavalcanti, P.K. Lam, H.A. Bachor, U.L. Andersen, and G. Leuchs, Rev. Mod. Phys. **81**, 1727 (2009), and references therein.

[23] L. Henderson and V. Vedral, J. Phys. A: Math. Gen. **34**, 6899 (2001).

[24] H. Ollivier and W. H. Zurek, Phys. Rev. Lett. **88**, 017901 (2002).

[25] J. Oppenheim, M. Horodecki, P. Horodecki, and R. Horodecki, Phys. Rev. Lett. **89**, 180402 (2002).

[26] M. Horodecki, K. Horodecki, P. Horodecki, R. Horodecki, J. Oppenheim, A. Sen(De), and U. Sen, Phys. Rev. Lett. **90**, 100402 (2003).

[27] M. Horodecki, P. Horodecki, R. Horodecki, J. Oppenheim, A. Sen(De), U. Sen, and B. Synak-Radtke, Phys. Rev. A **71**, 062307, (2005).

[28] K. Modi, A. Brodutch, H. Cable, T. Paterek, and V. Vedral, Rev. Mod. Phys. **84**, 1655 (2012).

[29] T.M. Cover and J.A. Thomas, *Elements of Information Theory*, J. Wiley, New York (1991).

[30] A. Wehrl, Rev. Mod. Phys. **50**, 221 (1978).

[31] R. Horodecki and P. Horodecki, Phys. Lett. A **194**, 147 (1994).

[32] N.J. Cerf and C. Adami, Phys. Rev. Lett. **79**, 5194 (1997).

[33] R. Dillenschneider, Phys. Rev. B **78**, 224413 (2008).

[34] M.S. Sarandy, Phys. Rev. A **80**, 022108 (2009).

[35] Y.-X. Chen and S.-W. Li, Phys. Rev. A **81**, 032120 (2010).

[36] T. Werlang, G.A.P. Ribeiro, and G. Rigolin, Phys. Rev. Lett. **83**, 062334 (2011).

[37] A.K. Pal and I. Bose, J. Phys. B: At. Mol. Opt. Phys. **44**, 045101 (2011).

[38] B.-Q. Liu, B. Shao, J.-G. Li, J. Zou, and L.-A. Wu, Phys. Rev. A **83**, 052112 (2011).

[39] M. Allegra, P. Giorda, and A. Montorsi, Phys. Rev. B **84**, 245133 (2011).

[40] T. Werlang and G. Rigolin, Phys. Rev. A **81**, 044101 (2011).

[41] S. Campbell, T.J.G. Apollaro, C.D. Franco, L. Banchi, A. Cuccoli, R. Vaia, F. Plastina, and M. Paternostro, Phys. Rev. A **84**, 052316 (2011).

[42] L. Mazzola and M. Paternostro, Nature Sci. Rep. **1**, 199 (2011).

[43] R. Prabhu, A. De Sen, and U. Sen, Phys. Rev. A **86**, 012336 (2012).

[44] J. Maziero, L.C. Cleri, R.M. Serra, and M.S. Sarandy, Phys. Lett. A **376**, 1540 (2012).

[45] A.K. Pal and I. Bose, Eur. Phys. J. B **85**, 36 (2012).

[46] A.K. Pal and I. Bose, Eur. Phys. J. B **85**, 277 (2012).

[47] Y. Huang, Phys. Rev. B **89**, 054410 (2014).

[48] H.-P. Breuer and F. Petruccione, *The Theory of Open Quantum Systems*, Oxford Univ. Press, Oxford, 2002.

[49] C.A. Rodriguez-Rosario and E.C.G. Sudarshan, Int. J. Quantum Inf. **9**, 1617 (2011).

[50] I. Chakrabarty, S. Banerjee, and N. Siddharth, Quantum Inf. Comput. **11**, 0541 (2011).

[51] B. Bellomo, R. Lo Franco, and G. Compagno, Phys. Rev. A **86**, 012312 (2012).

[52] A.L. Grimsmo, S. Parkins, and B.-S.K. Skagerstam, Phys. Rev. A **86**, 022310 (2012).

[53] A. Streltsov, H. Kampermann, and D. Bruß, Phys. Rev. Lett. **106**, 160401 (2011).

[54] M. Piani, S. Gharibian, G. Adesso, J. Calsamiglia, P. Horodecki, and A. Winter, Phys. Rev. Lett. **106**, 220403 (2011).

[55] F.F. Fanchini, M.F. Cornelio, M.C. de Oliveira, and A.O. Caldeira, Phys. Rev. A **84**, 012313 (2011).

[56] H.S. Dhar, R. Ghosh, A. Sen(De), and U. Sen, EPL **98**, 30013 (2012).

[57] H.S. Dhar, R. Ghosh, A. Sen(De), and U. Sen, Phys. Lett. A **378**, 1258 (2014).

[58] M. Ali, A.R.P. Rau, and G. Alber, Phys. Rev. A **81**, 042105 (2010).

[59] A. Sen(De), U. Sen, and M. Lewenstein, Phys. Rev. A **72**, 052319 (2005).

[60] S. Sachdev, *Quantum Phase Transitions*, Cambridge Univ. Press, Cambridge (1999).

[61] J.J. Garcia-Ripoll and J.I. Cirac, Phil. Trans. R. Soc. London A **361**, 1537 (2003).

[62] L.M. Duan, E. Demler, and M.D. Lukin, Phys. Rev. Lett. **91**, 090402 (2003).

[63] E. Lieb, T. Schultz, and D. Mattis, Ann. Phys. (N.Y.) **16**, 407 (1961).

[64] E. Barouch, B.M. McCoy, and M. Dresden, Phys. Rev. A **2**, 1075 (1970).

[65] E. Barouch and B.M. McCoy, Phys. Rev. A **3**, 786 (1971).

[66] E. Barouch and B.M. McCoy, Phys. Rev. A **3**, 2137 (1971).

[67] G. Vidal and R.F. Werner, Phys. Rev. A **65**, 032314 (2002).

[68] S. Hill and W.K. Wootters, Phys. Rev. Lett. **78**, 5022 (1997).

[69] W.K. Wootters, Phys. Rev. Lett. **80**, 2245 (1998).

[70] A. Peres, Phys. Rev. Lett. **77**, 1413 (1996).

[71] M. Horodecki, P. Horodecki, and R. Horodecki, Phys. Lett. A **223**, 1 (1996).

[72] C.H. Bennett, D.P. DiVincenzo, J.A. Smolin, and W.K. Wootters, Phys. Rev. A **54**, 3824 (1996).

[73] K. Sengupta, S. Powell, and S. Sachdev, Phys. Rev. A **69**, 053616 (2004).

[74] A. Das, K. Sengupta, D. Sen, and B.K. Chakrabarti, Phys. Rev. B **74**, 144423 (2006).

[75] T.W.B. Kibble, J. Phys. A: Math. Gen. **9**, 1387 (1976).

[76] W.H. Zurek, Nature **317**, 505 (1985).

[77] E.G. Dalla Torre, E. Demler, and A. Polkovnikov, Phys. Rev. Lett. **110**, 090404 (2013).

[78] M. Heyl, A. Polkovnikov, and S. Kehrein, Phys. Rev. Lett. **110**, 135704 (2013).

[79] L.M. Sieberer, S.D. Huber, E. Altman, and S. Diehl, Phys. Rev. Lett. **110**, 195301 (2013).

[80] W.H. Zurek, U. Dorner, and P. Zoller, Phys. Rev. Lett. **95**, 105701 (2005).

[81] A. Polkovnikov, Phys. Rev. B **72**, 161201 (2005).

[82] C.K. Thomas, D.A. Huse, and A.A. Middleton, Phys. Rev. Lett. **107**, 047203 (2011).

[83] M. Kolodrubetz, B.K. Clark, and D.A. Huse, Phys. Rev. Lett. **109**, 015701 (2012), and references therein.

Quantum correlation dynamics in two-photon states generated using classically driven three-level atoms

We are trying to prove ourselves wrong as quickly as possible, because only in that way can we find progress. – Richard P. Feynman

We investigate the dynamics of two-photon quantum correlation generated by the interaction of a three-level atom in the Ξ, Δ or V configuration, with two classical external driving fields, under the rotating-wave approximation and in presence of level decays. Using the example of a rubidium atom in each configuration, with field strengths validating the single-photon approximation, we compute information-theoretic quantum correlation, such as measurement induced disturbance, quantum discord, and quantum work-deficit, and compare the results with that of entanglement, as quantified by concurrence. The results exhibit interesting inter-relation, hierarchy and qualitative monotonicity between entanglement and the information-theoretic quantum correlation measures in various dynamical regimes, parametrically controlled through the choice of atomic decay constants and external driving field strengths.[1]

5.1 Introduction

The interaction of atomic systems and external electromagnetic fields is a principal source for the generation and classification of nonclassical correlation [1]. The quantum nature of these atom-photon interactions and the ability to implement such systems in controlled experimental settings make them important tools in the study of nonclassical features [2]. From the perspective of quantum information theory (QIT), atomic systems are the quintessential computational hardware needed for the future implementation of quantum information protocols [3–6], and photons are the basic building blocks of quantum communication [7, 8] and cryptography [9]. Hence, the generation and manipulation of nonclassical correlations in complex atomic systems interacting with radiation fields are the most challenging aspects of future applications of QIT.

The nonclassical properties of three-level atomic systems have been well studied in quantum optics for understanding quantum-coherence phenomena, such as electromagnetically-induced transparency (EIT) [10–12], lasing without inversion [13], and coherent trapping [14]. Three-level atoms interacting with low-strength driving fields, similar to EIT systems, have been used to generate entangled two-mode photon states which can be suitably manipulated to yield desired correlations [15]. The potential of emitted photons to encode and transfer quantum correlation stored in atomic systems may prove immensely useful in designing future QIT systems for communications and computation. However, the generation and characterization of mixed state quantum correlation is a very challenging prospect. Well established processes, such as parametric down-conversion [16] generate pure entangled states with poor conversion efficiency and few control parameters, whereas processes, such as resonance fluorescence have low signal-to-noise ratio with poor control over the emission statistics [15]. Quantum optical processes, such as coherent superposition operations have also been traditionally used to generate and characterize nonclassical and entangled states [17–20]. The use of generic quantum optical models, such as the considered semiclassical three-level atomic system, that can be experimentally implemented and observed, can serve as an important tool to generate and control nonclassical correlation and their features. Incidentally, they also serve as an useful prototype model to investigate the dynamical relation between entanglement [21] and other information-theoretic quantum correlations [22].

In this chapter, we investigate the quantum correlation properties of the photon states emitted from a three-level atomic system interacting with two classical driving fields. The interactions generate two-mode single photon states, arising from two controlled coherent transitions connecting the three levels, under the single photon approximation (SPA) [23]. The system can be set up in three different configurations, cascade Ξ, Λ and V. We study
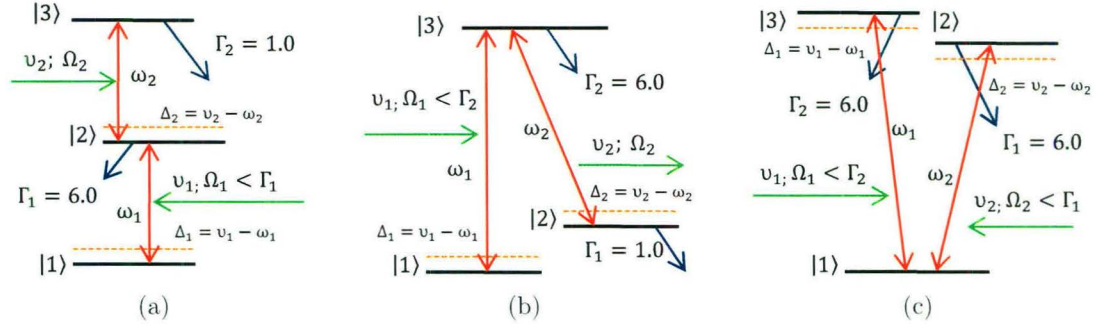
Figure 5.1: A three-level atom in the (a) Ξ, (b) Λ, and (c) V configuration. Γ_1 and Γ_2 are the decay constants (numbers shown in units of MHz) of the levels $|2\rangle$ and $|3\rangle$. ν_1, ν_2, and Ω_1, Ω_2 are the optical frequencies and the Rabi frequencies of the two near-resonant driving fields. ω_1 and ω_2 are the two atomic transition frequencies. Δ_1 and Δ_2 are the field detunings, set to zero in this study.

the correlated two-mode photon state that is generated, and characterize the dynamics of the different measures of quantum correlation. We seek to establish a qualitative relation between the two different theoretical classes of quantum correlations, namely, entanglement [21] and the information-theoretic quantum correlation measures, such as quantum discord (QD), quantum work-deficit (QWD) and measurement induced disturbance (MID), defined in Section 1.4. The control parameters in the system enable us to define specific dynamical regimes where certain quantum correlations are enhanced based on the nature of the output photon states. We also analyze various features of the quantum correlation generated by the interaction to throw light into the monotonicity and hierarchy of the set of measures considered in the study [24]. The arrangement of the chapter is as follows. We briefly discuss the different configurations of the three-level atom in Section 5.2. In Section 5.3, we define the theoretical model used and the working approximations considered in the analysis. In Section 5.4, the numerical results for the different quantum correlation measures, obtained from the theoretical model, are analyzed. We conclude in Section 5.5, with a summary of the results obtained and their possible ramifications.

5.2 The three-level atom

In this section, we briefly review our system. A three-level atom can be used in three different configurations, namely, Ξ, Λ and V [25, 26]. As a specific example, we focus on a gas of rubidium (Rb) atoms [27]. The energy levels $5S_{1/2}$, $5P_{3/2}$ and $5D_{5/2}$ of Rb can be suitably used to generate each of the three configurations, shown in Figure 5.1(a)-(c), as elaborated in the subsections below. Level $5S_{1/2}$ is the ground state and does not decay. Level $5D_{5/2}$ is

metastable, with a decay rate, $\Gamma_D \approx 1.0$ MHz while the decay rate of level $5P_{3/2}$ is $\Gamma_P \approx 6.0$ MHz [27]. The conditions on the driving field Rabi frequencies Ω_i shown in Figure 5.1(a)-(c) are explained later in Section 5.3.3.

5.2.1 The Ξ system

The cascade Ξ system (Figure 5.1(a)) uses the allowed dipole transitions $|1\rangle \leftrightarrow |2\rangle$ and $|2\rangle \leftrightarrow |3\rangle$, with two classical fields of Rabi frequencies Ω_1 and Ω_2 driving these transitions, respectively. The field detunings are Δ_1 and Δ_2, set to zero throughout our analysis for near-resonant fields. The transition $|1\rangle \leftrightarrow |3\rangle$ is dipole forbidden. Levels $|1\rangle$, $|2\rangle$ and $|3\rangle$ correspond to the atomic levels $5S_{1/2}$, $5P_{3/2}$ and $5D_{5/2}$ of the Rb atom, respectively. Thus the decay rates of $|3\rangle$ and $|2\rangle$ are $\Gamma_2 \equiv \Gamma_D = 1.0$ MHz and $\Gamma_1 \equiv \Gamma_P = 6.0$ MHz, respectively. Level $P_{3/2}$ serves as the shared level $|2\rangle$ during the interaction. The initial atomic state is ground state ($|1\rangle$) populated and the levels $|2\rangle$ and $|3\rangle$ are unpopulated. Ξ systems have been extensively used in coherent population trapping [28] and also in experiments to achieve laser cooling in trapped ions [29].

5.2.2 The Λ system

The Λ system configuration can be obtained by folding the Ξ, with levels $5S_{1/2}$, $5P_{3/2}$ and $5D_{5/2}$ of the Rb atom now marked as levels $|1\rangle$, $|3\rangle$ and $|2\rangle$, respectively, as shown in Figure 5.1(b). With this identification for Rb, we observe that level $|2\rangle$ is energetically higher than level $|3\rangle$. This corresponds to a negative transition frequency ω_2. The rotating wave approximation (RWA) thus holds for the negative frequency term of the field in the Hamiltonian [27]. Hence, the transition from level $|3\rangle$ to $|2\rangle$ annihilates a photon instead of creating a photon. The allowed dipole transitions are now $|1\rangle \leftrightarrow |3\rangle$ and $|2\rangle \leftrightarrow |3\rangle$, with two driving fields with Rabi frequencies Ω_1 and Ω_2 now acting on these transitions. Level $|3\rangle$ is the shared level, and the transition $|1\rangle \leftrightarrow |2\rangle$ is now dipole forbidden. The decay rates of $|2\rangle$ and $|3\rangle$ are $\Gamma_1 \equiv \Gamma_D = 1.0$ MHz and $\Gamma_2 \equiv \Gamma_P = 6.0$ MHz, respectively. The initial atomic system is again ground state ($|1\rangle$) populated, and the detunings are taken to be zero. The interactions of the three levels are distinctly different from the Ξ system, and hence can be associated with different nonclassical behavior. Λ systems have been extensively used in demonstrating diverse coherent phenomena, such as stimulated raman adiabatic passage [30] and electromagnetically induced transparency (EIT) [10-12].

5.2.3 The V system

The configuration of the V system (Figure 5.1(c)) is considerably different from the Ξ and the Λ systems. This is due to the fact that the shared level in the V system is the ground state. For the V system using Rb, we consider level $5S_{1/2}$ as the shared ground level ($|1\rangle$) and

two hyperfine levels of $5P_{3/2}$ as the two-excited levels ($|2\rangle$ and $|3\rangle$). Hence, $\Gamma_1 = \Gamma_2 \equiv \Gamma_P = 6.0$ MHz. The allowed transitions are $|1\rangle \leftrightarrow |3\rangle$ and $|1\rangle \leftrightarrow |2\rangle$, driven by the classical fields of Rabi frequencies Ω_1 and Ω_2, respectively. The transition $|2\rangle \leftrightarrow |3\rangle$ is dipole-forbidden, i.e., the ground state excitations take the system to two excited levels that cannot be coupled, and interactions are thus limited to ground state transitions. The initial atomic system is again ground state ($|1\rangle$) populated, and the detunings are set to zero. V systems are widely used to study nonclassical phenomena, such as quantum jumps [31], quantum Zeno effect [32, 33] and quantum beats [14].

5.3 Atom-photon interaction

Three-level atomic systems have been extensively used to study quantum and nonlinear features under the realm of the semiclassical atom-field theory [25]. The nonclassical nature of the emitted radiation in such systems have also been investigated [34]. From the perspective of QIT, entanglement properties of different features of the three-level atomic systems have also been examined [35-37]. However, an exhaustive discussion on the generation and control of quantum correlation, both entanglement and information-theoretic measures, for such atom-field systems is not present, and we seek to investigate and compare the important features of such quantum correlation using this versatile system [24].

5.3.1 The Hamiltonian

The Hamiltonian for a general three-level atom interacting with two classical driving fields, in the RWA, can be written as [14]:

$$\mathcal{H} = \mathcal{H}_0 + \mathcal{H}_I, \tag{5.1}$$

$$\mathcal{H}_0 = \hbar\omega_{11}|1\rangle\langle1| + \hbar\omega_{22}|2\rangle\langle2| + \hbar\omega_{33}|3\rangle\langle3|,$$

$$\mathcal{H}_I = -\hbar/2\,(\Omega_1 e^{-i\phi_1}e^{-i\nu_1 t}|m\rangle\langle n| + \Omega_2 e^{-i\phi_2}e^{-i\nu_2 t}|l\rangle\langle k| + \text{H.c.}), \tag{5.2}$$

where $\hbar\omega_{ii}$ is the energy of level $|i\rangle$ ($i = 1,2,3$); $\Omega_j e^{-i\phi_j}$ ($j = 1,2$) is the complex Rabi frequency corresponding to the classical driving field of frequency ν_j, $m,n,l,k = \{1,2,3\}$ denote the three atomic levels as appropriate for the Ξ, Λ or V configuration. For the Ξ configuration, $(m,n,l,k) = (2,1,3,2)$ correspond to the atomic transitions $|1\rangle \leftrightarrow |2\rangle$ and $|2\rangle \leftrightarrow |3\rangle$. For the Λ configuration, $(m,n,l,k) = (3,1,3,2)$ correspond to the transitions $|1\rangle \leftrightarrow |3\rangle$ and $|2\rangle \leftrightarrow |3\rangle$, and for the V configuration, $(m,n,l,k) = (3,1,2,1)$ correspond to the transitions $|1\rangle \leftrightarrow |3\rangle$ and $|1\rangle \leftrightarrow |2\rangle$ (Figure 5.1(a)-(c)).

5.3.2 The Atomic Density Matrix

The state of the atomic system, at any time t, can be written in the following form:

$$|\psi(t)\rangle_A = C_1(t)e^{-i(\omega_{11}+\xi_1)t}|1\rangle + C_2(t)e^{-i(\omega_{22}+\xi_2)t}|2\rangle + C_3(t)e^{-i(\omega_{33}+\xi_3)t}|3\rangle, \quad (5.3)$$

where ξ_i ($i = 1, 2, 3$) are phases that depend on the detunings in a specific configuration. The detunings are defined as

$$\Delta_1 = \nu_1 - \omega_1,$$
$$\Delta_2 = \nu_2 - \omega_2,$$

where $\omega_1 = \omega_{mm} - \omega_{nn}$, and $\omega_2 = \omega_{ll} - \omega_{kk}$, are the transition frequencies. (m, n, l, k) have been defined earlier and are different for the three configurations.

Using the wavefunction in Equation (5.3), one can create an atomic density matrix $\rho_A(t)$ which depends on the classical driving field frequencies $\nu_j (j = 1, 2)$. We take phenomenological parameters to denote spontaneous decays of the excited atomic levels [14]. The parametrized decay terms may lead to spontaneously generated coherences in the decay paths [38]. Such phenomenological decay models are commonly used in the study of quantum features in EIT [27], in quantum state tomography of emitted field states [15], and in earlier studies on atom-photon entanglement [39]. With the level decay terms, the dynamics of the system is in general mixed, and can be obtained using the von Neumann (quantum Liouville) equation of motion,

$$\dot{\rho}_A(t) = -\frac{i}{\hbar}[\mathcal{H}, \rho_A(t)] - \frac{1}{2}\{\Gamma, \rho_A(t)\}, \quad (5.4)$$

where the elements of the relaxation matrix Γ are the decay rates, $\langle i|\Gamma|j\rangle = \Gamma_{i-1}\delta_{ij}$, $i, j = 1, 2, 3$. The time-evolved mixed atomic density matrix can be obtained provided the initial states of the atom (before interaction) are known.

5.3.3 Characterization of the two-photon correlated state

The nonclassical nature of the emitted radiation depends on the interaction between the three-level atomic system and the two-mode classical driving fields. The desired output, in our case, is to limit the generation to single photons for the two modes emitted after the interaction, so that at any given time within the lifetime of the atom, there will exist two photon states for each mode. Thus the two-photon density matrix can be written as

$$\rho_{ph} = \sum \rho_{ij,i'j'}|ij\rangle\langle i'j'|.$$

where $|i, j\rangle$ ($|i', j'\rangle$) stands for the two-photon states, with i and j (i' and j') = 0, 1 representing the number of photons in the first and second modes, respectively. Such a two-photon

state can be achieved using the single photon approximation (SPA) [23] within the rotating wave approximation (RWA) [14]. The RWA ensures that a photon is created only when an atomic de-excitation takes place. The SPA is applied by ensuring that the excitation time (due to the driving field strength) is larger than the decay time. If Ω is the driving field Rabi frequency and Γ is the atomic decay rate, we require $1/\Omega > 1/\Gamma$ for the SPA to be valid, so that the time taken for an atom to excite is much greater than the decay time and for small times only a single de-excitation will occur generating a single photon.[2] Hence, the ground state excitation strength Ω should be smaller than the upper-level decay rate Γ [24].

The output state is thus a two-qubit (bipartite) photon state. For a semiclassical interaction involving atoms and driving fields, it has been shown that the density matrix of the output radiation state can be completely derived from the atomic density matrix [15]. Under the far-field approximation [14, 40], for an atom located at $\vec{r}_0$, the field operators of the emitted radiation at the point of detection $\vec{r}$ are proportional to the atomic spin operators at the retarded time $(t - |\vec{r} - \vec{r}_0|/c)$. This equivalence leads to an expression for the photon density matrix $\rho_{ph}(t)$ that is identical to the atomic density matrix at an earlier time, $\rho_A(t - r/c)$, calculated using the von Neumann equation of motion. The photon density matrix has a reduced rank three.[3] It has been shown [15] that such an equivalence leads to the complete determination of the output photon state using quantum state tomography, where measurements can be made on either the atomic or the photonic operators. Since the photon states can be completely determined by the atomic density matrix, the coherence of the photon correlation is closely related to the evolution of the atomic state. The purity of the output photon state is determined using the relation $1 - \text{tr}(\rho_{ph}^2)$.

5.4 Dynamics of quantum correlation

We use concurrence as our measure of bipartite entanglement between the two-mode photon pair. The numerical calculation of the quantum correlation measures, both entanglement and information-theoretic, are done based on their definition given in Sections 1.3 and 1.4. The optimal measurement strategy used in the evaluation of the information-theoretic quantum correlation measures in the two-mode photon is similar to one devised in Section 4.2.2.

As mentioned in Section 5.2, the system, we consider, is a gas of Rb atoms. The three levels $5S_{1/2}$, $5P_{3/2}$ and $5D_{5/2}$ of the Rb atom are appropriated to obtain the Ξ, Λ and V

---

[2]We consider evolution times much smaller than the lifetime of the atom, since the condition of single photon emission may not remain valid due to spontaneous decay over a longer period.

[3]The atomic density matrix is a 3×3 matrix pertaining to the three-dimensional single atom. The two-mode photon density matrix is a 4×4 matrix, since each photon has two orthogonal states $|0\rangle$ and $|1\rangle$. The equivalence is possible because the atom-field interaction ensures that the photon density matrix has a Schmidt decomposition that reduces its rank to 3.

configurations. All rates and frequencies are rendered dimensionless by scaling with the metastable level decay rate (≈ 1 MHz). The scaled decay rates of $5P_{3/2}$ and $5D_{5/2}$ are $\Gamma_P = 6.0$ and $\Gamma_D = 1.0$, respectively, and $5S_{1/2}$ is the ground state (with $\Gamma_S = 0$) [27]. For desired results of two-mode single photon generation, we restrict ourselves to regimes that satisfy the SPA. In the Ξ and Λ configuration (Figure 5.1(a) and (b)), since the shared level is $5P_{3/2}$, we take the ground state excitation field (Ω_1) to be always less than the decay constant of $5P_{3/2}$ (in Ξ, $\Omega_1 < \Gamma_1 \equiv \Gamma_P = 6.0$; in Λ, $\Omega_1 < \Gamma_2 \equiv \Gamma_P = 6.0$). For the V configuration (Figure 5.1(c)), the ground state excitation leads to transitions to the hyperfine levels of $5P_{3/2}$, and hence both the driving fields Ω_1 and Ω_2 are less than the decay constant of $5P_{3/2}$ ($\Omega_{1,2} < \Gamma_{1,2} \equiv \Gamma_P = 6.0$). In our analysis, we set the atom-field detunings to be zero.[4] We calculate the information-theoretic quantum correlation measures and entanglement of the output two-mode photon density matrix that can be derived using the atomic density matrix (Section 5.3.1), obtained from the von Neumann equation of motion [Equation (5.4)], in the three different configurations.

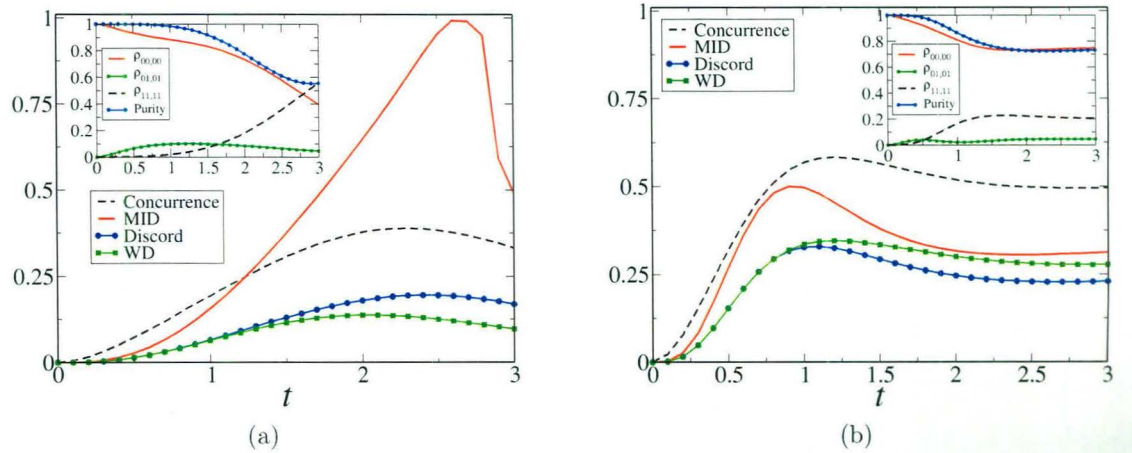(a)   (b)

Figure 5.2: The time evolution for correlation measures MID (red continuous), QD (blue circles) and QWD (green squares) along with the entanglement measure concurrence (black dashed) for the cascade (Ξ) configuration. The field detunings are $\Delta_1 = \Delta_2 = 0$, and the phases of the Rabi frequencies are $\phi_1 = \phi_2 = 0$. The level decay rates are $\Gamma_1 = 6.0$, $\Gamma_2 = 1.0$. SPA for this configuration requires that $\Omega_1 < \Gamma_1$. The driving field strengths are (a) $\Omega_1 = 2.0$, $\Omega_2 = 1.0$, and (b) $\Omega_1 = 2.0$, $\Omega_2 = 5.0$. The inset shows the evolution of population elements of the two-photon density matrix and its purity.

We discuss interesting aspects of the quantum correlation generated in the two-mode photon state in specific parameter regimes using the Ξ configuration as the reference. Some general observations can be made that are consistent with known results: MID always serves

---

[4]It is observed that the qualitative nature of the correlation dynamics is not very sensitive to finite detunings.
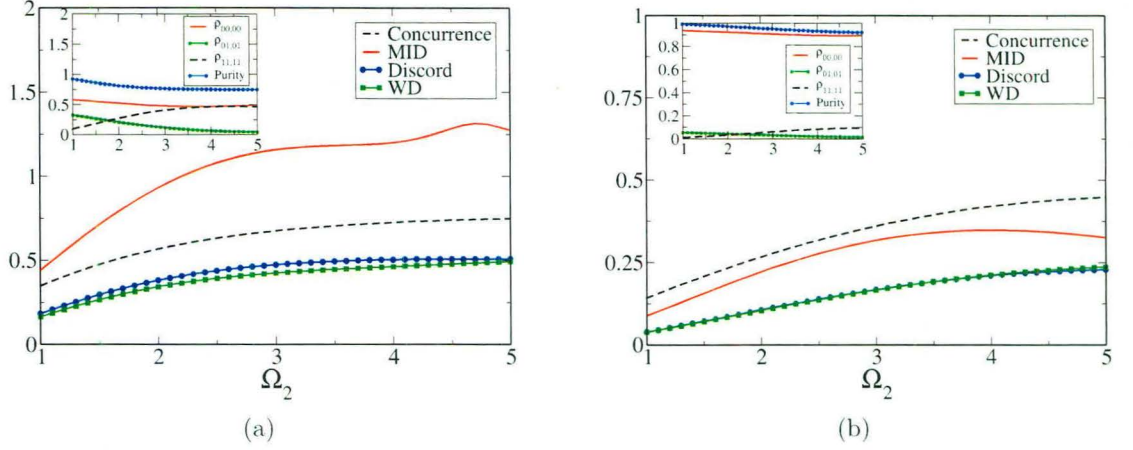
Figure 5.3: Fixed time ($t = 1.0$) MID (red continuous), QD (blue circles), QWD (green squares), and concurrence (black dashed) in the Ξ configuration as a function of the driving field strength Ω_2. The field detunings are $\Delta_1 = \Delta_2 = 0$, and the phases of the Rabi frequencies are $\phi_1 = \phi_2 = 0$. The level decay rates are $\Gamma_1 = 6.0$, $\Gamma_2 = 1.0$. SPA for this configuration requires that $\Omega_1 < \Gamma_1$. One driving field strength Ω_1 is fixed at (a) 1.5, and (b) 3.5. The inset shows the variation of population elements of the two-photon density matrix and its purity.

as an upper bound on the other information-theoretic quantum correlation, such as QD and QWD [41]. The evolution of MID with respect to concurrence can be varied using the control parameters. There are two specific parameter regimes that correspond to two different hierarchies in the photon correlation. In Figure 5.2, we consider the Ξ configuration in two specific regimes of the driving classical fields. The decay constants for the Ξ configuration are $\Gamma_1 = 6.0$, $\Gamma_2 = 1.0$. Hence, the driving field strengths are in the range $(\Omega_1, \Omega_2) < 6.0$. The detunings and the Rabi frequency phases have been set to zero. In Figure 5.2(a), we consider the regime where $\Omega_1 > \Omega_2$. Figure 5.2(b), corresponds to the field regime $\Omega_1 < \Omega_2$ $(\Omega_1 = 2.0, \Omega_2 = 5.0)$. For $\Omega_1 > \Omega_2$, MID is non-monotonic and forms an upper bound on concurrence at times $t > 1.0$. For the field regime $\Omega_1 < \Omega_2$ $(\Omega_1 = 2.0, \Omega_2 = 5.0)$, concurrence forms an upper bound on the information-theoretic correlation. We observe that the behavior of the correlation is closely related to the dynamics of the populations (inset of Figure 5.2). The non-monotonic behavior of MID is associated with the population difference in the two photon modes $|00\rangle$ and $|11\rangle$. It is clear from the plots that the sudden increase in MID occurs when the populations of the modes $|00\rangle$ and $|11\rangle$ are nearly equal. This could be due to the fact that the non-optimization of the correlation measure in MID is skewed in these regions. For cases where MID is monotonic with the other information-theoretic measures, the population is distinctly unequal. Observing the purity in these regimes, one can state that the monotonicity is observed at higher levels of purity [24].
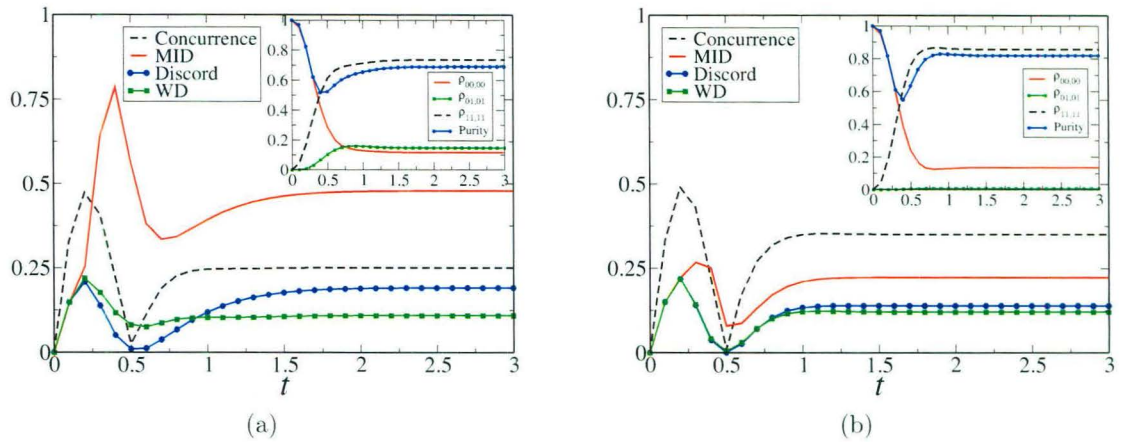
Figure 5.4: The time evolution for MID (red continuous), QD (blue circles), QWD (green squares) and concurrence (black dashed) for the Λ configuration. The field detunings are $\Delta_1 = \Delta_2 = 0$, and the phases of the Rabi frequencies are $\phi_1 = \phi_2 = 0$. The level decay rates are $\Gamma_1 = 1.0$, $\Gamma_2 = 6.0$. SPA for this configuration requires that $\Omega_1 < \Gamma_2$. The driving field strengths are thus taken as (a) $\Omega_1 = 4.0$, $\Omega_2 = 5.0$, and (b) $\Omega_1 = 4.0$, $\Omega_2 = 1.0$. The inset shows the evolution of population elements of the two-photon density matrix and its purity.

A similar dichotomy in behavior can also be observed for fixed time dynamics of the system if the interaction is allowed to vary across driving field strengths. In Figure 5.3, keeping the evolution time fixed ($t = 1.0$) and varying the two classical driving field strengths, a similar behavior of the correlation is observed. MID is greater than concurrence and non-monotonic at times where the population levels are equal with significantly lower purity (Figure 5.3(a)) as compared to regimes with unequal populations and higher purity where the information-theoretic quantum correlation and concurrence are monotonic (Figure 5.3(b)). Hence, we observe that the fixed time dynamics allows us to manipulate the correlation hierarchy by changing the ground-state driving field strength, Ω_1. The generation of correlation can be controlled by using parameter regions that allow higher purity in the output photon state.

Similar parameter regimes can also be generated in the Λ and V configuration as shown in Figure 5.4 and Figure 5.5, respectively. Interestingly, the monotonic nature of the correlation in the Λ and V configuration is different from that of the Ξ configuration. In the relatively high ground state excitation regime (high Ω_1) in Figure 5.4 we observe that the correlation attain steady-state values faster than in the Ξ configuration. The information-theoretic correlations are not monotonic at smaller times unlike in the Ξ configuration where concurrence, QD and QWD are always monotonic. There is a temporal discontinuity of concurrence around $t \approx 0.5$. The concurrence collapses to a small finite value before reviving sharply. The revival of entanglement is associated with an increase in discord in the
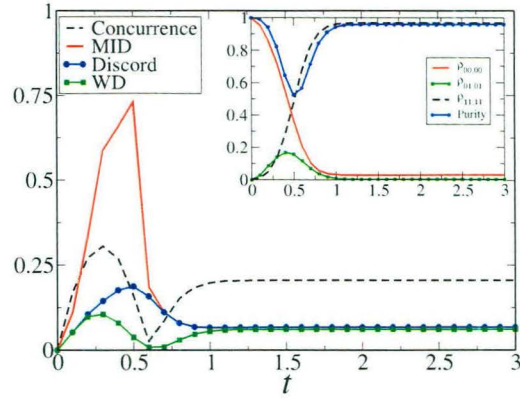
Figure 5.5: The time evolution for MID (red continuous), QD (blue circles), QWD (green squares) and concurrence (black dashed) for the V configuration. The field detunings are $\Delta_1 = \Delta_2 = 0$, and the phases of the Rabi frequencies are $\phi_1 = \phi_2 = 0$. The level decay rates are $\Gamma_1 = \Gamma_2 = 6.0$. SPA for this configuration requires that $\Omega_{1,2} < \Gamma_{1,2}$. The driving field strengths are $\Omega_1 = 2.0$, $\Omega_2 = 4.0$. The inset shows the evolution of population elements of the two-photon density matrix and its purity.

vicinity of the collapse. Such an interplay of the quantum correlation has been reported in many-body systems [42], as shown in Section 4.4.1. Other measures do not exhibit any discontinuity. At greater times ($t \geq 1.0$), the correlations are steady and weakly monotonic. The behavior of the correlation is again related to the population dynamics and purity of the density matrix as evident from Figure 5.4 and Figure 5.5.

The different behavior of the correlation monotonicity in the Λ and V configuration as compared to Ξ can be understood from the structural difference in the arrangement of the atomic levels. The highest excited level in the Ξ configuration is the metastable state with a decay rate $\Gamma_2 \approx 1.0$. In contrast, the Λ and V configurations have $\Gamma_2 \approx 6.0$. Hence, the evolution of population dynamics and the temporal steady state occurs faster ($t \approx 0.5$) than in the Ξ configuration. However, the steady state bounds of MID or concurrence in different parameter regimes are common to all the configurations. From Figure 5.5, we observe that the steady state population dynamics in the V system results in high purity. We get an overlap of all information-theoretic correlation bounded by a low concurrence. This is due to the uniform decay rates of the two excited levels leading to a uniform distribution of population probabilities between $|00\rangle$ and $|11\rangle$ with negligible population in $|01\rangle$.

In Figure 5.6, we present a comparative study of the behavior in the three configurations under investigation, by choosing a common parameter regime that satisfies the SPA for all configurations. We consider a region of moderately low values of the driving fields ($\Omega_1 = \Omega_2 = 2.0$) and another region of higher values ($\Omega_1 = \Omega_2 = 4.0$). Some of the aspects of the correlation that can be qualitatively studied are monotonicity, temporal steady state,
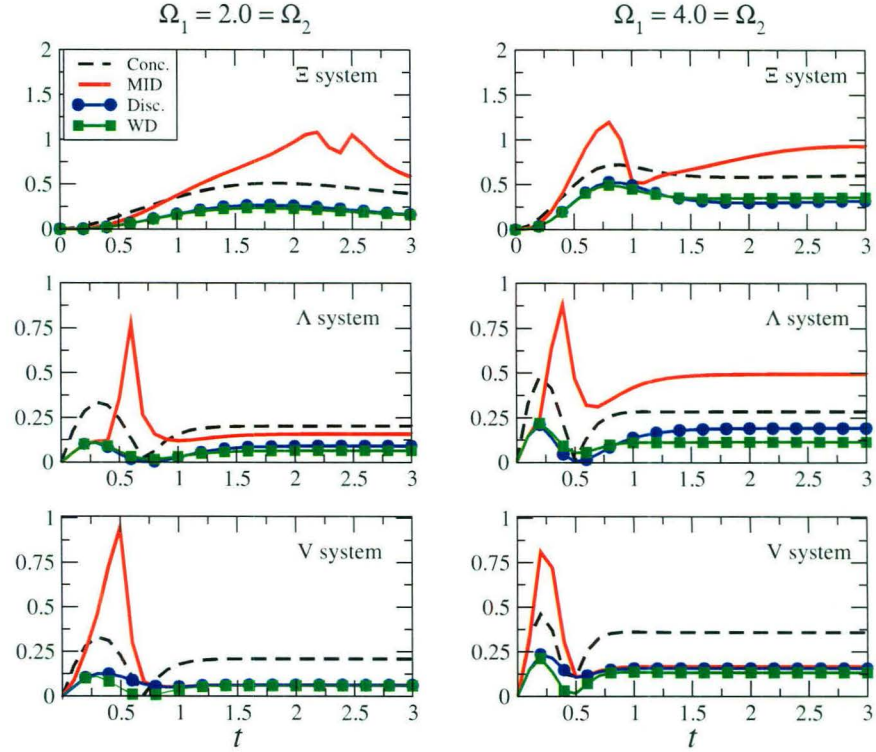
Figure 5.6: Time evolutions of MID (red continuous), QD (blue circles), QWD (green squares) and concurrence (black dashed) for all the three configurations, Ξ (top), Λ (middle) and V (bottom). The field detunings are $\Delta_1 = \Delta_2 = 0$, and the phases of the Rabi frequencies are $\phi_1 = \phi_2 = 0$. The chosen driving field strengths of $\Omega_1 = \Omega_2 = 2.0$ (left panel) and $\Omega_1 = \Omega_2 = 4.0$ (right panel) satisfy the SPA for all three configurations.

qualitative hierarchy and the purity of the two-photon density matrix.

The correlation dynamics of the Ξ system is dominated by the population dynamics of the photon state which evolves relatively slow due to the metastable nature of the highest excited level. We observe that the correlation do not achieve temporal steadiness in the observed times. This also leads to a lack of genuine monotonicity, with MID forming an upper bound in both the high and low field regimes. In comparison, the Λ and V systems have less stable excited states and hence achieve steady state correlation faster. For the Λ system, steady state quantum correlations are fairly monotonic with concurrence bound at lower fields and MID bound at higher fields. V systems have relatively low values of steady-state quantum correlation, as compared to the long time values in Ξ systems, with a concurrence bound at all fields.

5.5 Conclusion

In this chapter, we have exploited a semiclassical three-level atom interacting with two classical driving fields to generate a quantum correlated two-mode photon pair, with a dynamical control using the driving field parameters and the atomic level decay. Under certain physical approximations, we have investigated the dynamics of quantum correlation in the two-mode photon, using measures defined from the entanglement-separability criteria, such as concurrence and information-theoretic concepts, such as quantum discord, quantum work-deficit, and measurement induced disturbance, for three different configurations, namely, Ξ, Λ and V, of the three-level atom driven by two controlled external classical driving fields. The qualitative inter-relation of the quantum correlation based on the monotonicity, general hierarchy and steady state behavior are achieved using the control field parameters and the atomic decay terms.

The generation of mixed state quantum correlation is an important problem in the context of future implementation of quantum information tasks. The characterization of such quantum correlation in a possible experimentally realizable model is thus an worthwhile exercise. With developments in experimental techniques for measurement of quantum discord [43–45], the importance of generating and analyzing information-theoretic quantum correlation has manifestedly increased in recent times. The possibility of using well studied quantum optical systems, such as the three-level atom to generate, characterize and parametrically control mixed state quantum correlation is indeed an encouraging step in this direction.

[1] C. Cohen-Tannoudji, J. Dupont-Roc, and G. Grynberg, *Atom-Photon Interactions: Basic Processes and Applications*, John Wiley and Sons, New York (1992).

[2] R. Loudon and P.L. Knight, J. Mod. Opt. **34**, 707 (1987).

[3] J.I. Cirac and P. Zoller, Phys. Rev. Lett. **74**, 4091 (1995);

[4] D. Leibfried, R. Blatt, C. Monroe, and D. Wineland, Rev. Mod. Phys. **75**, 281 (2003);

[5] M. Riebe, H. Häffner, C.F. Roos, W. Hänsel, J. Benhelm, G.P.T. Lancaster, T.W. Körber, C. Becher, F. Schmidt-Kaler, D.F.V. James, and R. Blatt, Nature **429**, 734 (2004).

[6] B. Julsgaard, J. Sherson, J.I. Cirac, J. Fiurášek, and E.S. Polzik, Nature **432**, 482 (2004).

[7] D. Bouwmeester, J.-W. Pan, K. Mattle, M. Eibl, H. Weinfurter, and A. Zeilinger, Nature **390**, 575 (1997);

[8] D. Boschi, S. Branca, F. De Martini, L. Hardy, and S. Popescu, Phys. Rev. Lett. **80**, 1121 (1998).

[9] N. Gisin, G. Ribordy, W. Tittel, and H. Zbinden, Rev. Mod. Phys. **74**, 145 (2002).

[10] O. Kocharovskaya and Ya.I. Khanin, Sov. Phys. JETP **63**, 945 (1986);

[11] K.-J. Boller, A. Imamoglu, and S.E. Harris, Phys. Rev. Lett. **66**, 2593 (1991);

[12] M. Fleischhauer, A. Imamoglu, and J.P. Marangos, Rev. Mod. Phys. **77**, 633 (2005).

[13] M.O. Scully, S.-Y. Zhu, and A. Gavrielides, Phys. Rev. Lett. **62**, 2813 (1989).

[14] M.O. Scully and M.S. Zubairy, *Quantum Optics*, Cambridge Univ. Press, Cambridge (1997).

[15] S.N. Sandhya and V. Ravishankar, Phys. Rev. A **82**, 062301 (2010).

[16] R. Ghosh and L. Mandel, Phys. Rev. Lett. **59**, 1903 (1987).

[17] Y. Yang and F. Li, Phys. Rev. A **80**, 022315 (2009);

[18] S. Lee and H. Nha, Phys. Rev. A 82, 053812 (2010);

[19] S. Lee, S. Ji, H. Kim and H. Nha, Phys. Rev. A 84, 012302 (2011);

[20] A. Chatterjee, H.S. Dhar and R. Ghosh, J. Phys. B: At. Mol. Opt. Phys. 45, 205501 (2012) and references therein.

[21] R. Horodecki, P. Horodecki, M. Horodecki, and K. Horodecki, Rev. Mod. Phys. 81, 865 (2009).

[22] K. Modi, A. Brodutch, H. Cable, T. Paterek, and V. Vedral, Rev. Mod. Phys. 84, 1655 (2012).

[23] B.R. Mollow, Phys. Rev. A 12, 1919 (1975).

[24] H.S. Dhar, S. Banerjee, A. Chatterjee, and R. Ghosh, Ann. Phys. 331, 97 (2013).

[25] F.T. Hioe and J.H. Eberly, Phys. Rev. A 25, 2168 (1982).

[26] J.P. Marangos, J. Mod. Opt. 45, 471 (1998).

[27] J. Gea-Banacloche, Y.-Q. Li, S.-Z. Jin, and M. Xiao, Phys. Rev. A 51, 576 (1995).

[28] H. Tajalli, M. Mahmoudi, and A.Ch. Izmailov, Las. Phys. 13, 1370 (2003).

[29] I. Marzoli, J.I. Cirac, R. Blatt, and P. Zoller, Phys. Rev. A 49, 2771 (1994).

[30] K. Bergman, H. Theuer, and B.W. Shore, Rev. Mod. Phys. 70, 1003 (1998).

[31] R.J. Cook and H.J. Kimble, Phys. Rev. Lett. 54, 1023 (1985).

[32] B. Misra and E.C.G. Sudarshan, J. Math. Phys. 18, 756 (1977);

[33] C.B. Chiu, E.C.G. Sudarshan, and B. Misra, Phys. Rev. D 16, 520 (1977).

[34] J.F. Clauser, Phys. Rev. D 9, 853 (1974).

[35] S. Furuichi and M. Abdel-Aty, J. Phys. A: Math. Gen. 34, 6851 (2001);

[36] N. Alioui, N.A. Amroun-Frahi, and C. Bendjaballah, EPL 59, 28 (2002);

[37] M. Abdel-Aty, J. Phys. A: Math. Gen. 37, 1759 (2004).

[38] J. Javanainen, EPL 17, 407 (1992).

[39] M. Abazari, A. Mortezapour, M. Mahmoudi, and M. Sahrai, Entropy 13, 1541 (2011).

[40] L. Mandel, E. Wolf, *Optical Coherence and Quantum Optics*, Cambridge Univ. Press, Cambridge (1995).

[41] B.R. Rao, R. Srikanth, C.M. Chandrashekar and S. Banerjee, Phys. Rev. A 83, 064302 (2011).

[42] H.S. Dhar, R. Ghosh, A. Sen(De), and U. Sen, EPL 98, 30013 (2012).

[43] J.-S. Xu, X.-Y. Xu, C.-F. Li, C.-J. Zhang, X.-B. Zou, and G.-C. Guo, Nature Commun. 1, 7 (2010);

[44] B. Dakić, Y.O. Lipp, X. Ma, M. Ringbauer, S. Kropatschek, S. Barz, T. Paterek, V. Vedral, A. Zeilinger, Č. Brukner, and P. Walther, Nature Phys. 8, 666 (2012);

[45] M. Gu, H.M. Chrzanowski, S.M. Assad, T. Symul, K. Modi, T.C. Ralph, V. Vedral, and P.K. Lam, Nature Phys. 8, 671 (2012).

CHAPTER 6

Summary and Outlook

Science is a wonderful thing if one does not have to earn one's living at it. –

Albert Einstein

6.1 Summary

The fundamental objective of the work presented in the thesis has been to obtain theoretical results that would advance our understanding of quantum correlation in complex many-body and quantum optical systems. The analysis of quantum correlations, in particular genuine multipartite entanglement in large superposed quantum spin states, is of interest due to potential applications of such many-body systems in scalable quantum computation [1, 2] and communication [3] tools of the future. The analysis of ground state properties of quantum spin liquids such as resonating valence bond states, provides us with important insights about the scaling behavior of short-range and global quantum correlations and its relation with lattice geometry. Such results may be important from the perspective of understanding topological order in spin liquids [4]. Further, the analytic recursion technique, the density matrix recursion method, developed in the thesis, is a powerful method to overcome computational complexity in ground state estimation to obtain important nearest-neighbor and multiparty correlation properties, in the considered class of spin states. Another important result obtained in this thesis pertains to the analysis of information-theoretic quantum correlations in both quantum spin systems and quantum optical states. With major developments in experimental techniques to detect information-theoretic quantum correlation measures such as quantum discord [5], the importance of understanding many-body behavior and information protocols from the perspective of these measures, has increased drastically

in recent years [6]. In the following paragraph, we summarize the important results obtained in the thesis.

The primary findings presented in the thesis can be divided into two exclusive, but conceptually related components. The study conducted in Part I of the thesis has concentrated on the characterization of bipartite as well as multipartite entanglement in quantum spin-1/2 lattices, with resonating valence bond (RVB) ground states [7]. For two-legged ladder systems, we have performed a theoretical analysis of entanglement in the system, using concepts from quantum information theory, such as monogamy of entanglement and quantum telecloning. Moreover, along with numerical simulation, we have observed the variation of both bipartite and multipartite entanglement with the geometry of the quantum spin lattices [8]. In particular, we have shown that the geometry of an RVB lattice can play an important role in determining the entanglement content of multiparty quantum states and how one can use quantum information tools to obtain strong bounds on the values of entanglement. We have analytically proved that isotropic quantum spin-1/2 states, with RVB ground states and periodic or infinite boundaries, are always genuinely multipartite entangled [9], using the concept of strong-subadditivity of von Neumann entropy [10]. In the Chapter 3, we have addressed the important question of whether one can develop an efficient analytical method to investigate the behavior of bipartite and multipartite entanglement for large-sized quantum spin-1/2 lattices. For quantum spin ladders and isotropic states, the properties of RVB ground state can be suitably simulated in terms of its reduced density matrices, using a technique, called the density matrix recursion method [9, 11]. The method allows us to numerically calculate the bipartite and multipartite entanglement of quantum spin-1/2 lattices with as many as 140 spins. Further, using finite-size scaling, we could derive an estimation of the genuine multipartite entanglement in an infinite 2D isotropic quantum spin-1/2 lattice. The method can also be applied to distinguish odd and even legged RVB ladders.

In Part II of the thesis, we have looked at the dynamics of quantum correlations, defined both from the traditional entanglement-separability paradigm and the more contemporary information-theoretic perspective [6, 10]. We have taken up two quintessential models, the quantum spin-1/2 XY spin chain and a quantum optical three-level atom interacting with two multimode electromagnetic fields. We have investigated the bipartite quantum correlation in nearest-neighbor spin states, and the two photons generated in the atom-field interaction. For the XY spin model, we have observed that the dynamical behavior of nearest-neighbor bipartite entanglement [12] can be suitably characterized and quantified by the behavior of information-theoretic measures such as quantum discord and quantum work-deficit [13, 14]. Since there does not exist any unique operational relation between the two paradigmatic quantum correlation measures, we believe that our results can be an important step in es-

tablishing a connection between the two quantum correlation paradigms. The presented numerical data and analytical quantification allow for non-trivial study of quantum correlation in understanding many-body phenomena. In the Chapter 5, we have studied the dynamics of quantum correlation measures between two-photons generated from a three-level atom interacting with two driving fields. The results show how the dynamics and montonicity of different quantum correlation measures can be generated and controlled using the system parameters [15]. The results could be useful in experimental study of quantum correlation and its operational inter-relation.

To conclude, in this thesis, we have provided some new results in the broad direction set by our initial objective. However, there are many pertinent questions that can be addressed from this juncture that may further help to develop the theory of quantum correlation in many-body and quantum optical systems. The interface of the field of many-body physics and quantum optics is the emerging ground for exciting physics of the future, and provides important components for practical realization of quantum computation and communication. Below, we present a brief outlook of research directions that may emerge as consequence of some of the results obtained in thesis, and indicate some progress already made in associated areas in recent times.

6.2 Outlook

The primary focus of the thesis has been on the analysis of quantum correlations on discrete-level quantum systems in both quantum many-body and quantum optical systems. However, an important ingredient of contemporary research in quantum information and computation is the machinery of continuous variable (CV) quantum systems. As discussed in the Introduction in Section 1.5, the experimental tools of quantum optics allow the generation and manipulation of quantum correlated CV states with relative ease, as compared to discrete-level systems. This makes CV resources extremely useful in practical applications of quantum information protocols such as quantum teleportation and cryptography (for a review, see [16]). Hence, analysis of quantum correlation in CV optical states generated through atom-photon interactions, non-linear operations and heralded photon generation is of immense importance. Interesting results have been obtained from the analysis of entanglement and information-theoretic quantum correlations in basic prototypes of single atom and multimode photon interactions [17]. The characterization of entanglement and information-theoretic quantum correlation in CV systems can be further developed to achieve greater control in applications. For example, obtaining quantifiable measures of multipartite entanglement in multimode CV systems will be an important step in designing scalable computation and communication protocols and investigating robustness against decoherence. Another impor-

tant aspect of CV quantum systems is the generation of heralded entanglement and quantum state engineering using quantum optical operations that can be experimentally implemented using tools of linear quantum optics and parametric down converters [18–20].[1] The control of quantum correlations in these CV states allows one to tailor quantum states suitable for specific quantum operations. For example, there has been a lot of interest, in recent years, on the generation of controlled microscopic-macroscopic entangled CV states, such as qubit-cat states [21]. Such micro-macro entangled systems allow the possibility of transitioning of quantum properties such as quantum correlations from the discrete-level to the CV system, and can be of potential use in information protocols including error-correction, information storage and quantum metrology [21]. A lot of interesting physics can also be unravelled by investigating quantum phenomena in these systems such as coherent population trapping and Raman transitions [22], that can be exploited in designing optimal quantum control [23] and quantum networking [24].

Though a lot of interesting research has already been done in many-body systems [25], there are still some pertinent areas that need attention. Most of these questions arise from the computational complexity involved in ground state estimation and quantification of important physical quantities in large many-body systems such as spin liquids. In this respect, the application of analytical tools such as our density matrix recursion method may prove useful in investigating both classical and quantum correlation properties in specific large spin systems. The study of highly superposed, genuinely multipartite entangled states such as resonating valence bond states and cluster states may have direct application in designing fault-tolerant [1] and measurement-based [2] quantum computation models. Importantly, the quantification of entanglement in interesting quantum spin lattices [26] is not only desirable for designing and developing applicable quantum information tools but also for understanding critical phenomena and long-range order in many-body systems [4]. Control of many-body spin ensembles in quantum optical cavities, that allow for a nice interplay of discrete-level and CV quantum properties, is a crucial component in designing quantum information storage and retrieval devices [27].

---

[1]See Appendix A for a study on the generation of entangled states using superposed non-Gaussian operations and its application in CV quantum teleportation, across generated nonclassical channels.

[1] A.Y. Kitaev, Ann. Phys. (Leipzig) **303**, 2 (2003).

[2] H.J. Briegel, D.E. Browne, W. Dür, R. Raussendorf, and M. Van den Nest, Nature Phys. **5**, 19 (2009).

[3] A. Sen(De) and U. Sen, Phys. News **40**, 17 (2010) (arXiv:1105.2412).

[4] X. Chen, Z.-C. Gu, and X.-G. Wen, Phys. Rev. B **82**, 155138 (2010).

[5] J.-S. Xu, X.-Y. Xu, C.-F. Li, C.-J. Zhang, X.-B. Zou, and G.-C. Guo, Nature Commun. **1**, 7 (2010); B. Dakić, Y.O. Lipp, X. Ma, M. Ringbauer, S. Kropatschek, S. Barz, T. Paterek, V. Vedral, A. Zeilinger, Č. Brukner, and P. Walther, Nature Phys. **8**, 666 (2012); M. Gu, H.M. Chrzanowski, S.M. Assad, T. Symul, K. Modi, T.C. Ralph, V. Vedral, and P.K. Lam, Nature Phys. **8**, 671 (2012).

[6] K. Modi, A. Brodutch, H. Cable, T. Paterek, and V. Vedral, Rev. Mod. Phys. **84**, 1655 (2012).

[7] P.W. Anderson, Science **235**, 1196 (1987).

[8] H.S. Dhar and A. Sen(De), J. Phys. A: Math. Theor. **44**, 465302 (2011).

[9] H.S. Dhar, A. Sen(De) and U. Sen, Phys. Rev. Lett. **111**, 070501 (2013).

[10] R. Horodecki, P. Horodecki, M. Horordecki and K. Horodecki, Rev. Mod. Phys. **81**, 865 (2009).

[11] H.S. Dhar, A. Sen(De) and U. Sen, New J. Phys. **15**, 013043 (2013).

[12] A. Sen(De), U. Sen, and M. Lewenstein, Phys. Rev. A **72**, 052319 (2005).

[13] H.S. Dhar, R. Ghosh, A. Sen(De), and U. Sen, EPL **98**, 30013 (2012).

[14] H.S. Dhar, R. Ghosh, A. Sen(De), and U. Sen, Phys. Lett. A **378**, 1258 (2014).

[15] H.S. Dhar, S. Banerjee, A. Chatterjee, and R. Ghosh, Ann. Phys. **331**, 97 (2013).

[16] S.L. Braunstein and P. van Loock, Rev. Mod. Phys. **77**, 513 (2005).

[17] H.S. Dhar, A. Chatterjee, and R. Ghosh, J. Phys. B: At. Mol. Opt. Phys. **47**, 135501 (2014).

[18] M.S. Kim, J. Phys. B: At. Mol. Opt. Phys. **41**, 133001 (2008) and references therein.

[19] A. Chatterjee, H.S. Dhar, and R. Ghosh, J. Phys. B: At. Mol. Opt. Phys. **45**, 205501 (2012) and references therein.

[20] H.S. Dhar, A. Chatterjee, and R. Ghosh, *Generating continuous variable entangled states for quantum teleportation using a superposition of number-conserving operations*, arXiv:1312.6226.

[21] B. Vlastakis, G. Kirchmair, Z. Leghtas, S.E. Nigg, L. Frunzio, S.M. Girvin, M. Mirrahimi, M.H. Devoret, R.J. Schoelkopf, Science **342**, 607 (2013) and references therein.

[22] M.O. Scully and M.S. Zubairy, Quantum Optics, Cambridge Univ. Press, Cambridge (1997).

[23] A. Verdeny, A. Mielke, and F. Mintert, Phys. Rev. Lett. **111**, 175301 (2013).

[24] H. J. Kimble, Nature **453**, 1023 (2008).

[25] M. Lewenstein, A. Sanpera, V. Ahufinger, B. Damski, A. Sen(De), and U. Sen, Adv. Phys. **56**, 243 (2007); L. Amico, R. Fazio, A. Osterloh, and V. Vedral, Rev. Mod. Phys. **80**, 517 (2008).

[26] C.-Y. Huang, X. Chen, and F. Pollmann, *Detection of Symmetry Enriched Topological Phases*, arXiv:1312.3093 (2013).

[27] B. Julsgaard, J. Sherson, J.I. Cirac, J. Fiurášek, and E.S. Polzik, Nature **432**, 482 (2004); M. P. Hedges, J.J. Longdell, Y. Li, and M. J. Sellars, Nature **465**, 1052 (2010).

Generating continuous variable entangled states for quantum teleportation using a superposition of number-conserving operations

In this Appendix, we provide an example of the generation of bimode entangled continuous variable (CV) optical states, using a superposition of number-conserving operations. The generated states are of importance for application as efficient quantum channels in CV quantum teleportation protocols [1]. The results show the applicability of engineered nonclassical optical states in performing important quantum information protocols.[1]. The strength of the protocol lies in the fact that the considered operations can be conveniently performed in quantum optical experiments.

The wide use of Gaussian and non-Gaussian electromagnetic field states in practical applications of various quantum tasks and protocols renders the generation and investigation of these quantum states essential aspects of modern research. Entangled states generated using both linear and non-linear quantum optical operations have been extensively used in applications of quantum information [2] and communications [3]. The accessibility of continuous variable optical states in quantum information theory has led to success in implementing novel quantum tasks such as quantum teleportation [4, 5], quantum cryptography [6] and quantum memory [7, 8] (for reviews, see [9–11]).

A recent method of generating nonclassicality in electromagnetic field states is by the operation of photon addition ($\hat{a}^\dagger$) [12] and subtraction ($\hat{a}$) [13]. A remarkable aspect of the non-Gaussian photon addition and subtraction operation is the relative efficiency with which these operations can be experimentally realized using linear optical devices and parametric down-converters [14]. These non-Gaussian operations are known to enhance entanglement [15] and other forms of CV quantum information protocols [16]. An extension of similar non-

---

[1]The findings presented in the Appendix are based on the results obtained in [1]

Gaussian operations such as photon addition followed by photon subtraction and vice-versa have also been implemented [17, 18]. The study of nonclassical optical states generated by such non-Gaussian operations have received considerable theoretical attention in quantum optics [19, 20]. Further, the experimental implementation of these operations have been used to prove the canonical commutation relation [21]. An interesting operation based on the idea of non-Gaussian photon-addition and subtraction protocols is the number-conserving generalized superposition of products (GSP) of field annihilation $(\hat{a})$ and creation $(\hat{a}^{\dagger})$ operators of the form $s\hat{a}\hat{a}^{\dagger} + t\hat{a}^{\dagger}\hat{a}$, with $s^2 + t^2 = 1$ [20]. Such an operation is a generalization of the experimental scheme proposed to study the bosonic canonical commutation in optical fields [21]. Using an analysis of quasi-probability functions, quadrature squeezing and sub-Poissonian statistics, we have shown elsewhere that such an operation introduces nonclassicality in single-mode coherent and thermal states [20]. The GSP operation can be experimentally designed and hence applied to perform suitable quantum operations.

We analyze below the description of nonclassicality introduced by the GSP operation from a quantum information perspective and investigate if the generated nonclassicality can enhance the performance of specific quantum information tasks. The GSP operation is applied to single- and two-mode input optical field states such as coherent, thermal and squeezed vacuum state. We show that the nonclassicality introduced in the states can be suitably converted into bipartite mode-entanglement via linear interactions, using a beam-splitter. The generated entanglement is characteristic of the nonclassicality of the GSP operated state as beam-splitters do not generate entanglement for classical inputs [22]. For relatively low field intensities, the mode-entangled state can be truncated from an infinite-dimensional to a finite-dimensional states and nonclassicality can be measured in terms of the bimode entanglement. From the continuous-variable (CV) perspective, the nonclassical state can be investigated for potential use as a quantum channel in a CV quantum teleportation protocol. We follow the Braunstein and Kimble (BK) teleportation protocol [5] and calculate the success of the operation in terms of the average fidelity obtained in teleporting a single-mode coherent and squeezed state. The teleportation capacity of the single- and two-mode states are further investigated by studying the phase-quadrature correlations or the Einstein-Podolsky-Rosen (EPR) correlations generated in the GSP operated quantum channels. We demonstrate that the GSP operation enhances the average fidelity of teleportation over the non-operated two-mode squeezed state even at relatively low squeezing. Interestingly, the GSP operations reduces the average fidelity for teleportation in the coherent and thermal channels. This result is important from the consideration of noisy quantum channels. The teleportation fidelity pattern observed is consistent with the observed EPR correlations in the two-mode quantum channel.

A.1 Measure of nonclassicality

The action of number-conserving operators formed by the GSP of field annihilation ($\hat{a}$) and creation ($\hat{a}^\dagger$) operators of the type $s\hat{a}\hat{a}^\dagger + t\hat{a}^\dagger\hat{a}$, with $s^2 + t^2 = 1$, on field modes introduces distinct nonclassicality in the operated states [20]. From the perspective of quantum information theory, the nonclassicality of the GSP operated state is known to be manifested in terms of the bimodal quantum correlation it develops upon interaction of the modes via some linear optical device. Nonclassical states upon interacting with another mode via a beam splitter will develop finite bipartite quantum correlations [22].

We use entanglement as a measure of quantum correlation developed between the modes of a GSP operated state. The protocol adopted to measure the nonclassicality using entanglement is different for the case of single-mode and two-mode inputs. To calculate the entanglement of a single-mode GSP operated state we interact the single-mode output with a vacuum mode via a 50:50 beam splitter to generate a two-mode bipartite output [23]. The generated bimode entanglement is measured using logarithmic negativity (LN), defined in Section 1.3.3.4. For instances where a classical input state interacts with the vacuum mode, the entanglement is zero [22]. For two-mode input states that are initially classical, such as the coherent and thermal states, the GSP operation is applied separately on each mode. This operation does not introduce any entanglement in the two-mode output since the GSP operations are local. However, the two GSP operated modes are individually nonclassical and this can again be converted into two-mode entanglement using a linear optical device such as a 50:50 beam splitter. The bimode entanglement is then calculated using LN. For two-mode input states that are initially entangled, such as two-mode squeezed state, the GSP operation is globally applied to the two-modes without further interaction between the modes. A schematic of the GSP protocol and the linear interaction is given in Figure A.1.

A.2 GSP operated output states

Single-Mode Coherent State: Let us consider the GSP operation acting on a single-mode coherent state $|\psi\rangle_a \equiv |\alpha\rangle_a$. The single-mode (in mode a) GSP operated coherent state is given by

$$|\alpha'\rangle_a = \frac{1}{\sqrt{N}}(s\hat{a}\hat{a}^\dagger + t\hat{a}^\dagger\hat{a})|\alpha\rangle_a = \frac{1}{\sqrt{N}}(s|\alpha\rangle_a + (s+t)\,\alpha\hat{a}^\dagger|\alpha\rangle_a), \tag{A.1}$$

where N is the normalization constant. In terms of the displacement operator, $D_a(\alpha) = \exp(\hat{a}^\dagger\alpha - \hat{a}\alpha^*)$, a coherent state can be written as $|\alpha\rangle_a = D_a(\alpha)|0\rangle_a$ [24]. Hence we can write Equation (A.1) as

$$|\alpha'\rangle_a = \frac{1}{\sqrt{N}}(sD_a(\alpha) + \alpha(s+t)\hat{a}^\dagger D_a(\alpha))|0\rangle_a = \frac{D_a(\alpha)}{\sqrt{N}}(s|0\rangle_a + \alpha(s+t)[|1\rangle_a + \alpha^*|0\rangle_a]), \tag{A.2}$$
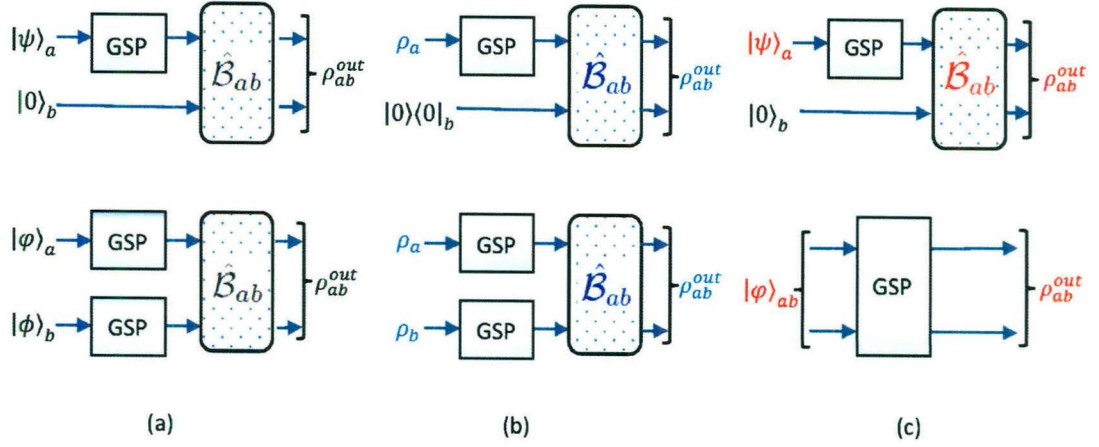
Figure A.1: Schematic of the generation of bipartite entangled output with single-mode state preparation (top row) and two-mode state preparation (bottom row) for (a) coherent input state, (b) thermal input state, and (c) squeezed input state. $\hat{\mathcal{B}}_{ab}$ represents the beam-splitter operation. The experimental scheme for performing a generalized superposition of products (GSP) operation is given in Reference [20].

where we have used the relation $D_a^\dagger(\alpha)\hat{a}^\dagger D_a(\alpha) = \hat{a}^\dagger + \alpha^*$. The single-mode GSP operated coherent state is then interacted with a vacuum mode via a 50:50 beam splitter. The two-mode output state after the interaction has the form $|\phi\rangle_{ab}^{out} = \hat{\mathcal{B}}_{ab}\,|\alpha'\rangle_a \otimes |0\rangle_b$, where $\hat{\mathcal{B}}_{ab} = \exp(\pi/2\{\hat{a}^\dagger\hat{b} - \hat{a}\hat{b}^\dagger\})$ is the beam-splitter operator with input ports a and b [see Figure A.1(a), top row]. Expanding the expression for $|\phi\rangle_{ab}^{out}$, we obtain

$$
\begin{aligned}
|\phi\rangle_{ab}^{out} &= \hat{\mathcal{B}}_{ab}\frac{D_a(\alpha)}{\sqrt{N}}\left[(s+(s+t)|\alpha|^2)|0\rangle_a|0\rangle_b + \alpha(s+t)|1\rangle_a|0\rangle_b\right] \\
&= \frac{\hat{\mathcal{B}}_{ab}D_a(\alpha)\hat{\mathcal{B}}_{ab}^\dagger}{\sqrt{N}}\hat{\mathcal{B}}_{ab}\left[p_1|0\rangle_a|0\rangle_b + p_2\hat{a}^\dagger|0\rangle_a|0\rangle_b\right],
\end{aligned}
\tag{A.3}
$$

where $p_1 = s + (s+t)|\alpha|^2$ and $p_2 = \alpha(s+t)$.

Using the fact that $\hat{\mathcal{B}}_{ab}D_a(\alpha)\hat{\mathcal{B}}_{ab}^\dagger = D_a(\alpha/\sqrt{2})D_b(-\alpha/\sqrt{2})$, and the beam-splitter relations, $\hat{\mathcal{B}}_{ab}\hat{a}^\dagger\hat{\mathcal{B}}_{ab}^\dagger = \frac{1}{\sqrt{2}}(\hat{a}^\dagger - \hat{b}^\dagger)$ and $\hat{\mathcal{B}}_{ab}\hat{b}^\dagger\hat{\mathcal{B}}_{ab}^\dagger = \frac{1}{\sqrt{2}}(\hat{b}^\dagger + \hat{a}^\dagger)$, we obtain

$$
|\phi\rangle_{ab}^{out} = \mathcal{A}_{ab}\left[p_1|0\rangle_a|0\rangle_b + p_2\hat{\mathcal{B}}_{ab}\hat{a}^\dagger\hat{\mathcal{B}}_{ab}^\dagger|0\rangle_a|0\rangle_b\right] = \mathcal{A}_{ab}\left[p_1|00\rangle_{ab} + \frac{p_2}{\sqrt{2}}(|01\rangle_{ab} + |10\rangle_{ab})\right],
\tag{A.4}
$$

where $\mathcal{A}_{ab} = D_a(\alpha/\sqrt{2})D_b(-\alpha/\sqrt{2})/\sqrt{N}$, $|ij\rangle_{ab} = |i\rangle_a|j\rangle_b$. The density matrix for the two-mode state given by Equation (A.4) is $\rho_{ab}^{out} = \mathcal{A}_{ab}\,\rho_{ab}^0\,\mathcal{A}_{ab}^\dagger$, where ρ_{ab}^0 is given by

$$
\rho_{ab}^0 = \begin{pmatrix} p_1^2 & p_1 p_2/\sqrt{2} & p_1 p_2/\sqrt{2} & 0 \\ p_1 p_2/\sqrt{2} & p_2^2/2 & p_2^2/2 & 0 \\ p_1 p_2/\sqrt{2} & p_2^2/2 & p_2^2/2 & 0 \\ 0 & 0 & 0 & 0 \end{pmatrix}.
\tag{A.5}
$$

The operator $\mathcal{A}_{ab}$ acts locally on the modes a and b, and hence cannot increase entanglement in the two-qubit density matrix in Equation (A.5). This reduces an infinite-dimensional bipartite interaction (in an infinite dimensional Fock state basis) to a two-qubit problem (in the $\{|0\rangle, |1\rangle\}$ basis). Hence, the entanglement can simply be calculated by computing the LN of the smaller two-qubit state.

Single-Mode Thermal State: A similar approach can be taken if the single-mode input is a classical thermal state. The thermal state is a maximally mixed state in the Fock state basis, and the thermal density matrix can be represented as

$$\rho_a^{th} = \frac{1}{1+\bar{n}} \sum_{n=0}^{\infty} \left(\frac{\bar{n}}{1+\bar{n}}\right)^n |n\rangle\langle n|_a, \tag{A.6}$$

where $\bar{n}$ is the average photon number. The action of GSP on the thermal field density matrix gives us the following operated state [20]:

$$\rho_a^{'\,th} = \frac{M^{-1}}{1+\bar{n}} \sum_{n=0}^{\infty} \left(\frac{\bar{n}}{1+\bar{n}}\right)^n (s + n(s+t))^2 |n\rangle\langle n|_a, \tag{A.7}$$

where M is the normalization constant. The GSP operated thermal state (A.7) is thus a mixed state in the infinite dimensional basis. It is known that the GSP operated single-mode thermal state has nonclassicality introduced by the operation and is non-Gaussian [20]. The GSP operated state (in mode a) is interacted with a vacuum state in mode b via a 50:50 beam splitter to generate a nonclassical two-mode output state. The operated two-mode state is of the form

$$\rho_{ab} = \hat{\mathcal{B}}_{ab} \left(\rho_a^{'\,th} \otimes |0\rangle\langle 0|_b\right) \hat{\mathcal{B}}_{ab}^{\dagger} = \hat{\mathcal{B}}_{ab} \left(\sum_{n=0}^{\infty} \frac{q_n}{n!} (\hat{a}^{\dagger})^n |00\rangle\langle 00|_{ab} (\hat{a})^n\right) \hat{\mathcal{B}}_{ab}^{\dagger}, \tag{A.8}$$

where $q_n = \left(\frac{M^{-1}}{1+\bar{n}}\right)\left(\frac{\bar{n}}{1+\bar{n}}\right)^n (s + n(s+t))^2$. The infinite-dimensional interaction between the two modes can be reduced by considering a truncated thermal state input with a low average photon number. For $\bar{n} \leq 0.1$, the two-mode density matrix (A.8) can be written as

$$\rho_{ab} = \hat{\mathcal{B}}_{ab} \left(q_0|00\rangle\langle 00|_{ab} + q_1\hat{a}^{\dagger}|00\rangle\langle 00|_{ab}\hat{a} + \frac{q_2}{2}(\hat{a}^{\dagger})^2|00\rangle\langle 00|_{ab}(\hat{a})^2\right) \hat{\mathcal{B}}_{ab}^{\dagger}, \tag{A.9}$$

where only the first three terms ($n = 0, 1, 2$) in the summation have been retained after truncation. Applying the unitary operation $\hat{\mathcal{B}}_{ab}$, we get the final two-mode output state as

$$\rho_{ab}^{out} = q_0|00\rangle\langle 00| + \frac{q_1}{2}\left(\hat{a}^{\dagger} - \hat{b}^{\dagger}\right)|00\rangle\langle 00|\left(\hat{a} - \hat{b}\right) + \frac{q_2}{4}\left(\hat{a}^{\dagger} - \hat{b}^{\dagger}\right)^2|00\rangle\langle 00|\left(\hat{a} - \hat{b}\right)^2. \tag{A.10}$$

The low average photon number ensures that the density matrix is effectively truncated to a discrete $3^{\otimes 2}$-dimensional bipartite system. Hence, the GSP operation generates a discrete two-mode nonclassical state.

Single-Mode Squeezed State: The GSP operation and subsequent conversion to a bimode entangled state for a single-mode squeezed state is similar to the approach adopted for coherent and thermal input states. However, the squeezed state is not a classical input state unlike the coherent and thermal inputs. The single-mode (in mode a) squeezed state can be written as

$$S(z)|0\rangle = \exp[(z/2)(\hat{a}^2 - \hat{a}^{\dagger 2})]|0\rangle_a = (1 - \lambda^2)^{1/4} \sum_{n=0}^{\infty} \frac{\sqrt{(2n)!}}{n!} \left(-\frac{\lambda}{2}\right)^n |2n\rangle_a, \quad (A.11)$$

where $S(z)$ is the squeezing operator, z is the squeezing parameter, and $\lambda \equiv \tanh z$. The GSP operated squeezed state is given by

$$\begin{aligned}
|\psi\rangle &= \frac{1}{\sqrt{N}}(s\hat{a}\hat{a}^{\dagger} + t\hat{a}^{\dagger}\hat{a})(1 - \lambda^2)^{1/4} \times \sum_{n=0}^{\infty} \frac{\sqrt{(2n)!}}{n!} \left(-\frac{\lambda}{2}\right)^n |2n\rangle_a \\
&= \sqrt{\frac{(1 - \lambda^2)^{1/2}}{N}} \sum_{n=0}^{\infty} \frac{\sqrt{(2n)!}}{n!} \left(-\frac{\lambda}{2}\right)^n \times (s + 2n(s + t))|2n\rangle_a, \quad (A.12)
\end{aligned}$$

where N is the normalization constant. The GSP operated single-mode squeezed state (in mode a) is interacted with a vacuum state (in mode b) via a 50:50 beam splitter. The resulting two-mode state is given by

$$|\psi'\rangle = \hat{B}_{ab} \sum_{n=0}^{\infty} c_n \frac{(\hat{a}^{\dagger})^{2n}}{\sqrt{(2n)!}}|0\rangle_a|0\rangle_b, \quad (A.13)$$

where $|0\rangle$ is the vacuum mode, $\hat{B}_{ab}$ is the beam-splitter operator, and

$$c_n \equiv \sqrt{\frac{(1 - \lambda^2)^{\frac{1}{2}}}{N}} \frac{\sqrt{(2n)!}}{n!} \left(-\frac{\lambda}{2}\right)^n (s + 2n(s + t)).$$

The infinite-dimensional two-mode output can be truncated by considering regimes where $\lambda \ll 1$. In the low λ regime, the GSP operated single-mode squeezed state can be written as

$$|\psi'\rangle = \hat{B}_{ab}(c_0|0\rangle_a|0\rangle_b + c_1(\hat{a}^{\dagger})^2|0\rangle_a|0\rangle_b), \quad (A.14)$$

where $c_0 = \sqrt{\frac{(1-\lambda^2)^{\frac{1}{2}}}{N}}s$, and $c_1 = -\sqrt{\frac{(1-\lambda^2)^{\frac{1}{2}}}{N}}\lambda(\frac{s}{2} + (s + t))$. Applying the beam-splitter operation, we get

$$|\psi'\rangle = c_0|00\rangle_{ab} + c_1\hat{B}_{ab}(\hat{a}^{\dagger})^2\hat{B}_{ab}^{\dagger}|00\rangle_{ab} = c_0|00\rangle_{ab} + \frac{c_1}{\sqrt{2}}|20\rangle_{ab} + \frac{c_1}{\sqrt{2}}|02\rangle_{ab} - c_1|11\rangle_{ab}. \quad (A.15)$$

The output two-mode density matrix is given by $\rho_{ab}^{out} = |\psi'\rangle\langle\psi'|$. The GSP operated two-mode output can be used as a quantum channel in CV teleportation.

Two-Mode Coherent State: For a classical coherent state input, the GSP operation is applied separately on the two modes a and b. Each mode operation is similar to the case for a single-mode input. The two modes than interact via the beam-splitter. The single-mode GSP

operated input coherent state is given by Equation (A.2). The beam-splitter interaction for the two modes can then be written as

$$|\phi\rangle_{ab}^{out} = \hat{B}_{ab} \frac{D_a(\alpha)D_b(\beta)}{\sqrt{N_1 N_2}} \left[(s_1|0\rangle_a +(s_1 + t_1)\alpha\left(|1\rangle_a + \alpha^*|0\rangle_a\right))(s_2|0\rangle_b \right.$$
$$\left. +(s_2 + t_2)\beta\left(|1\rangle_b + \beta^*|0\rangle_b\right)) \right]. \tag{A.16}$$

Here $|\alpha\rangle_a$ and $|\beta\rangle_b$ are the two input coherent states. The action of the beam splitter on the two-mode input can be described as

$$|\phi\rangle_{ab}^{out} = \mathcal{A}_{ab}^{local} \left[p_1'|0\rangle_a|0\rangle_b + p_2' \hat{B}_{ab}\hat{b}^\dagger\hat{B}_{ab}^\dagger|0\rangle_a|0\rangle_b + p_3'\hat{B}_{ab}\hat{a}^\dagger\hat{B}_{ab}^\dagger|0\rangle_a|0\rangle_b \right.$$
$$\left. +p_4' \hat{B}_{ab}\hat{a}^\dagger\hat{b}^\dagger\hat{B}_{ab}^\dagger|0\rangle_a|0\rangle_b \right], \tag{A.17}$$

where

$$\mathcal{A}_{ab}^{local} = \frac{\hat{B}_{ab}D_a(\alpha)D_b(\beta)\hat{B}_{ab}^\dagger}{\sqrt{N_1 N_2}} = \frac{1}{\sqrt{N_1 N_2}} \times D_a\left(\frac{\alpha}{\sqrt{2}}\right)D_b\left(\frac{-\alpha}{\sqrt{2}}\right)D_a\left(\frac{\beta}{\sqrt{2}}\right)D_b\left(\frac{\beta}{\sqrt{2}}\right),$$

and $p_1' = s_1 s_2 + s_1(s_2 + t_2)|\beta|^2 + s_2(s_1 + t_1)|\alpha|^2 + (s_1 + t_1)(s_2 + t_2)|\alpha|^2|\beta|^2$, $p_2' = s_1(s_2 + t_2)\beta + (s_1 + t_1)(s_2 + t_2)|\alpha|^2\beta$, $p_3' = s_2(s_1 + t_1)\alpha + (s_1 + t_1)(s_2 + t_2)|\beta|^2\alpha$, and $p_4' = \alpha\beta(s_1 + t_1)(s_2 + t_2)$. Hence, applying the beam-splitter operation in Equation (A.17), we obtain

$$|\phi\rangle_{ab}^{out} = \mathcal{A}_{ab}^{local} \left[p_1' + p_2'\frac{\hat{b}^\dagger + \hat{a}^\dagger}{\sqrt{2}} + p_3'\frac{\hat{a}^\dagger - \hat{b}^\dagger}{\sqrt{2}} + p_4'\left(\frac{\hat{a}^\dagger - \hat{b}^\dagger}{\sqrt{2}}\right)\left(\frac{\hat{b}^\dagger + \hat{a}^\dagger}{\sqrt{2}}\right) \right] |00\rangle_{ab}$$

$$= \mathcal{A}_{ab}^{local} \left[p_1''|00\rangle_{ab} + p_2''|01\rangle_{ab} + p_3''|10\rangle_{ab} - p_4''|02\rangle_{ab} + p_4''|20\rangle_{ab} \right], \tag{A.18}$$

where $p_1'' = p_1'$, $p_2'' = \frac{p_2' - p_3'}{\sqrt{2}}$, $p_3'' = \frac{p_2' + p_3'}{\sqrt{2}}$ and $p_4'' = \frac{p_4'}{\sqrt{2}}$.

The two-mode output density matrix can be written in the form $\rho_{ab}^{out} = \mathcal{A}_{ab}^{local} \rho_{ab}^0 \mathcal{A}_{ab}^{local\dagger}$. Hence, the entanglement between the two modes of the output is encoded in the density matrix ρ_{ab}^0, since the operation $\mathcal{A}_{ab}^{local}$ only acts locally on the two modes.

Two-Mode Thermal State: The two-mode GSP operated thermal input state can be calculated using an approach similar to that for the two-mode input coherent state. The two modes are operated separately and then interact via a 50:50 beam-splitter. The single-mode GSP operated thermal state can be written in a form similar to Equations (A.7) and (A.8). The action of the beam-splitter can be represented as the following:

$$\rho_{ab}^{out} = \hat{B}_{ab}\left(\rho_a'^{th} \otimes \rho_b'^{th}\right)\hat{B}_{ab}^\dagger = \hat{B}_{ab}\left(p_1^a p_1^b|00\rangle\langle00| + p_1^a p_2^b|01\rangle\langle01| + p_2^a p_1^b|10\rangle\langle10| \right.$$
$$\left. + p_2^a p_2^b|11\rangle\langle11|\right)\hat{B}_{ab}^\dagger, \tag{A.19}$$

where $p_{n+1}^x = \left(\frac{M_x^{-1}}{1+\bar{n}_x}\right)\left(\frac{\bar{n}_x}{1+\bar{n}_x}\right)^n (s^x + n(s^x + t^x))^2$ corresponds to the two input thermal modes $x = a, b$. We have used the low average photon number approximation and retained

terms up to $n < 2$. Since the most of the terms in the GSP operated density matrix are product of the probabilities from the single-mode GSP operated thermal state, the smaller probabilities can be neglected for low average photon number.

The two-mode output state generated, using Equation (A.19), is of the form

$$\rho_{ab}^{out} = p_1^a p_1^b |00\rangle\langle00| + p_1^a p_2^b \left(\frac{\hat{b}^\dagger + \hat{a}^\dagger}{\sqrt{2}}\right) |00\rangle\langle00| \left(\frac{\hat{b} + \hat{a}}{\sqrt{2}}\right) + p_2^a p_1^b \left(\frac{\hat{a}^\dagger - \hat{b}^\dagger}{\sqrt{2}}\right) |00\rangle\langle00|$$

$$\times \left(\frac{\hat{a} - \hat{b}}{\sqrt{2}}\right) + p_2^a p_2^b \left(\frac{\hat{a}^\dagger - \hat{b}^\dagger}{\sqrt{2}}\right) \left(\frac{\hat{b}^\dagger + \hat{a}^\dagger}{\sqrt{2}}\right) |00\rangle\langle00| \times \left(\frac{\hat{a} - \hat{b}}{\sqrt{2}}\right) \left(\frac{\hat{b} + \hat{a}}{\sqrt{2}}\right). \quad (A.20)$$

On solving, we get

$$\rho_{ab}^{out} = q_1' |00\rangle\langle00| + q_2' (|01\rangle\langle01| + |10\rangle\langle10|) - q_3' (|01\rangle\langle10| + |10\rangle\langle01|)$$

$$+ q_4' (|20\rangle\langle20| + |02\rangle\langle02| - |20\rangle\langle02| - |02\rangle\langle20|), \quad (A.21)$$

where $q_1' = p_1^a p_1^b$, $q_2' = \left(p_1^a p_2^b + p_2^a p_1^b\right)/2$, $q_3' = \left(p_2^a p_1^b - p_1^a p_2^b\right)/2$, and $q_4' = \left(p_2^a p_2^b\right)/2$.

The nonclassical properties of the two-mode output GSP operated thermal state can be obtained using the density matrix ρ_{ab}^{out} in Equation (A.21).

Two-Mode Squeezed State: The two-mode squeezed state is a well-known Gaussian state that can be experimentally prepared by applying suitable unitary operations on any pure Gaussian state. The initial squeezed state is an entangled two-mode state and hence it is not necessary to interact the modes via any active linear optical media as in the case of coherent or thermal input states. The two-mode squeezed state is an infinite dimensional superposition state of the two modes. The two-mode squeezed state can be written as,

$$|\psi\rangle_{ab} = \exp[r \, (\hat{a}^\dagger \hat{b}^\dagger - \hat{a}\hat{b})]|0\rangle_a|0\rangle_b = \sqrt{1 - \lambda^2} \sum_{n=0}^{\infty} \lambda^n |n\rangle_a|n\rangle_b, \quad (A.22)$$

where r is the squeezing parameter and $\lambda = \tanh r$. Applying the GSP operation on the two-mode squeezed state [see Figure A.1(c), bottom row], we obtain

$$|\psi'\rangle_{ab} = \sqrt{\frac{1}{N}} \, (s_1 \hat{a}\hat{a}^\dagger + t_1 \hat{a}^\dagger \hat{a})(s_2 \hat{b}\hat{b}^\dagger + t_2 \hat{b}^\dagger \hat{b}) \times \sqrt{1 - \lambda^2} \sum_{n=0}^{\infty} \lambda^n |n\rangle_a|n\rangle_b$$

$$= \sqrt{\frac{1 - \lambda^2}{N}} \sum_{n=0}^{\infty} \lambda^n \, [s_1 s_2 + n(s_1(s_2 + t_2) + s_2(s_1 + t_1) + n^2(s_1 + t_1)(s_2 + t_2))$$

$$\times |n\rangle_a|n\rangle_b], \quad (A.23)$$

where N is the normalization constant. The infinite dimensional two-mode squeezed state can be reduced by considering the low squeezing region. For $\lambda \ll 1$, the GSP operated squeezed state reduces to

$$|\psi'\rangle_{ab} = \sqrt{\frac{1 - \lambda^2}{N}} \, [s_1 s_2 |0\rangle_a|0\rangle_b + \lambda[s_1 s_2 + s_1(s_2 + t_2)$$

$$+ s_2(s_1 + t_1) + (s_1 + t_1)(s_2 + t_2)]|1\rangle_a|1\rangle_b]. \quad (A.24)$$

The GSP operated two-mode squeezed state in Equation (A.24) gives us the two-mode output pure state density matrix ρ_{ab}^{out} $(= |\psi'\rangle\langle\psi'|_{ab})$ that can be used to study its nonclassical properties.
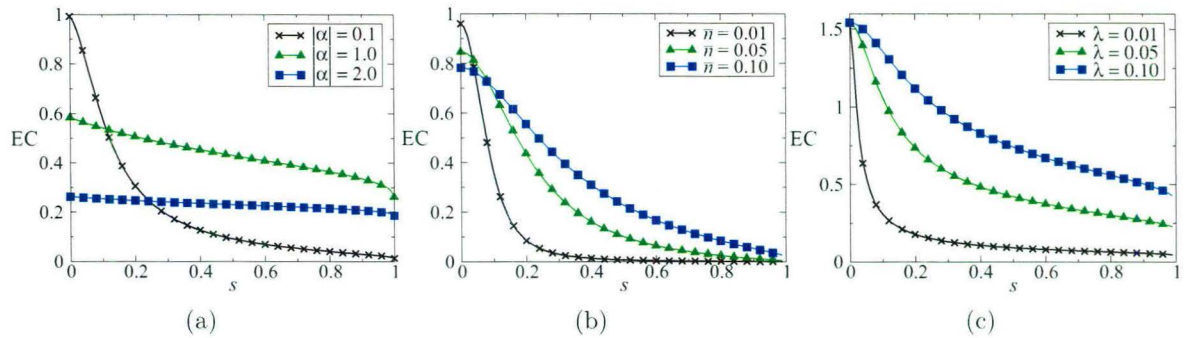

Figure A.2: Behavior of the entanglement (EC) for two-mode output states generated from GSP operated single-mode input states interacting with a vacuum mode. EC is shown as a function of the GSP operator parameter s for (a) different coherent state amplitudes ($|\alpha| =$ 0.1, 1.0, 2.0), (b) different thermal state average photon number ($\bar{n} = 0.01, 0.05, 0.10$) for a thermal input state, and (c) different values of $\lambda(\equiv \tanh z = 0.01, 0.05, 0.10)$, where z is the squeezing parameter of squeezed input state.
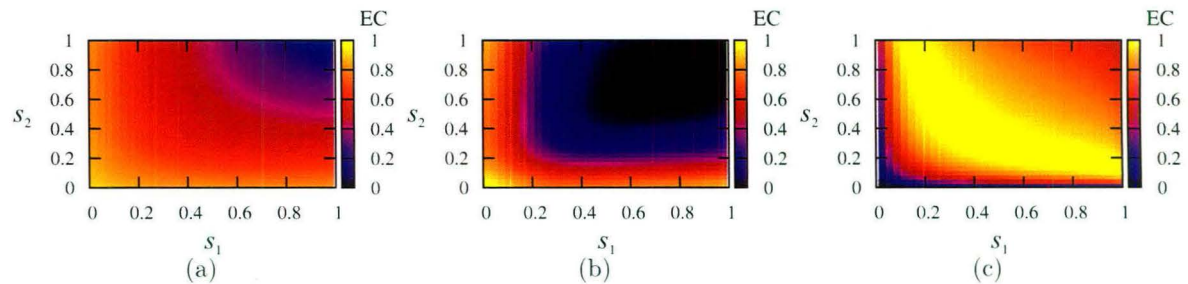

Figure A.3: Behavior of the entanglement (EC) for two-mode output states generated from GSP operated two-mode input states. The variation of EC is shown with respect to the two-mode GSP operator parameters s_1 and s_2 for (a) coherent state amplitudes $|\alpha| = |\beta| =$ 0.5, (b) thermal state average photon number, $\bar{n}_a = \bar{n}_b = 0.05$, and (c) for a fixed value of λ $(\equiv \tanh r) = 0.05$, where r is the squeezing parameter of the two-mode squeezed input.

A.3   Entanglement properties

We consider the low average field-intensity regime to reduce the infinite-dimensional state to a truncated discrete bipartite state. The entanglement $(EC)^2$ of the single- and two-mode GSP operated input states is calculated using logarithmic negativity. The parameters that

---

[2]The abbreviation EC is motivated from the definition of entanglement capacity, as introduced in Reference [23], for beam-splitter generated bimode entanglement.

control the entanglement of the single- and two-mode inputs after the GSP operation are the initial field parameters such as the amplitude of coherent state, average photon number of thermal input and the squeezing parameter of squeezed input along with the GSP operation parameter s.

Single-mode states: The variation of EC with GSP operation parameter s and field parameters for the single-mode input states is given in Figure A.2. In Figure A.2(a), we observe that high EC is observed for lower values of s and the amplitude ($|\alpha|$) of the coherent state input. The operation generates maximal entanglement at $s \approx 0$. For greater $|\alpha|$, the states have lower values of EC but are not very sensitive to variation in s. We also observe that for the truncated input thermal state [Figure A.2(b)], the EC is maximum at $s \approx 0$ and steadily decreases with increase in s. The maximum EC corresponds to the lowest average photon number ($\bar{n} = 0.01$). This is due to the fact that the classicality of coherent and thermal states increases with increase in average photon number. Figure A.2(c) gives us the variation of EC with $\lambda(= \tanh z)$, where z is the squeezing parameter of the input single-mode squeezed state. The maximum EC is obtained at $s > 0$, and the EC decreases with increasing s. The state is seen to be more entangled for higher values of λ for all values of s away from $s = 0$. Hence, the squeezed output with high λ is nonclassical for all ranges of the GSP operation. *Two-mode states*: The EC of the GSP operated two-mode coherent, thermal and squeezed input states is shown in Figure A.3. The variation of the EC is with respect to the two-mode GSP operation parameters s_1 and s_2 for fixed values of field parameters such as amplitude, average photon number and squeezing parameter for coherent, thermal and squeezed states, respectively. For coherent and thermal fields, we consider inputs with equal field parameters for both the input modes.

Figure A.3(a) gives us the variation of EC with the two-mode GSP operator parameters s_1 and s_2 for the two-mode coherent state input with equal amplitudes, $|\alpha| = |\beta| = 0.5$. We observe that low values of either of the mode operators s_1 and s_2 are sufficient for obtaining entangled states. The only region that produces low entanglement is the region corresponding to simultaneous high values of both s_1 and s_2 marked by the dark region in the color scheme of Figure A.3(a). In contrast, the plot for the EC of two-mode thermal state input in Figure A.3(b), with fixed photon number averages $\bar{n}_a = \bar{n}_b = 0.05$, shows that regions of relatively high entanglement is restricted to a small region along the two axes that correspond to the small values of s_1 ($\ll 1$) or s_2 ($\ll 1$). For other values of s_1 and s_2, the output state has very low entanglement. The behavior of EC for the two-mode squeezed state ($\lambda = 0.05$) is completely opposite of that of the two-mode thermal state. Figure A.3(c) shows that the EC remains high at most values of s_1 and s_2, dropping in the region of $s_1, s_2 \approx 0$. The two-mode input squeezed state, unlike the two-mode coherent and thermal state, is entangled prior to

the GSP operation. However, the GSP operation enhances the amount of entanglement [17] over the range of parameters s_1 and s_2.

Hence, it is seen that the GSP operated states under low-field truncation can generate highly entangled low-dimensional discrete systems. Under appropriate control of the input field parameters and GSP parameters, these states can be used as entangled photon source in quantum optical experiments and information tasks. The nonclassicality of the GSP generated states can also be utilized in the continuous variable regime.

A.4   Average fidelity of continuous variable teleportation

Quantum teleportation was originally devised as a quantum information protocol that involved sending an unknown qubit, from one party to another, across an entangled EPR channel shared between the two parties [25]. In the CV regime, the earliest example of teleportation was formulated for a one-dimensional phase-space particle [4]. A more practical version of the CV quantum teleportation was devised by Braunstein and Kimble [5], who proposed the teleportation of quadrature components of an electromagnetic field using finite degrees of correlation. CV quantum teleportation protocol is experimentally realizable [26].

The success of a teleportation protocol is indicated by the average fidelity of the teleported output state with the input state to be teleported. Perfect teleportation protocols with infinitely nonclassical resources have fidelity of 1. For teleporting a coherent state via a classical channel, the upper limit of average fidelity (F_{class}) is $\frac{1}{2}$ [27]. This is the maximum permissible fidelity without entangled quantum channels. In terms of quantum cloning, the lower limit for any quantum teleportation is set at $\frac{2}{3}$ [28], which is the fidelity of cloning (F_{clone}) an arbitrary state. Any protocol that delivers a fidelity greater than the classical fidelity, F_{class}, can be considered a basic quantum teleportation protocol. In the CV quantum teleportation formulated by BK, the two-mode quantum channel and the input state to be teleported are described by a joint Wigner function $W(\gamma, \xi, \eta) = W_{in}(\gamma) \otimes W_{ch}(\xi, \eta)$. The Wigner function description can be more clearly stated in terms of the symmetrically ordered characteristic function [24, 29]. The average fidelity of BK quantum teleportation is [30]

$$F = \frac{1}{\pi} \int d^2\gamma \; \chi_{in}(\gamma)\chi_{out}(-\gamma), \qquad (A.25)$$

where $\chi_{out}(\gamma) = \chi_{in}(\gamma)\chi_{ch}(\gamma^*, \gamma)$ [31]. χ_{in} and χ_{ch} being the characteristic functions of the input state to be teleported and the two-mode quantum channel, respectively.

An important part of the calculation of the average fidelity of CV teleportation is to obtain the characteristic function of the two-mode nonclassical teleportation channel. The characteristic functions of the bipartite entangled GSP operated single-mode and two-mode input states are formulated below.
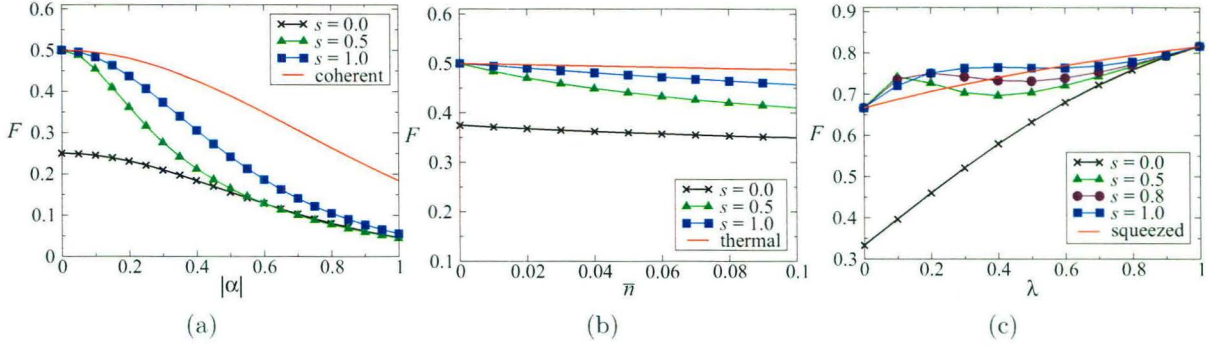
(a)   (b)   (c)

Figure A.4: Behavior of the average fidelity (F) of teleporting a single-mode coherent state (of any amplitude) using two-mode output states generated from GSP operated single-mode input states interacting with a vacuum mode. F is shown as a function of (a) the amplitude ($|\alpha|$) of a coherent input state, (b) the average photon number ($\bar{n}$) of a thermal input state, and (c) λ ($= \tanh z$), where z is the squeezing parameter of a squeezed input state. The plots are for different values of the GSP operator parameter: $s = 0$ (black crosses), $s = 0.5$ (green triangles), $s = 0.8$ (brown circles) [shown only in (c)], $s = 1.0$ (blue squares), and unoperated states (red continuous line).

Single-mode states: We have considered three different single-mode input states for the GSP operation, namely, coherent, thermal and squeezed states. These input states undergo GSP operation and then interact via a symmetric beam-splitter with a vacuum mode to generate a two-mode bipartite entangled output state, as shown in Section A.2. The generated two-mode nonclassical states are used as a quantum channel in CV teleportation.

For a single-mode GSP operated coherent state coupled to a vacuum mode, the characteristic function of the state is given by

$$
\begin{aligned}
\chi_{ch}(\xi, \eta) &= N^{-1}\left(s^2 + (s+t)^2|\alpha|^2\{1 + (\alpha + X)(\alpha^* - X^*)\} + s(s+t)\{\alpha(\alpha^* - X^*) \right. \\
&+ \left. \alpha^*(\alpha + X)\}\right) \exp\left[\frac{1}{2}(|X|^2 + |Y|^2)\right] \exp(\alpha^* X - \alpha X),
\end{aligned} \tag{A.26}
$$

where $X = (\xi - \eta)/\sqrt{2}$ and $Y = (\xi + \eta)/\sqrt{2}$. N is the normalization constant given by $[s^2 + (s+t)(3s+t)|\alpha|^2 + (s+t)^2|\alpha|^4]$. The fidelity can be calculated using Equation (A.25).

For the GSP operated single-mode thermal state, the characteristic function can be calculated using the density matrix expression for the truncated GSP operated two-mode density matrix given by Equation (A.10). The characteristic function of any two-mode state with a density matrix ρ is given by

$$
\chi(\xi, \eta) = \sum_{n',n,m',m=0}^{\infty} \rho_{nm,n'm'} \langle nm|\hat{D}_a(\xi)\hat{D}_b(\eta)|n'm'\rangle, \tag{A.27}
$$

where $\hat{D}_a$ is the displacement operator acting on mode a. The detailed derivation of the characteristic function for any two-mode density matrix in the number state basis is shown

in Appendix A of Reference [1].

The characteristic function of a single-mode GSP operated squeezed state interacting with a beam-splitter can be written as

$$
\begin{aligned}
\chi(\xi, \eta) &= N^{-1}\big(s^2 + s(s+t)\{2p_0 - p_1(X'^{*2} + X'^2)\} + s^2(s+t)^2\{p_0^2 - p_0 p_1(X'^{*2} + X'^2) \\
&\quad + p_1^2(1 - 2|X'|^2 + \frac{|X'|^4}{2}\}\big) \exp\left[-\frac{1}{2}(|X'|^2 + |Y|^2)\right],
\end{aligned}
\tag{A.28}
$$

where $X = (\xi - \eta)\sqrt{2}$ and $Y = (\xi + \eta)\sqrt{2}$. $X' = X \cosh z - Y^* \sinh z$. $p_0 = \sinh^2 z$ and $p_1 = \sinh z \cosh z$. The normalization constant is $N = s^2 + 2s(s+t)p_1 + (s+t)^2(p_1^2 + 2p_2^2)$. The symbols s, t and z have the usual meanings as in Section A.2.

Two-mode states: We again consider three two-mode input states in our analysis. The first two are the classical two-mode GSP operated coherent and thermal input state interacting via a symmetric beam splitter to generate a bimode entangled two-mode nonclassical output. The third is the GSP operated two-mode squeezed state.

For a two-mode coherent input state, the derivation of the characteristic function of the GSP operated output bimode state, given by Equation (A.18), is given in Appendix B in Reference [1]. Further, the characteristic function of the two-mode GSP operated thermal state and squeezed state is derived in Appendix A and B in Reference [1], respectively. The average fidelity of teleportation of a state across the nonclassical two-mode GSP operated coherent input can be calculated using Equation (A.25).

In the following subsections, we consider the CV quantum teleportation of two single-mode states: (a) single-mode coherent state, and (b) single-mode squeezed state.

A.4.1   Teleporting a single-mode coherent state

We consider the quantum teleportation of a single-mode coherent state using the GSP operated nonclassical two-mode states, discussed in Section A.2, as the teleportation channel. The teleportation is conducted using the BK protocol. The symmetrically ordered characteristic function of the input coherent state $|\alpha\rangle$ is

$$
\chi^{coh}(\gamma) = \exp\left[-\frac{1}{2}|\gamma|^2\right] \exp(\alpha^* \gamma - \alpha \gamma^*).
\tag{A.29}
$$

The fidelity of CV quantum teleportation of a coherent state input is independent of the amplitude of the state to be teleported.

Let us consider the average fidelity of quantum teleporting a single-mode coherent state via a two-mode output generated from a GSP operated single-mode input interacting with vacuum mode. The characteristic functions of the GSP operated single-mode coherent, thermal and squeezed inputs interacting with vacuum are given by Equations (A.26), (A.27)
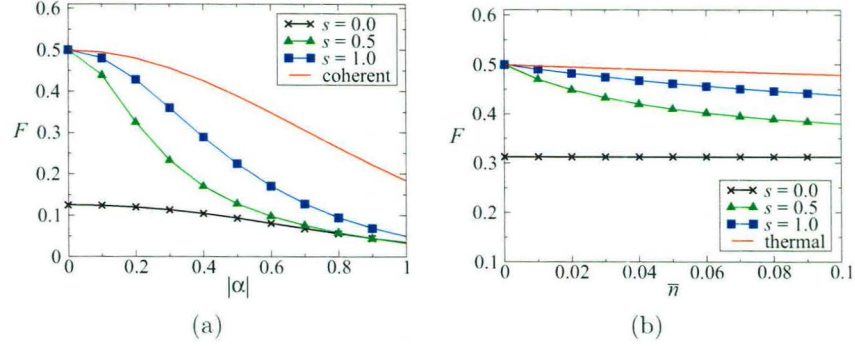
Figure A.5: Behavior of the average fidelity (F) of teleporting a single-mode coherent state (of any amplitude) using a two-mode output generated from GSP operated two-mode input states. F is shown as a function of (a) the amplitude ($|\alpha|$) of a coherent input state, and (b) the average photon number ($\bar{n}$) of a thermal input state. The plots are for different symmetric values of the GSP operator parameters, $s_1 = s_2 = s$: $s = 0$ (black crosses), $s = 0.5$ (green triangles), $s = 1.0$ (blue squares), and unoperated states (red continuous line).

and (A.28), respectively. Figure A.4 shows the variation of the average fidelity (F) with changing field parameters of the quantum channel at different values of the GSP operation parameter s. We observe in Figure A.4(a), that for the GSP operated single-mode coherent state channel, the maximum average fidelity is $F_{max} \approx 0.5$. This value is the classical upper limit of teleportation, F_{class} and is well below the the threshold of cloning fidelity. The maximum fidelity is achieved at very low values of the channel field amplitude $|\alpha|$ and is independent of the GSP operator parameter s. Interestingly, the decay of F with increasing $|\alpha|$ for the GSP operated state is always bounded above by the non-operated bipartite state. Hence, the GSP operations is able to reduce the average classical fidelity. Figure A.4(b) gives us the fidelity for the GSP operated single-mode thermal state channel for varying average photon number. The maximum fidelity, $F_{max} \approx 0.5$, which, again, is the threshold for classical teleportation.

The enhancement of the average fidelity, under the operation, is observed for the GSP operated single-mode squeezed channel. From Figure A.4(c), we can observe that a high fidelity, $F_{max} \approx 0.816$, can be achieved for highly squeezed states. This value breaches the threshold for quantum cloning. Even at the low squeezing regime, GSP operation can highly enhance the average fidelity. For low squeezing parameters, $\lambda \leq 0.2$, the GSP operated states at $s \geq 0.5$ offer enhanced fidelity values, $F \geq 0.74$, which is again higher than the cloning fidelity, $F_{clone} = \frac{2}{3}$, and also higher than the non-operated squeezed channel.

Let us now consider the average fidelity of teleporting a single-mode coherent state via a bipartite two-mode output generated from a GSP operated two-mode input state. The average fidelity (F) for the two-mode GSP operated coherent and thermal state channel
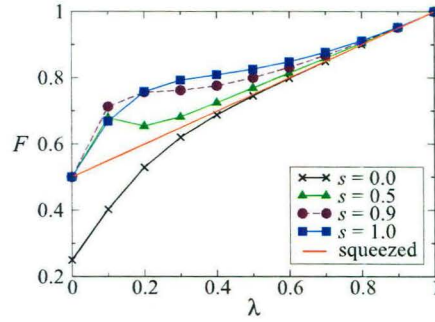
Figure A.6: Behavior of the average fidelity (F) of teleporting a single-mode coherent state (of any amplitude) using a two-mode output generated from a GSP operated two-mode input squeezed state. F is shown as a function of λ ($= \tanh r$), where r is the squeezing parameter of the squeezed state input. The plots are for different symmetric values of the GSP operator parameters, $s_1 = s_2 = s$: $s = 0$ (black crosses), $s = 0.5$ (green triangles), $s = 0.9$ (brown circles), $s = 1.0$ (blue squares), and unoperated states (red continuous line).

can be observed in Figure A.5 as a function of the field parameters $|\alpha|$ and $\bar{n}$. We have considered symmetric field parameters for the two modes. The behavior of the average fidelity for the two-mode case is similar to the results for the single-mode fidelity. The GSP operation on two-mode thermal and coherent state reduces the average classical fidelity across the channels. Figure A.6 gives us the average fidelity (F) for a two-mode GSP operated squeezed state channel with varying field parameter λ, where $\lambda = \tanh r$ and r is the two-mode squeezing parameter. F is calculated for different values of the GSP operator parameter s. The maximum fidelity, $F_{max} = 1$ is achieved for all values of s at high squeezing ($\lambda = 1$). In the low-squeezing regime, for $\lambda \leq 0.2$, the highest fidelity, $F \approx 0.76$ is achieved at $s = 0.9$. At higher squeezing, $0.2 \leq \lambda \leq 0.8$, the highest fidelity, $F \approx 0.91$ is achieved at $s = 1.0$. Figure A.7 shows the variation of average fidelity F with the two-mode GSP operator
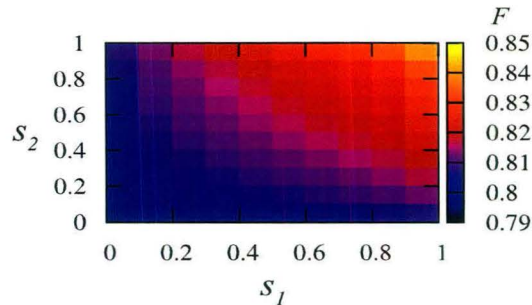

Figure A.7: Behavior of the average fidelity (F) of teleporting a single-mode coherent state (of any amplitude) using a two-mode output generated from a GSP operated two-mode input squeezed state. F is shown as a function of the two-mode GSP operator parameters s_1 and s_2, with λ ($= \tanh r$) fixed at 0.6, where r is the squeezing parameter of the two-mode squeezed input state.
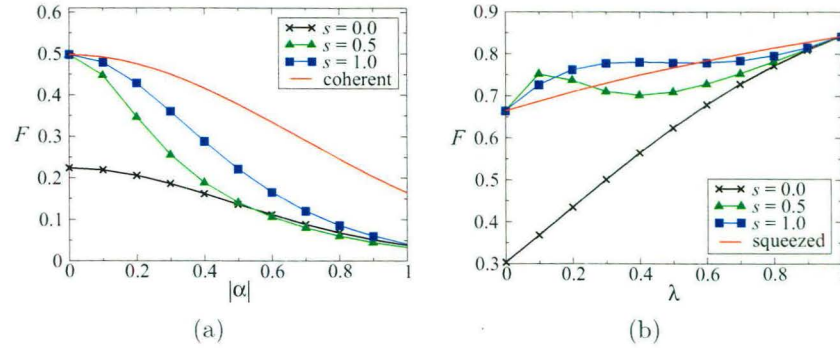
Figure A.8: Behavior of the average fidelity (F) of teleporting a single-mode squeezed state with squeezing parameter, $r' = 0.1$, using a two-mode output generated from GSP operated single-mode input states interacting with vacuum mode. F is shown as a function of (a) the amplitude ($|\alpha|$) of a coherent input state, and (b) λ (= $\tanh z$), where z is the squeezing parameter of a squeezed input state. The plots are for different values of the GSP operator parameter: $s = 0$ (black crosses), $s = 0.5$ (green triangles), $s = 1.0$ (blue squares), and unoperated states (red continuous line).

parameters s_1 and s_2 applied on a two-mode squeezed state, with $\lambda = 0.6$. The average fidelity is independent of the amplitude of the single-mode coherent state to be teleported. F varies over a small range of values (0.79–0.85) for different values of s_1 and s_2, with the higher range corresponding to higher values of the GSP operator parameters. Hence, for a fixed squeezing, λ, the fidelity is not very sensitive to the operator parameters.

A.4.2 Teleporting a single-mode squeezed state

We now consider the quantum teleportation of single-mode squeezed vacuum state using the GSP operated two-mode output states. The symmetrically ordered characteristic function of the input squeezed vacuum state, $\exp[(r'/2)(\hat{a}^2 - \hat{a}^{\dagger 2})]|0\rangle$ is

$$\chi_{sqz}(\gamma) = \exp\left[-\frac{\cosh 2r'}{2}|\gamma|^2 - \frac{\sinh 2r'}{4}(\gamma^2 + \gamma^{*2})\right]. \tag{A.30}$$

For the teleportation of the single-mode squeezed state, we consider the single- and two-mode GSP operated coherent and squeezed state quantum channels. The average fidelity of teleportation is not independent of the squeezing parameter r' of the squeezed state to be teleported. Figure A.8 shows the average fidelity (F) of teleporting a single-mode squeezed state, with squeezing parameter r'=0.1, using a GSP operated single-mode coherent and squeezed state input. For a single-mode GSP operated coherent state, as shown in Figure A.8(a), the maximum average fidelity is $F_{max} \approx 0.5$, which is the threshold for classical fidelity, F_{class}. The average fidelity is again bounded by the non-operated input state. The GSP operation again reduces the average fidelity of teleportation. Figure A.8(b) shows the
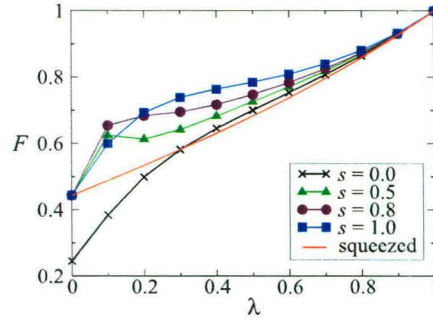
Figure A.9: Behavior of the average fidelity (F) of teleporting a single-mode squeezed state with squeezing parameter, $r' = 0.5$, using a two-mode output generated from a GSP operated two-mode squeezed input state. F is shown as a function of λ ($= \tanh r$), where r is the squeezing parameter of the input state. The plots are for different symmetric values of the GSP operator parameters, $s_1 = s_2 = s$: $s = 0$ (black crosses), $s = 0.5$ (green triangles), $s = 0.8$ (brown circles), $s = 1.0$ (blue squares), and unoperated states (red continuous line).

average fidelity of teleportation using a single-mode GSP operated squeezed state channel. The maximum average fidelity is $F_{max} = 0.842$, at $\lambda = 1$, for highly squeezed channels. At low squeezing limits, the GSP operations enhance the average fidelity over the non-operated state. For $\lambda \leq 0.2$, the highest fidelity is 0.752 for $s \approx 0.5$. Figure A.9 shows the average fidelity (F) of teleporting a single-mode squeezed state, with squeezing parameter $r' = 0.5$, using a GSP operated two-mode squeezed state input. The maximum fidelity is $F_{max} = 1$, achieved for highly squeezed channels with $\lambda \approx 1.0$. At the mid-squeezing range, in the vicinity of $\lambda \approx 0.5$, we observe that all GSP operated states have enhanced average fidelity over the non-operated state, with the highest fidelity, $F = 0.785$, achieved at $s = 1.0$. The behavior of the average fidelity for a two-mode GSP operated coherent channel is similar to the single-mode coherent channel.

We observe that the GSP operation, while enhancing the teleportation fidelity for the nonclassical two-mode squeezed input state channel, reduces the fidelity for channels formed by GSP operated classical thermal and coherent input states. In other words, the GSP protocol enhances efficient quantum teleportation while simultaneously reducing the low fidelity due to classical channels which could arise due to noise. Due to the linear nature of the characteristic function, a noisy quantum channel can often be simulated using a low intensity thermal channel in the characteristic function of the two-mode channel [32]. Hence reduction of fidelities across classical channel will enhance the quantum fidelity of the noisy quantum teleportation protocol.
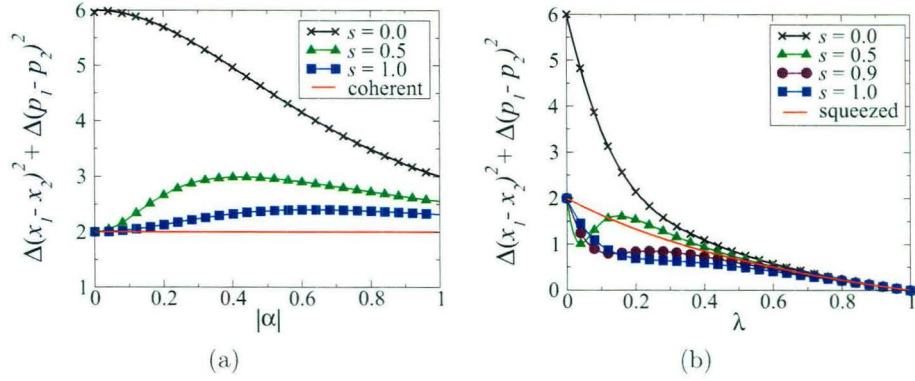
Figure A.10: Behavior of EPR correlations, $\Delta(\hat{x}_1 - \hat{x}_2)^2 + \Delta(\hat{p}_1 + \hat{p}_2)^2$, for GSP operated (a) two-mode input coherent state, and (b) two-mode input squeezed state, with respect to varying (a) coherent field amplitude, and (b) λ ($= \tanh r$) where r is the squeezing parameter, for different values of the GSP operator parameter: $s = 0$ (black crosses), $s = 0.5$ (green triangles), $s = 0.9$ (brown circles) [not shown in (a)], $s = 1.0$ (blue squares), and unoperated states (red continuous line).

A.5 EPR correlations

The success of the CV teleportation protocol is dependent on the correlations developed between the phase-quadrature components of the GSP operated two-mode output states. These correlations also known as Einstein-Podolosky-Rosen correlations can be quantified in terms of the variance of the differences of the quadrature components of the two modes. The quadrature operators are defined as

$$\hat{x}_1 = \frac{1}{\sqrt{2}}(\hat{a} + \hat{a}^\dagger), \ \hat{p}_1 = \frac{1}{i\sqrt{2}}(\hat{a} - \hat{a}^\dagger), \ \hat{x}_2 = \frac{1}{\sqrt{2}}(\hat{b} + \hat{b}^\dagger), \ \hat{p}_2 = \frac{1}{i\sqrt{2}}(\hat{b} - \hat{b}^\dagger), \qquad (A.31)$$

for the two modes a and b, respectively. The EPR correlation is then defined as the total variance of the operators $\hat{x}_1 - \hat{x}_2$ and $\hat{p}_1 + \hat{p}_2$. The correlation for the EPR state [33], which is a maximally entangled state, is $\Delta(\hat{x}_1 - \hat{x}_2)^2 = \Delta(\hat{p}_1 + \hat{p}_2)^2 = 0$. For a two-mode vacuum state, the EPR correlation is $\Delta(\hat{x}_1 - \hat{x}_2)^2 + \Delta(\hat{p}_1 + \hat{p}_2)^2 = 2$. For states with classical EPR correlation the variance difference is always greater than 2. Figure A.10 gives us the variance of the EPR operator for the two-mode GSP operated coherent and squeezed state inputs. From the values of the variance, with changing field parameters, it is evident that the two-mode GSP operated coherent state is not EPR correlated at any field value. The variance for the two-mode non-operated coherent state is constant at 2.0. The EPR correlation patterns throw light into the teleportation fidelity plots of the two-mode coherent state [Figure A.5(a) and A.8(a)]. The maximum fidelity achieved for low $|\alpha|$, $F_{max} = 0.5$, which is at the upper limit of teleportation using unentangled quantum channels ($F_{class} = \frac{1}{2}$) and below the cloning fidelity ($F_{clone} = \frac{2}{3}$). This is explained by the fact that the two-mode

state is not EPR correlated for all $|\alpha|$ and has no quadrature entanglement. Hence, the GSP operation is unable to introduce phase-quadrature entanglement in the GSP operated coherent state even though low intensity truncated states are entangled. In comparison, Figure A.10(b) shows that the two-mode squeezed state is strongly EPR correlated, with the GSP operation enhancing the correlation. This results in high teleportation fidelity above the cloning fidelity limit even for relatively low squeezing values (λ). The variances in the EPR quadrature operators are equal and behave as $\exp[-2r]$, where r is the squeezing parameter. Hence, at maximum squeezing the GSP operated state is maximally EPR correlated.

A.6 Discussion

In the Appendix, we have used a generalized superposition of products of annihilation and creation operators to engineer nonclassical continuous variable field states. We have applied the GSP operator along with linear optical interaction on single- and two-mode CV states such as coherent, thermal and squeezed states to obtain entangled two-mode output states. By considering low field intensities, the infinite-dimensional CV field inputs can be truncated to form discrete system. Upon application of the GSP protocol, there is a heralded generation of bimode entangled optical states.

The second aspect of the study is the application of the GSP operated states as quantum channels in CV quantum teleportation. We have observed that the GSP operations enhance average fidelity of teleporting single-mode coherent and squeezed states using two-mode entangled channels obtained from single- and two-mode squeezed state inputs. The optimized GSP operation outperforms most non-Gaussian operations, in the low-squeezing regime, with regard to fidelity enhancement in CV teleportation. Interestingly, the GSP operation reduces the classical fidelity of teleportation across the two-mode GSP operated classical thermal and coherent channels. The maximum fidelity achieved using the coherent and thermal channels is the maximum classical capacity that is achieved without entangled resources. Hence, the CV teleportation protocol is enhanced for the quantum channel with a reduction in the fidelity arising from the classical channels. This result could prove immensely fruitful in the control of noise in experimental application of CV quantum teleportation. The experimental advances in the generation of photon-added and photon-subtracted field states ensure that the advantages of non-Gaussian operations will be put to further applications in the future. In the light of such developments the importance of theoretical studies on non-Gaussian states cannot be over-emphasized.

[1] H.S. Dhar, A. Chatterjee, and R. Ghosh, *Generating continuous variable entangled states for quantum teleportation using a superposition of number-conserving operations*, arXiv:1312.6226.

[2] S.L. Braunstein and P. van Loock, Rev. Mod. Phys. **77**, 513 (2005).

[3] H.J. Briegel, W. Dur, J.I. Cirac, and P. Zoller, Phys. Rev. Lett. **81**, 5932 (1998); D.Y. Vasylyev, A.A. Semenov, and W. Vogel, Phys. Rev. Lett. **108**, 220501 (2012).

[4] L. Vaidman, Phys. Rev. A **49**, 1473 (1994).

[5] S.L. Braunstein and H.J. Kimble, Phys. Rev. Lett. **80**, 869 (1998).

[6] M. Hillery, Phys. Rev. A **61**, 022309 (2000); D. Gottesman and J. Preskill, Phys. Rev. A **63**, 022309 (2001); M. Navascués, F. Grosshans, and Antonio Acín, Phys. Rev. Lett. **97**, 190502 (2006).

[7] A.I. Lvovsky, B.C. Sanders, and W. Tittel, Nature Photon. **3**, 706 (2009); K. Jensen, W. Wasilewski, H. Krauter, T. Fernholz, B. M. Nielsen, M. Owari, M. B. Plenio, A. Serani, M. M. Wolf, and E. S. Polzik, Nature Phys.**7**, 13 (2011).

[8] K. Hammerer, A.S. Søorensen, and E.S. Polzik, Rev. Mod. Phys. **82**, 1041 (2010);

[9] N.J. Cerf, G. Leuchs, and E.S. Polzik (eds.), *Quantum Information with Continuous Variables of Atoms and Light* (Imperial College Press, London, 2007).

[10] X.B. Wang, T. Hiroshima, A. Tomita, and M. Hayashi, Phys. Rep. **448**, 1 (2007).

[11] C. Weedbrook, S. Pirandola, R. García-Patrón, N.J. Cerf, T.C. Ralph, J.H. Shapiro, and S. Lloyd, Rev. Mod. Phys. **84**, 621 (2012).

[12] A. Zavatta, S. Viciani, and M. Bellini, Science **306**, 660 (2004).

[13] J. Wenger, R. Tualle-Brouri, and P. Grangier, Phys. Rev. Lett. **92**, 153601 (2004).

[14] A. Zavatta, V. Parigi, M.S. Kim, H. Jeong, and M. Bellini, Phys. Rev. Lett. **103**, 140406 (2009).

[15] A. Ourjoumtsev, A. Dantan, R. Tualle-Brouri, and P. Grangier, Phys. Rev. Lett. **98**, 030502 (2007); M. Takahashi, J.S. Neergaard-Nielsen, M. Takeuchi, M. Takeoka, K. Hayasaka, A. Furusawa, and M. Sasaki, Nature Photon. **4**, 178 (2010).

[16] T. Opatrny, G. Kurizki, and D.G. Welsch, Phys. Rev. A **61**, 032302 (2000); A. Kitagawa, M. Takeoka, M. Sasaki, and A. Chefles, Phys. Rev. A **73**, 042310 (2006).

[17] Y. Yang and F.L. Li, Phys. Rev. A **80**, 022315 (2009).

[18] J. Fiurášek, Phys. Rev. A **82**, 042331 (2010); C. Navarrete-Benlloch, R. García-Patrón, J.H. Shapiro, and N.J. Cerf, Phys. Rev. A **86**, 012328 (2012).

[19] G.S. Agarwal and K. Tara, Phys. Rev. A **43**, 492 (1991); S.S. Mizrahi and V.V. Dodonov, J. Phys. A: Math. Theor. **35**, 8847 (2002); A.R. Usha Devi, R. Prabhu, and M.S. Uma, Eur. Phys. J. D. **40**, 133 (2006); S.Y. Lee and H. Nha, Phys. Rev. A **82**, 053812 (2010).

[20] A. Chatterjee, H.S. Dhar, and R. Ghosh, J. Phys. B: At. Mol. Opt. Phys. **45** 205501 (2012).

[21] M.S. Kim, H. Jeong, A. Zavatta, V. Parigi, and M. Bellini, Phys. Rev. Lett. **101**, 260401 (2008).

[22] M.S. Kim, W. Son, V. Buzek, and P.L. Knight, Phys. Rev. A **65**, 032323 (2002).

[23] J.K. Asboth, J. Calsamiglia, and H. Ritsch, Phys. Rev. Lett. **94**, 173602 (2005).

[24] M.O. Scully and M.S. Zubairy, *Quantum Optics* (Cambridge University Press, Cambridge, 1997).

[25] C.H. Bennett, G. Brassard, C. Crépeau, R. Jozsa, A. Peres, and W.K. Wootters, Phys. Rev. Lett. **70**, 1895 (1993).

[26] A. Furusawa, J.L. Sorensen, S.L. Braunstein, C.A. Fuchs, H.J. Kimble, and E.S. Polzik, Science **282**, 706 (1998).

[27] S.L . Braunstein, C.A. Fuchs, H.J. Kimble, and P. van Loock, Phys. Rev. A **64**, 022321 (2001).

[28] F. Grosshans, P. Grangier, Phys. Rev. A **64**, 010301 (2001)(R).

[29] S.M. Barnett and P.M. Radmore, *Methods in Theoretical Quantum Optics* (Clarendon Press, Oxford, 1997).

[30] A.V. Chizhov, L. Knöll, and D.-G. Welsch, Phys. Rev. A **65**, 022310 (2002).

[31] P. Marian and T.A. Marian, Phys. Rev. A **74**, 042306 (2006).

[32] F. Dell'Anno, S.D. Siena, L.A. Farias, and F. Illuminati, Eur. Phys. J. -ST **160**, 115 (2008), and references therein.

[33] A. Einstein, B. Podolsky, and N. Rosen, Phys. Rev. **47**, 777 (1935).